

AD-A227 473

WRDC-TR-90-2020  
Volume II



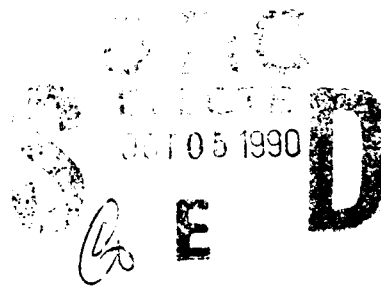
**ADVANCED STRUCTURAL INSTRUMENTATION**

Volume II

A. J. Dennis  
Graham B. Fulton  
United Technologies Research Center  
East Hartford, Connecticut

Final Report for Period Feb. 83 - Nov. 89

Approved for public release; distribution unlimited.



**AERO PROPULSION AND POWER LABORATORIES  
WRIGHT RESEARCH DEVELOPMENT CENTER  
AIR FORCE SYSTEMS COMMAND  
WRIGHT PATTERSON AIR FORCE BASE, OHIO 45433-6563**

## NOTICE

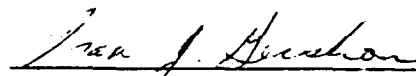
WHEN GOVERNMENT DRAWINGS, SPECIFICATIONS, OR OTHER DATA ARE USED FOR ANY PURPOSE OTHER THAN IN CONNECTION WITH A DEFINITELY GOVERNMENT-RELATED PROCUREMENT, THE UNITED STATES GOVERNMENT INCURS NO RESPONSIBILITY OR ANY OBLIGATION WHATSOEVER. THE FACT THAT THE GOVERNMENT MAY HAVE FORMULATED OR IN ANY WAY SUPPLIED THE SAID DRAWINGS, SPECIFICATIONS, OR OTHER DATA, IS NOT TO BE REGARDED BY IMPLICATION, OR OTHERWISE IN ANY MANNER CONSTRUED, AS LICENSING THE HOLDER, OR ANY OTHER PERSON OR CORPORATION; OR AS CONVEYING ANY RIGHTS OR PERMISSION TO MANUFACTURE, USE, OR SELL ANY PATENTED INVENTION THAT MAY IN ANY WAY BE RELATED THERETO.

THIS REPORT HAS BEEN REVIEWED BY THE OFFICE OF PUBLIC AFFAIRS (ASD/PA) AND IS RELEASABLE TO THE NATIONAL TECHNICAL INFORMATION SERVICE (NTIS). AT NTIS IT WILL BE AVAILABLE TO THE GENERAL PUBLIC INCLUDING FOREIGN NATIONS.

THIS TECHNICAL REPORT HAS BEEN REVIEWED AND IS APPROVED FOR PUBLICATION.

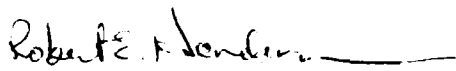


WILLIAM A. STANGE  
Project Engineer  
Components Branch  
Aero Propulsion and Power  
Laboratory



ISAK J. GERSHON  
Technical Area Manager  
Components Branch  
Aero Propulsion and Power  
Laboratory

FOR THE COMMANDER



ROBERT E. HENDERSON  
Deputy for Technology  
Turbine Engine Division  
Aero Propulsion and Power  
Laboratory

IF YOUR ADDRESS HAS CHANGED, IF YOU WISH TO BE REMOVED FROM OUR MAILING LIST, OR IF THE ADDRESSEE IS NO LONGER EMPLOYED BY YOUR ORGANIZATION PLEASE NOTIFY WRDC/POTC, WRIGHT-PATTERSON AFB, OH 45433-6563 TO HELP MAINTAIN A CURRENT MAILING LIST.

COPIES OF THIS REPORT SHOULD NOT BE RETURNED UNLESS RETURN IS REQUIRED BY SECURITY CONSIDERATIONS, CONTRACTUAL OBLIGATIONS, OR NOTICE ON A SPECIFIC DOCUMENT.

Unclassified

SECURITY CLASSIFICATION OF THIS PAGE

REPORT DOCUMENTATION PAGE				Form Approved OMB No. 0704-0188	
1a. REPORT SECURITY CLASSIFICATION <b>UNCLASSIFIED</b>			1b. RESTRICTIVE MARKINGS		
2a. SECURITY CLASSIFICATION AUTHORITY N/A		3. DISTRIBUTION/AVAILABILITY OF REPORT Approved for Public Release, Distribution Unlimited			
2b. DECLASSIFICATION/DOWNGRADING SCHEDULE					
4. PERFORMING ORGANIZATION REPORT NUMBER(S) R-89-2330			5. MONITORING ORGANIZATION REPORT NUMBER(S) WRDC-TR-90-2020, Vol. II		
5a. NAME OF PERFORMING ORGANIZATION United Technologies Research Center		6b. OFFICE SYMBOL (If applicable)	7a. NAME OF MONITORING ORGANIZATION Aero Propulsion and Power Laboratory (WRDC/POTC) Wright Research Development Center		
5c. ADDRESS (City, State, and ZIP Code) Silver Lane East Hartford CT 06108			7b. ADDRESS (City, State, and ZIP Code) WPAFB OH 45433-6563		
6a. NAME OF FUNDING SPONSORING ORGANIZATION Aero Propulsion and Power Laboratory		6b. OFFICE SYMBOL (If applicable) POTC	9. PROCUREMENT INSTRUMENT IDENTIFICATION NUMBER F33615-83-C-2330		
8c. ADDRESS (City, State, and ZIP Code) WRDC/POTC WPAFB OH 45433-6563			10. SOURCE OF FUNDING NUMBERS		
			PROGRAM ELEMENT NO. 62203F	PROJECT NO. 3066	TASK NO. 12
					WORK UNIT ACCESSION NO. 91
11. TITLE (Include Security Classification)  <b>ADVANCED STRUCTURAL INSTRUMENTATION, VOL. II</b>					
12. PERSONAL AUTHOR(S) A. J. Dennis and G. B. Fulton					
13a. TYPE OF REPORT FINAL		13b. TIME COVERED FROM Feb 83 TO Nov 89		14. DATE OF REPORT (Year, Month, Day) 90/06/11	15. PAGE COUNT 172
16. SUPPLEMENTARY NOTATION					
17. COCOSA CODES			18. SUBJECT TERMS (Continue on reverse if necessary and identify by block number)		
FIELD	GROUP	SUB-GROUP	Instrumentation, Static strain, Strain measurement, Temperature measurement, Sensors, Turbine measurements		
21	05				
14	01				
19. ABSTRACT (Continue on reverse if necessary and identify by block number)  This report presents the results of the development and test of a variety of steady-state strain and temperature sensors specifically aimed at application in hot sections of advanced gas turbines. In each case, the sensors have shown success in the laboratory, and tests and results described herein were designed to simulate the actual turbine environment. Most of the testing was carried out in the UTRC vacuum spin rig which was able to achieve speeds and temperatures characteristic of advanced gas turbines. Volume I is an overview of the sensors, physical description, summary comparison of results and conclusions and recommendations. Volume II gives the details of the sensor fabrication and installation as well as evaluation of the data acquired. The report is divided into the sections each of which gives the details of a specific sensor tested in this program.  (Continued)					
20. DISTRIBUTION/AVAILABILITY OF ABSTRACT <input checked="" type="checkbox"/> UNCLASSIFIED/UNLIMITED <input type="checkbox"/> SAME AS RPT <input type="checkbox"/> DTIC USERS			21. ABSTRACT SECURITY CLASSIFICATION Unclassified		
22a. NAME OF RESPONSIBLE INDIVIDUAL William A. Stange			22b. TELEPHONE (Include Area Code) (513) 255-2081		22c. OFFICE SYMBOL WRDC/POTC

DD Form 1473, JUN 86

Previous editions are obsolete.

SECURITY CLASSIFICATION OF THIS PAGE

UNCLASSIFIED

CONTINUATION from DD Form 1473, Block #19.

Temperature sensors tested in the present program include conventional wire thermocouples and an advanced type of thin film thermocouple deposited directly on the test piece. The temperature measuring capability of twin core optical fiber sensor technology has also been demonstrated. Remote sensing of temperature was achieved with a thermographic phosphor technique, and optical pyrometry was used as a control throughout the program. Additionally, the feasibility of advanced concept heat flux sensors on a turbine blade was demonstrated.

Advanced strain gages were also tested. Two types of wire strain gages were bonded to the turbine disk, the first, a conventional commercially available Nickel-Chrome alloy type, and the other, a modified FeCrAl alloy developed by the Chinese. Strain was also measured with several types of sputtered thin film sensors as well as the twin core optical fiber sensor. Speckle photogrammetry was used for noncontacting strain measurement throughout the spin rig testing.

Accession For	
NTIS GRA&I	<input checked="" type="checkbox"/>
DTIC TAB	<input type="checkbox"/>
Unannounced	<input type="checkbox"/>
Justification	
By _____	
Distribution/	
Availability Codes	
Dist	Avail and/or Special
A-1	

## CONTENTS

<u>Section</u>	<u>Page</u>
LIST OF TABLES .....	vi
LIST OF FIGURES .....	vii
<b>I. INTRODUCTION .....</b>	<b>1-1</b>
<b>II. STRAIN MEASUREMENT BY SPECKLE PHOTOGRAMMETRY OF ROTATING OBJECTS .....</b>	<b>2-1</b>
1. INTRODUCTION .....	2-1
2. INTERFEROMETRIC PHOTOCOMPARATOR .....	2-2
3. MATHEMATICAL THEORY .....	2-4
4. PHOTOCOMPARATOR PROCEDURE .....	2-7
5. BUILD 1 - SPECKLE PHOTOGRAMMETRY .....	2-8
6. DATA PROCESSING .....	2-11
7. DISCUSSION .....	2-14
8. CONCLUSIONS AND RECOMMENDATIONS FROM BUILD 1 .....	2-16
9. ADVANCED STRUCTURAL INSTRUMENTATION BUILD 2 - SPECKLE PHOTOGRAMMETRY .....	2-18
10. DATA PROCESSING .....	2-19
11. DISCUSSION .....	2-24
<b>III. HEAT FLUX SENSORS .....</b>	<b>3-1</b>
1. SUMMARY .....	3-1
2. INTRODUCTION .....	3-1
3. DESCRIPTION OF SENSORS .....	3-2
4. FABRICATION OF SENSORS INTO THE BLADES .....	3-4
5. CALIBRATION .....	3-6
6. TEST RESULTS .....	3-10
7. CONCLUSIONS AND RECOMMENDATIONS .....	3-12
8. REFERENCES .....	3-12

## CONTENTS (CONTINUED)

<u>Section</u>	<u>Page</u>
<b>IV. FIBER OPTIC SENSORS</b> .....	<b>4-1</b>
1. INTRODUCTION .....	4-1
2. BACKGROUND .....	4-1
3. SENSOR CONCEPT AND DEVELOPMENT .....	4-4
4. NONROTATING RISK REDUCTION TESTS—THE FERRIS WHEEL EXPERIMENT .....	4-12
5. ROTATING TESTS—THE SPIN RIG EXPERIMENT .....	4-22
6. DISCUSSION .....	4-33
APPENDIX A FERRIS WHEEL DATA BASE .....	4A-1
<b>V. RESISTANCE STRAIN GAGES</b> .....	<b>5-1</b>
1. INTRODUCTION .....	5-1
2. OBJECTIVE .....	5-1
3. STATE OF THE RESISTANCE STRAIN GAGE ART .....	5-2
4. APPROACH TO DEMONSTRATION TEST .....	5-4
5. DEMONSTRATION TESTS OF THE FeCrAl BHP-700C WIRE STRAIN GAGES .....	5-6
6. DEMONSTRATION TESTS OF THE PdCr SPUTTERED-FILM STRAIN GAGES .....	5-18
7. CONCLUDING REMARKS .....	5-40
8. ACKNOWLEDGEMENTS .....	5-41
9. BIBLIOGRAPHY .....	5-41
<b>VI. TEST FACILITY</b> .....	<b>6-1</b>
1. ABSTRACT .....	6-1
2. INTRODUCTION .....	6-1
3. SPIN RIG DESCRIPTION .....	6-2
4. MODIFICATIONS FOR HEATED TESTS .....	6-7
5. TEST HARDWARE .....	6-14
6. DATA ACQUISITION SYSTEM .....	6-15
7. TEST PROCEDURE .....	6-21
8. CONCLUDING REMARKS .....	6-22
9. REFERENCE .....	6-22
APPENDIX A DATA ACQUISITION SYSTEM COMPONENT SPECIFICATIONS .....	6A-1
<b>VII. DISK STRESS ANALYSIS</b> .....	<b>7-1</b>

## TABLES

<u>Table</u>		<u>Page</u>
1.	Speeds and temperatures at which data were taken .....	2-11
2.	Tsss measured sensor response (unattached devices) .....	4-12
3.	Sensor inventory; Ferris wheel experiment .....	4-17
4.	Instrumentation; Ferris wheel experiment .....	4-17
5.	Load and strain relation .....	4-19
6.	Spin rig sensor parameters .....	4-24
7.	Analytically predicted, unattached calibration constants and response (per inch of sensor length) .....	4-25
8.	Test summary spin test of wire-form static strain gages .....	5-11
9.	Test summary static test of sputtered-film static strain gages .....	5-26
10.	Test summary spin test 2; sputtered-film static strain gages .....	5-30
11.	Test summary spin test 3; sputtered-film static strain gages .....	5-37

## FIGURES

<u>Figure</u>		<u>Page</u>
2-1.	Protocomparator block diagram. ....	2-3
2-2.	Specklegram schematic. ....	2-4
2-3.	Optical arrangement in spin rig. ....	2-9
2-4.	Laser control schematic. ....	2-10
2-5.	Build 1 strain vs. speed squared, 300 K. ....	2-12
2-6.	Build 1 strain vs. speed squared, 422 K. ....	2-13
2-7.	Build 1 strain vs. speed squared, 589 K. ....	2-13
2-8.	Build 1 strain vs. speed squared, 755 K. ....	2-14
2-9.	Build 1 effect of gage length on measured strain for various temperatures. ....	2-17
2-10.	Build 2, strain vs. speed squared. Ambient temperature, clockwise rotation. ....	2-25
2-11.	Build 2, strain vs. speed squared. Ambient temperature, counterclockwise rotation. ....	2-25
2-12.	Build 2, strain vs. speed squared. 422 K temperature, counterclockwise rotation. ....	2-26
2-13.	Build 2, strain vs. speed squared. 589 K temperature, counterclockwise rotation. ....	2-26
2-14.	Build 2, strain vs. speed squared. 755 K temperature, counterclockwise rotation. ....	2-27
2-15.	Build 2, strain vs. speed squared. 950 K temperature, counterclockwise rotation. ....	2-27
3-1.	Schematic of the embedded thermocouple heat flux sensor. ....	3-3
3-2.	Schematic of the Gardon gauge heat flux sensor. ....	3-4
3-3.	High intensity quartz lamp bank. ....	3-7

## FIGURES (Continued)

3-4.	Airfoil positioned in quartz lamp rig with water-cooled shields - bottom view. ....	3-7
3-5.	Airfoil positioned in quartz lamp rig with water-cooled shields - side view. ....	3-8
3-6.	High intensity quartz lamp rig. ....	3-9
3-7.	Calibration data for embedded thermocouple sensor. ....	3-11
3-8.	Data from two sensors from the advanced structural instrumentation spin test. ....	3-11
3-9.	AC noise level on heat flux sensor output. ....	3-13
3-10.	Leadwire failure at airfoil exit. ....	3-13
3-11.	Failure of leadwire external to airfoil. ....	3-14
4-1.	Fiber optic strain sensor. Typical engine layout. ....	4-2
4-2.	Fiber optic strain sensor. Disk environment. ....	4-2
4-3.	Optical fiber sensor technology development. ....	4-5
4-4.	Twin-core fiber optic sensor concept. ....	4-6
4-5.	Strain and temperature response. ....	4-6
4-6.	Instrumentation concept. ....	4-7
4-7.	Twin core optical fiber sensor. Germanium-doped silica sensor with aluminosilicate compressive layer. ....	4-9
4-8.	Apparatus for metal coating. ....	4-10
4-9.	Fiber optic strain sensor. Multi-mode output fiber cross section. ....	4-10
4-10.	Fiber optic strain sensor. Basic optical unit design. ....	4-11
4-11.	Fiber optic strain sensor. Fully assembled sensor using fusion-splice technique. ....	4-12
4-12.	Comparison of measured and computed strain sensitivity. ....	4-13

## FIGURES (Continued)

4-13.	Twin-core fiber optic sensor. Predicted and measured temperature sensitivity. ....	4-13
4-14.	Twin-core optical fiber sensor. Ferris wheel experiment; F 100 disk. ....	4-14
4-15.	Fiber optic strain sensor. Attachment study. ....	4-15
4-16.	Fiber optic strain sensor. Attachment study (sample 10A-2 GA-100). ....	4-16
4-17.	Sensor array. Ferris wheel experiment. ....	4-16
4-18.	Twin-core optical fiber sensor. Ferris wheel Experimental Facility. ....	4-18
4-19.	Ferris wheel test program. ....	4-20
4-20.	Twin-core optical fiber sensor. Temperature response. Ferris wheel data; run No. 4, sensor 6, 633 nm. ....	4-20
4-21.	Twin-core optical fiber sensor. Load response at 589 K, run No. 4, sensor 6, 633 nm. ....	4-21
4-22.	Twin-core optical fiber sensor. Temperature response. Ferris wheel data; run No. 10, sensor 6, 830 nm. ....	4-21
4-23.	Twin-core optical fiber sensor. Load response at 933 K. Ferris wheel data; run No. 10, sensor 6, 830 nm. ....	4-22
4-24.	Twin-core sensors. Ferris wheel test; modified F100 disk with sensors No. 6, 5, 4. ....	4-23
4-25.	Detailed empirical model. Calibration constants. ....	4-26
4-26.	Detailed empirical model. Crosstalk vs. wavelength; WPB No. 6, L = 38.6 mm, OD = 186 mm, spectran No. 4. ....	4-26
4-27.	Detailed empirical model. WPB No. 6; L = 38.6 mm, OD = 186 mm, spectran No. 4. ....	4-27
4-28.	Detailed empirical model. WPB No. 6; L = 38.6 mm, OD = 186 mm, spectran No. 4. ....	4-27
4-29.	Detailed empirical model. Strain and temperature sensitivity coefficients. WPB No. 6; L = 38.6 mm, OD = 186 mm, spectran No. 4. ....	4-28

## FIGURES (Continued)

4-30.	Twin-core optical fiber sensor. Temperature response; WPB No. 6, unattached. ....	4-29
4-31.	Twin-core optical fiber sensor. Flame-spray attachment to Modified F100 turbine disk. ....	4-29
4-32.	Twin-core optical fiber sensor. Miniature 2 - $\lambda$ transmitter; version 1. ....	4-31
4-33.	Twin-core optical fiber sensor. Miniature 2 - $\lambda$ transmitter; version 2. ....	4-31
4-34.	Twin-core optical fiber sensor. Miniature 2 - $\lambda$ receiver. ....	4-32
4-35.	Twin-core optical fiber sensor. Spin rig experiment. ....	4-32
4-36.	Spin rig test program. Build 3/4 B. ....	4-33
4-37.	Twin-core optical fiber sensor. Temperature response at 1000 r/min. Spin rig data; run No. 5, 830 nm. ....	4-34
4-38.	Twin-core optical fiber sensor. Load response at 422 K. Spin rig data; run No. 5, 830 nm. ....	4-34
4-39.	Twin-core optical fiber sensor. Load response at 589 K. Spin rig data; run No. 830 nm. ....	4-35
4-40.	Sensor comparison 152 mm radius, 6600 r/min. ....	4-36
4-41.	Sensor comparison. Twin-core and speckle data superposed. ....	4-38
4-42.	Sensor comparison. Twin-core and speckle data superposed. ....	4-38
4A-1.	Twin-core optical fiber sensor. ....	4A-3
4A-2.	Twin-core optical fiber sensor. ....	4A-4
4A-3.	Twin-core optical fiber sensor. ....	4A-5
4A-4.	Twin-core optical fiber sensor. ....	4A-6
5-1.	The wire strain gage configuration used is 3 millimeters by 3 millimeters. ....	5-3
5-2.	Metallurgical instability data for five strain gage alloys. ....	5-3

## FIGURES (Continued)

5-3.	Change in resistance vs. temperature after different soak times at 1250 K for a sample FeCrAl Alloy (Fe-11Cr-12Al).	5-5
5-4.	Change in resistance vs. temperature after different soak times for a sample PdCr alloy (Pd-16Cr-8Co).	5-5
5-5.	Pretest photo before 950 K spin test 2.	5-7
5-6.	Gage factor vs. temperature for one of four wire strain gages mounted on a cantilever bend test bar of Inconel 718.	5-8
5-7.	Apparent strain vs. temperature during cool-down for one of three wire strain gages mounted on a flat rectangular test bar of IN100 turbine disk material.	5-8
5-8.	Temperature vs. time for four cooldown rates for which apparent strains were measured.	5-9
5-9.	Detailed photo after the 950 K spin test 2. The wire gage installation shows no visible major deterioration.	5-10
5-10a.	Spin test strain data obtained at 165 millimeter radius, versus $r/min$ .	5-13
5-10b.	Conclusion of data at 165 millimeter radius.	5-14
5-11a.	Spin test strain data obtained at 152 millimeter radius, versus $r/min$ .	5-15
5-11b.	Conclusion of data at 152 millimeter radius.	5-16
5-12.	Four thin-film gages mounted on a test bar for gage factor testing.	5-19
5-13.	Good strain transfer is demonstrated in tension (+) and compression (-) from the test bar to the welded gages.	5-21
5-14.	Pretest photo of the turbine disk installed in the P&W heated "Ferris wheel" rig for static radial loading tests.	5-21
5-15.	An example of catastrophic delamination of the Si <sub>3</sub> N <sub>4</sub> sputtered insulation at 950 K during a preliminary trial of the foil-mounted gages on a turbine disk.	5-22
5-16.	Pretest photo before 950 K static Ferris wheel test.	5-23
5-17.	Measured strain vs Ferris wheel radial load.	5-23

## FIGURES (Continued)

5-18.	Post-test photo after the 950 K static Ferris wheel test. ....	5-25
5-19.	Detailed pretest photo before 950 K spin test 2. ....	5-27
5-20.	Post-test photo after the 950 K spin test 2. ....	5-28
5-21.	Detailed pretest photo before 950 K spin test 3, before cementing of lead wires. ....	5-33
5-22.	Pretest photo before 950 K spin test 3 of the completed installation of the overcoated thin-film strain gages. ....	5-34
5-23.	Post-test detailed view of the overcoated thin-film strain gages after 950 K spin test 3. ....	5-35
6-1.	Overall view of UTRC spin rig. ....	6-2
6-2.	UTRC spin rig cross-sectional schematic. ....	6-3
6-3.	Drive spindle and bearing support system. ....	6-4
6-4.	Spin rig fluid systems. ....	6-6
6-5.	Section through the hot chamber. ....	6-8
6-6.	Induction heater load cell. ....	6-8
6-7.	Uncooled rotating junction can configuration for Build 1. ....	6-10
6-8.	Water cooled junction can with labyrinth shield. ....	6-11
6-9.	Final configuration of junction can. ....	6-12
6-10.	Comparison of disk and junction temperatures. ....	6-13
6-11.	Cross-sectional view of a test rotor. ....	6-15
6-12.	Data acquisition schematic. ....	6-16
6-13.	Strain gage bridge arrangement. ....	6-17
6-14.	Test sequence for static strain. ....	6-19
7-1.	HPT module. ....	7-2

## FIGURES (Concluded)

7-2.	Cross-sectional view of test rotor. ....	7-3
7-3.	Finite element model of spin test disk. ....	7-3
7-4.	Assumed disk temperature gradients. ....	7-4
7-5a.	Radial strain at gage locations vs. thermal gradient, 13,200 r/min. ....	7-4
7-5b.	CIRC strain at gage locations vs. thermal gradient, 13,200 r/min. ....	7-5

## I. INTRODUCTION

The new generation of gas turbines being introduced into service are operating at unprecedented levels of temperature and speed, levels which are dictated by the demand for improved performance and reduced fuel consumption. At the same time, it is required to achieve the higher levels of performance with no degradation of durability. The materials used in the hot section environment of these engines are working in a regime where small changes in temperature or stress have large effects on component life. We must, therefore, develop instrumentation technology to accurately and reliably measure strain and temperature in the hostile turbine environment so that component life may be accurately predicted.

This report presents the results of the development and test of a variety of sensors specifically aimed at application in the hot sections of advanced gas turbines. In each case, the sensors have shown success in the laboratory, and the tests and results described herein were designed to simulate the actual turbine environment. Volume I is an overview of the sensors, physical description, summary comparison of results, and conclusions and recommendations. Volume II gives the details of the sensor fabrication and installation as well as evaluates the data acquired. The report is divided into the sections tabulated below, with the principal authors, each one of which gives the details of a specific sensor tested in this program.

<u>SECTION</u>	<u>TITLE</u>	<u>AUTHOR</u>
I	Introduction	
II	Speckle Photogrammetry	K. Stetson, UTRC
III	Heat Flux Sensors	R. Strange, W. Atkinson, P&WA
IV	Fiber Optic Sensors	J. Dunphy, UTRC
V	Resistance Strain Gages	H. P. Grant, W. L. Anderson, J. S. Przybyszewski, P&WA
VI	Test Facility	A. J. Dennis, G. Fulton, UTRC
VII	Disk Stress Analysis	G. Fulton/T. Vasko, UTRC

## II. STRAIN MEASUREMENT BY SPECKLE PHOTOGRAMMETRY OF ROTATING OBJECTS

### 1. INTRODUCTION

a. Technical Concept—Speckle photogrammetry is a noncontact method to measure strain particularly useful at high temperatures. The technique involves illuminating the sample with laser light and photographically recording its image through a telecentric lens system. The random scattering of the laser light by the object surface causes a speckle pattern to form in the photographic image that uniquely identifies each area on the object surface. A heterodyne interferometer is used as a high precision photocomparator to measure small differential displacements between pairs of photographs (specklegrams). Comparison of specklegrams taken before and after a stress is applied to an object can reveal two-dimensional strain patterns over a substantial surface area. This technique has a definite advantage in the study of objects at high temperatures because the surface of the object itself is measured without any strain sensor materials having to be bonded to it.

Previous work has demonstrated that this technique can be applied with good results on laboratory samples up to 1140 K. Two-dimensional strains have been measured up to 1.4 percent with accuracies of a few hundred microstrain and gage lengths of 5 mm (0.2 in.).

b. Application to Rotating Components - Basic Approach—The first problem to be faced in applying speckle photogrammetry to rotating objects is how to deal with the rotational motion of the object. One solution is to photograph the object through an image derotator, which can be set to remove the rotational movement. Certain practical difficulties arise with this approach, however, in that axial illumination and viewing of the object are required. This further requires that the center of rotation be at the center of the image field. Because of the limited amount of resolution of the image derotator, it is impossible to obtain an effective closeup of an eccentric segment of the object.

An alternative is to record a direct image of the object at the radius desired and employ a very short laser pulse to stop the image motion. As an example, an object point at a 300-mm radius, rotating at 11,000 r/min, will translate 7  $\mu\text{m}$  during a 20-nsec Q-switched laser pulse. This is less than the resolution limit of an  $f/20$  imaging system. The next problem that is encountered is synchronization of

the laser firing so that the object is in the same position with respect to the optical system on each successive exposure. This synchronizaiton may be achieved to within a few microseconds, and the object position can be held to within a millimeter or so, which is adequate.

(1) Illumination and Observation Geometries--The illumination and observation of a rotating turbine disk must be accomplished according to certain restrictions if a successful speckle photogrammetry is to be achieved. The observation by the telecentric lens should be normal to the plane of rotation of the disk. The viewing port should be of optical quality fused silica to minimize distortions due to thermal effects on the window.

The illumination of the disk must be such that the speckles formed at the entrance of the lens move as little as possible because of the rotation of the disk. This can be determined by the correspondence between speckle motion and fringe localization in hologram interferometry. We know that if the disk is illuminated from a point along the axis of rotation, the locus of zero speckle motion will be a line from the center of the disk that is nearly complementary to the central illumination ray.

A telecentric lens system was designed to be compatible with the long working distance required (up to 600 mm) in the spin rig. The computer optimization was performed with the viewing port window as part of the optical system.

The following sections include a discussion of the photo comparator which was used to analyze the data, the calculations used to determine strain from the specklegrams and discussion of the test data from the spin rig builds.

## **2. INTERFEROMETRIC PHOTOCOMPARATOR**

The system used for evaluating the specklegrams is shown in the block diagram of Figure 2-1. This symmetrical arrangement of six mirrors and two beamsplitters provides a stable and adjustable configuration that allows equal paths between the beamsplitters while allowing the specklegrams to be mounted in the same plane and equidistant from the output beamsplitter. The eight components are grouped into input and output sections, comprising those before and after the specklegrams respectively. The components of each section are mounted on a common platform for stability. Each

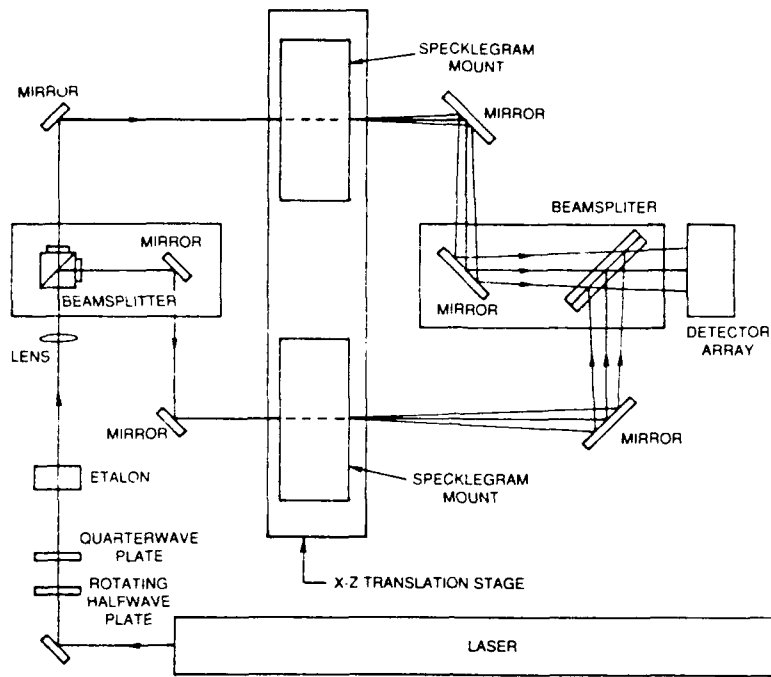


Figure 2-1. Protocomparator block diagram.

beamsplitter and the central mirror near it are mounted on a common translation stage for centering adjustment. All mirrors and beamsplitters are adjustable for tilt. These adjustments make it possible to align all beams so as to lie in a common plane.

The optics before the interferometer consist of a lens to focus the beam at the plane of the output detectors, an etalon for translating the beam, and an arrangement for generating a Doppler shift. The Doppler shift is generated by a rotating halfwave plate followed by a quarterwave plate set at  $45^\circ$  to the vertical axis. The etalon is rotated either about a horizontal axis to translate the beam vertically or about a vertical axis to translate it horizontally.

The specklegrams are mounted on an X/Z translation stage to position them so that the beam passes through the spot where a strain measurement is desired. Each mount has horizontal and vertical translation adjustments as well as a rotation adjustment which allows a new specklegram to be placed on it and aligned with the one on the other stage.

The output detector array consists of 24 silicon photodiodes, each with an amplifier. These are connected to a multiplexer that connects diametral pairs to a pair of high-Q filters which feed their signals to a phase meter. The phase meter, the multiplexer, the X/Z translation stages, and the etalons are all under computer control so that the system can operate automatically once a pair of specklegrams have been aligned in the system.

### 3. MATHEMATICAL THEORY

The calculations for strain can be described from Figure 2-2. The two specklegrams appear

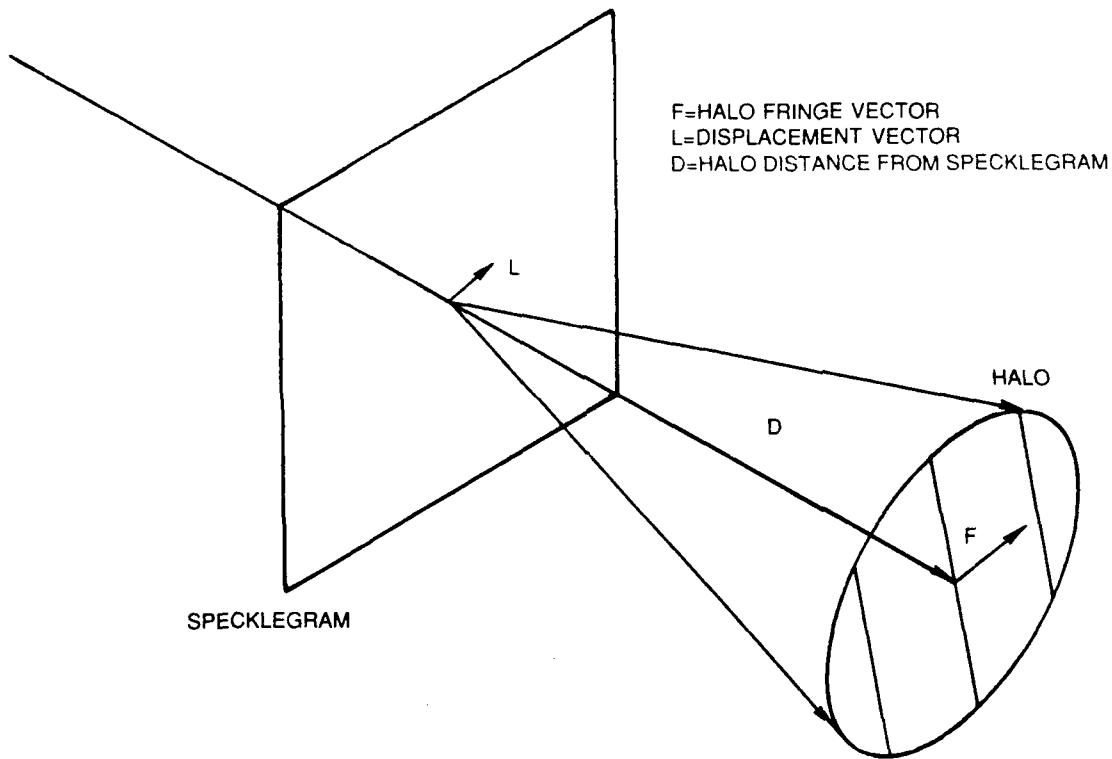


Figure 2-2. Specklegram schematic.

superposed when viewed through the output beamsplitter, except for the small displacement,  $L$ . This displacement generates the fringes seen in the halo which may be described by the fringe vector,  $F$ , from the center of the halo to the first bright fringe. These vectors are related by the equation

$$L = \lambda DF, \quad (1)$$

where  $D$  is the distance from the specklegram plane to the halo plane. Taking the differential of Eq. (1) gives

$$\Delta L = \lambda D \Delta F, \quad (2)$$

If the object was strained between the two specklegram recordings, a small shift of the readout beam,  $\Delta R$ , will generate the differential displacement according to

$$\Delta L \approx \{f\} \Delta F, \quad (3)$$

where  $\{f\}$  is a matrix describing the inplane strains  $\{\epsilon\}$  and rotations  $\{\theta\}$ , i.e.,

$$\{f\} = \{\epsilon\} + \{\theta\}. \quad (4)$$

Combining Eqs. (2) and (3) gives

$$\{f\} \Delta R = \lambda D \Delta F \quad (5)$$

Equation (5) can be written for each of two orthogonal displacements of the readout beam and these equations can be combined into a matrix equation which can be solved for the strain rotation matrix.

$$\{f\} = \lambda D \{\Delta F\} \{\Delta R\}^{-1}. \quad (6)$$

If the x and y scans are equal and have the magnitude  $\Delta S$ , then the matrix  $\{\Delta R\} = \{I\} \Delta S$  where  $\{I\}$  is an identity matrix. From this we may rewrite Eq. (6) as

$$\{f\} = \{\Delta F\} \lambda D / \Delta S. \quad (7)$$

Now let us compute the scalar phase change between two detectors in the halo as a result of the scan of the readout beam. This may be written as

$$\phi = \Delta t / \tau = d \cdot \Delta F, \quad (8)$$

where  $d$  is the vectorial separation between the two detectors in the halo,  $\Delta t$  is the time between zero crossings of their signals, and  $\tau$  is the signal period. We wish to find the  $\Delta F$  that best fits the data from detector pairs. Arranging the  $\Delta t$  measurements into a vector,  $(\Delta t)$ , and the detector separations into a matrix,  $\{d\}$ , we may solve for the  $\Delta F$  that gives least square error by

$$\Delta F = (1/\tau) \{d^T d\}^{-1} \{d^T\} (\Delta t). \quad (9)$$

Substituting this into Eq. (7) gives

$$\{f\} = (\lambda D / \tau \Delta S) \{d^T d\}^{-1} \{d^T\} \{\Delta t\}. \quad (10)$$

This is the equation used to compute the strains and rotations from the output measurements of the interferometer. The strains are obtained by taking the symmetrical portion of  $\{f\}$ , i.e.,

$$\{\epsilon\} = [\{f^T\}] / 2. \quad (11)$$

#### 4. PHOTOCOMPARATOR PROCEDURE

This is a description of the procedure followed with the *photocomparator*. First, the two specklegrams to be compared were placed in their holders on the X/Z translation stage with the radial direction vertical. The position and angle of one was adjusted until the two images seen through the beamsplitter merged. This was adequate to obtain halo fringes which were used to make fine adjustments. The position and angle of one specklegram was adjusted until the fringes were as broad as possible with the best possible contrast when the beam passed through the center of the region of interest. A further check on the angular alignment was obtained by moving the stage so as to scan the beam across the specklegrams. The best angular alignment was when the fringes did not rotate with the scan.

Four points were located at the 152-mm radius and four at the 165-mm radius. The stage coordinates that positioned these points under the readout beam were recorded, and these were stored in the computer. The program was initialized and ran. This consisted of moving the stages to the first point, rotating the etalon to scan the beam up, down, and back up, followed by left, right and back to left. The total beam scan was 1.3 mm. All detector pairs were read at each of the six positions and the

data stored. Values for  $\Delta t$  were computed from the first three, and the second three values for each detector pair by the formula

$$\Delta t = (\Delta t_1 + \Delta t_3 - 2\Delta T_2)/2, \quad (12)$$

which compensated for linear drift of the readings. The two values for  $\Delta t$  obtained became elements for the  $\{\Delta t\}$  matrix in the computation of Eq. (10). The strain-rotation matrix was calculated for each point and the four points at each radius were averaged to reduce errors. The symmetrical portions of the matrices were taken as the strains. Generally, the shear terms were negligible indicating that the principle strain axes were radial and circumferential.

## 5. BUILD 1 - SPECKLE PHOTOGRAMMETRY

a. Data Recording—During Build 1 of this contract, the UTRC speckle photogrammetry system was used to record data on the turbine disk. The system assembled at the spin rig included:

1. Q-Switched Pulsed Ruby Laser (JK Lasers, Ltd., Output of 10 J in 30 nsec)
2. Specklegram Recording System
3. Programmable Control Box for Laser Firing and Operation of the Recording System

The laser system consisted of a laser head, cooling system, flash lamp firing electronics, and Q-switch firing electronics. An external cooling source (in the form of an ice bath) had to be provided to the laser cooling system because the local tap water was too warm. The specklegram recording system consisted of a telecentric lens system with electronic shutter, a photographic plate changer, a 45° mirror to rotate the vertical lens axis 90° to the plate changer, and two high power mirrors and a diverging lens to direct the illuminating beam to the disk. The 45° mirror mount also held an alphanumeric display and relay lens to allow run number, plate number, and rotation speed to be printed on each plate. This system is diagrammed in Figure 2-3.

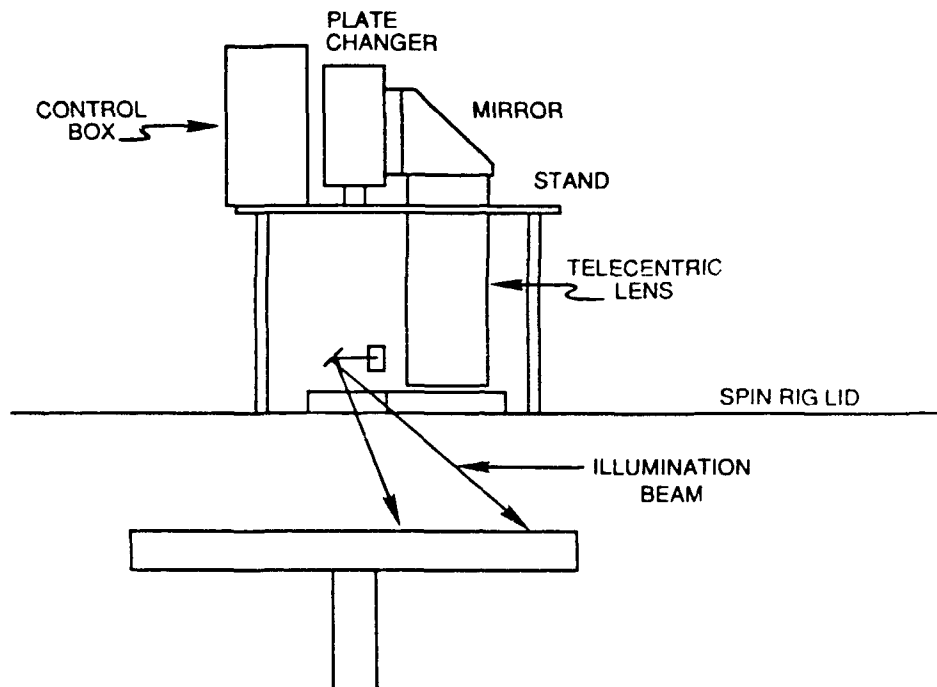


Figure 2-3. Optical arrangement in spin rig.

The programmable control box was interconnected with the system as indicated in Figure 2-4. Timing pulses from the spin rig (1/rev) were received by the control box and synchronized by a phase-lock loop so as to provide a precursor pulse to fire the flash lamps a set time before the timing pulse. These pairs of flash lamp and timing pulses were fed through gates to the laser flash lamp firing controls and the Q-switch firing control. (The latter had to be added to the laser control box from information provided by the manufacturer.) When the fire button was pushed, a command was sent to the shutter to open it and to start a counter to measure the spin rig speed. The flash synchronization switch on the shutter sent a signal to open the gates that inhibited the flash lamp and Q-switch signals. This allowed the next pair of pulses to fire the laser (provided the system is in phase lock) after which the shutter closed. The output of the laser was monitored on an oscilloscope, and, if a laser pulse had occurred, a keyboard command continued the sequence which printed the information on the plate and advanced the plate changer. If no pulse occurred, the system was reset and the unexposed plate used again.

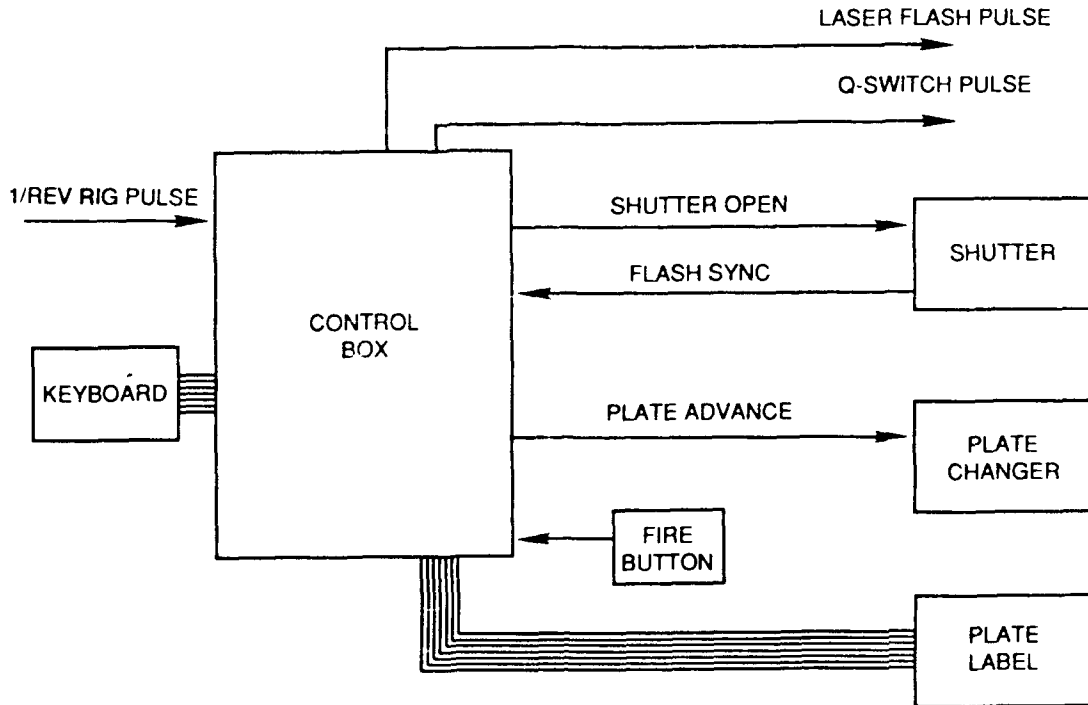


Figure 2-4. Laser control schematic.

Initial exposures showed large image shifts between photographs at different speeds due to a large time delay in the signal from the spin rig. After this was eliminated, the image shift between lowest (1620 r/min) and highest (13,200 r/min) speeds was in the order of 5 mm, which corresponds to about 25  $\mu$ s delay. Difficulties were also experienced with the plate changer, which required replacement of four internal springs. Difficulties were also experienced with the spin rig heaters and with the actuator that opened the view to the heated chamber.

Data were taken at five speeds at each of four temperatures. The target speeds were:

1600 r/min - plate 1    6600 r/min - plate 2    9330 r/min - plate 3

11430 r/min - plate 4    13200 r/min - plate 5

These were chosen to give equal increments in the square of rotation speed and thus equal increments in stress to the disk.

## 6. DATA PROCESSING

The photographs were developed in HC110B Developer after which they were inspected for image correlation. After this they were converted to dichromated gelatin images for use in the heterodyne photocomparator. Due to three errors the following data points were not obtained:

1. Ambient Temperature - Plates 3 and 4.

The plate changer did not advance after plate 3 was exposed. the reason for this was never determined, and it did not happen again.

Plates 2 and 5 were analyzed and provided data that bridged this gap.

2. 589 K - Plate 1.

Plate 1 was missed when the plate transport was unloaded for development. Plate 2 at ambient temperature was compared with plate 2 at 589 K to provide a reference for the 589 K run. Isotropic expansion due to the temperature change was subtracted from the resultant data.

3. 589 K - Plate 3.

Plate 3 was loaded into its holder glass side out and exposed backwards. Plates 2 and 4 were analyzed to bridge this gap.

The actual speeds at which useable data were recorded are tabulated below in Table 1.

**TABLE 1. SPEEDS AND TEMPERATURES AT WHICH DATA WERE TAKEN**

	<b>300 K</b>	<b>422 K</b>	<b>589 K</b>	<b>755 K</b>
1.	1680	1630	1590	
2.	6870	6770	6610	6550
3.	9420	9250		
4.	11,490	11,340	11,320	
5.	13,480	13,320	13,110	13,170

Eight points were located on a spare photograph, points 1 - 4 at a radius of 165 mm from the center of the disk and points 5 - 8 at a radius of 152 mm. This plate was placed in the comparator and the stages moved until the readout beam passed through each point.

This allowed the desired stage positions to be entered into the computer. The plate was also used as a reference to assure that the plates from each data run were evaluated at the same locations.

Pairs of data plates were placed in the photocomparator and aligned, after which they were processed for differential strain. The strain results for each location were printed and stored in the computer. The results for points 1 - 4 (165 mm radius) were averaged as were the results for points 5 - 8 (152 mm radius). The averages are plotted versus the square of rotation speed  $[\text{r/min}]^2$  in Figures 2-5.

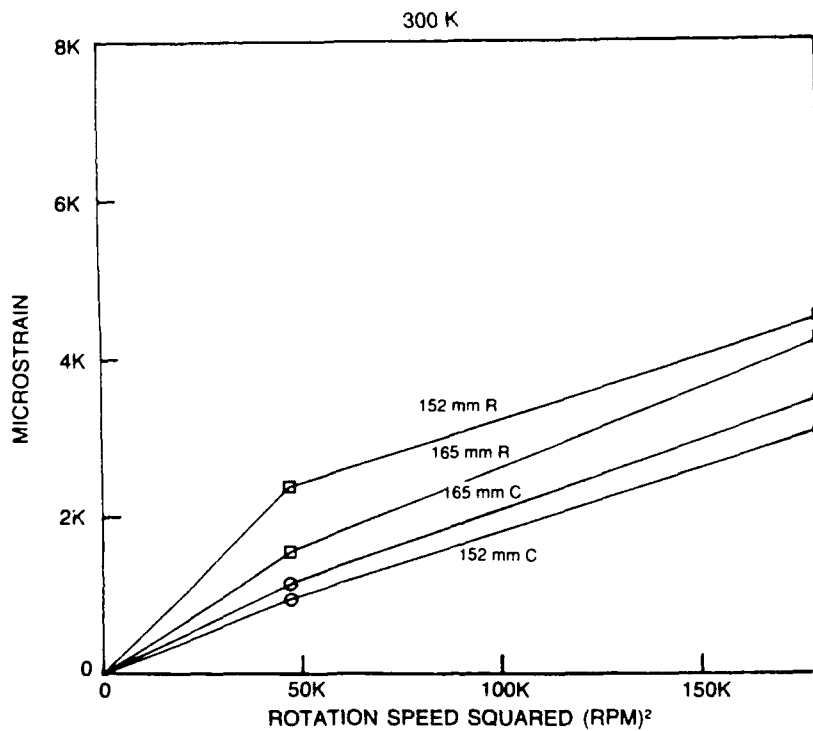


Figure 2-5. Build 1 strain vs. speed squared, 300 K.

2-6, 2-7, and 2-8 corresponding to temperatures of 300 K, 422 K, 589 K, and 755 K respectively. The curves plotted are labeled according to radius (165 mm or 152 mm) and strain orientation (R = radial and C = circumferential).

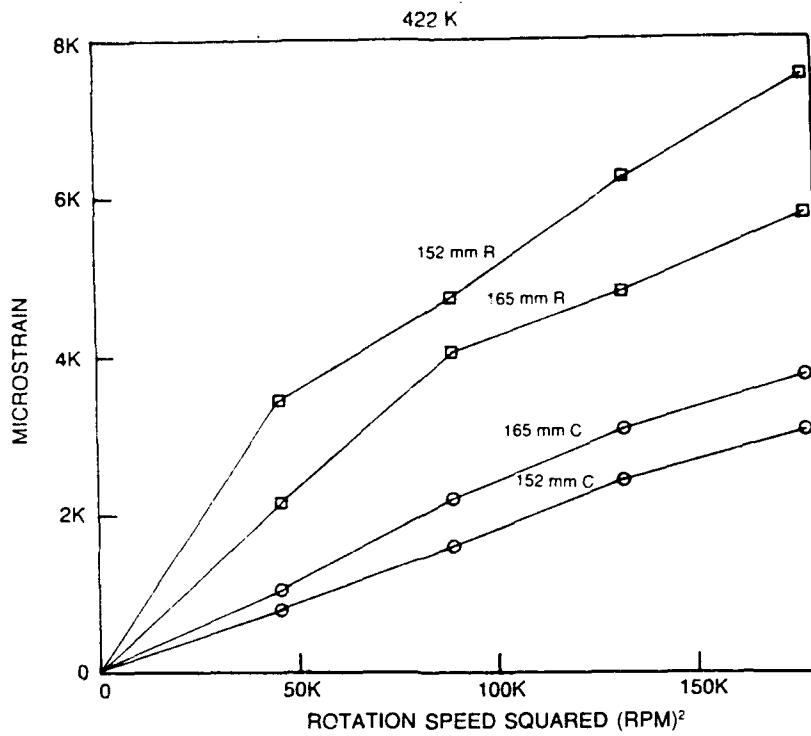


Figure 2-6. Build 1 strain vs. speed squared, 422 K.

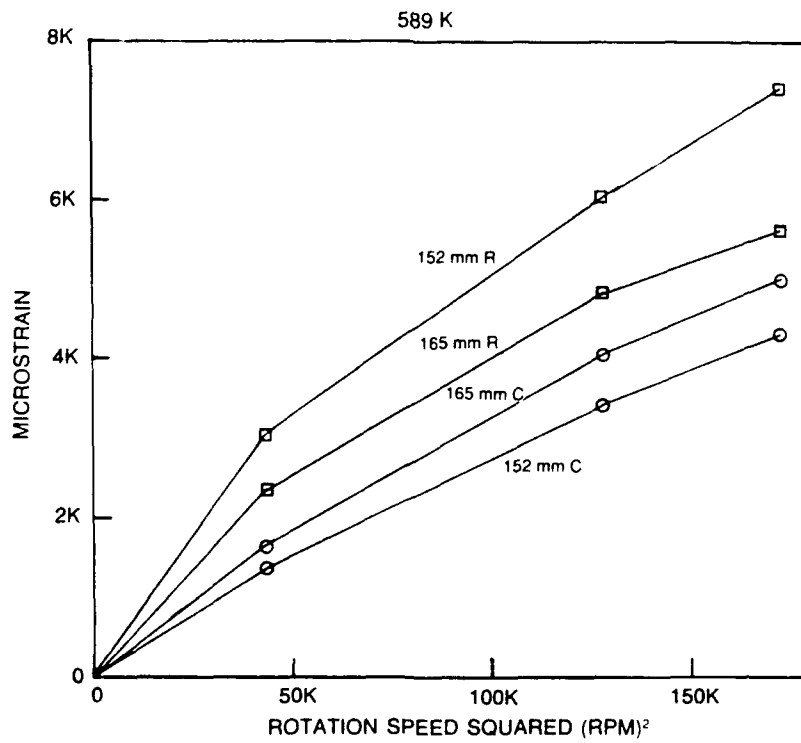


Figure 2-7. Build 1 strain vs. speed squared, 589 K.

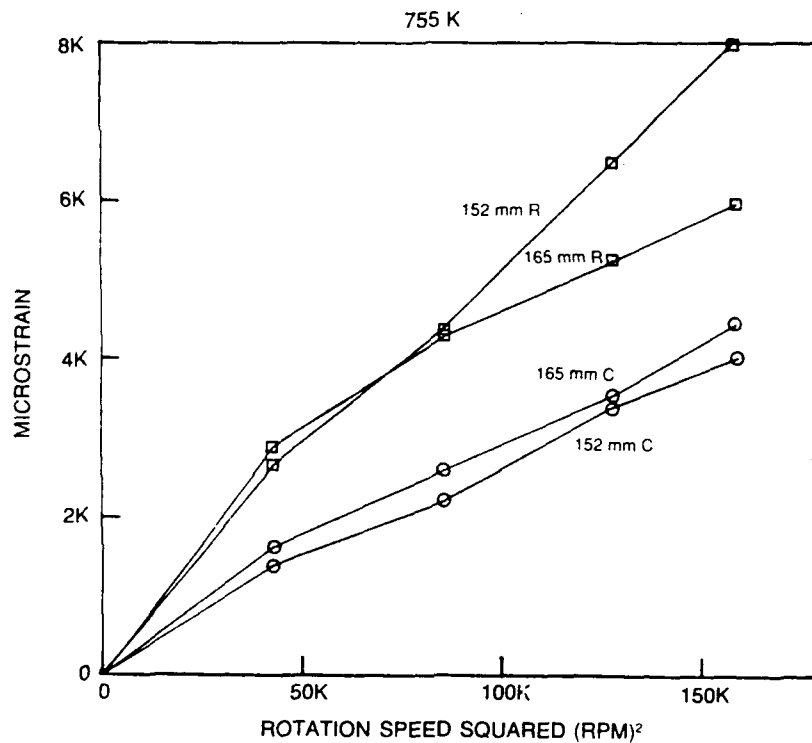


Figure 2-8. Build 1 strain vs. speed squared, 755 K.

## 7. DISCUSSION

The results plotted in Figures 2-5 through 2-8 show excessively large values for the radial strains, particularly at the three elevated temperatures. The peak strains measured would correspond to values of stress greater than  $1380 \text{ MNm}^{-2}$ , which should cause the disk to yield. Also, the slopes of the radial strain plots decrease as the square of speed increases. This appears to indicate the presence of an apparent radial strain that is directly proportional to speed and not related to stress. To estimate the magnitude of this apparent strain, the data at each temperature were fit to the following function:

$$\text{Strain} = A [\text{speed}] + B [\text{speed}]^2, \quad (13)$$

where A and B are coefficients determined by a least-square-error fit. The average value of the linear component of radial strain is approximately  $4.1 \times 10^{-2}$ .

The only thing within the entire setup that varies linearly with speed is the angular position of the disk. This was measured to be about 30 mrad between low speed and full speed. It is generated by the 25  $\mu$ s delay between the once-per-revolution pulse of the rig and the laser light pulse. If the object surface were exactly focused on the photographic plate, this translation and rotation would have no effect on the process because speckles observed on the surface of the object cannot move relative to that surface. Speckles observed above or below the object surface may exhibit slewing due to tilts of the object surface, but this effect is generally a uniform speckle translation that does not generate apparent strain.

The primary source of apparent strain comes from a linear variation of defocusing, i.e. an inclination of the object surface to the focal plane. This causes admixture of the observed strains with surface rotations and also a variation of speckle slewing across the focal plane. The surface of the disk was profiled to determine its variations in height as a function radius. The slope in the radial direction was found to be 0.066 at 152 mm in and 0.037 at 165 mm.

Further analysis of the particular geometry used in the spin rig tests, i.e. illumination from a point source located on the axis of rotation, showed that this eliminates apparent strain due to angular rotation of the disk. The simple explanation for this is that the curvature of the illuminating wavefront is matched to the curved track of any point on the disk. The angular rotation of the disk does not cause it to move relative to the apparent illumination, and, therefore, the speckles cannot move relative to the disk itself, regardless of defocusing. Even if this were not the case, however, the very small slope of the disk surface would not allow apparent strains large enough to account for the observations.

Another source of apparent strain could come from distortions of the mirror that rotates the optical axis by 90°. For example, cylindrical bending of the mirror would cause the image to be magnified differently along one axis than at right angles to that axis. This can cause angular rotations to appear as apparent strains according to the formula,

$$\epsilon_{ap} = \theta_z(m^2 - 1)/2m \quad (14)$$

where  $\epsilon_{ap}$  is the apparent strain,  $\theta_z$  is the angular rotation, and  $m$  is the unidirectional magnification. To convert 30 mrad into 4.1 millistrain would require a unidirectional magnification of 1.075. This would be observable by the naked eye when looking through the mirror.

Nonetheless, tests were performed to check for such effects. The lens and mirror were mounted on the optics table in the laboratory, and an object was constructed that could be made to pivot about an axis simulating that of the disk in the spin rig. Specklegrams were recorded before and after rotations of 30 mrad and 15 mrad. Analysis of these pairs of specklegrams showed that some apparent strain was caused by the mirror, but that its pattern was geometrically random and its magnitude was in the order of 500 to 600 microstrain. We must conclude that the mirror distortions present are insufficient to cause the apparent errors that were observed.

Finally, additional tests were performed to confirm the correct operation of the interferometric photocomparator. First, the photocomparator was run with a pair of calibrated, unidirectional strain specklegrams, and these confirmed the correct operation of the comparator. Second, the specklegrams from the spin rig were evaluated on the comparator in a manual mode. Pairs of plates were aligned on the comparator, the stage that moves the pair of plates was incremented by 10 mm, and the amount of displacement of one specklegram required to rezero the halo fringes was measured and divided by 10 mm. The effective gage length by this method becomes 10 mm in contrast to 1 mm by the automated method. This was done for plates 1 and 2, and for plates 2 and 5 for each run, and the results are plotted in Figure 2-9, together with averaged results from the automated analysis. The strains measured manually uniformly exceed those measured by the automated method. This makes it difficult to disprove the photocomparator measurements.

## **8. CONCLUSIONS AND RECOMMENDATIONS FROM BUILD 1**

The speckle photogrammetry measured strains on the spinning disk. These measurements had an excessively large component of radial strain for which no error source could be identified. The 45°

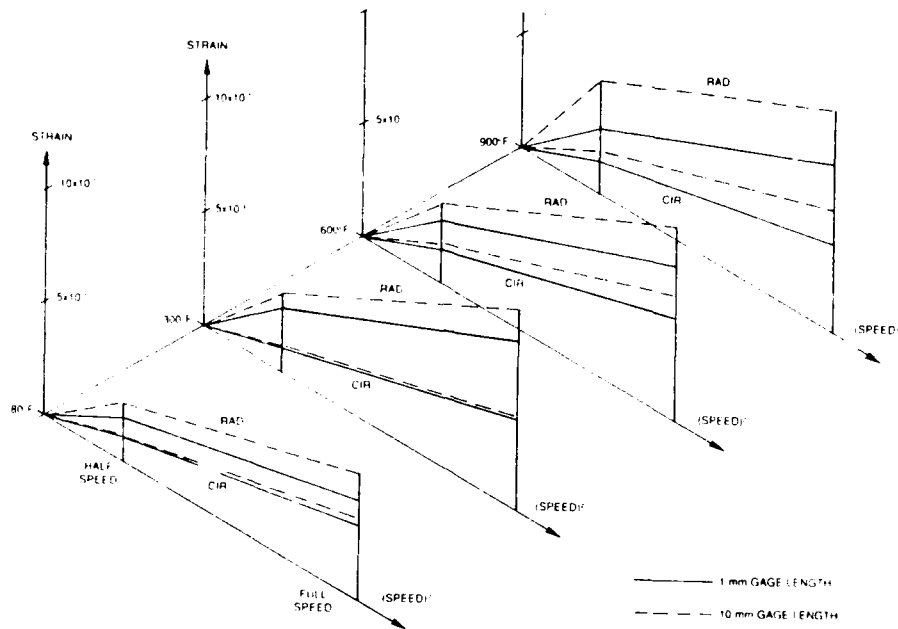


Figure 2-9. Build 1 effect of gage length on measured strain for various temperatures.

mirror was designated to be replaced with a thicker and flatter one to improve system accuracy, and further tests were scheduled for the next build to help identify sources of error. Such tests were to include the following:

1. Specklegrams would be recorded during the next build for both accelerating and decelerating rig speeds. This would check for some time varying effects such as laser heating and heat propagation through the disk.
2. Two sets of specklegrams would be recorded at room temperature on the disk, one with the rig rotating in one direction and the other with it rotating in the other direction. If a speed related apparent strain is present, its sign would reverse with reversal of the rotation direction. Even if the mechanism could not be determined, the effect could be numerically removed from the data by this test.

## 9. ADVANCED STRUCTURAL INSTRUMENTATION BUILD 2 - SPECKLE PHOTOGRAMMETRY

a. Data Recording--The specklegram recording equipment was set up at the spin rig as in Build 1 with the following changes:

1. The circuitry used to provide pulses to fire the flash lamps and Pockels cell of the laser was rebuilt to utilize digital logic circuitry in place of the phase-locked loop used in Build 1. This provided more noise resistance and allowed operation over a wider range of rig rotation speeds.
2. The 45° mirror used to reflect the image to the plate holder was replaced with a thicker mirror of more accurate figure, and it was mounted so that no bending stresses were applied.
3. A new high-speed detector was designed to provide the 1/revolution pulse from the spin rig. This provided less time delay than the previous circuitry and reduced the angular rotation of the image between minimum and maximum speeds to about 2.5 mm which is half the amount observed in Build 1.

The same target speeds were used as in Build 1 except for the lowest speed which was 1200 rpm. The target speeds and temperatures are tabulated below.

Target Speeds	Target Temperatures
1200 rpm	ambient
6600 rpm	422 K
9330 rpm	589 K
11,430 rpm	755 K
13,200 rpm	950 K

Except for the ambient temperature runs, ten specklegrams were recorded at each temperature run, five as the speed was increased, and five as it was decreased. At ambient temperature, five

specklegrams were recorded while the speed was increasing, however, data were taken for both clockwise and counterclockwise rotations. Data were recorded successfully at all speeds and at all temperatures except for the speed of 9330 rpm at ambient temperature with counterclockwise rotation. All of the high temperature data were taken with the rig running in the counterclockwise direction.

## 10. DATA PROCESSING

The specklegrams were developed and bleached to colloidal silver for processing in the heterodyne photocomparator. The quality of the data was generally very good and the strain results obtained during this build are those in which the most confidence is placed with regard to the technique of speckle photogrammetry. The image magnifications measured by the heterodyne photocomparator were first corrected by subtracting a systematic error in the comparator measured by analyzing a pair of identical specklegrams. When comparing specklegrams at high temperatures, thermal expansions were estimated from thermocouple measurements and subtracted. A correction was also made to the resulting data based upon measurements of the slope of the surface of the disk and of measurements of surface tilt as a function of speed. The tilt creates an apparent enlargement of the disk in the radial direction. These corrections amounted to the following:

Speed (r/min)	165-mm radius $\mu$ Strain	152-mm radius $\mu$ Strain
6600	124	221
9330	75	140
11,430	53	101
13,200	33	66

An additional feature was obtainable with this set of data. Comparisons could be made between the low speed specklegrams at neighboring temperatures, and these made it possible to define the initial strain state of the disk at each new temperature by subtracting the thermal expansion. The strain measurements are tabulated as follows:

Strain at Room Temperature - Clockwise

Speed [rpm]	165 mm Radial $\mu$ Strain	165 mm Circ. $\mu$ Strain	152 mm Radial $\mu$ Strain	152 mm Circ. $\mu$ Strain
1207	0	0	0	0
6605	630	701	1166	659
9325	1535	1330	2141	1265
11,398	2097	1996	2859	1919
13,198	2588	2536	3514	2568

Strain at Room Temperature # - # Counterclockwise

Speed [rpm]	165 mm Radial $\mu$ Strain	165 mm Circ. $\mu$ Strain	152 mm Radial $\mu$ Strain	152 mm Circ. $\mu$ Strain
1209	0	0	0	0
6607	829	748	1143	747
11,424	2058	2091	3284	1876
13,204	2453	2717	4044	2566

Strain at 422 K

Speed [rpm]	165 mm Radial $\mu$ Strain	165 mm Circ. $\mu$ Strain	152 mm Radial $\mu$ Strain	152 mm Circ. $\mu$ Strain
1207	733	-347	627	-483
6603	1900	315	1940	241
9345	2575	1200	3028	1063
11,415	3681	1764	4447	1578
13,215	4008	2565	4968	2295
13,210	4054	2586	4960	2336
11,402	3430	2018	4194	1677
9334	2800	1450	3338	1138
6613	1730	812	2191	498
1203	362	92	465	-92

Strain at 589 K

Speed [rpm]	165 mm Radial $\mu$ Strain	165 mm Circ. $\mu$ Strain	152 mm Radial $\mu$ Strain	152 mm Circ. $\mu$ Strain
1209	1626	-854	1566	-1197
6609	2727	177	3063	-181
9296	3643	1106	4078	710
11,398	4151	1714	4771	1524
13,204	4949	2384	5711	2133
13,204	4950	2409	5769	2297
11,398	4337	1837	4932	1781
9331	3431	1334	3944	1234
6605	2477	607	2779	530
1206	1279	-33	1065	96

Strain at 755 K

Speed [rpm]	165 mm Radial $\mu$ Strain	165 mm Circ. $\mu$ Strain	152 mm Radial $\mu$ Strain	152 mm Circ. $\mu$ Strain
1197	2433	-405	2627	-685
6609	3600	270	3955	39
9319	4304	1104	5044	746
11.424	5256	1901	6134	1555
13.140	5824	2815	7051	2460
13.204	5774	2797	7032	2296
11.415	5057	2064	5971	1642
9337	4501	1314	5213	852
6603	3484	666	3766	301
1219	2099	-277	2088	-544

Strain at 950 K

Speed [rpm]	165 mm Radial $\mu$ Strain	165 mm Circ. $\mu$ Strain	152 mm Radial $\mu$ Strain	152 mm Circ. $\mu$ Strain
1197	2083	-878	1776	-938
6609	3950	-75	4092	-108
9319	5083	689	5479	630
11.424	5822	1428	6544	1601
13.140	6839	2478	7788	2553
13.204	6337	2250	7324	2260
11.415	6057	1372	6742	1519
9337	5327	692	5752	833
6603	4430	-115	4506	68
1219	1637	-1084	1714	-672

These data are also plotted in Figures 2-10 through 2-15 with solid lines indicating the data for increasing speeds and dotted lines indicating the data for decreasing speeds.

Comparisons were made between the first and last photographs in each of the high temperature runs. These provided an indication of the cumulative error encountered in the processing of the ten plates in sequence and also confirmed the change in strain state of the disk over the time period of the test. The following is a tabulation of these data together with the data from analysis of the sequence of ten plates.

422 K		
location/	10-1 direct	10-1 sequential direction
	$\mu$ Strain	$\mu$ Strain
165 mm radial	-261	-371
165 mm circum.	446	439
152 mm radial	-159	-162
152 mm circum.	494	391

589 K		
location/	10-1 direct	10-1 sequential direction
	$\mu$ Strain	$\mu$ Strain
165 mm radial	-520	-347
165 mm circum.	996	821
152 mm radial	-200	-501
152 mm circum.	1127	1293

755 K		
location/	10-1 direct $\mu$ Strain	10-1 sequential direction $\mu$ Strain
165 mm radial	-265	-334
165 mm circum.	414	128
152 mm radial	-275	-530
152 mm circum.	444	141

950 K		
location/	10-1 direct $\mu$ Strain	10-1 sequential direction $\mu$ Strain
165 mm radial	-261	-446
165 mm circum.	216	-206
152 mm radial	-279	-62
152 mm circum.	375	266

## 11. DISCUSSION

The plots of strain versus speed (Figs. 2-10 - 2-15) are much more linear in this build than in the previous one. This is due in part to the correction for surface tilting of the disk with increasing speed. It is assumed that the disk flexes so that the rim bends upward relative to the hub. It was also significant that very little difference was detected in the strains measured with the disk rotating in the clockwise and counterclockwise directions. This supports the conclusion that the strains measured here are very likely accurate to within a few hundred microstrain.

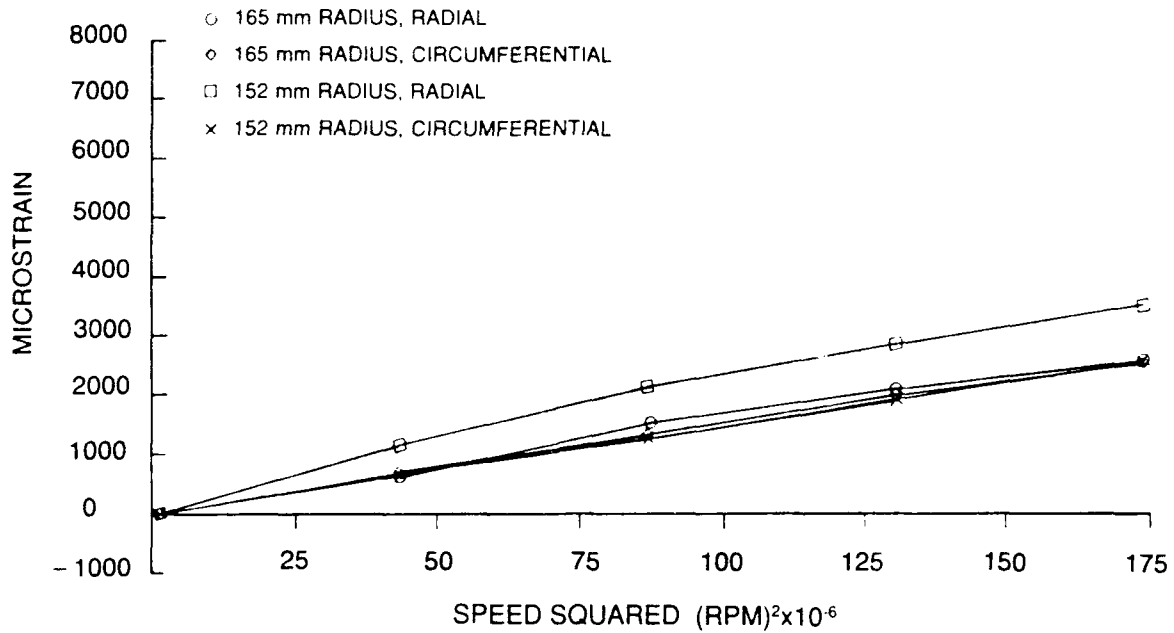


Figure 2-10. Build 2, strain vs. speed squared. Ambient temperature, clockwise rotation.

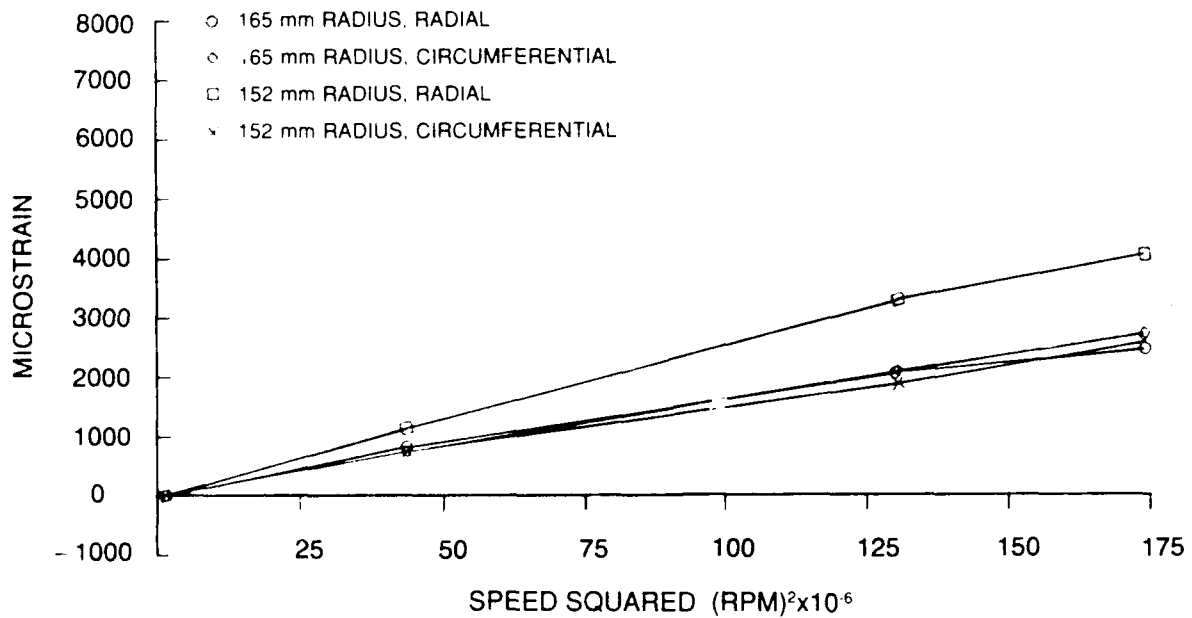


Figure 2-11. Build 2, strain vs. speed squared. Ambient temperature, counterclockwise rotation.

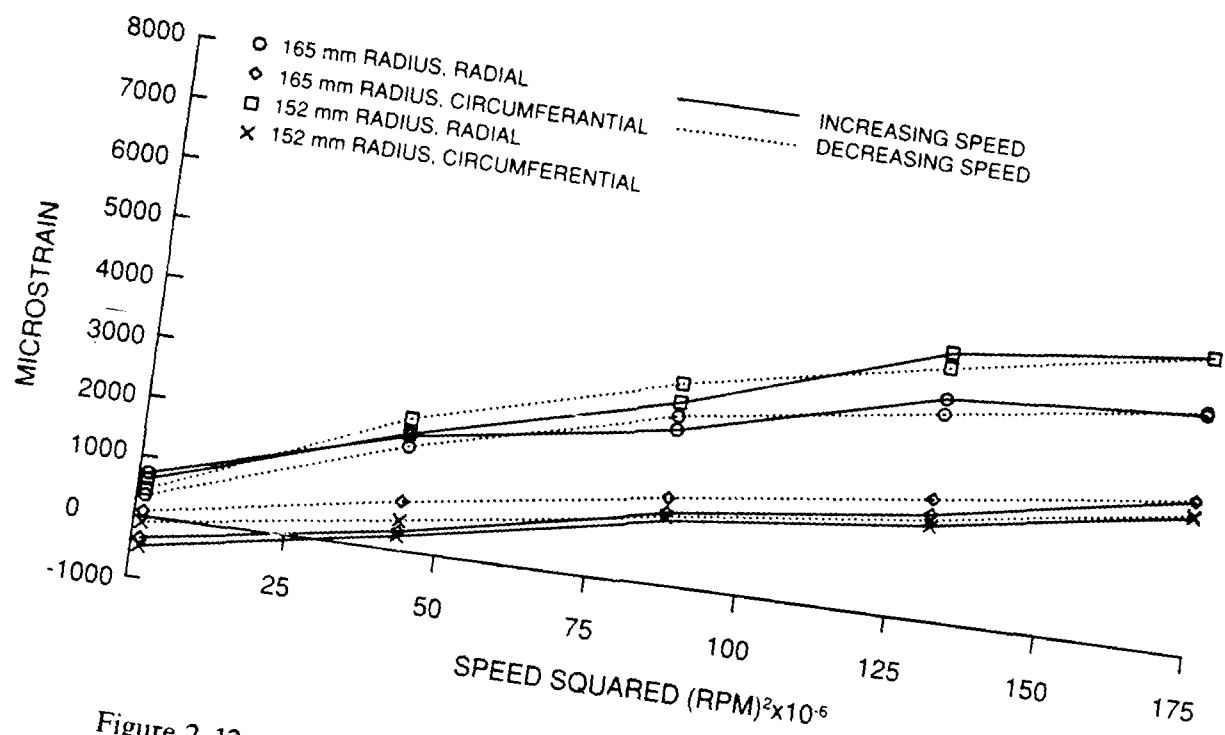


Figure 2-12. Build 2, strain vs. speed squared. 422 K temperature, counterclockwise rotation.

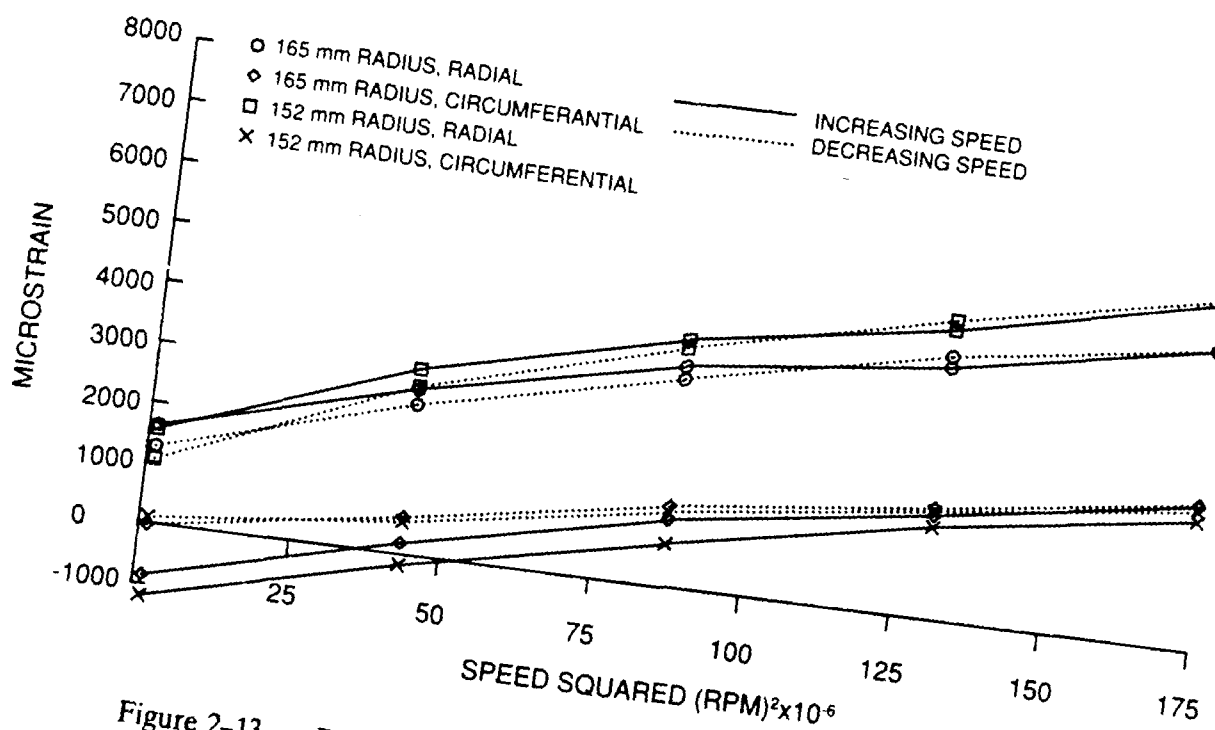


Figure 2-13. Build 2, strain vs. speed squared. 589 K temperature, counterclockwise rotation.

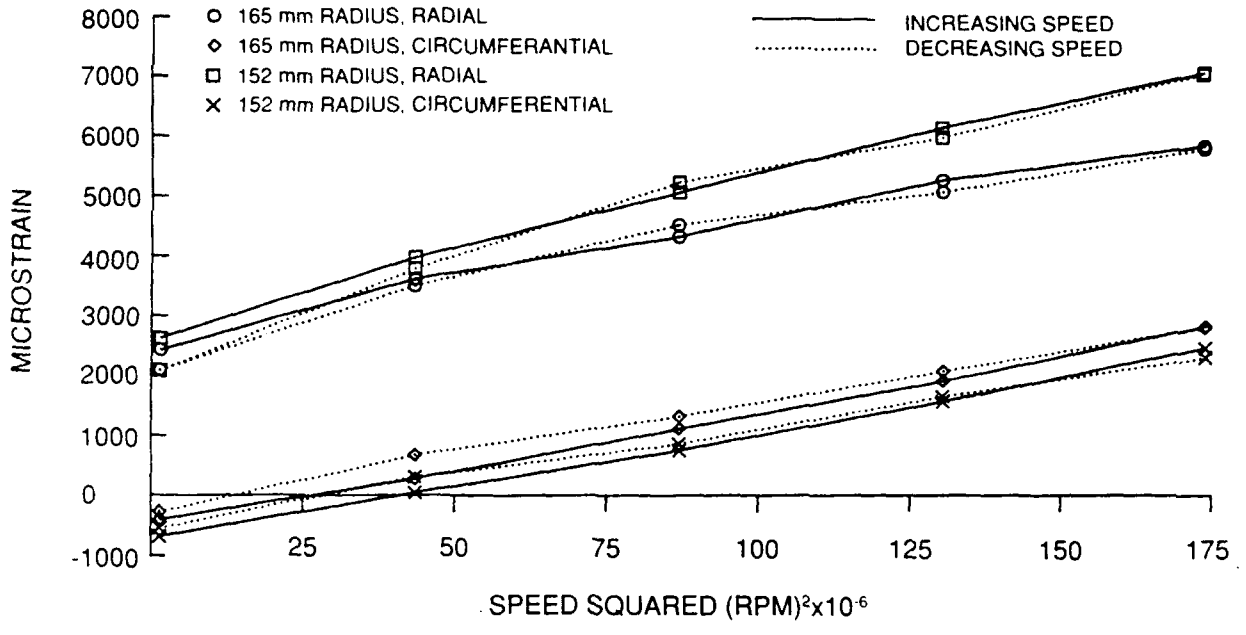


Figure 2-14. Build 2, strain vs. speed squared. 755 K temperature, counterclockwise rotation.

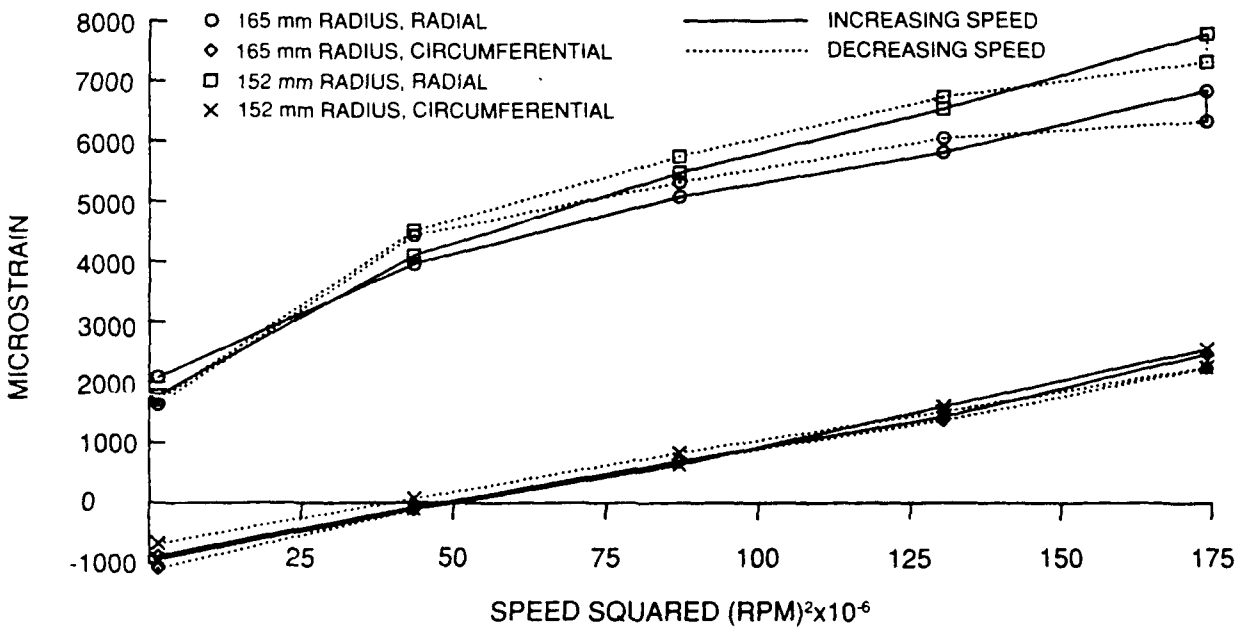


Figure 2-15. Build 2, strain vs. speed squared. 950 K temperature, counterclockwise rotation.

It is of particular interest to note the amount of initial strain on the disk as the temperature increased. This can be explained to some extent by the initial difference in temperature between the bore and the rim of the disk. The initial and final temperature differences were:

Temperature	Initial diff. $\mu$ Strain	Final diff. $\mu$ Strain
422 K	120	25
589 K	293	29
755 K	195	79
950 K	202	-28

Close examination of the data shows that whereas at 422 K the final strain is nearly zero, as would be expected by the reduction of the bore-to-rim temperature difference, this becomes less and less the case as the overall temperature increases. The final strains at 950 K are very nearly equal to the initial strains. It is easy to see in retrospect that photographs should have been recorded at ambient temperature and low speed at the beginning of each run to serve as a check for plastic strain since the data obtained here strongly suggests that it may have been occurring. This is supported to some extent by a physical measurement of the disk that did indicate some enlargement on another run.

### **III. HEAT FLUX SENSORS**

#### **1. SUMMARY**

Under the Advanced Structural Instrumentation program, heat flux sensors were fabricated into turbine blades and tested under rotation in a spin pit rig. The heat flux sensors were constructed into blade halves which were later joined by brazing. After assembly, the blades underwent final machining to demonstrate the feasibility of machining the blades with small diameter lead wires installed. The heat flux sensors were then calibrated using a quartz lamp bank as a heat source. During Build 2 of the ASI rig, the blades were installed on a disk and then mounted in the spin rig. A slip ring assembly was used to route the sensor leads out of the rig. Although there was minimal heat flux and no coolant flow through the blades, the heat flux sensor outputs and blade temperatures were monitored during the rotational testing. One sensor failed early in the test program and the thermocouple in that sensor functioned intermittently. Post-test analyses showed all sensor failures were in the external lead wires, indicating that the heat flux sensor fabrication technique produces sensors capable of withstanding the centrifugal forces created by rotation. Based on the test results, recommendations for improved techniques for handling the external lead wires were generated.

#### **2. INTRODUCTION**

Designing durable turbine airfoils, which use a minimum amount of cooling air (and are, therefore, more efficient and economical), requires detailed knowledge of heat flux characteristics within the hot section of advanced aircraft gas turbine engines. Considerable development has been done on both low and high temperature heat flux sensors for such diverse purposes as basic boundary layer experiments, solar power and energy conservation investigations, research on thermal protection systems for advanced aircraft and spacecraft, and application in advanced aircraft combustors. None of those applications combines the requirement for materials compatibility, miniaturization, and survivability in a hostile environment that is necessary for a viable turbine airfoil heat flux sensor. Due to the inherent limitations of current sensors, it has been impossible to collect hard empirical data relating to the heat transfer taking place in operating turbine airfoils in aircraft gas turbine engines. As an undesirable alternative, investigators have been forced to rely on heat flux predictions derived

from ad hoc analytical models. These models are themselves unverifiable due to the very lack of empirical data they seek to remedy.

From this standpoint, the importance of accurate and durable heat flux sensors in the development of advanced gas turbine engines becomes apparent. The development of these sensors would provide a diagnostic tool enabling the verification or modification of analytical procedures used to design improved durability and longer life turbine airfoils. These, in turn, would promote a longer component life while minimizing the amount of cooling required, thus advancing fuel efficiency and maintenance economy.

To address the requirement for heat flux sensors suitable for use on turbine airfoils, a development effort was initiated at Pratt & Whitney under the NASA Hot Section Technology (HOST) (Refs. 1 and 2) program. Tests of the resulting sensors in a full scale rotating rig under the ASI program were a continuation of that development effort.

### **3. DESCRIPTION OF SENSORS**

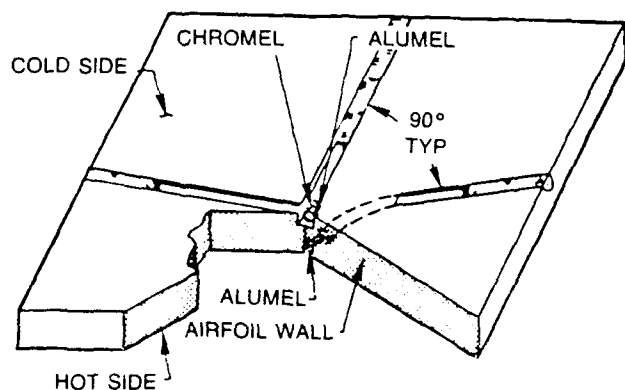
For gas turbine applications, heat flux measurements are required under steady state as well as transient conditions. For that reason, development was concentrated on sensors, capable of making both types of heat flux measurements.

Two types of heat flux sensors were chosen for fabrication into the blades used in the ASI program. These were an embedded thermocouple sensor and a Gardon gauge sensor.

Embedded thermocouple heat flux sensors determine heat flux by measuring the differential thermoelectric output from Alumel wires in the hot and cold side of the airfoil wall. This output is the result of the thermal drop across the wall generated by the transmitted heat flux.

Embedded thermocouple sensors require installation of lead wires in both the hot and cold side of the airfoil wall. In order to maximize thermocouple wire size to increase durability while keeping the required slots in the airfoil wall small, these sensors were designed with three single conductor swaged wires. Figure 3-1 illustrates the design for the embedded thermocouple sensor. In this design, both an

### EMBEDDED SWAGED WIRE THERMOCOUPLES



### ELECTRICAL SCHEMATIC EMBEDDED THERMOCOUPLE SENSOR

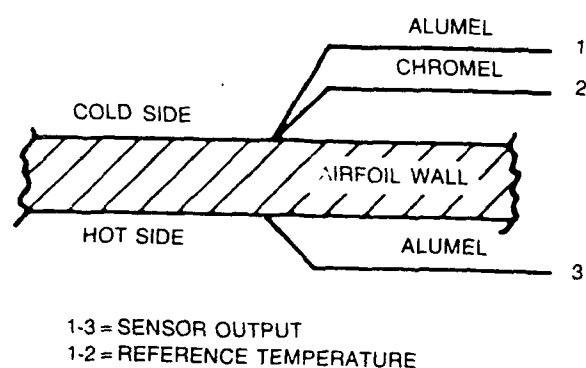


Figure 3-1. Schematic of the embedded thermocouple heat flux sensor.

Alumel and Chromel wire were embedded in the cold side of the blade and an Alumel wire was embedded on the hot side. The sensor output was obtained as a differential signal from the Alumel wires. The Chromel/Alumel thermocouple yielded a reference temperature.

The Gardon gauge sensors also depend on a thermal differential generated by heat flow in the airfoil wall. For these sensors the heat flow is in a radial direction through a thin disk of airfoil material on the hot side of the airfoil wall.

Gardon gauge sensors require installation of lead wires on only the cold side of the airfoil. In order to minimize machining, these sensors were designed with a single sheathed three-conductor cable. Figure 3-2 shows a schematic for the Gardon gauge sensor. For this design, two Alumel wires and one Chromel wire were installed in a single sheath that was embedded in the cold side surface. This unique three-conductor cable was produced to our specifications by Idaho Labs (Ref. 3). The cavity required to form the Gardon gauge foil was formed by electro-machining the cold side of the airfoil wall. One Alumel lead was attached to the bottom center of the cavity; the other Alumel lead and

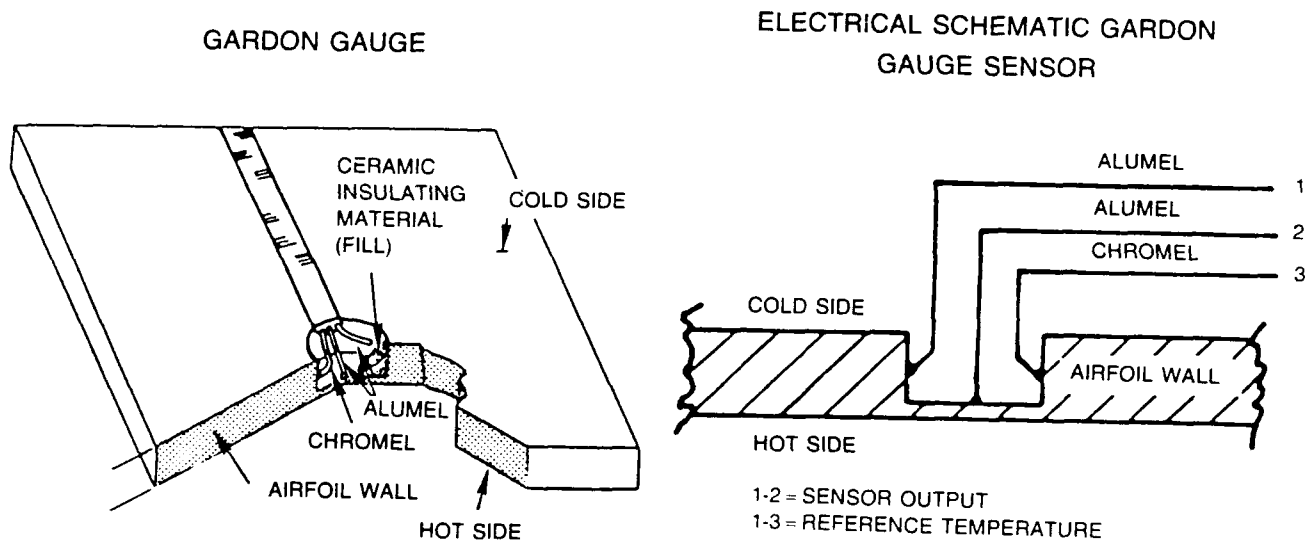


Figure 3-2. Schematic of the Gardon gauge heat flux sensor.

the Chromel lead were attached to the wall of the cavity near the bottom. Sensor output was obtained from the two Alumel wires, while a reference temperature was obtained from the Chromel and Alumel wires attached to the wall. The cavity made for the Gardon gauge was filled with a ceramic cement which provided aerodynamic integrity on the cold side as well as support and oxidation protection for the fine thermocouple wires.

#### 4. FABRICATION OF SENSORS INTO THE BLADES

The embedded thermocouple sensor was formed by machining a groove into the hot side wall and two grooves into the cold side wall to accept the thermocouple wires. The grooves were cut by electrical discharge machining and were 0.3 mm wide and 0.3 mm deep. At the thermocouple junction end of the groove, the depth was reduced to 0.13 mm to keep the thermocouple junction as close to the surface as possible. The thermocouple junctions were directly opposite each other on the airfoil wall, and the grooves were approximately 90° apart to reduce the structural impact on the airfoil. The lead wires were routed in a serpentine pattern to accommodate the centrifugal loading on the wires. The

thermocouple wire used was 0.25 mm diameter single-conductor swaged Chromel and Alumel wire. The swaged thermocouple wires were installed in the grooves and held in place by fillet wires of Chromel P which were resistance welded in place. After the thermoelectric junctions were made by resistance welding, the area around the thermocouple junction was filled with powdered MgO insulation material to protect the thermoelectric junctions. A Hastelloy-X cap was welded over the sensing area, and the entire groove filled with Chromel P fillet wire. After the wires were installed, the area was smoothed by hand to restore aerodynamic integrity.

The Gardon gauge sensor was fabricated by machining a cavity 1.5 mm in diameter into the cold side surface to a depth that left a sensor foil of the desired thickness at the bottom of the cavity. A groove 0.55 mm wide and 0.55 mm deep was machined into the cold side wall for the lead wire. A serpentine pattern was used to route the lead wire in order to accommodate the centrifugal loading on the wire. The wire used to fabricate these sensors was a three-conductor swaged wire 0.5 mm in diameter with two Alumel and one Chromel conductor. The thermocouple wire was installed in the channel utilizing the technique discussed above using Chromel P as a fillet wire. One Alumel wire was attached by resistance welding in the center at the bottom of the cavity. The other Alumel wire was attached to the sidewall of the cavity at the bottom and was oriented in the direction where the minimum temperature gradient was anticipated. The Chromel wire was attached to the sidewall of the cavity directly opposite the Alumel wire and was also located near the bottom of the cavity. After the thermocouple junctions were made, the cavity was filled with M-Bond GA100 (Ref. 4) ceramic cement. This cement provided both structural support and oxidation protection for the small wires. After the ceramic was given an oven cure, the surface was smoothed by hand to restore aerodynamic integrity.

The heat flux sensors were installed into two-piece blades. The use of two-piece blades allowed installation of the sensors prior to assembling the blades. The normal method of joining blade halves is to use transient liquid phase (TLP)<sup>®</sup> bonding. A previous study by Pratt & Whitney indicated that the thermocouple installations would not survive the TLP bond cycle of 20 hours at 1475 K. The experimental instrumented blades did not require a long, low cycle fatigue life for this program. Therefore, an alternate method using a 1200 K braze was used to join the blade halves. After brazing

the blade halves together, the blades were sent to a vendor for final machining of the blade attachment area below the platform. The lead wires were coiled in a 150-mm-diameter loop, and attached loosely to the airfoil so that they could be moved easily when fixturing the blade for machining. Four blades were instrumented. Two blades had the lead wires damaged during machining by excessive flexing where the lead wires exited the blade. This failure rate during machining could be reduced in the future by the construction of rigid supports for the lead wires to prevent flexure at the point of exit from the blade.

## 5. CALIBRATION

After fabrication, a program was undertaken to provide calibrations of the heat flux sensors to determine the output versus transmitted heat flux relationship. A quartz lamp bank test facility was used for all testing, and the blades were cooled with internal cooling air. The heat source used was a quartz lamp bank with six parallel quartz halogen bulbs, each rated at 6 kW. The bulbs are 25.4 cm long, and the width of the lamp assembly is 7.6 cm. This lamp assembly is capable of producing a maximum heat flux incident on the sensors of  $1.7 \text{ MW/M}^2$ . During routine operation, the lamp operation is limited to approximately  $1.0 \text{ MW/M}^2$  to maximize lamp life.

A photograph of the lamp face is shown in Figure 3-3. The reflector on the lamp is water-cooled, and the bulbs are air-cooled to permit continuous operation. The airfoil under test is positioned below the lamp and is surrounded with polished, water-cooled shields to concentrate the energy onto the airfoil. This shielding arrangement is shown in Figures 3-4 and 3-5. The airfoil is positioned so that the surface of the sensor area is parallel to the plane of the lamps and as close to the lamps as possible. The polished shields are adjustable to accommodate various airfoil orientations. The heat flux output of the lamp is monitored by a reference heat flux sensor mounted in the shield. After the shields are positioned for a particular airfoil orientation, the airfoil is removed from the lamp assembly and a second reference sensor is mounted at the location to be occupied by the airfoil sensor. A calibration of the assembly is then performed to determine the relationship between the heat flux incident at the blade location to that at the reference sensor location. This relationship is used to correct the data measured by the reference sensor during the blade calibration. The position of the two reference

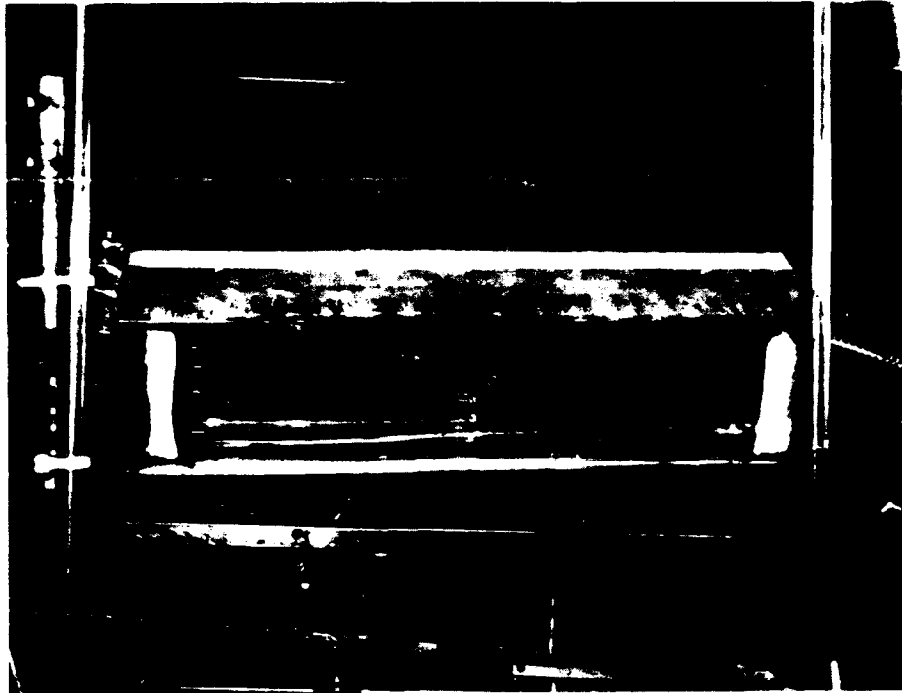


Figure 3-3. High intensity quartz lamp bank.



Figure 3-4. Airfoil positioned in quartz lamp rig with water-cooled shields - bottom view.



Figure 3-5. Airfoil positioned in quartz lamp rig with water-cooled shields - side view.

sensors is exchanged, and the calibration is repeated to minimize the effect of any bias in the reference sensor calibrations on the blade calibration result. An overall view of the rig is shown in Figure 3-6.

The calibrations were conducted under two sets of conditions: varying incident heat load at a constant sensor temperature, and varying incident heat load at constant blade coolant flow. The heat flux transmitted through the airfoil wall was calculated by determining the heat absorbed and subtracting the heat losses from the front face of the sensor due to convection and reradiation. The absorbed heat flux is equal to the incident heat flux as measured by the reference sensor, corrected to the test sensor location, times the emittance of the airfoil surface. Zynolyte (Ref. 5) 800 K "Hi-Temp" paint was used to coat the blade in order to provide a constant known emittance of 0.89 for calibration. The convective loss is equal to the convection heat transfer coefficient as previously measured with a convective probe times the temperature differential between the sensor surface and the ambient air temperature. The reradiation loss is the emittance of the sensor face times the difference in the fourth

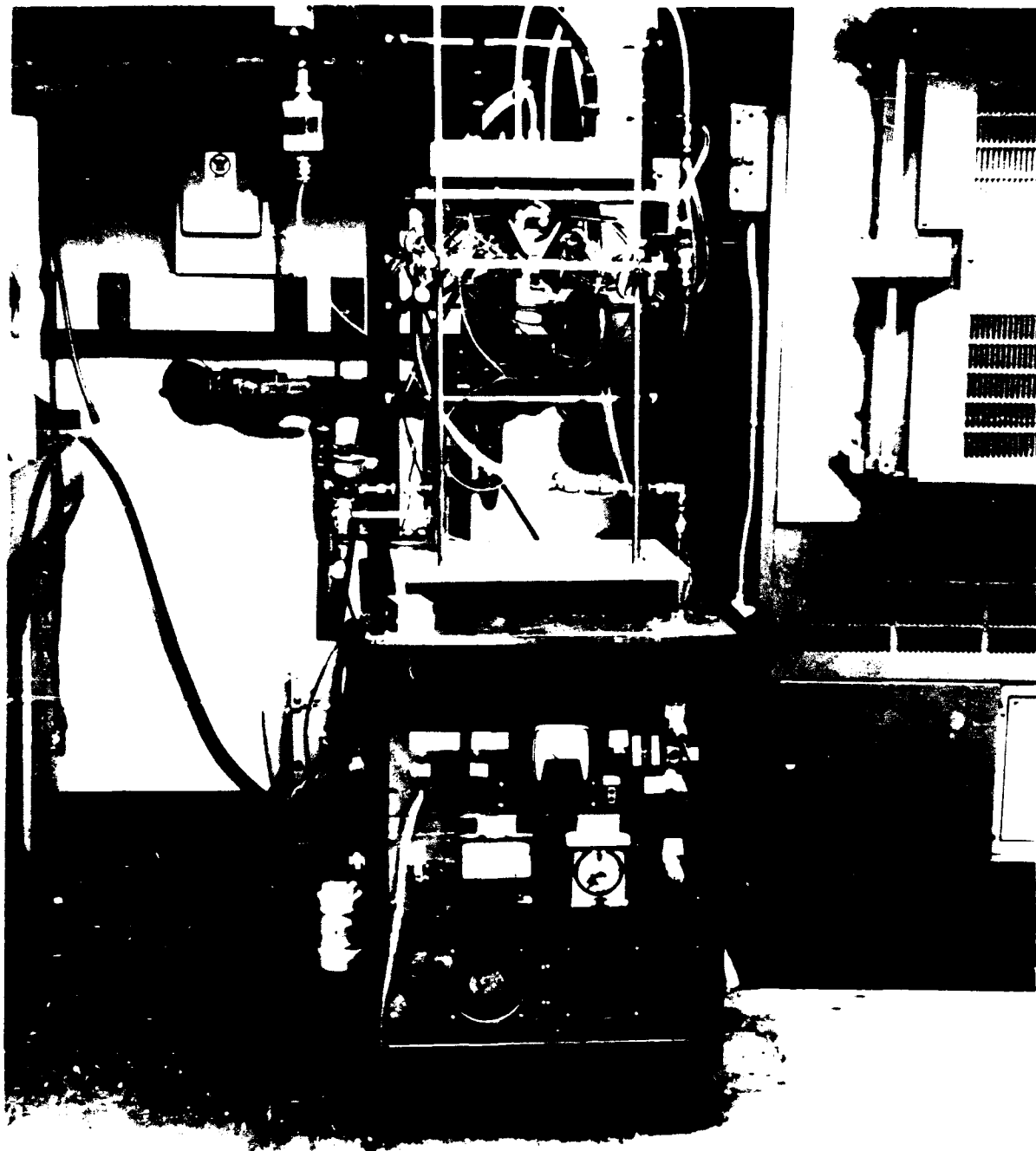


Figure 3-6. High intensity quartz lamp rig.

powers of the sensor surface temperature and the sink temperature. The sink temperature was experimentally determined as approximately 400 K for this calculation.

The results of a typical sensor calibration are shown in Figure 3-7.

## 6. TEST RESULTS

During the ASI program, the sensors were tested to rotating speeds in excess of 13,000 r/min and to disk temperatures above 950 K. Since the airfoils themselves were not directly heated but depended on conduction of heat from the disk, sensor temperatures were limited to approximately 700 K. The temperatures measured by the thermocouples in the two sensors are shown in Figure 3-8. One sensor failed early in the test program. The thermocouple associated with that sensor became erratic and would read correctly a portion of the time and read near room temperature the rest of the time. The problem clearly is an intermittent short circuit in a low temperature area. This was confirmed during post-test inspection when significant damage was discovered in the cool lead wire area of the rig. The other sensor and thermocouple functioned well throughout the test program.

Post-test analysis of the data showed that during those periods of time when both thermocouples were functioning properly, there was good agreement between the two temperature measurements. No measurable DC output was obtained from the heat flux sensor. This was as expected since there was no heat flux through the blades. These results confirmed that neither the heating or rotation introduced a zero offset to the heat flux sensor output.

To evaluate the AC noise level on the heat flux sensor output, several measurements were taken at each data point, and the standard deviation of those measurements was calculated. These results are shown in Figure 3-9. There is a low noise level (1 sigma) of about  $\pm 0.5$  counts. Some of the data, however, shows much higher noise levels. It was eventually determined that all these data were inadvertently recorded with power on to the inductive heater used to heat the turbine disk. When the data with the heater on was eliminated, there were no noise signals on either the heat flux sensor or the thermocouple that were measurable above the slip ring noise measurement.

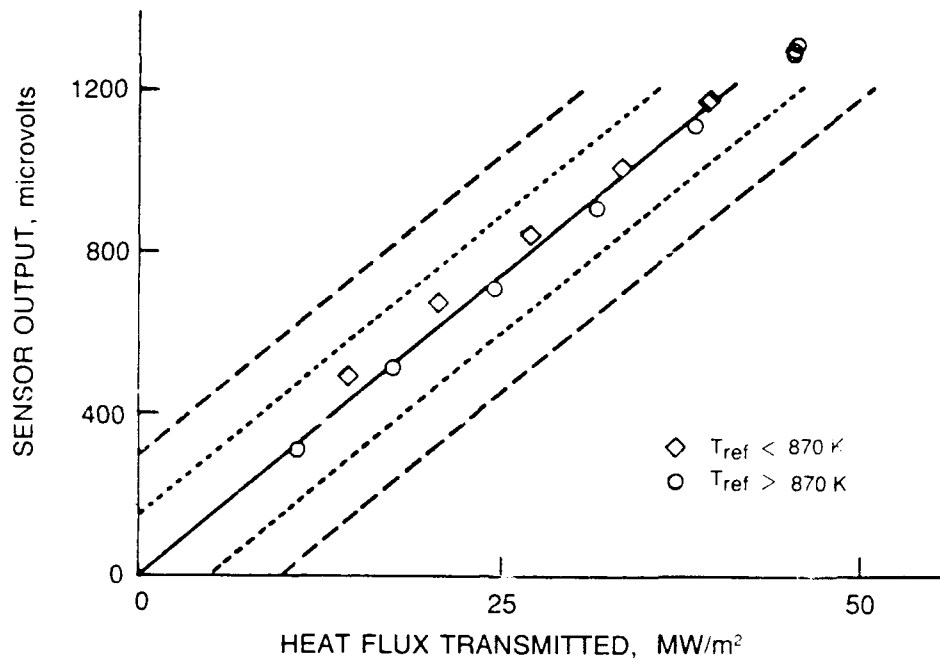


Figure 3-7. Calibration data for embedded thermocouple sensor.

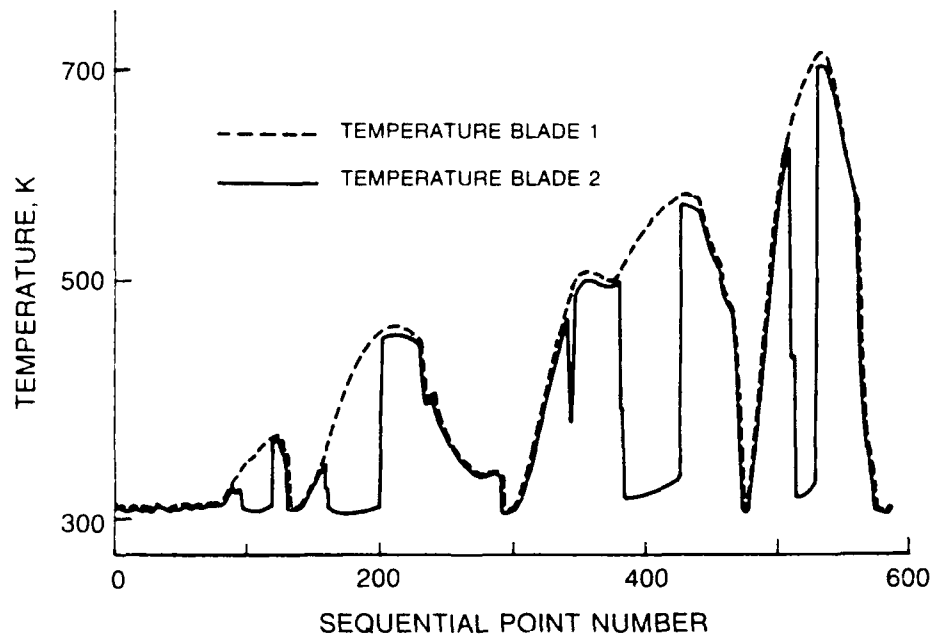


Figure 3-8. Data from two sensors from the advanced structural instrumentation spin test.

Post-test inspection showed that for the leads that failed, all lead failures were either at the airfoil exit (Fig. 3-10) or external to the airfoil (Fig. 3-11).

## **7. CONCLUSIONS AND RECOMMENDATIONS**

Techniques for installation of heat flux sensors into turbine blades have been demonstrated.

The feasibility of final machining the blade root area after installation of the sensors was proven. In the future, rigid fixturing to support the lead wires at the exit from the blade is recommended to reduce the failure rate.

Tests in a realistic rotating environment have shown that the sensors will survive and that the noise levels introduced by rotation are negligible.

Application of these sensors in the rotating components of an engine should be considered.

The ASI rig has proved to be a valuable tool for instrumentation development as an intermediate step between laboratory development and full scale engine tests.

## **8 REFERENCES**

1. Atkinson, W. H., Cyr, M. A. and Strange, R. R., Turbine Blade and Vane Heat Flux Sensor Development; Phase I - Final Report, NASA Contractor Report CR-168297, August 1984.
2. Atkinson, W. H., Cyr, M. A. and Strange, R. R., Turbine Blade and Vane Heat Flux Sensor Development; Phase II - Final Report, NASA Contractor Report CR-174995, October 1985.
3. Idaho Laboratories Corporation; 2101 Hemmert Avenue; Idaho Falls, Idaho; 83401.
4. Measurements Group Inc.; P. O. Box 27777; Raleigh, North Carolina; 27611.
5. Zynolyte Products Company, Compton, California; 90220.

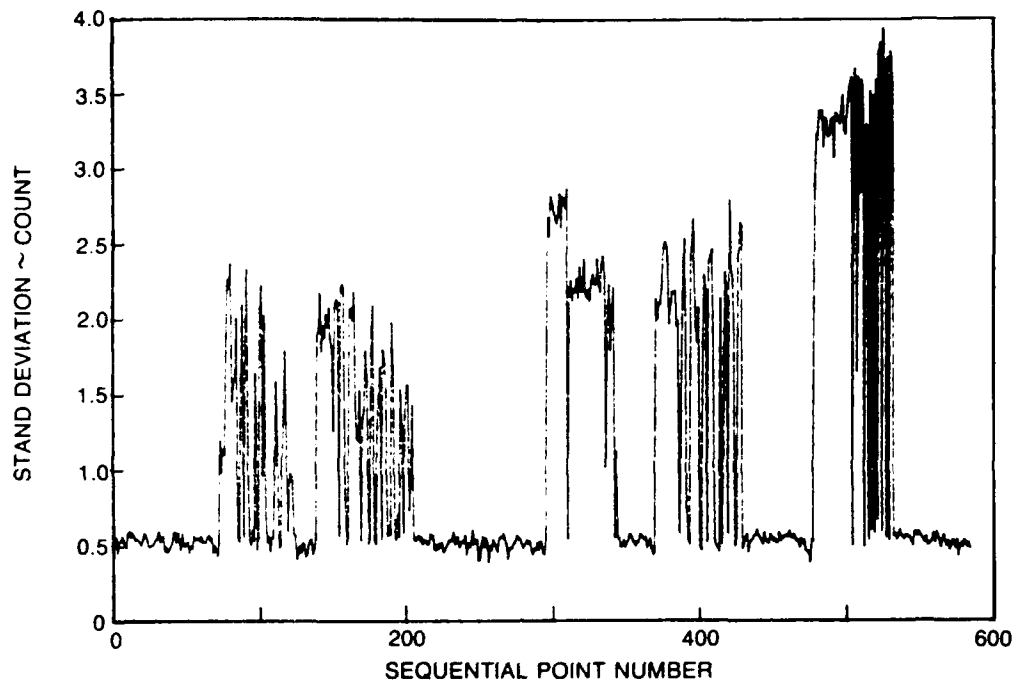


Figure 3-9. AC noise level on heat flux sensor output.

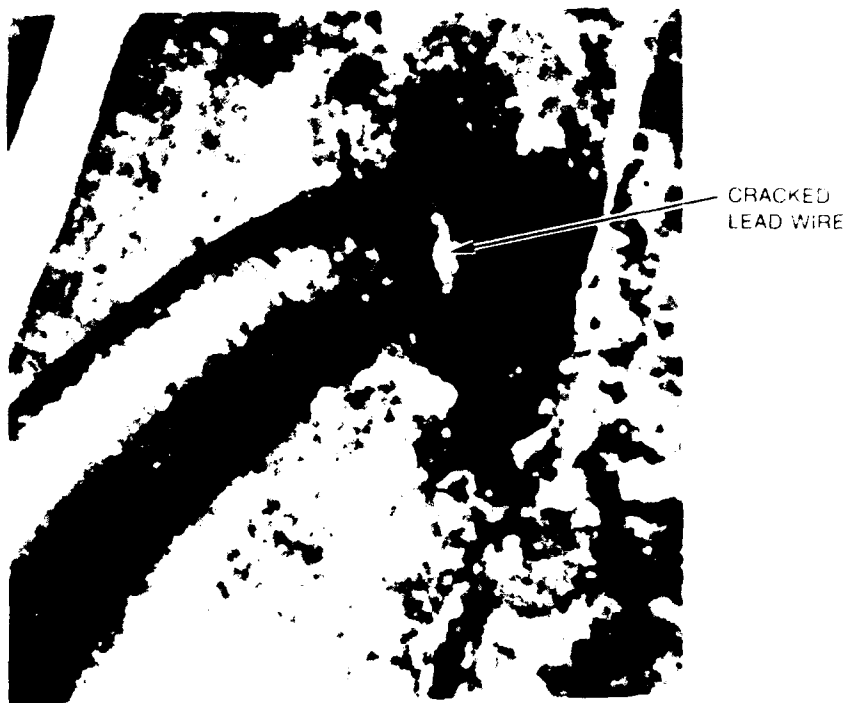


Figure 3-10. Leadwire failure at airfoil exit.

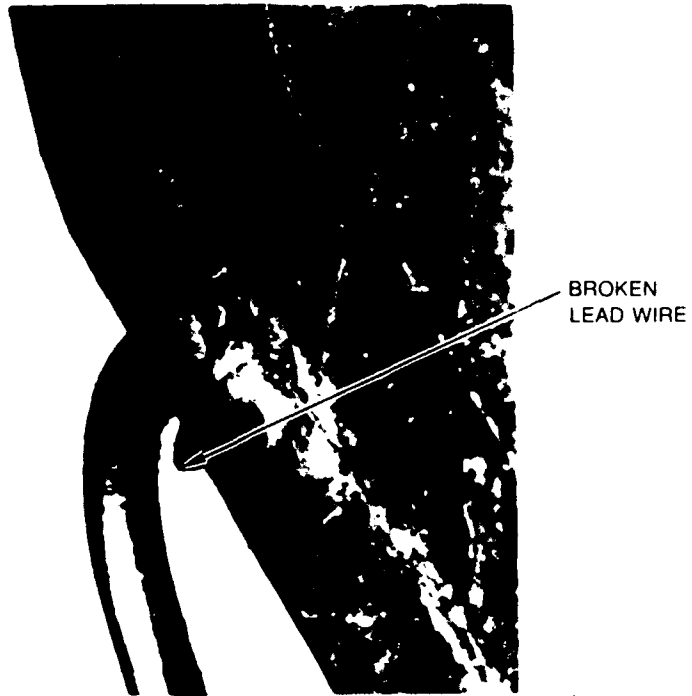


Figure 3-11. Failure of leadwire external to airfoil.

## **IV. FIBER OPTIC SENSORS**

### **1. INTRODUCTION**

Quantitative diagnostics are desirable for use during optimization studies of turbine engine performance and lifetime. Static strain at high temperature is a diagnostic parameter of key interest in such engineering research and is important in understanding the response of materials to the harsh operating conditions within turbine engines. Typical gas temperatures for the different sections of a turbine engine are shown in Figure 4-1. Of particular interest is the turbine; a complex structure which must be inserted directly in the hot gas stream. The average operating conditions for a turbine are illustrated in Figure 4-2. It must function durably in temperatures peaking above 922 K. No static strain sensors exist for measurements while attached to turbine engine components elevated to these high temperatures. United Technologies Research Center has been developing an optical fiber sensor to address these needs. In addition to its small, nonintrusive dimensions and inherent immunity to EMI, the twin-core optical fiber sensor is capable of simultaneous measurement of static strain and temperature. The purpose of this report is to present a review of recent sensor development and demonstration. For instance, the optical fiber sensor has been attached to modified F100 turbine disks and operated to temperatures higher than 922 K. Nonrotating (the Ferris wheel) and rotating (the spin rig) experiments have been implemented to simulate turbine disk loading to several thousand microstrains. Details are provided in sections entitled: Background, Sensor Concept and Development, Nonrotating Risk Reduction Tests and Rotating Tests.

### **2. BACKGROUND**

Early work at UTRC on optical fiber strain sensors identified potentially unique aspects of the twin-core fiber geometry in application to strain sensing: existence of two stable modes for interferometric applications, strain and temperature response coefficients which could be derived from first principals and the potential for temperature independent strain sensing. The sensor concept was verified in the laboratory when fabricated with a low melting temperature glass system. It was then proposed that the sensor concept could be transferred to a new glass system, based on fused silica, to address higher temperature ranges and turbine applications. This proposal led to

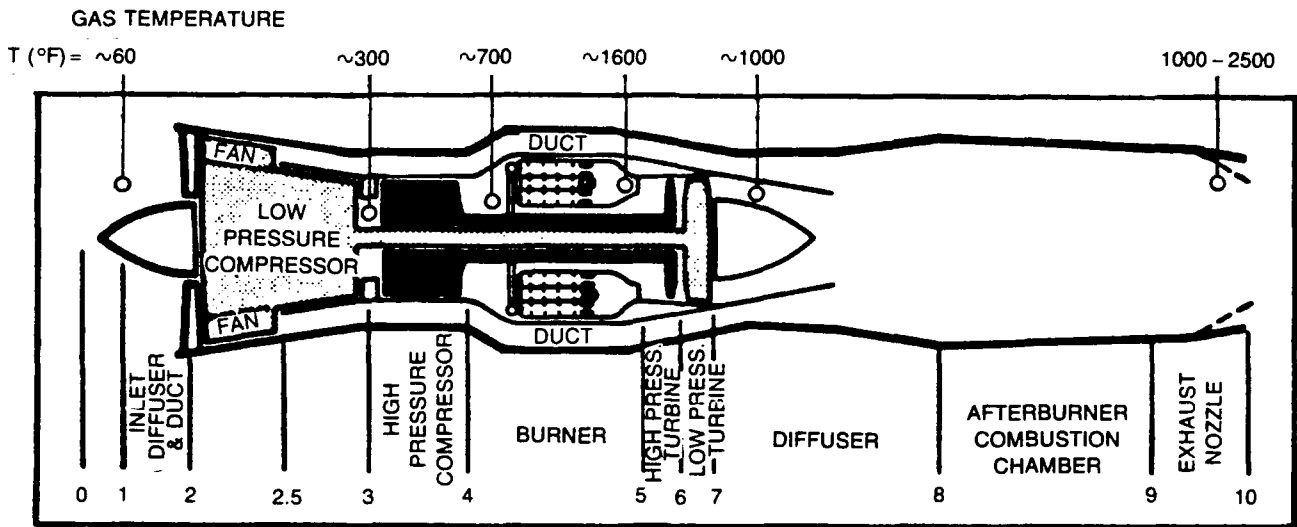


Figure 4-1. Fiber optic strain sensor. Typical engine layout.

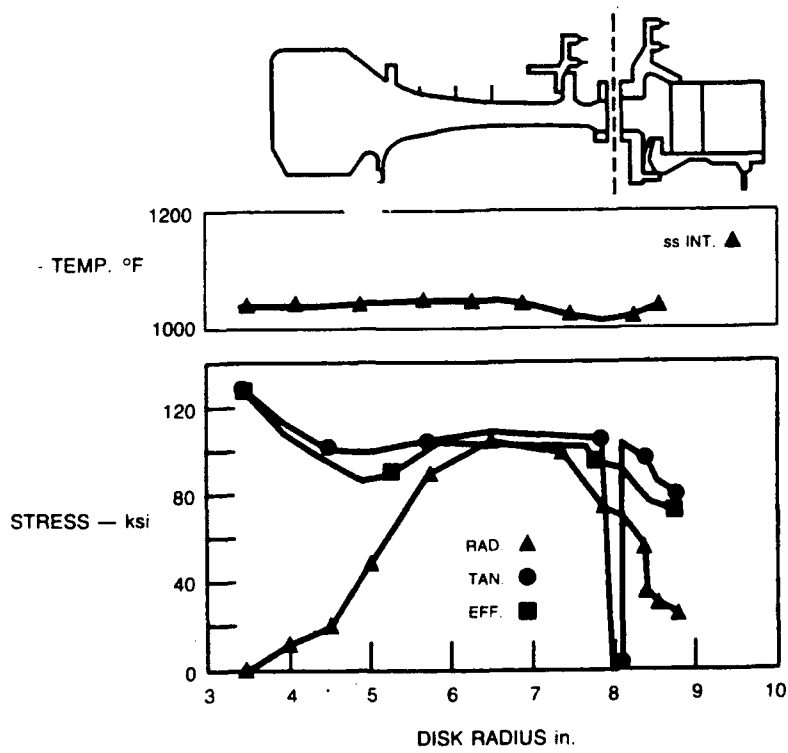


Figure 4-2. Fiber optic strain sensor. Disk environment.

participation in AF Contract No.F33615-80-C-2044, Turbine Steady-State Strain Gage Development Program (TSSS). During that contract, several technologies were reviewed for potential development and application to the turbine disk strain sensing problem. The optical fiber sensor and thin metal film sensors were identified as technologies with the most potential for success. Additional development of the twin-core sensor was pursued under that contract while the metal film sensor was supported under a NASA contract.

Under support of the TSSS program, germanium-doped fused silica cores with pure fused silica cladding was selected as the high temperature glass system. We were successful converting the twin-core sensor geometry to this combination of materials. Demonstrations were conducted with the upgraded sensor attached to IN-100 material test coupons with ceramic cement and operated to 922 K. At this point, the gage length was undefined except by attachment; no input or output lead configurations were conveniently available. In addition, no protective surface coating had been developed, so that test conditions were difficult to meet without a high probability of sensor damage. Handling of the sensor usually degraded the surface to a strength on the order of 209 - 350 MPa. This meant a limitation on the bend diameters which could be imposed on the device and a limitation on the total strain (thermal plus mechanical) which it could endure. Finally, manufacturing tolerances made it difficult to fabricate a sensor with specifications to meet the temperature independent operating condition; an alternative mode of 2-wavelength operation potentially yielding strain and temperature simultaneously was recommended.

These deficiencies were addressed during the present contract, No.F33615-83-C-2330, Advanced Structural Instrumentation (ASI). Aluminum coating for the glass surfaces was developed for practical 'on-line' implementation during fabrication, enabling fiber as strong as 6980 MPa to be fabricated. For long lead lengths of about 10 m, we are able to maintain an average strength above 2095 MPa. The gage length was limited by application of fusion splicing techniques to connect nonresponsive input and output leads to a gage region of finite length. Furthermore, instrumentation was advanced to enable 2-wavelength operation in large scale, nonrotating lab experiments. Most recently, instrumentation was ruggedized and miniaturized to enable 2-wavelength operation in rotating turbine simulations. Finally, attachment methods were upgraded to more durable

configurations by development of flame spraying techniques. Instrumentation durability, a lack of realtime readout and the need for improved calibration methods were key weaknesses uncovered by the ASI program. In addition, recent interest in high temperature static strain measurements for conditions to 1366 K cannot be addressed by the aluminum coated germanium-doped-silica/pure-silica configuration.

Development of the twin-core optical fiber sensor is continuing under the Advanced Turbine Engine Gas Generator (ATEGG) program and under a UTRC internal program, High Temperature Optical Fiber Strain Sensor Development. The IR&D program is emphasizing development of twin-core sensors functional to 1366 K. In addition, the ATEGG program is emphasizing nonrotating engine application with enhancements in calibration, installation, and realtime readout of strain and temperature. The device will be demonstrated on an ATEGG test which will have four engine case-mounted sensors located remotely from the control room instrumentation.

As seen in Figure 4-3, the ASI program has provided a crucial step in development of advanced strain sensing for turbine engines. Sensor reliability and operation have been significantly improved with system configurations elevated from laboratory operation to configurations closely resembling those required for full-up engine ground-test application.

### **3. SENSOR CONCEPT AND DEVELOPMENT**

This report section covers the theoretical sensor concept and one configuration for practical implementation. In discussing these topics, we will cover the basic sensor operational characteristics, the 2-wavelength mode of operation for simultaneous measurement of strain and temperature, assembly of a device with limited, finite gage length which is protected with a high durability coating. Emphasis is initially placed on an understanding of the basic device characteristics.

The optical fiber geometry under consideration is shown in Figure 4-4. This structure is configured with two closely-spaced, matched waveguides designed to limit propagation to two fundamental modes: a symmetric twin-core mode and an asymmetric counterpart. Their respective propagation constants are slightly different, leading to periodic interference along the device length.

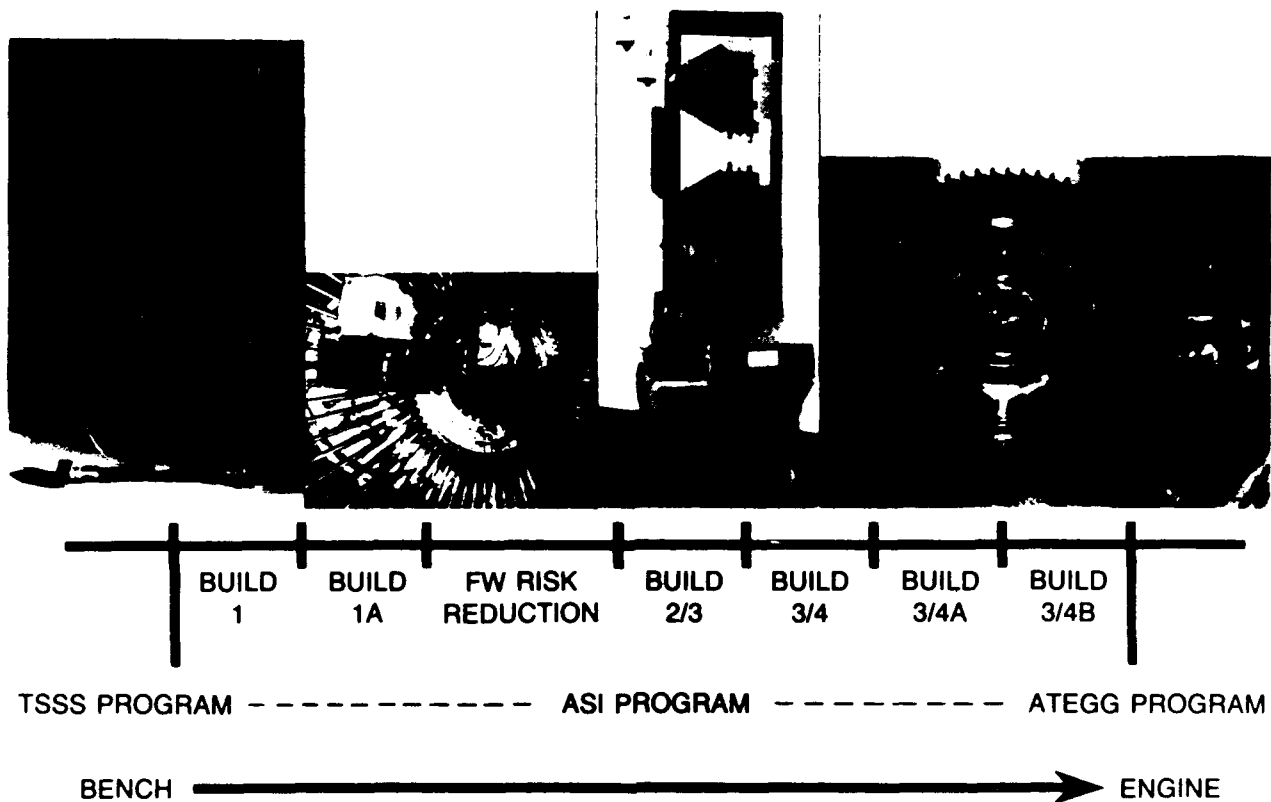


Figure 4-3. Optical fiber sensor technology development.

This aspect results in complete switching of the optical power, alternately, from one core to the adjacent and then back again: crosstalk. The length of the crosstalk period is defined as the beat length,  $\lambda_b$ . External disturbances change the sensor length and beat length to yield a net phase shift ( $\delta\phi$ ) between the two modes at the output of the sensor. When such a phase shift occurs, the light appears to switch from one core to the other in a cosinusoidal fashion which can be calibrated to provide a measurement of temperature and strain. The switching is most conveniently parameterized by the normalized core contrast function  $Q = (P_1 - P_2) / (P_1 + P_2)$ .  $P_i$  represents the total power which exits from the  $i$ th core.

The relative phase shift between the modes at the sensor output is a function of wavelength ( $\lambda$ ), strain ( $\epsilon$ ) and temperature ( $T$ ) as illustrated in Figure 4-5. In the expression of Figure 4-5, the coefficients A and B contain the device sensitivities to temperature and wavelength. For instance, A combines the effects of thermo-optic and stress-optics changes induced by thermal strain of the core

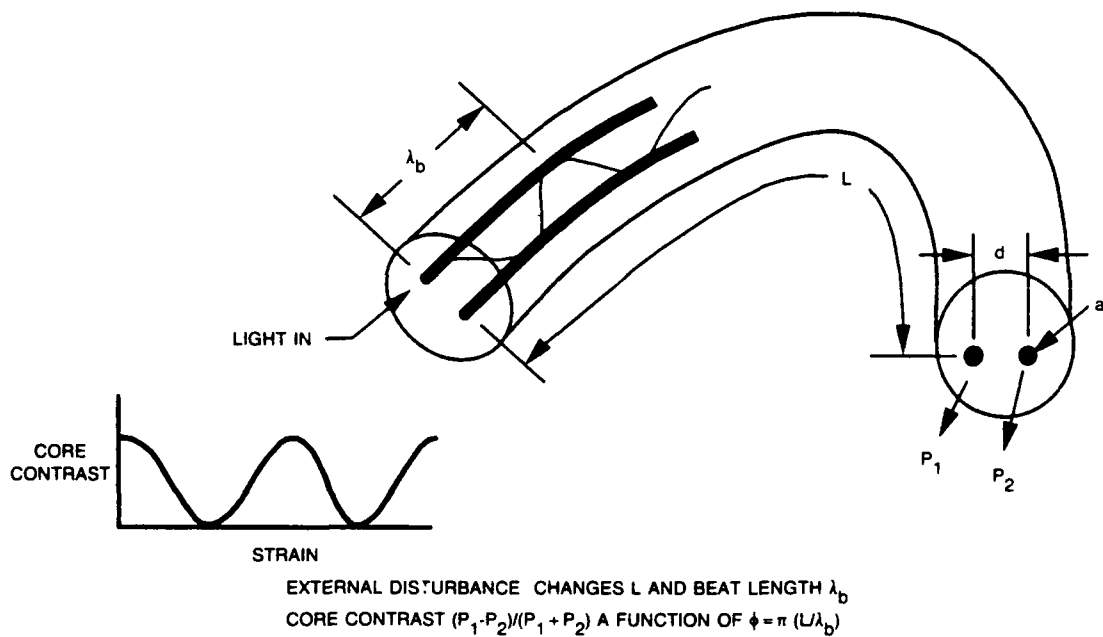


Figure 4-4. Twin-core fiber optic sensor concept.

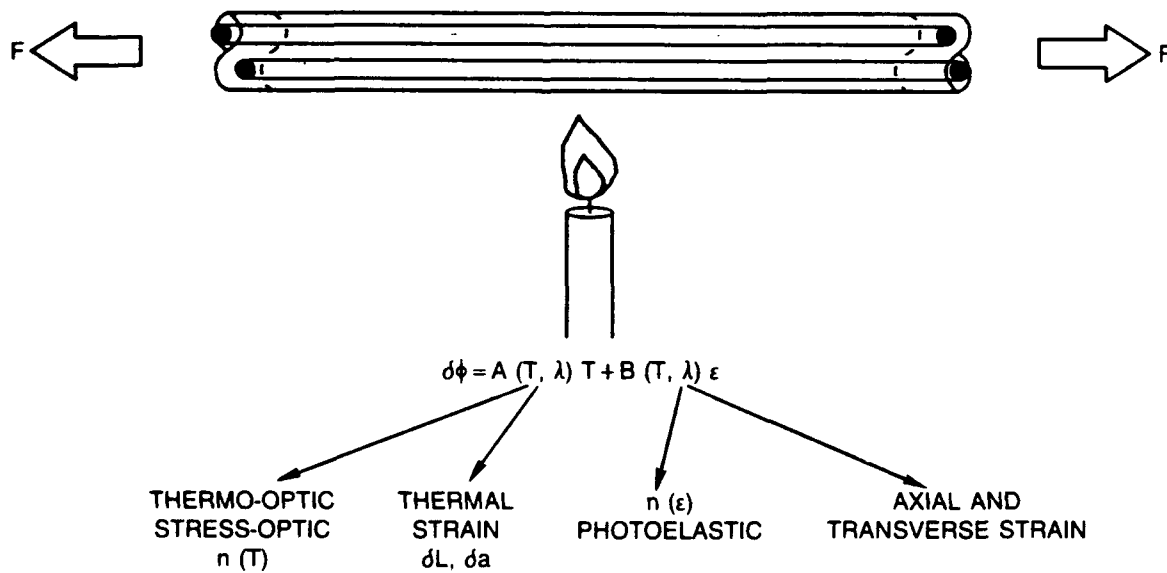


Figure 4-5. Strain and temperature response.

radius,  $a$ , and the length,  $L$ . The photoelastic changes imposed on the device are contained in  $B$ , accounting for all axial and transverse mechanical strains. To a good approximation, these two coefficients are uncoupled. Therefore, simultaneous operation of the device at two wavelengths corresponds to establishing a simple array of two equations with temperature and strain as the unknowns. See Figure 4-6. Analytically predicted or laboratory measured calibration information

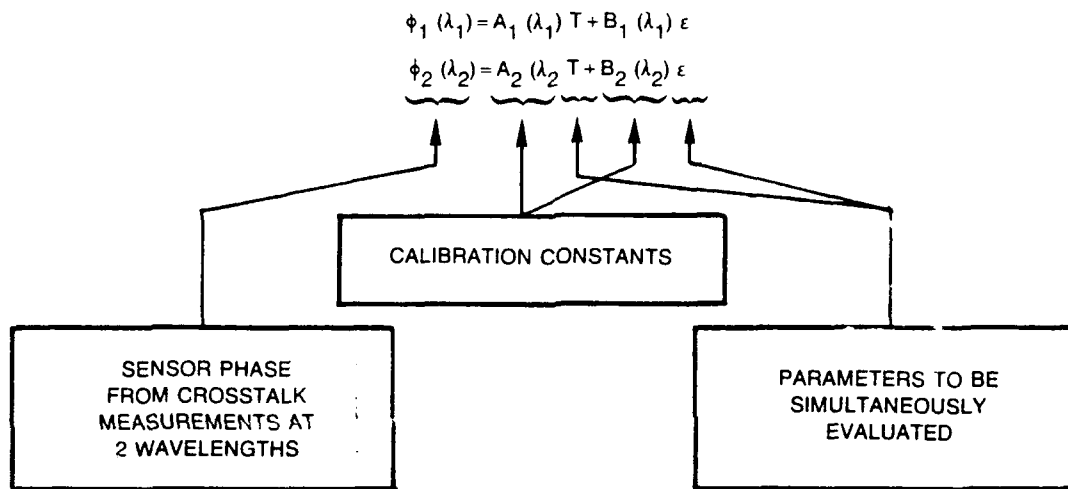


Figure 4-6. Instrumentation concept.

along with measurements of the accumulated sensor phase change at the two wavelengths provide all the numerical information necessary to extract  $T$  and  $\epsilon$ .

During a previous contract, the rod and tube preform method was used to fabricate sensors of low temperature glasses for proof of concept testing. We observed that laboratory devices exhibited strain and temperature responses equal to that predicted by a comprehensive theory. However, from a practical point of view, the operating temperature of the sensor needed to be increased to about 922 K to be useful for simulated engine tests. This extension to 922 K was accomplished during the TSSS program, using germanium-doped fused silica for the higher temperature version of the twin-core sensor. The upper operating temperature of this system is limited by diffusion of the germanium dopant in the single mode waveguide regions. We have observed practical operating lifetimes on the order of 50 hours at the desired temperature.

However, a critical problem involving sensor durability develops as we attempt to address harsh environments. Polymer protective coatings supplied by many vendors will decompose when exposed to high temperatures. Once decomposed, the residues do not protect the surface, and in some cases, lead to embrittlement of the fiber. If the polymer coating is stripped off, then the sensor surface usually becomes marred during installation. This handling related degradation can lead to serious limitations. For instance, the intrinsic strength of fused silica approaches 13970 MPa. After handling an unprotected surface, fiber strength can fall to 209 MPa. To understand the significance of this degradation, note that the applied measurement stress on a fiber is related to the sum of the thermally induced strain from expansion of the substrate and the true mechanical strain of the substrate. For IN-100 heated to 922 K, 670 MPa is applied to the sensor. A typical 3000 microstrains mechanical strain of the substrate will apply 209 MPa additional stress, for a total measurement stress of 880 MPa. Obviously, a fiber of 209 MPa strength would not survive. Strengths above 1397 MPa are desirable for successful application with some safety margin.

We investigated two methods of preserving fiber strength at elevated temperatures: encasing the fiber in a compressive layer of glass and applying a metal protective coating. In the first case, we gain fiber strength by the amount of surface compression achieved when the sensor is encased in a glass with a higher thermal expansion coefficient. To accomplish this, we surrounded the twin-core fiber preform (thermal expansion coefficient of about  $6 \times 10^{-7}$  per  $^{\circ}\text{C}$ ) with rods of aluminosilicate glass (thermal expansion coefficient of about  $42 \times 10^{-7}$  per  $^{\circ}\text{C}$ ) and then inserted the combination into another silica tube. This composite was then drawn down to normal sensor dimensions. Figure 4-7 provides a cross-sectional picture of the sensor fabricated in this manner. The bare, modified sensor exhibited a promising strength improvement of 1048 MPa over an extended period of time at room temperature. Unfortunately there were several problems. For instance, the aluminosilicate glass melted at a lower temperature than the silica, allowing it to flow from the rod-inclusion geometry to a nonuniform, encasing layer. This caused the fiber to curl. In addition, the extra complication during preform assembly led to unusually frequent bubble formation.

Metal protective coatings were also investigated. Preliminary sputtering tests showed that nickel, a candidate because of its high temperature capability, adhered well to the silica filaments but created



Figure 4-7. Twin core optical fiber sensor. Germanium-doped silica sensor with aluminosilicate compressive layer.

some difficulties. Sputtered onto the fiber surface, the thin film became so highly stressed that the brittle metal layer would crack and then initiate breaking of the glass filament when the device was bent. An annealing process might alleviate this problem. However, we also sputtered aluminum and found it to be very well behaved when subjected to bending. Aluminum is more ductile than nickel and will yield under stressed conditions instead of cracking as nickel does. As a result, aluminum coated fiber was more tolerant of bending. Hence we developed an in-line coating process to apply aluminum to the optical fibers before they were touched in any other manner. Figure 4-8 provides a diagram of the system which we implemented for application of the aluminum buffer layer to the optical fibers. A cross-sectional view of a coated fiber is shown in Figure 4-9.

In summary, we implemented an on-line method for coating the glass fiber with aluminum to provide surface protection. Functionality of this coating is limited to environmental conditions below the melting temperature of aluminum. Furthermore, since the germanium-doped silica system has a useful lifetime for temperatures less than 922 K, we have assembled glasses and coatings with compatible operating temperature capabilities.

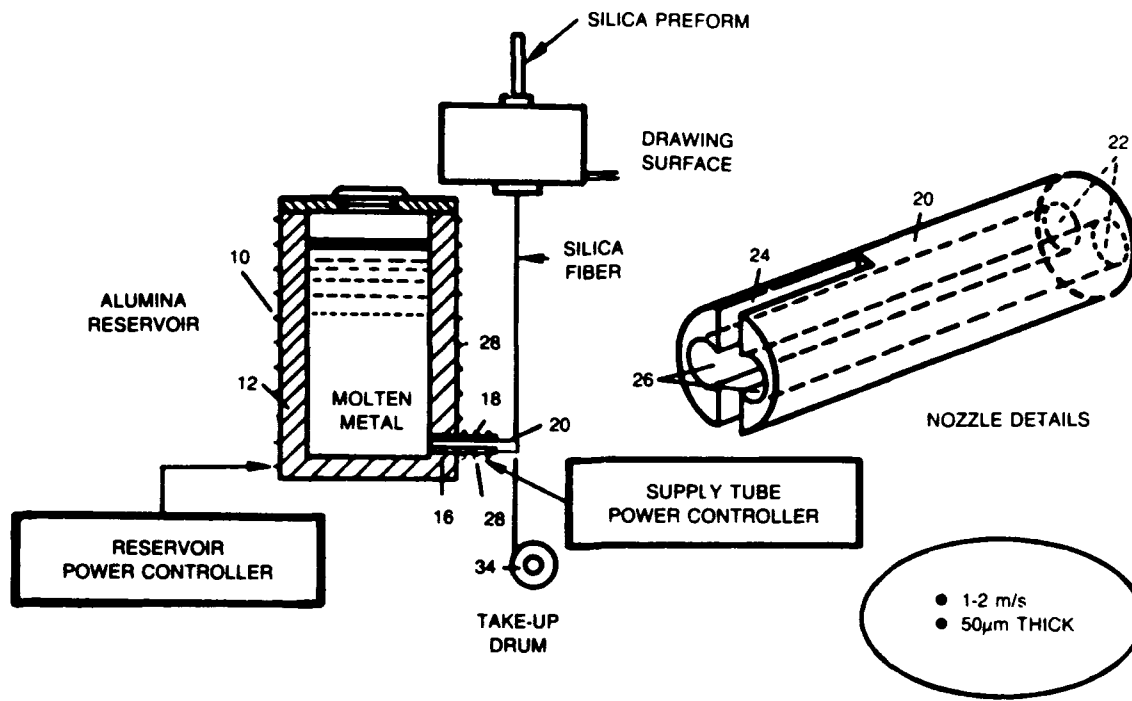


Figure 4-8. Apparatus for metal coating.

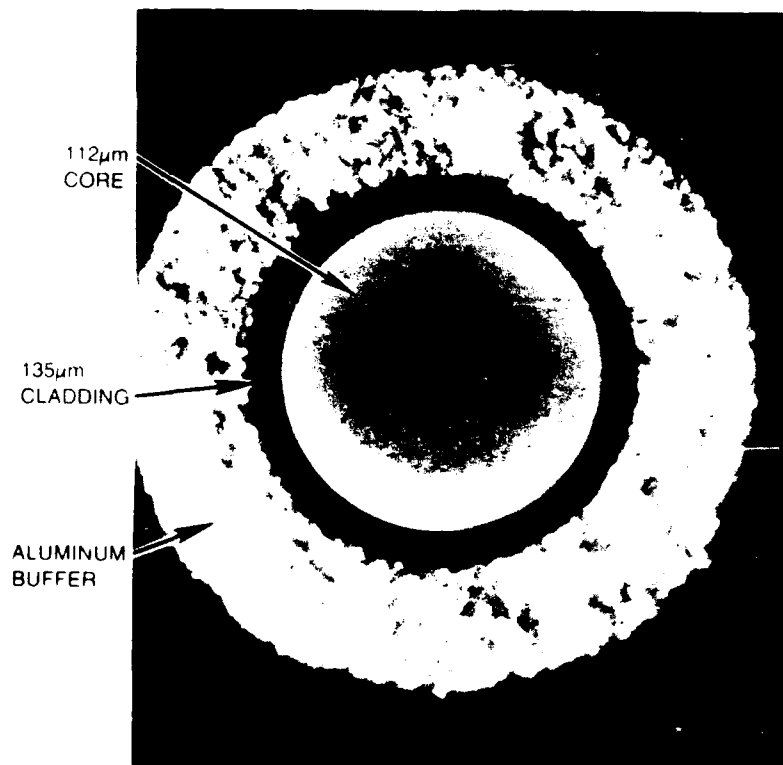


Figure 4-9. Fiber optic strain sensor. Multi-mode output fiber cross section.

Finally, turbine diagnostics require quasi-point measurements, implying limitation of the sensor gage length. To accomplish this, we attach input and output leads to short sections of sensor in the arrangement of Figure 4-10. All connections are made by fusion-splicing techniques to maintain

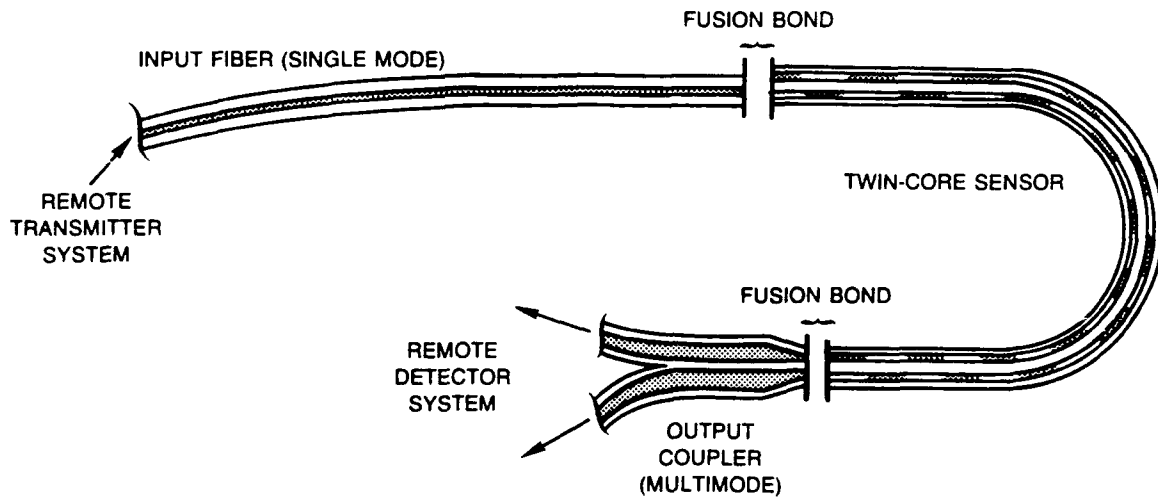


Figure 4-10. Fiber optic strain sensor. Basic optical unit design.

compatibility with the elevated temperatures. The input lead is a matched single-core single-mode fiber aligned with one core at the sensor excitation end, and the output leads consist of two multimode fibers which intercept the power from each core at the sensor output end. The operations just described are quite demanding because stringent alignment and splicing tolerances must be maintained. We found that in-process diagnostics are essential for completion of successful assemblies. Prior to splicing, the aluminum must be etched from short sections of the fiber. After assembly, we apply a final silver paint coating to protect the spliced regions. When materials and geometries are properly matched, the fusion joints exhibit strengths in excess of 698 MPa. A photograph of a real twin-core device assembled in this manner is provided by Figure 4-11. Note that the sensor length can be cut to whatever gage length is required to yield a good phase shift for the anticipated disturbances. The output signal corresponds to the integral of the disturbance-induced phase shift over the total gage length. Application of the device is described next.

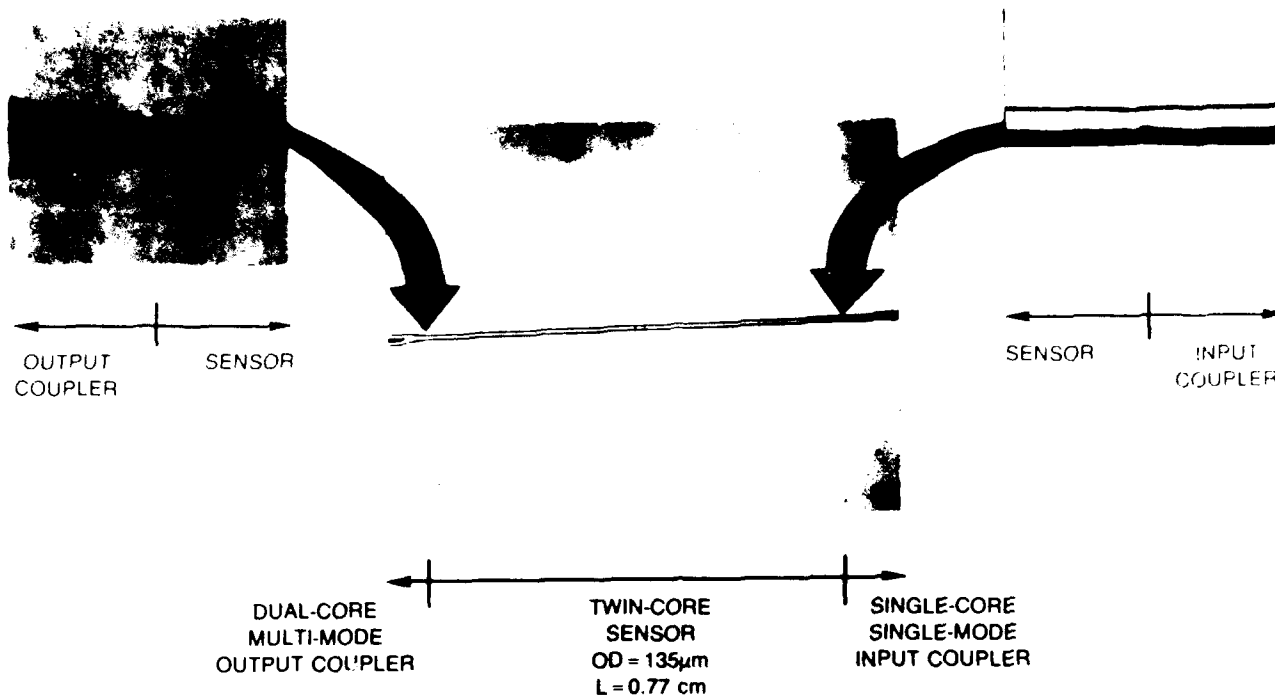


Figure 4-11. Fiber optic strain sensor. Fully assembled sensor using fusion-splice technique.

#### 4. NONROTATING RISK REDUCTION TESTS--THE FERRIS WHEEL EXPERIMENT

The twin-core optical fiber sensors utilized for the Ferris wheel experiment were essentially the same as those developed and tested during the TSSS program. The strain and temperature responses of typical devices are illustrated in Figures 4-12 and 4-13. The effective sensitivity coefficients for unattached devices are reviewed in Table 2 for unattached sensors.

TABLE 2. TSSS MEASURED SENSOR RESPONSE  
(UNATTACHED DEVICES)

	633 nm	830 nm
$\frac{1}{L} \frac{d\phi}{d\epsilon} \left( \frac{R_{AD}}{\mu\epsilon in.} \right)$	$5.49 \times 10^{-4}$	$6.00 \times 10^{-4}$
$\frac{1}{L} \frac{d\phi}{dT} \left( \frac{R_{AD}}{^{\circ}F in.} \right)$	$5.79 \times 10^{-3}$	$3.52 \times 10^{-3}$

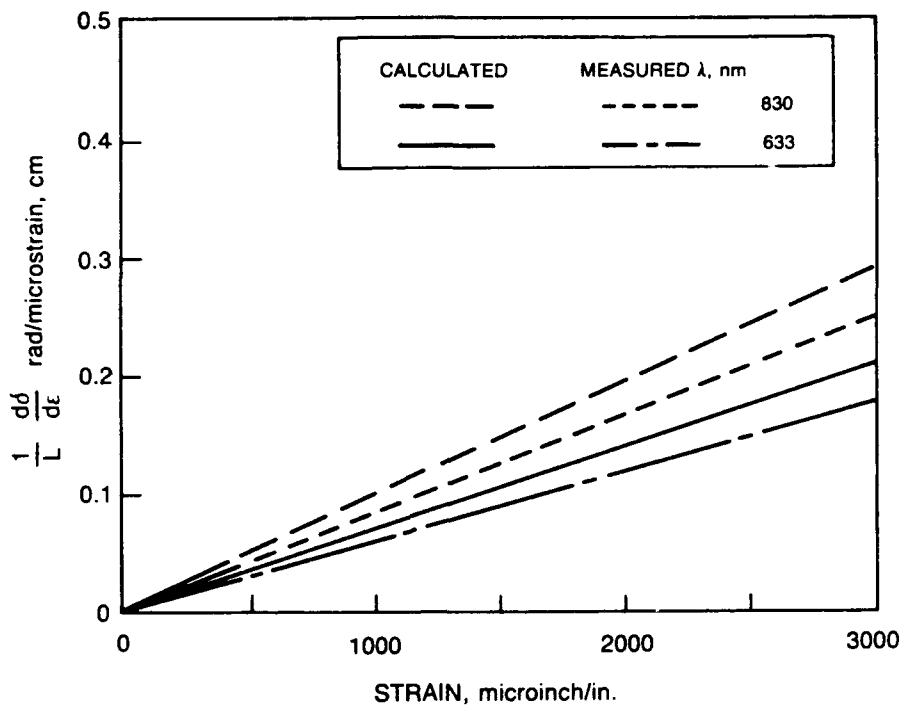


Figure 4-12. Comparison of measured and computed strain sensitivity.

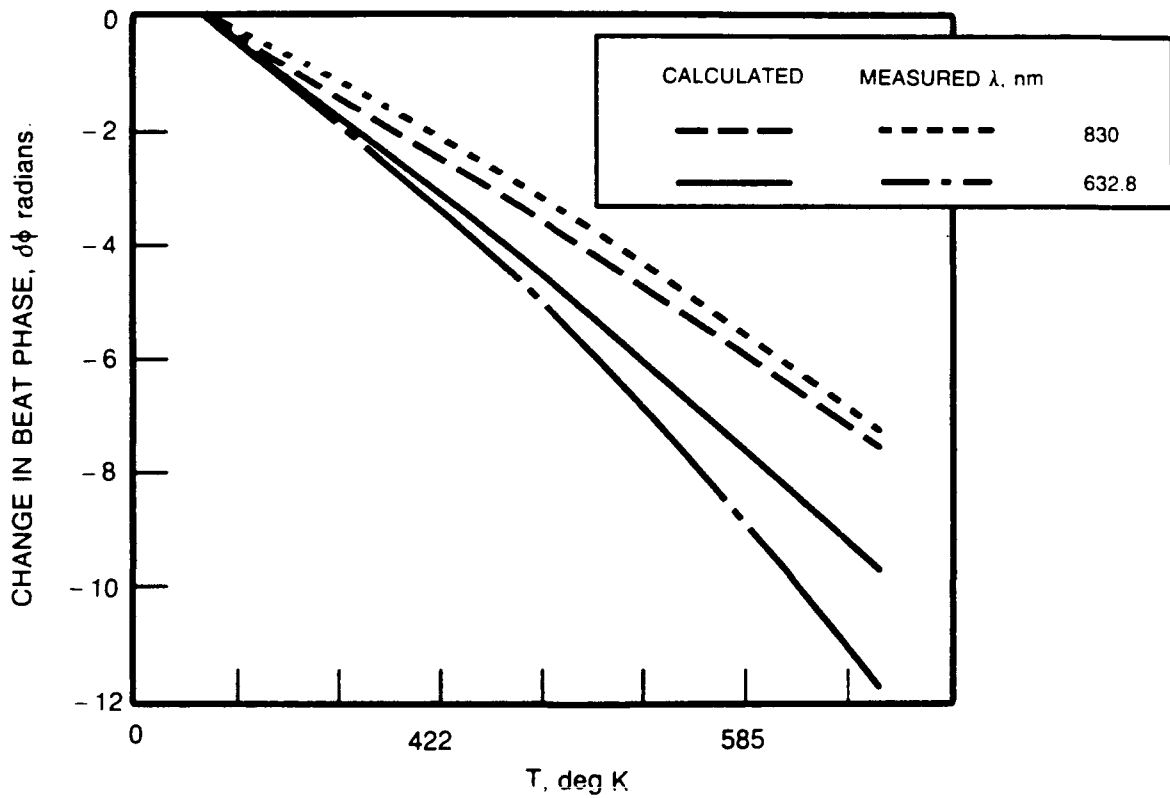


Figure 4-13. Twin-core fiber optic sensor. Predicted and measured temperature sensitivity.

To conduct the Ferris wheel experiments, it was necessary to establish turbine-engine-compatible installation and attachment methods. The selected configuration is shown in Figure 4-14. The

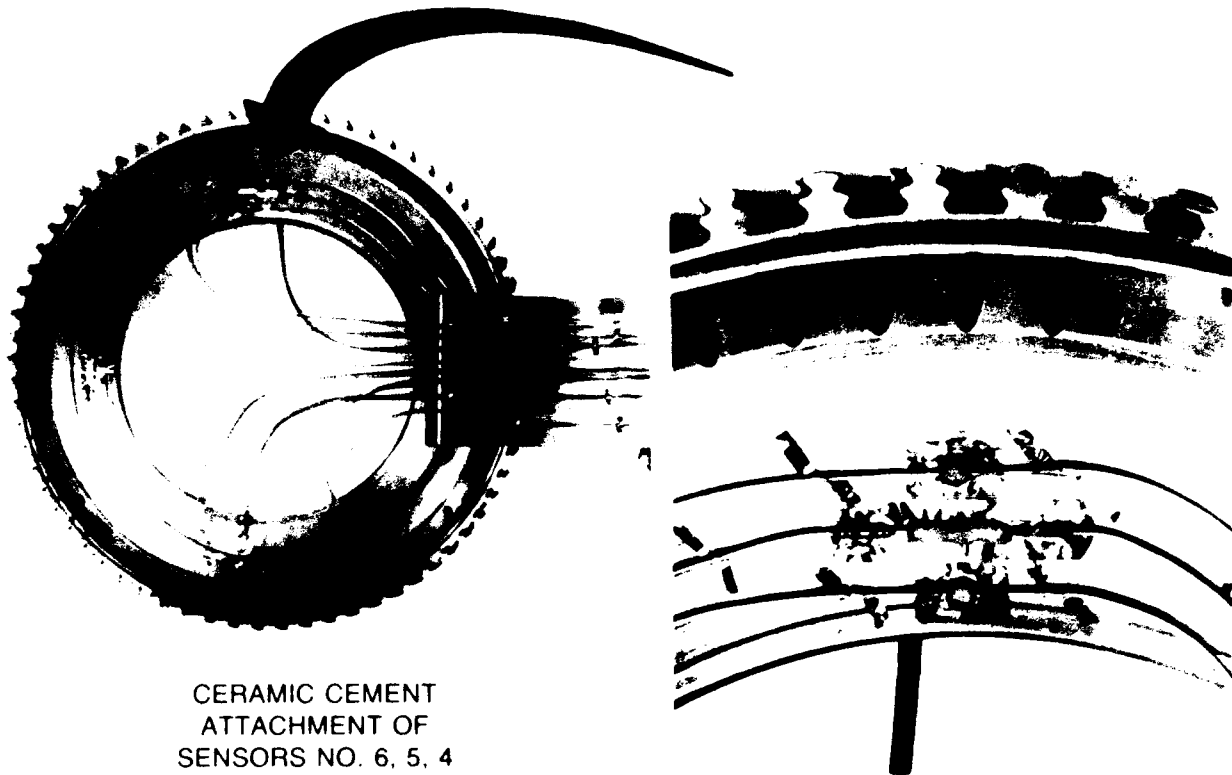


Figure 4-14. Twin-core optical fiber sensor. Ferris wheel experiment; F 100 disk.

installation procedure includes mounting small diameter stainless steel tubing on the disk surface with spot welded straps to provide a miniature conduit for routing the sensor to the measurement site. At the measurement location, the active portion of the optical fiber sensor was attached with a single-component ceramic cement.

Ceramic cement was selected because of its accepted use for attachment of high temperature sensors. However, during the TSSS program we had experienced some difficulty with the cement cracking free from the IN-100 disk material. It was hypothesized that this resulted from mismatches in the thermal expansion coefficient of the cement in comparison with the metal substrate. There can be

as much as a factor of 10 discrepancy. In an attempt to improve attachment durability, we tested methods for grading a coarse match in expansion coefficients by introducing secondary layers of other cements with differing coefficients. See Figure 4-15. Each graded configuration was tested with a

<u>MATERIAL</u>	<u><math>\alpha</math> (in./in./°F)</u>
SiO <sub>2</sub>	0.3
GA-100	0.8
503	4.0
31	6.3
501	7.0
IN-100	7-8

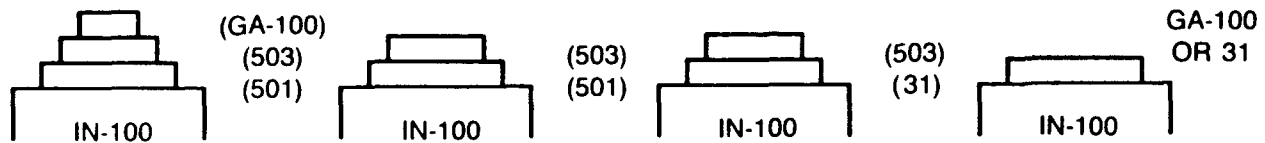


Figure 4-15. Fiber optic strain sensor. Attachment study.

fiber attached to a small IN-100 test specimen as shown in Figure 4-16. After curing of the cement, each specimen was baked at 922 K. Then a pullout test was performed while a force measurement system was attached to the fiber. The cement attachment strength was recorded on an oscilloscope at the moment of failure. We found that all combinations performed more poorly than a single application of GA-100. Hence, the Ferris wheel experiment utilized GA-100.

Six twin-core optical fiber sensors were attached to the disk. An overview of the layout is shown in Figure 4-17. The supporting instrumentation consisted of high temperature thermocouples, high temperature thin film strain gages, and conventional strain gages. A complete sensor inventory is provided in Table 3. The instrumented disk was mounted in the test facility with all leads (10m to 12m in length) coming to a single location for interfacing to the laboratory instrumentation.

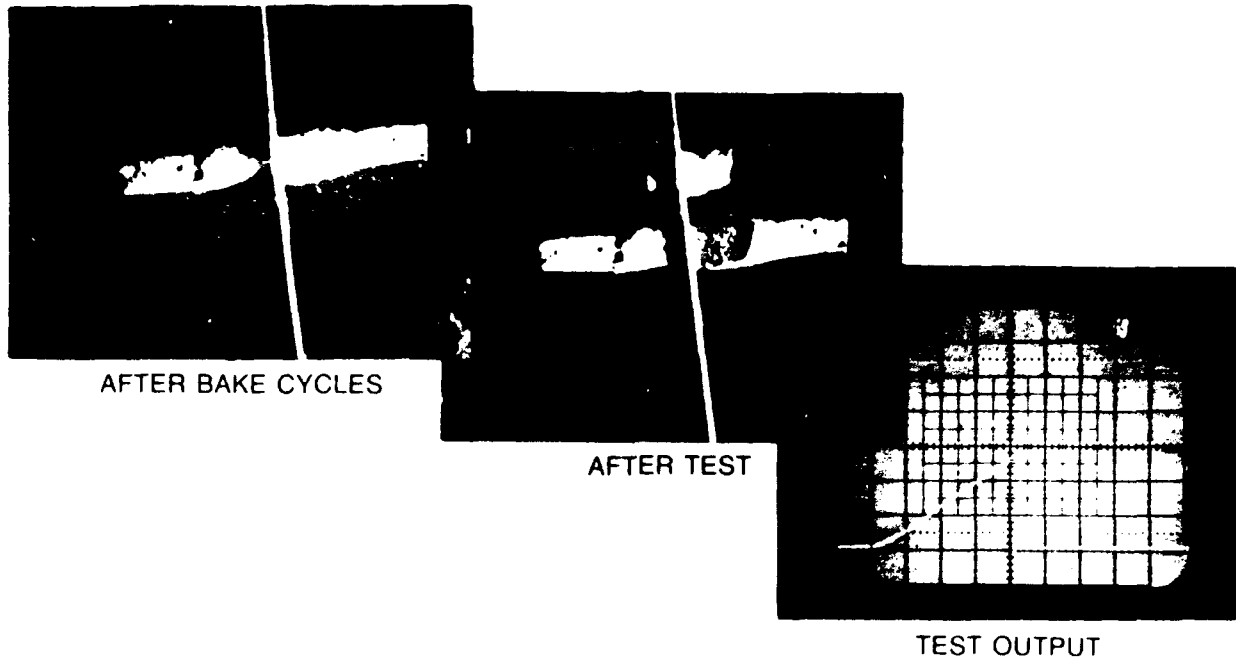


Figure 4-16. Fiber optic strain sensor. Attachment study (sample 10A-2 GA-100).

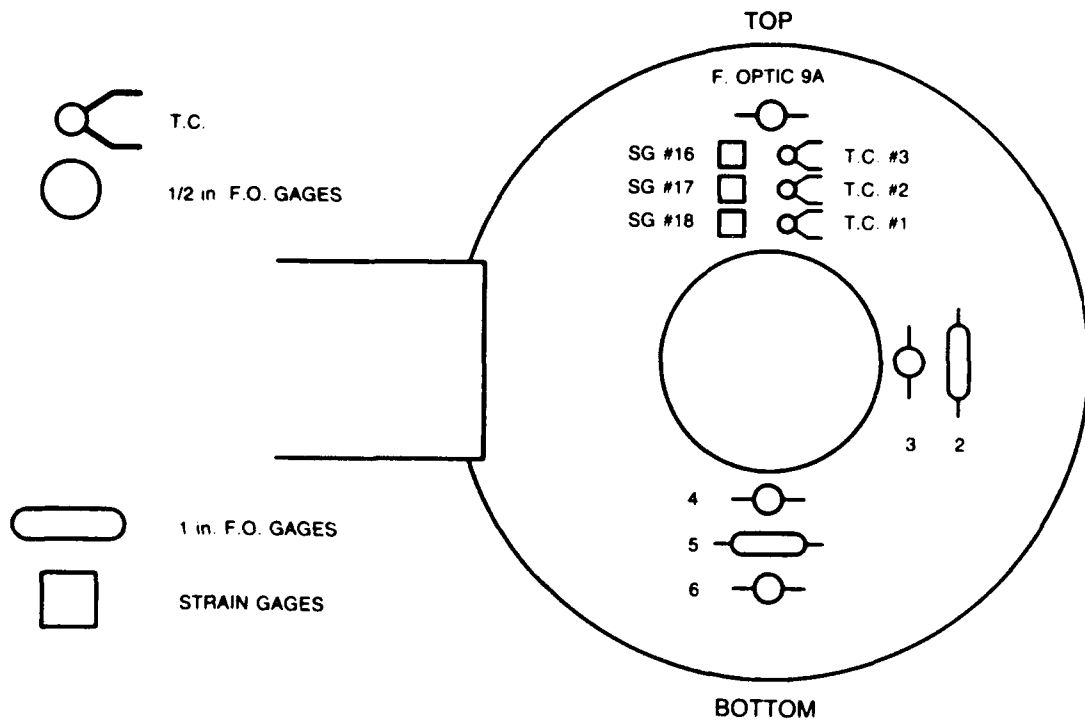


Figure 4-17. Sensor array. Ferris wheel experiment.

---

**TABLE 3. SENSOR INVENTORY; FERRIS WHEEL EXPERIMENT**

---

- \* 6 PdCr static thin film strain gages
  - \* 6 FeCrAl static thin film strain gages
  - \* 6 Ni/30Cr dynamic thin film strain gages
  - \* 6 twin-core fiber optic strain and temperature sensors
  - \* 6 standard electrical strain gages
  - \* 6 type K thermocouples
- 

Wavelength multiplexing was selected to implement two color transmitter operation; a helium neon laser (633 nm) and a laser diode (830 nm) were coaxially combined with a dichroic beam combiner. After equal division with a non-wavelength-sensitive splitter, two sets of beam-to-fiber matching optics enabled us to excite two sensors simultaneously. The receiver system utilized a dichroic splitter to separate the signals from each output lead. Therefore, to complete the measurements we recorded 8 detector signals (2 sensors, 4 output leads, 2 colors) in addition to the signals from the supporting instrumentation on a computer-supported acquisition system backed up by an FM instrumentation tape recorder (Table 4). All signal processing was conducted after the tests. The instrumentation is shown in Figure 4-18.

---

**TABLE 4. INSTRUMENTATION; FERRIS WHEEL EXPERIMENT**

---

- \* HP-85 with dual floppy disk storage
  - \* HP-3497 data acquisition unit
  - \* 44427A(3) plug-in for strain gage bridge completion/measurement
  - \* 44422A(1) plug-in for thermocouple and twin-core sensor measurement
  - \* multi-channel FM tape recorder for backup
-

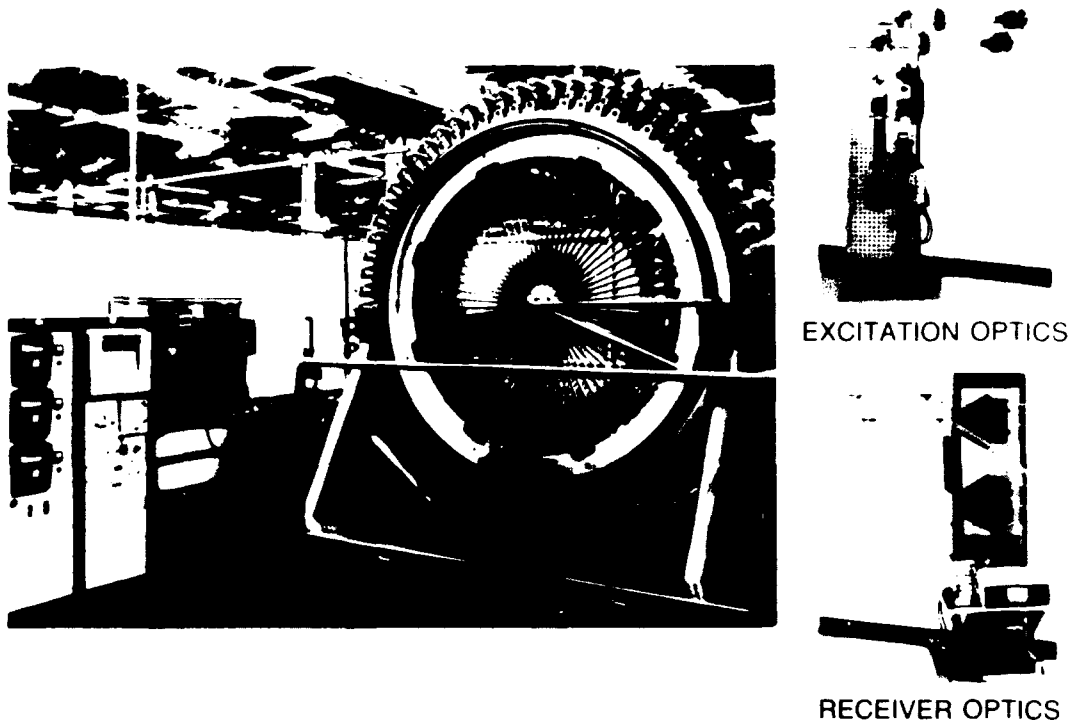


Figure 4-18. Twin-core optical fiber sensor. Ferris wheel Experimental Facility.

Figure 4-18 also shows a disk positioned within the Ferris wheel test facility (at Pratt & Whitney, West Palm Beach, Florida). Hydraulically driven rods are used to simulate spin loads applied to the disk. Table 5 correlates rod loading levels with strain applied to the sensor locations. A movable pipe structure is used to support a clamshell oven in position, covering each side of the disk. The entire disk and support system is rotated in an oscillatory fashion at 1 r/min to maintain uniform elevated temperatures on the disk.

**TABLE 5. LOAD AND STRAIN RELATION**

<b>Ferris wheel Experiments</b>	
<b>Load (N)</b>	<b>Strain (<math>\mu\epsilon</math>)</b>
2,896	$459 \begin{pmatrix} +21 \\ -29 \end{pmatrix}$
5,792	$923 \begin{pmatrix} +37 \\ -30 \end{pmatrix}$
8,688	$1,391 \begin{pmatrix} +39 \\ -41 \end{pmatrix}$
11,584	$1,853 \begin{pmatrix} +47 \\ -53 \end{pmatrix}$
14,480	$2,321 \begin{pmatrix} +59 \\ -61 \end{pmatrix}$

The test program conducted with this facility is shown in Figure 4-19. Highlights of the most important results of the Ferris wheel experiment are reviewed in this section. An outline narrative of all test results is contained in Appendix A: Ferris wheel Data Base.

Characteristic sensor response (unprocessed data) to 589 K is illustrated in Figure 4-20 which presents the core contrast function plotted against the approximate temperature of the disk. Clearly present is the cosine discriminant of the twin-core sensor response with a contrast limitation for this device equivalent to about 0.5. The signal can be linearized simply by application of an arccosine inversion. While at 589 K, a load survey was conducted. Figure 4-21 shows excellent sensor load response.

In subsequent tests, sensor operation was verified above 922 K while slippage of the attachment was observed during the load survey. For example, Figure 4-22 provides one sensor signal which responds nicely with the increase in temperature from ambient conditions to more than 922 K. However, on the way down in temperature after a load survey, there is an offset in the quiescent signal. We believe that this occurred as the result of the sensor slipping within the ceramic cement during the load survey. That survey is plotted in Figure 4-23, where we notice no effective sensor response to strain even though it is obviously working as evidenced by the thermal response.

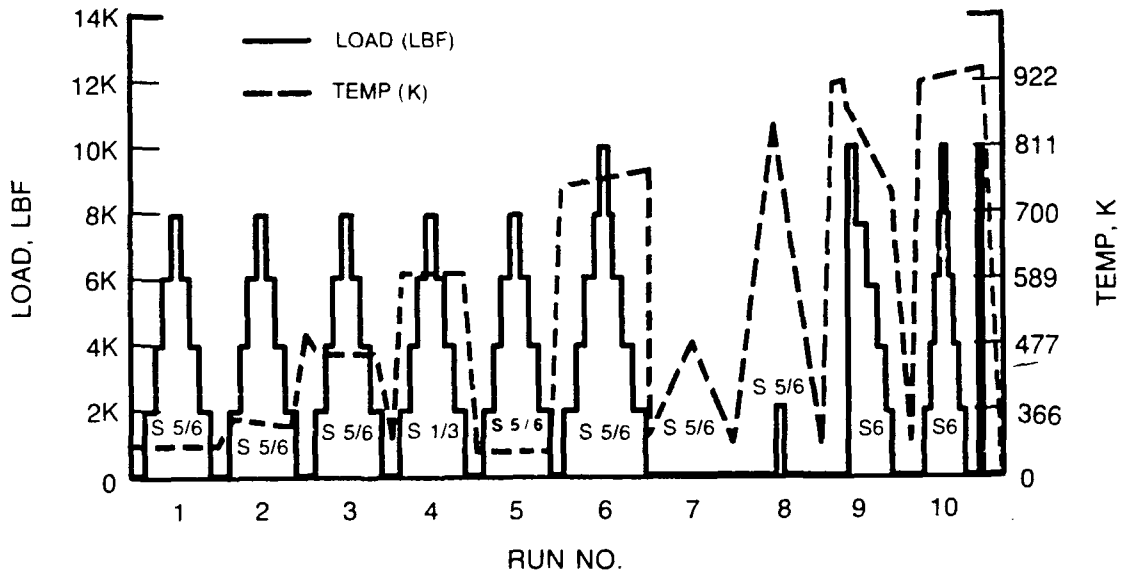


Figure 4-19. Ferris wheel test program.

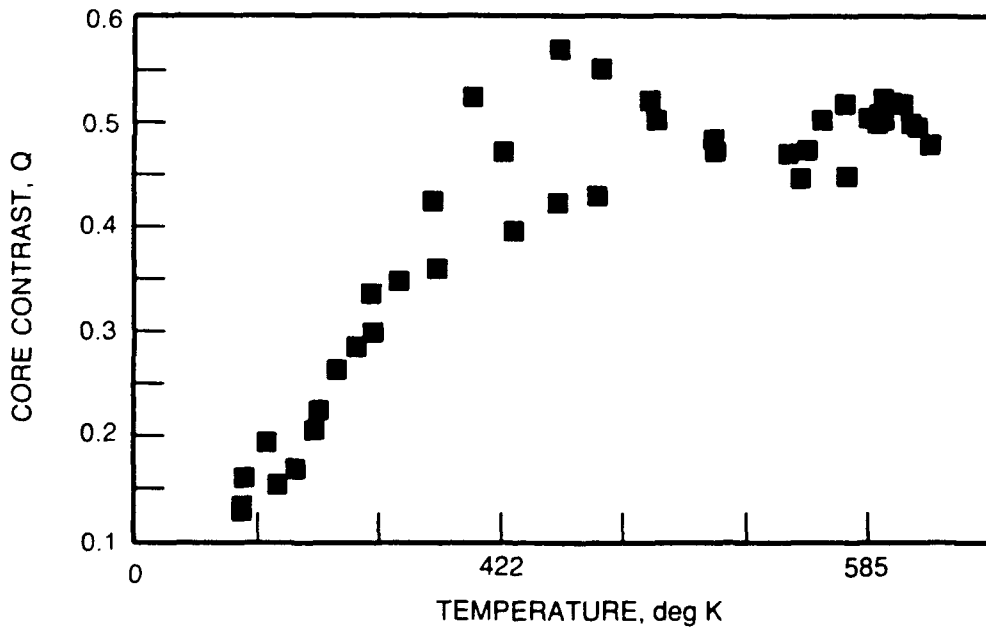


Figure 4-20. Twin-core optical fiber sensor. Temperature response. Ferris wheel data; run No. 4, sensor 6, 633 nm.

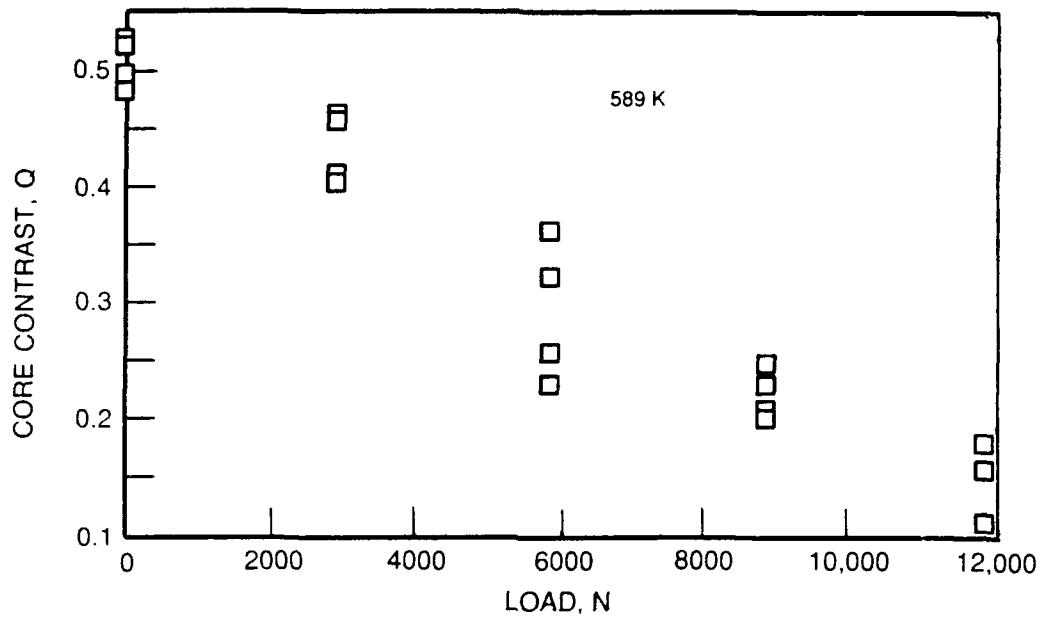


Figure 4-21. Twin-core optical fiber sensor. Load response at 589 K, run No. 4, sensor 6, 633 nm.

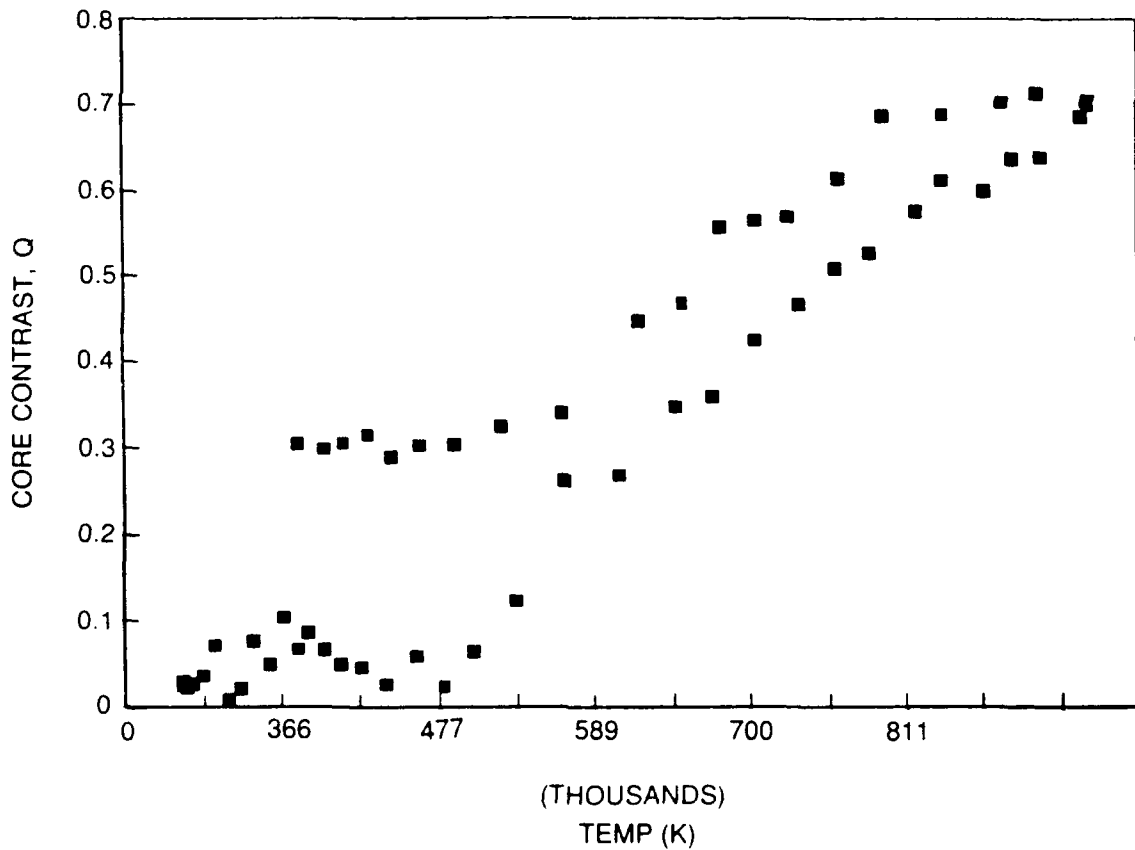


Figure 4-22. Twin-core optical fiber sensor. Temperature response. Ferris wheel data; run No. 10, sensor 6, 830 nm.

In summary, the twin-core optical fiber sensor survived the simulated engine test conditions as demonstrated by the signals and the before/after photographs in Figure 4-24, verifying our selection of sensor materials and coating materials. Unfortunately, problems were encountered with the attachment of the devices to the disk and with reliability of some of the instrumentation. Most of the significant issues were further addressed during the spin rig experiments.

## 5. ROTATING TESTS--THE SPIN RIG EXPERIMENT

In support of instrumentation developments discussed in this section, the twin-core sensor was fabricated with different dimensions for the Spin rig experiment. Operational wavelengths for this test phase were changed such that both were in the near infrared region. As a result, the waveguide dimensions could be increased, yielding larger throughput signals. Table 6 lists the parameters for the new sensor measured by two methods, with an optical microscope and with an index profiler. When the preform for the sensor is assembled with an outside diameter of the order of 2 cm, the spatial

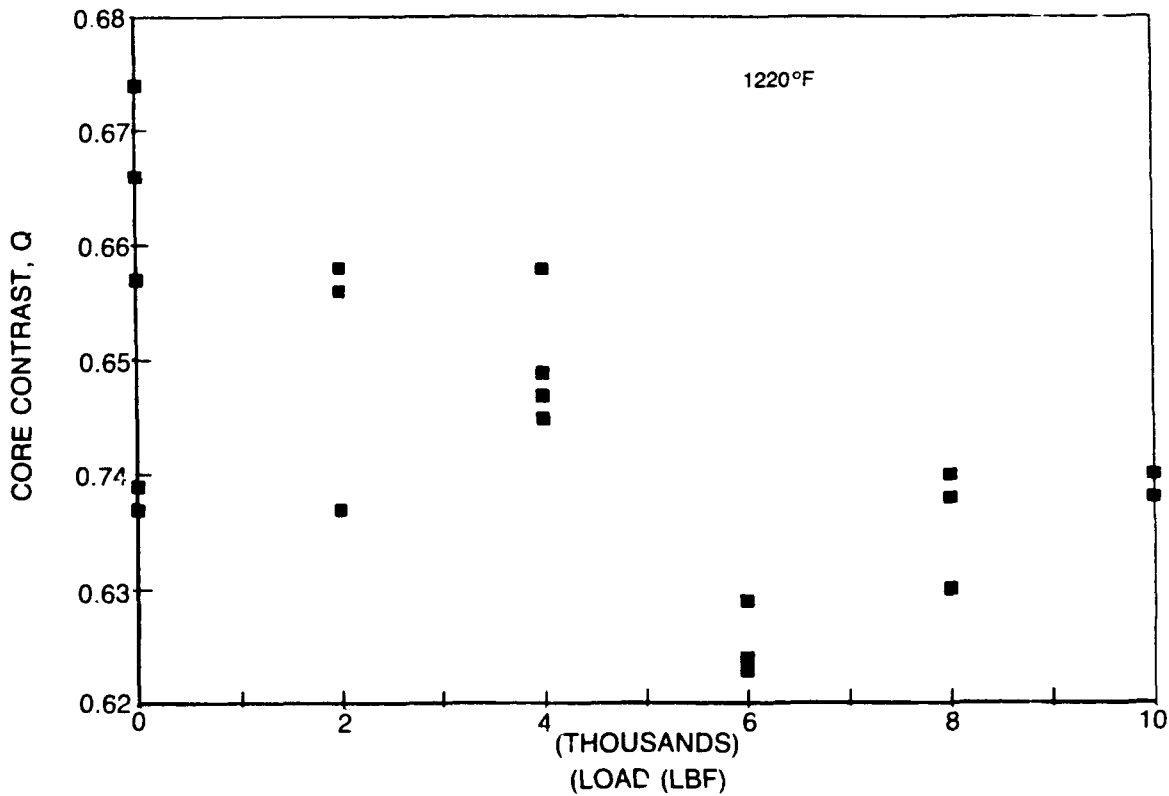
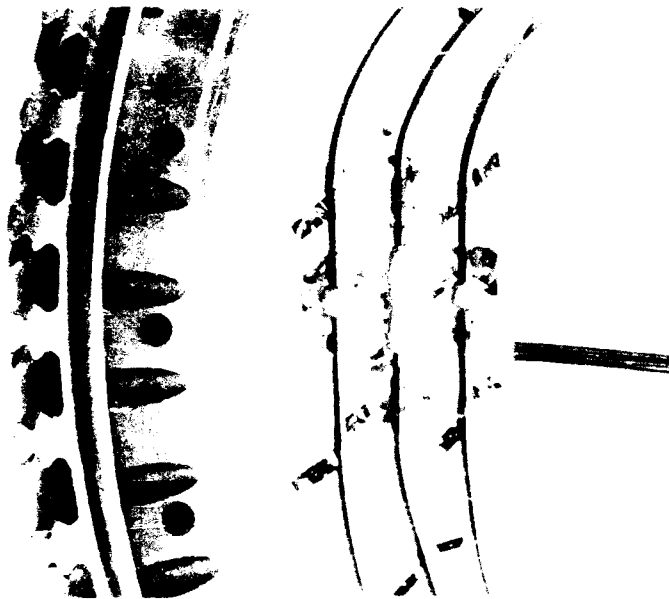


Figure 4-23. Twin-core optical fiber sensor. Load response at 933 K. Ferris wheel data; run No. 10, sensor 6, 830 nm.

BEFORE TEST



AFTER TEST



Figure 4-24. Twin-core sensors. Ferris wheel test; modified F100 disk with sensors No. 6, 5, 4.

distribution of the index of refraction across the diameter of the sensor is representative of a perfect step function for each core. However, the extrusion process used to fabricate the functional devices with final outside dimensions of the order of  $186\mu\text{m}$  can cause some diffusion of the germanium dopant from each core into the surrounding cladding. The resulting spatial distribution of the index of refraction is no longer a perfect step function but representative of a distribution between step and Gaussian. This fact has an affect on the actual sensitivity of the device in comparison with the predicted response. Initially, a detailed analytic model was used to predict the response of the sensor. The analytic model assumes either a step index distribution or a Gaussian distribution. The predicted sensitivities of the sensor to temperature and strain changes are given in Table 7. This table also lists the anticipated total signals for a device subjected to a thermally induced strain which results from attachment to IN-100 elevated to 866 K and to a mechanically induced strain of 2000 microstrains. Note that the core contrast (Q) phase shift,  $\Delta\Phi$ , is calculated as twice the beat phase shift,  $\delta\phi$ . We observe that there is a significant difference in the response of a device with a step function distribution compared with a Gaussian distribution and this difference depends on wavelength.

---

**TABLE 6. SPIN RIG SENSOR PARAMETERS**

---

**Optical Microscope Measurements**

---

OD =  $186\mu\text{m}$   
d =  $6.51\mu\text{m}$   
a =  $1.77\mu\text{m}$

---

**Index Profiler Measurements**

---

OD =  $185.5\mu\text{m}$   
d =  $6.1\mu\text{m}$   
a =  $1.55\mu\text{m}$   
NA =  $1.43\mu\text{m}$

---

**TABLE 7. ANALYTICALLY PREDICTED, UNATTACHED CALIBRATION  
CONSTANTS AND RESPONSE  
(PER INCH OF SENSOR LENGTH)**

	750 nm; step	750 nm; gauss	830 nm; step	830 nm; gauss
$\frac{d\phi}{d\epsilon}$ ( $\%/\mu\epsilon$ )	$1.5 \times 10^{-3}$	$2.5 \times 10^{-3}$	$2.0 \times 10^{-3}$	$3.0 \times 10^{-3}$
$\frac{d\phi}{dT}$ ( $\%/^{\circ}C$ )	$-1.6 \times 10^{-2}$	$-4.5 \times 10^{-2}$	$-1.8 \times 10^{-2}$	$-4.5 \times 10^{-2}$
%Q(2000 $\mu\epsilon$ mech)	6.0	10	8.0	12
%Q(8000 $\mu\epsilon$ thermo) (IN - 100% 866K)	24	40	32	48
%Q(866K temp)	-19	-54	-22	-54
Total %Q	11	-4	18	6.0

Since the index distribution is neither perfectly step nor perfectly Gaussian, a new detailed empirical modelling method was implemented to develop predictions for the effective calibration constants. The modelling process is outlined in Figure 4-25. To begin with, the response to a temperature perturbation is shown to be a function of the derivative of the coupling factor F with V. On the other hand, the strain coefficient is a function of F and dF/dV. These functional relationships provide the clue to a valuable method of using nondestructive test data from a real sensor with a real index distribution for derivation of the calibration constants. If Q is measured as a function of wavelength,  $\lambda$ , we should have data that takes into account core-to-core coupling for the effective index distribution and then be able to derive the effective calibration constants. This is feasible because of the simple functional relationships shown in Figure 4-25.

The wavelength response for a specific sensor is shown in Figure 4-26. Next, Figure 4-27 shows  $d\phi/d\lambda$  for this data and for a second, longer range data set. Then dF/dV and F(V) can be derived (Fig. 4-28). These finally yield  $d\phi/d\epsilon$  and  $d\phi/dT$  of Figure 4-29, the calibration coefficients. What we discover is that the effective calibration coefficients fall between those of the analytically predicted

$$\frac{d\phi}{dT} = f\left(\frac{dF}{dV}\right); \quad V = \frac{2\pi a (NA)}{\lambda}$$

$$\frac{d\phi}{d\varepsilon} = f\left(F, \frac{dF}{dV}\right)$$

BUT

$$F = f(V, \text{ie., } \lambda^{-1})$$

SO MEASURE

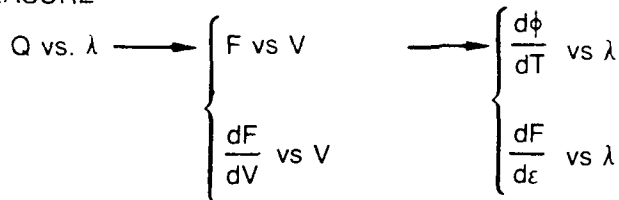


Figure 4-25. Detailed empirical model. Calibration constants.

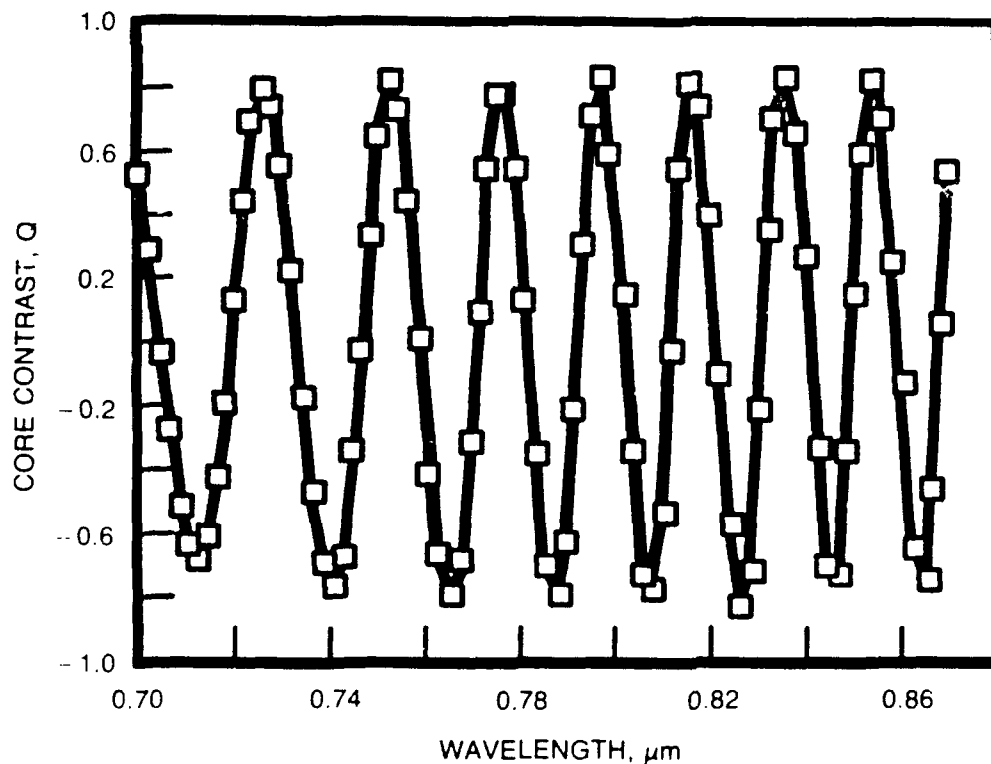


Figure 4-26. Detailed empirical model. Crosstalk vs. wavelength; WPB No. 6. L = 38.6 mm, OD = 186 μm, spectran No. 4.

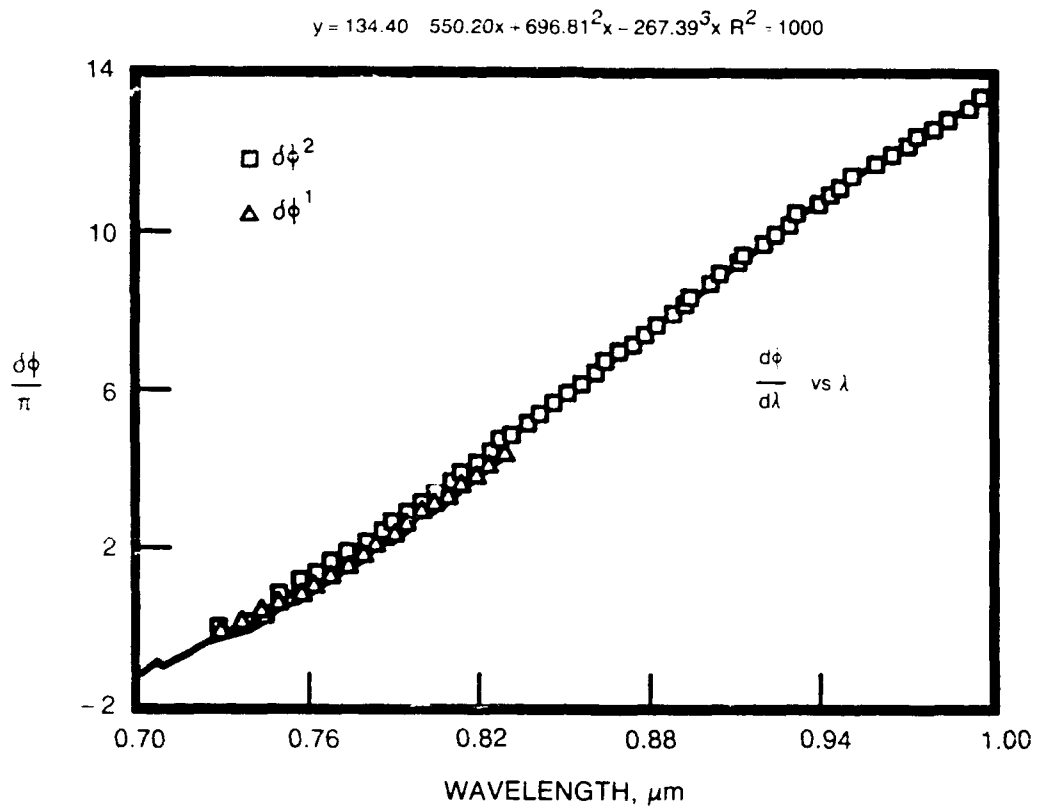


Figure 4-27. Detailed empirical model. WPB No. 6;  $L = 38.6$  mm,  $OD = 186$   $\mu\text{m}$ , spectran No. 4.

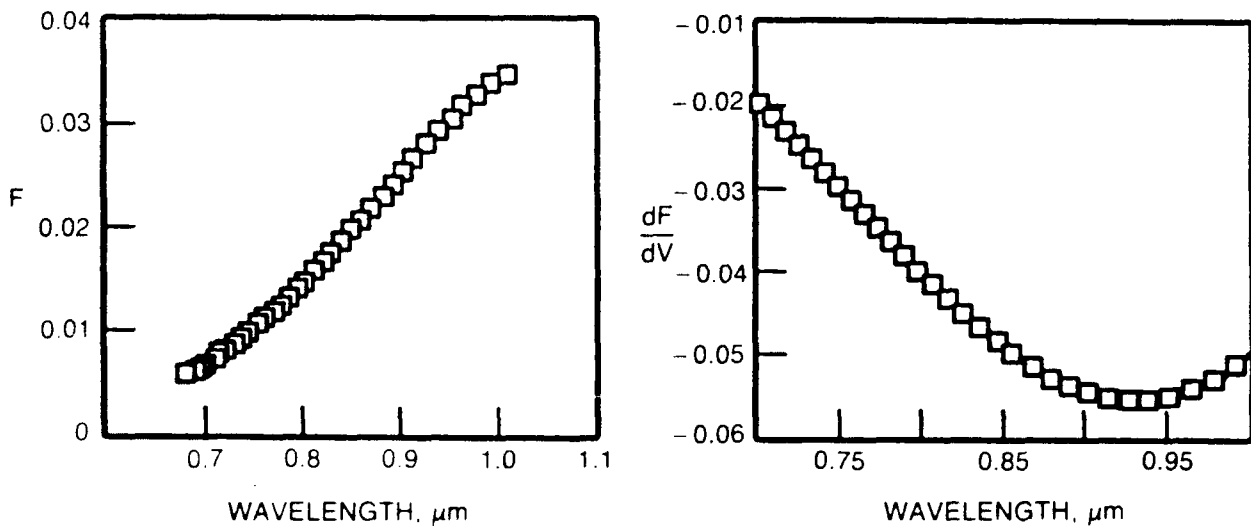


Figure 4-28. Detailed empirical model. WPB 36;  $L = 38.6$  mm,  $OD = 186$   $\mu\text{m}$ , spectran No. 4.

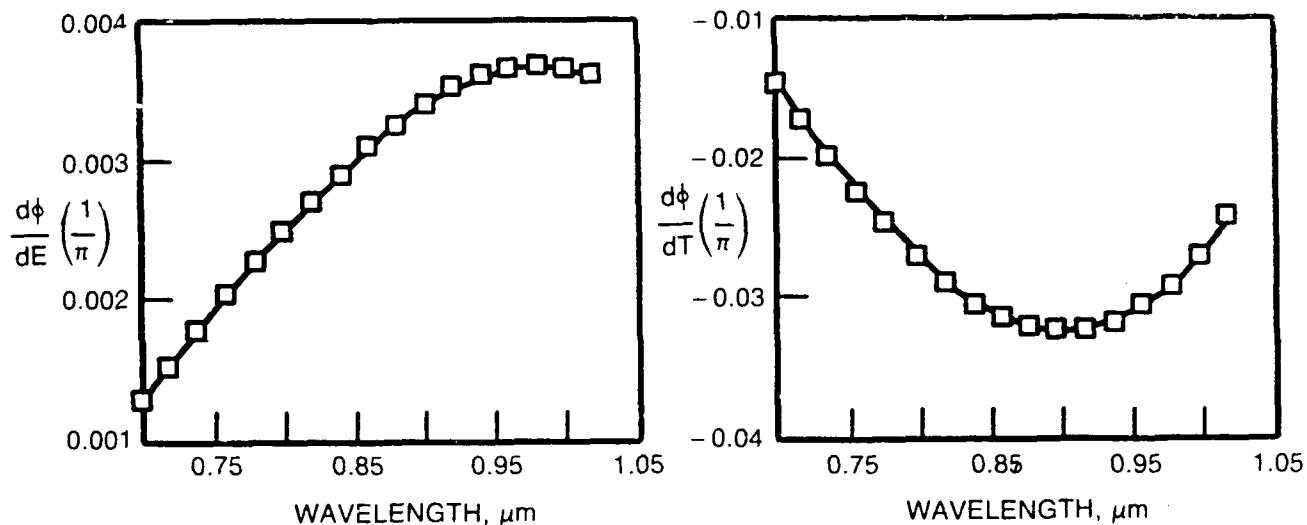


Figure 4-29. Detailed empirical model. Strain and temperature sensitivity coefficients. WPB No. 6; L = 38.6 mm, OD = 186 μm, spectran No. 4.

values for step and Gaussian index distributions; more step like at shorter wavelengths where the optical field is more tightly contained within the core and more Gaussian-like at longer wavelengths where the optical field tends to spread out into the cladding. Data verifying the temperature response is given in Figure 4-30.

To implement the rotating test phase of these new sensors, two additional key areas required attention: attachment and miniaturization of the supporting electronics. To begin with, the Ferris wheel phase of testing proved that the twin-core optical fiber sensor survived operation above 922 K, but indicated slippage in the attachment of the device to the disk above 755 K. Resolution of this design issue is portrayed in Figure 4-31. Ceramic cement attachment has been superseded by a method called flame spraying. During the flame spray attachment process (performed by Pratt & Whitney, West Palm Beach, Florida), the sensor is held in contact with the prepared surface of the disk while molten droplets of aluminum oxide are blown over the sensor gage length and the adjacent portion of the disk. As the ceramic droplets impact the working surfaces, they bond together, freeze, and build up to a durable coating. Attachments assembled in this form have proven integrity which exceeds ceramic cements under harsh conditions.

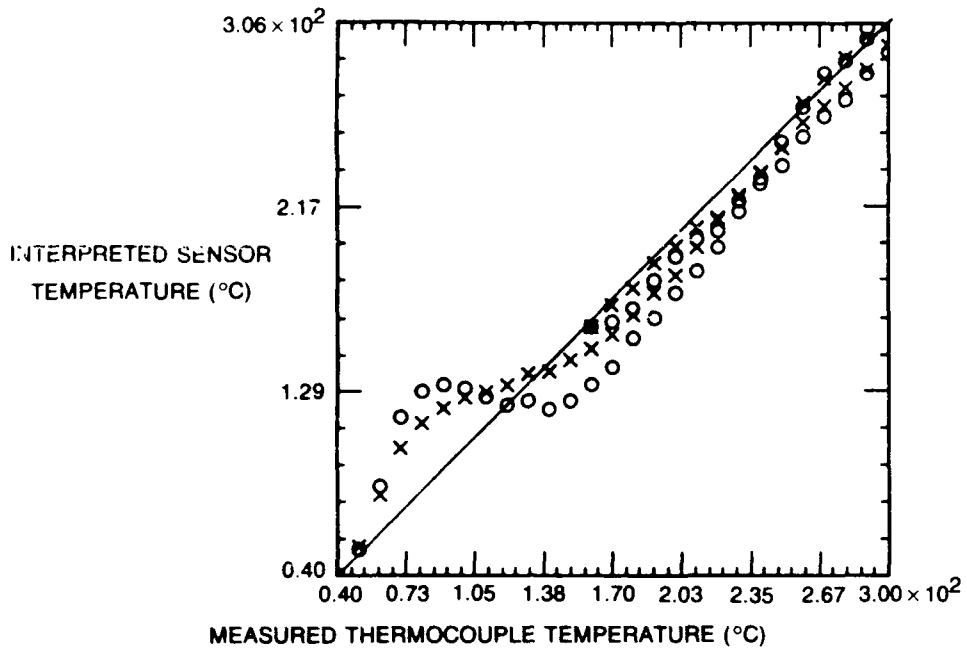


Figure 4-30. Twin-core optical fiber sensor. Temperature response; WPB No. 6, unattached.

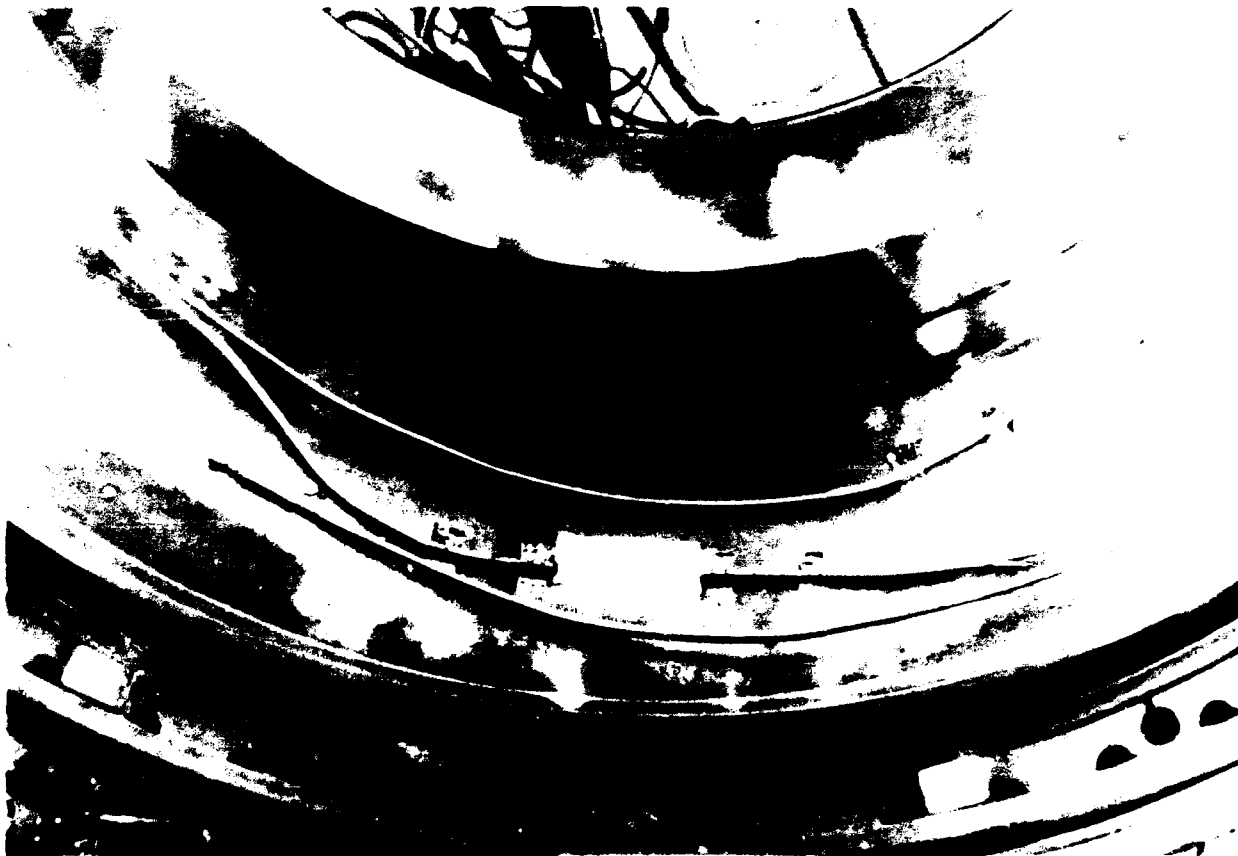


Figure 4-31. Twin-core optical fiber sensor. Flame-spray attachment to Modified F100 turbine disk.

A significant change was also required in the supporting instrumentation. For instance, the large rack of equipment shown in Figure 4-18 cannot be accommodated in the spin rig. During planning of the rotating tests, an appropriate optical slip ring for use with single mode sensors was not available; hence, the system was designed around use of an electrical slip ring to transfer power and signals to/from the rotating disk. This approach necessitated placement of the laser sources in the hub of the test piece. The required miniaturization was accomplished by using two laser diodes arranged to fit on a small transmitter circuit board. Again, wavelength multiplexing was implemented. The first version of the transmitter used microlenses and a coupling prism, shown in Figure 4-32 prior to encapsulation. This unit was destroyed in an early run of the spin rig after the mechanical support for the instrumentation can failed, precipitating a catastrophic imbalance in the spinning system. The rebuilt transmitter is shown with a different geometry in Figure 4-33 where a narrow-band optical fiber multiplexing coupler was used for beam combining. The temperature of the diodes was actively regulated with a thermoelectric cooler. The transmitter board mates with two receiver boards, each containing microlens/microprism wavelength demultiplexers and other circuitry (Fig. 4-34). The boards mount in the hub of the disk and receive power and control signals on wires installed in the drive shaft. All circuitry was encapsulated in high temperature epoxy for stable operation during rotationally-induced g-fields to 1000 g. These advances in instrumentation development are shown in the composite photograph of Figure 4-35, along with photographs of the installed disk and the spin rig facility. The spin rig (Section VI) facility consists of a large vacuum chamber with a drive system to spin the disk, an induction heater to elevate the disk temperature and a slip ring to communicate with instrumentation in the spinning work frame. The spin rig test program is summarized in Figure 4-36 which indicates a limitation in conditions, short of the 922 K and 13,200 r/min goals. A vibration, which could not be conveniently damped, limited the spin rate to less than 8000 r/min. After balancing attempts, several breaks were discovered in interconnecting fiber between the three circuits boards. This limited the experimental conditions to runs up to 589 K. At the time of the interconnecting fiber failure, the sensors and the encapsulated transmitter and receiver systems were functional. Funding limitations have obviated repair and further experimentation.



Figure 4-32. Twin-core optical fiber sensor. Miniature 2 -  $\lambda$  transmitter; version 1.



Figure 4-33. Twin-core optical fiber sensor. Miniature 2 -  $\lambda$  transmitter; version 2.

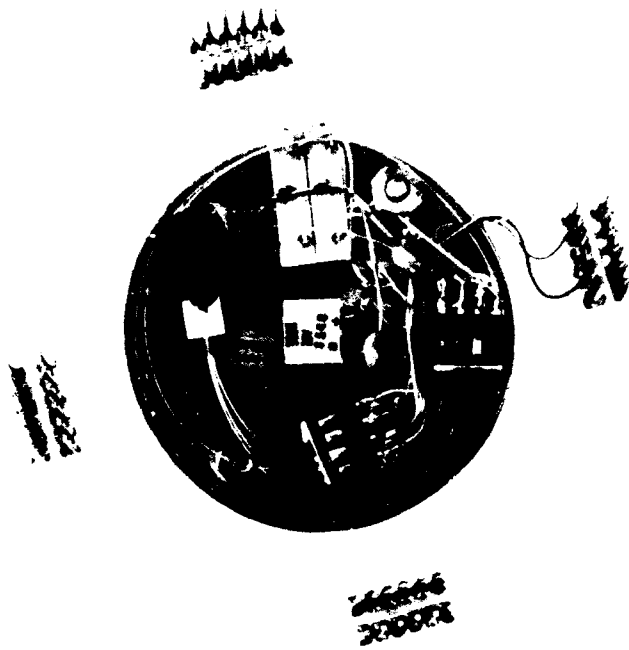


Figure 4-34. Twin-core optical fiber sensor. Miniature 2 -  $\lambda$  receiver.

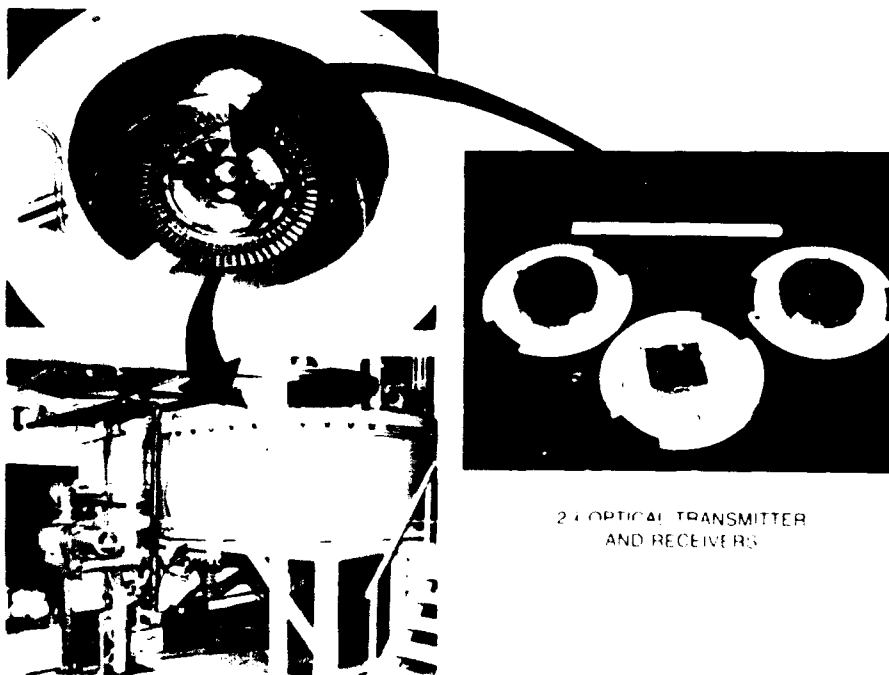


Figure 4-35. Twin-core optical fiber sensor. Spin rig experiment.

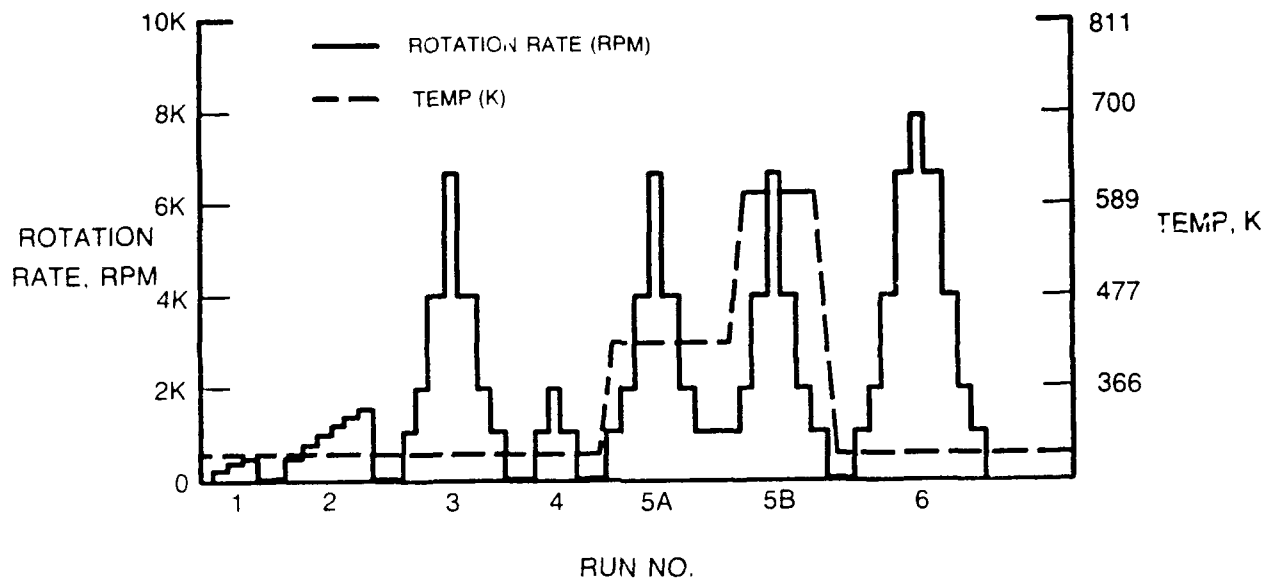


Figure 4-36. Spin rig test program. Build 3/4 B.

Representative data samples from the spin rig experiment begin with Figure 4-37. This example provides raw sensor data from the system spinning at 1000 r/min while the temperature was increased from ambient conditions to more than 589 K and then cooled. Next, the temperature was held relatively stable at 422 K. At this temperature, Figure 4-38 shows the sensor response to acceleration in spin rate from 1000 r/min to nearly 7000 r/min. A similar test sequence is provided in Figure 4-39 for operation at 589 K. In all three cases, the sensor response shows what appears to be hysteresis. However, other sensor measurements at the time of this experiment indicate that the response is not sensor hysteresis, but is indeed related to the stress state of the disk. The disk is not heated uniformly from the blades to the hub, and therefore a radially distributed strain gradient exists. The temperature distribution that induces this gradient is time dependent. Therefore the radial strain distribution on the disk web is different during the acceleration run in comparison with the deceleration sequence. The twin-core sensor was capable of detecting the effect of this evolving stress state.

## 6. DISCUSSION

The purpose of this section is to discuss the results from the spin rig experiment, comparing the twin-core sensor with other sensors which were available during appropriate ranges of conditions. The

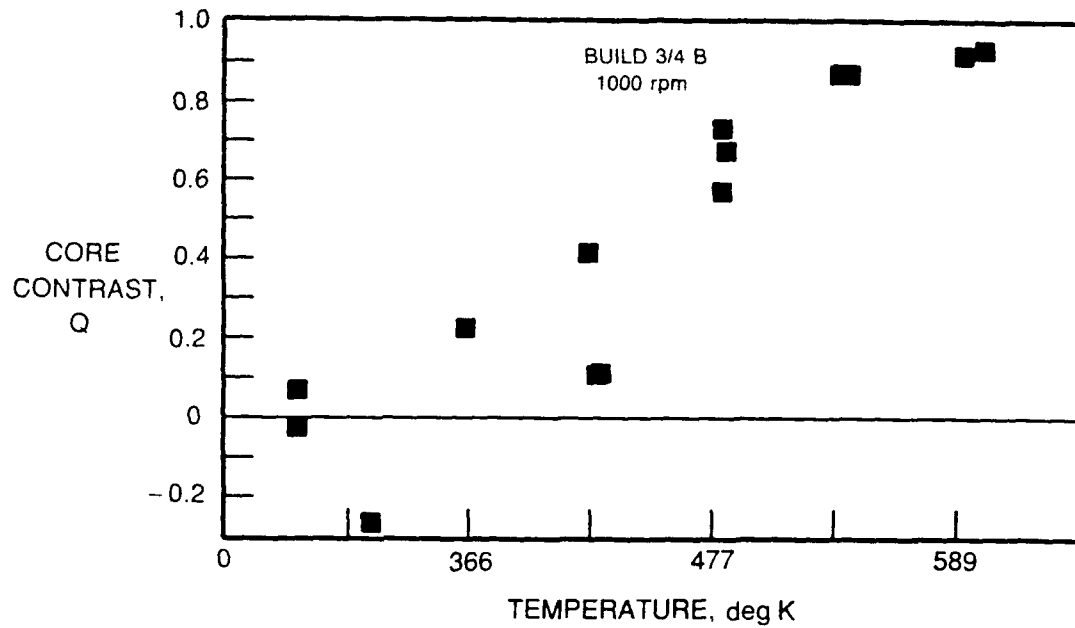


Figure 4-37. Twin-core optical fiber sensor. Temperature response at 1000 r/min. Spin rig data; run No. 5, 830 nm.

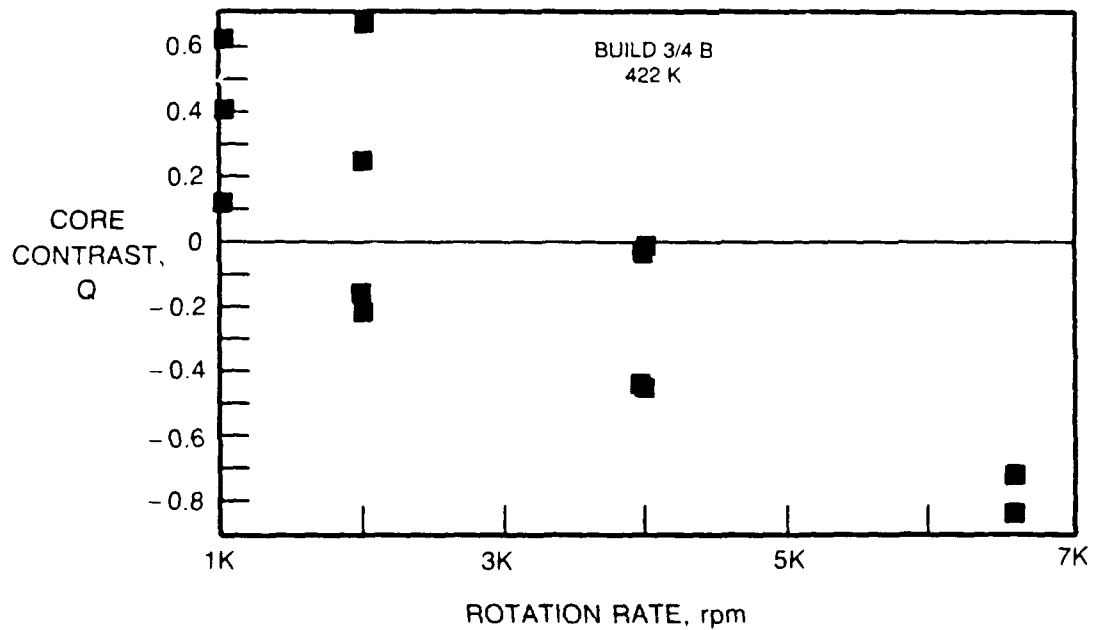


Figure 4-38. Twin-core optical fiber sensor. Load response at 422 K. Spin rig data; run No. 5, 830 nm.

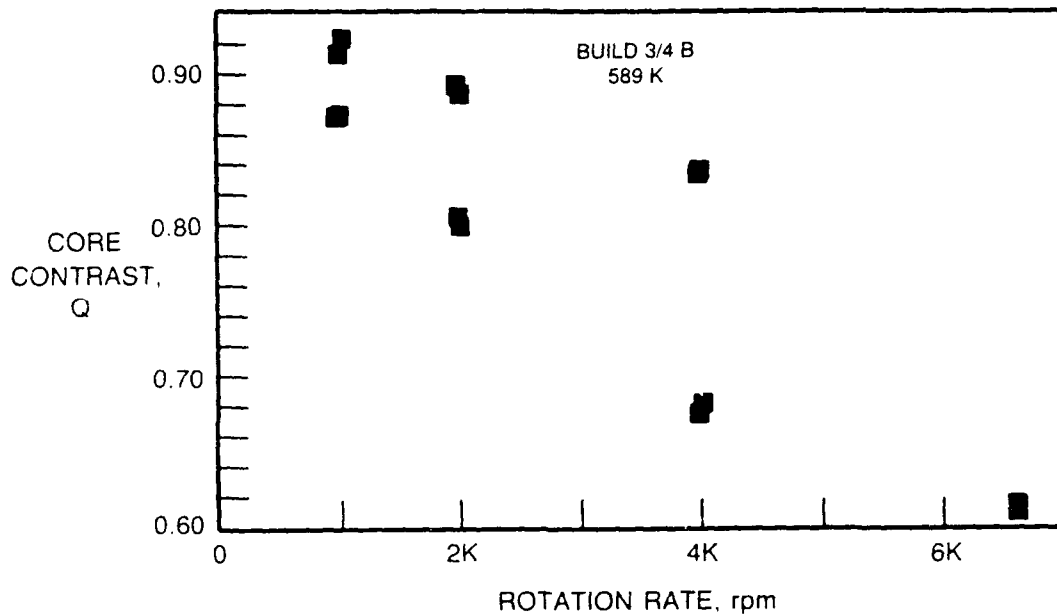


Figure 4-39. Twin-core optical fiber sensor. Load response at 589 K. Spin rig data; run No. 830 nm.

Ferris wheel experiment is not included in the analyses presented here, owing to the fact that it was a risk reduction implementation emphasizing a shake out of installation and instrumentation issues. On the other hand, the spin rig tests provided a more carefully controlled data base for correlation of different sensors.

Figure 4-40 compares the output of various strain sensors attached to the disk at a radius of 152 mm as a function of variations in nominal web temperature. The parameter used for comparison is the difference in strain reading between the high speed 6600 r/min case and the reference low speed 1000-1200 r/min case. The strain difference parameter is plotted as a function of temperature to minimize drift and zero shifts from various sensors. The shaded region on the graph indicates the theoretically predicted strain differences for a possible range of anticipated thermal gradients on the disk. It is necessary to present the predicted results as a range of values because insufficient data were available to document the exact state of thermal gradients which can be expected to impact the local strain measurements from each sensor. The thermal gradients result from nonuniform heating of the

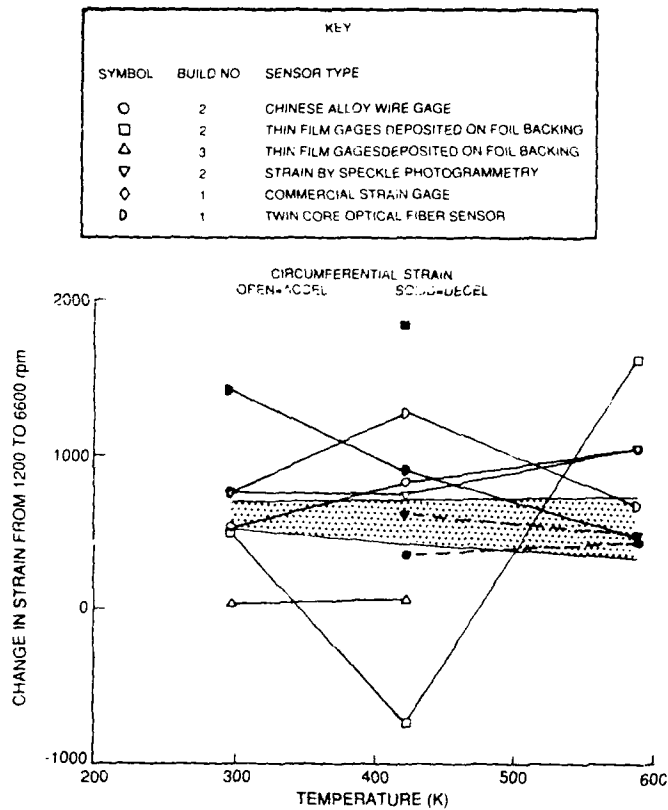


Figure 4-40. Sensor comparison 152 mm radius, 6600 r/min.

disk by the induction heating element during the time of the tests. Furthermore, we must remember that the thermal gradients during acceleration portions of a test (early in the experiment) will be different from deceleration portions of a test (late in the experiment) because of time development of the gradients.

To accomplish the calibration of the twin-core optical fiber sensor, the measured  $Q$  response parameter was converted to a normalized  $Q_{bar}$  response parameter to accommodate nonideal characteristics of the devices. The  $Q_{bar}$  response follows a cosine discriminant. Hence, the arccosine function is used next to create a phase parameter which can be calibrated and is linear in strain or temperature.

During the spin rig experiments, one of the laser diodes in the twin-core sensor instrumentation package did not operate properly, hampering attempts to apply the unique calibration methods of Section 5 to this data. As an alternative, the twin-core sensor data was referenced to the room temperature data of the speckle photogrammetry system and then plotted to yield Figure 4-40. The

two types of data show similar trends except for the room temperature deceleration twin-core sensor measurement. This measurement is somewhat erratic because it comes from the first test and exercise of the attached sensor; a situation which typically yields some additional hysteresis-like effects.

Other comparisons between the twin-core sensor data and speckle photogrammetry data were conducted. For instance, the strain response at 422 K as a function of disk rotation rate is shown in Figure 4-41. Note that the x-axis is plotted as the rotation rate squared divided by 1,000,000. Strain on the disk should be linearly proportional to this parameter. Indeed this appears to be verified with the acceleration data. In contrast, the deceleration data show a hysteresis-like effect which results from the time-dependent thermal stresses imposed on the spinning disk by the nonuniform heater. A least squares algorithm was used to calibrate the twin-core response to the speckle data.

Similar results are shown in Figure 4-42 for a comparison at 589 K. The key difference here is that the speckle experiment encompassed a much harsher, more extensive range of conditions, causing more hysteresis in the data. Since the twin-core sensor encountered more limited conditions, the hysteresis effects are less severe.

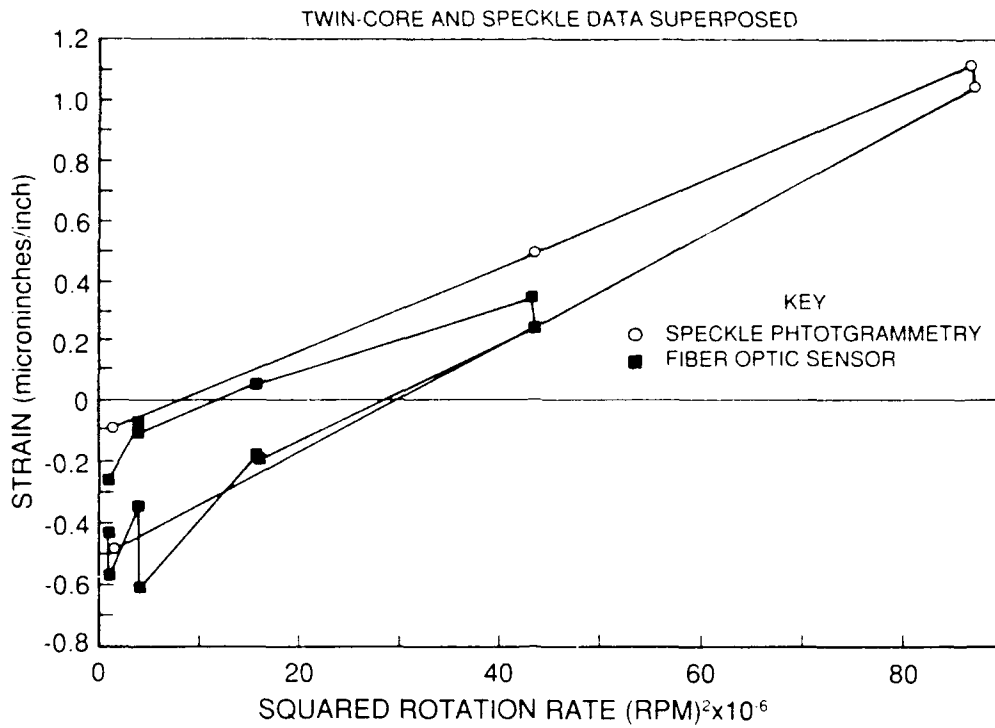


Figure 4-41. Sensor comparison. Twin-core and speckle data superposed.

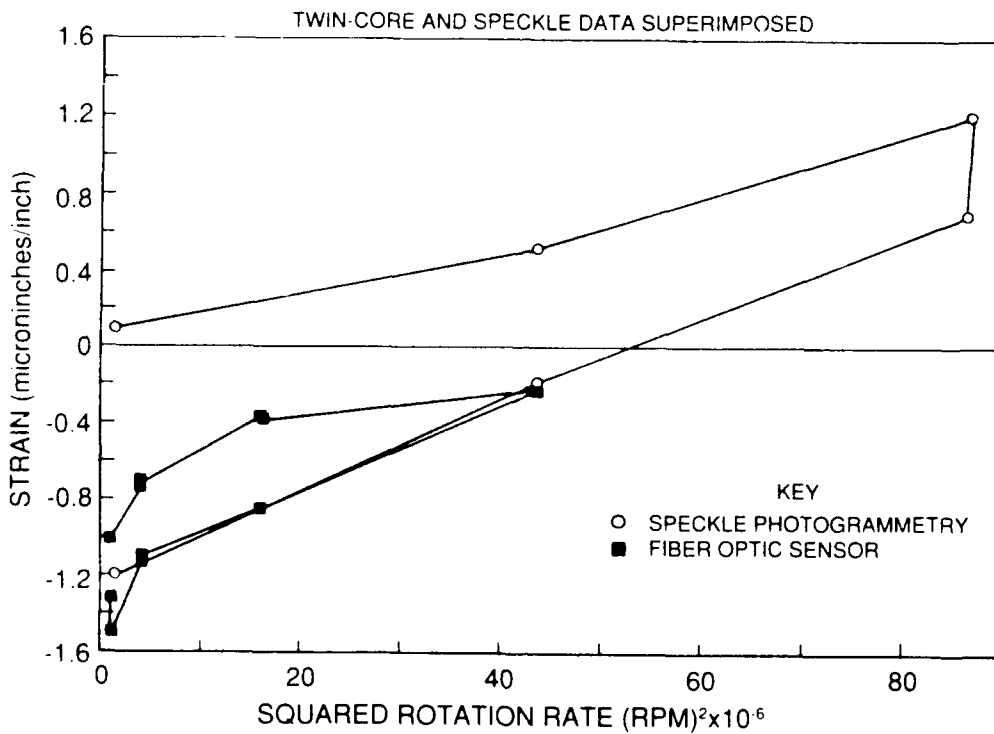


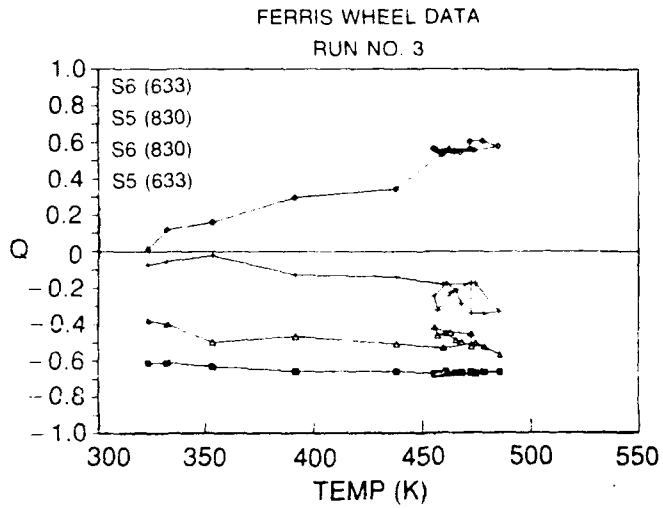
Figure 4-42. Sensor comparison. Twin-core and speckle data superposed.

**APPENDIX A**  
**FERRIS WHEEL DATA BASE**

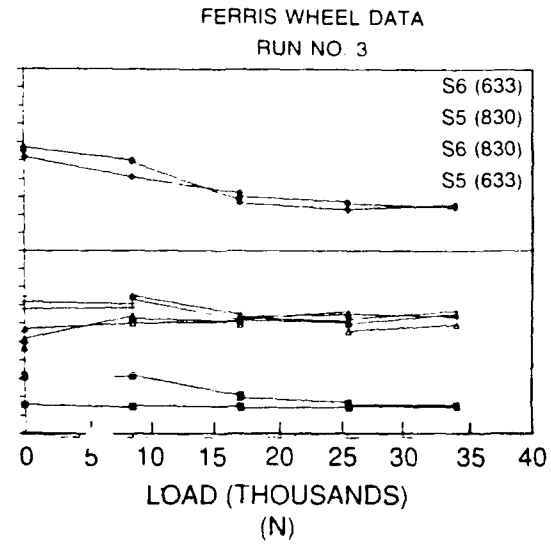
**APPENDIX A**  
**FERRIS WHEEL DATA BASE**

Figures 4A-1 through 4A-4 represent the primary results from the twin-core optical fiber sensor during the Ferris wheel experiments. Each figure indicates the sensor response at two wavelengths (633 nm and 830 nm) for various sensors (S5 and S6) as they react to a temperature increase in the disk, and then the strain response as the heated disk is loaded. All responses are given in terms of the crosstalk parameter Q. Further, each figure provides an expanded view of the most important data from the test.

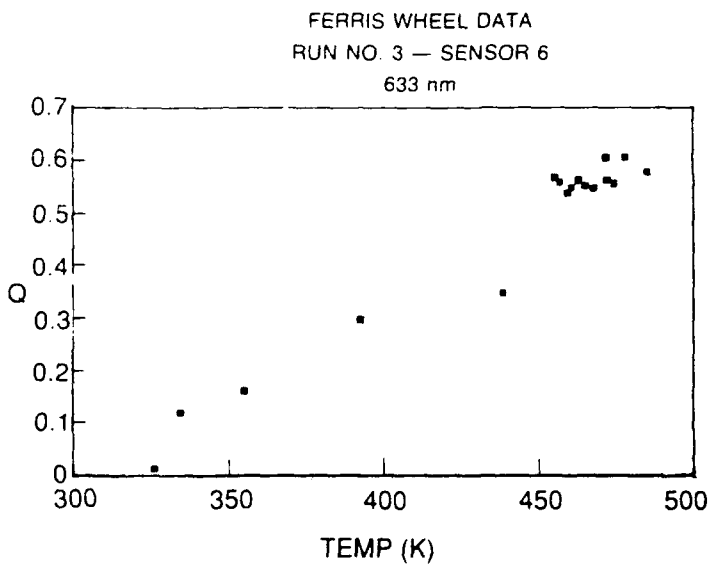
(a) TEMPERATURE RESPONSE



(b) STRAIN RESPONSE AT 463 K



(c) TEMPERATURE RESPONSE



(d) STRAIN RESPONSE AT 463 K

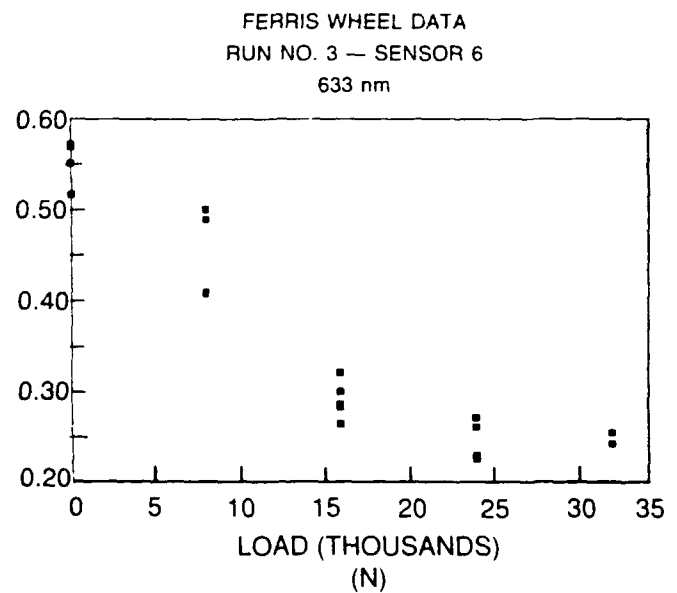


Figure 4A-1. Twin-core optical fiber sensor.

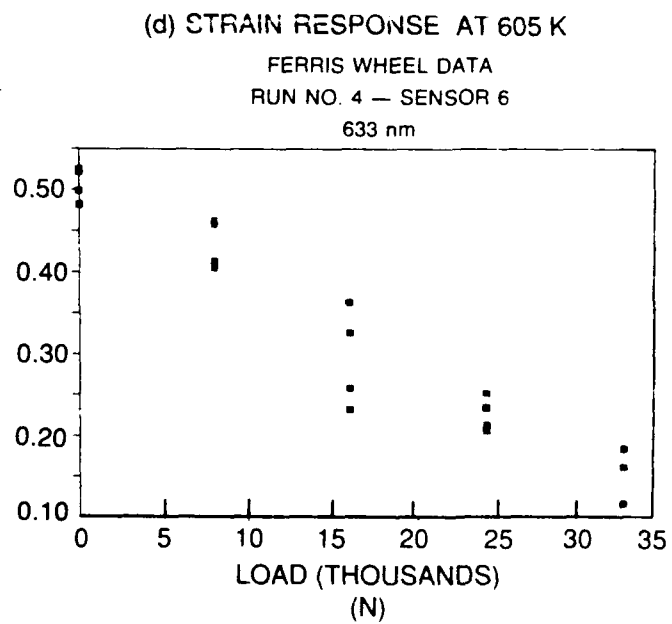
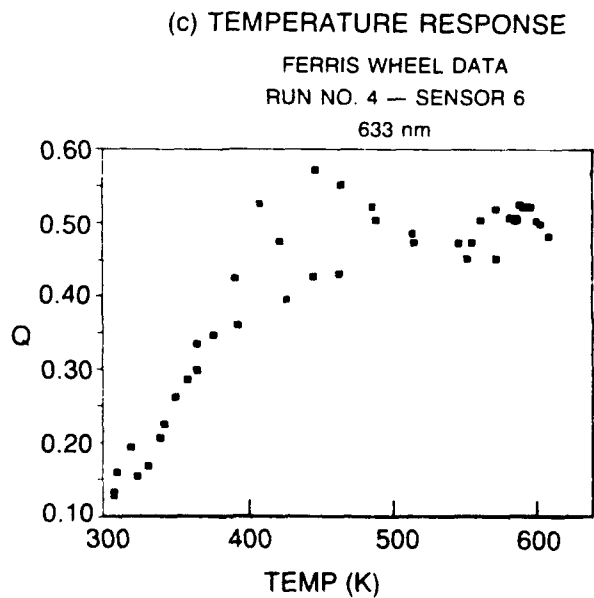
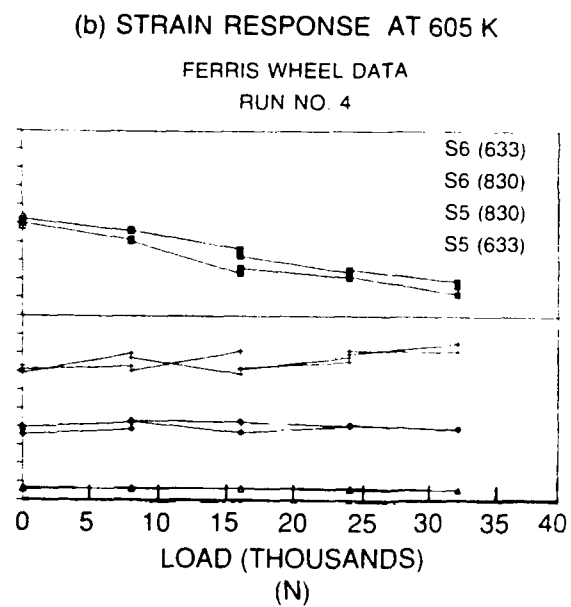
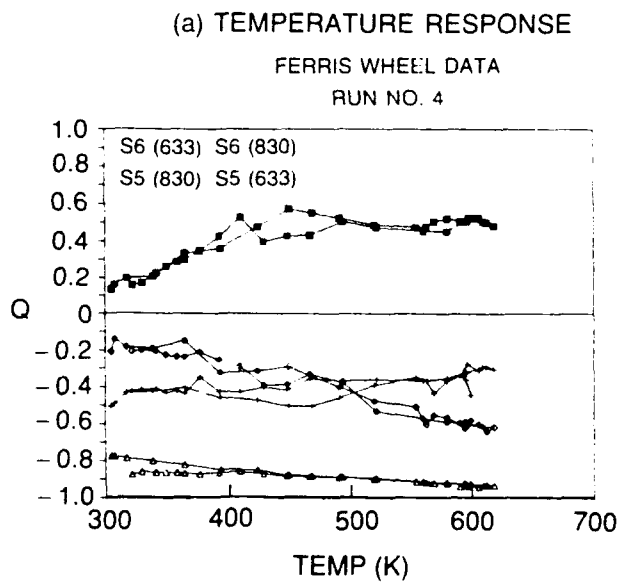


Figure 4A-2. Twin-core optical fiber sensor.

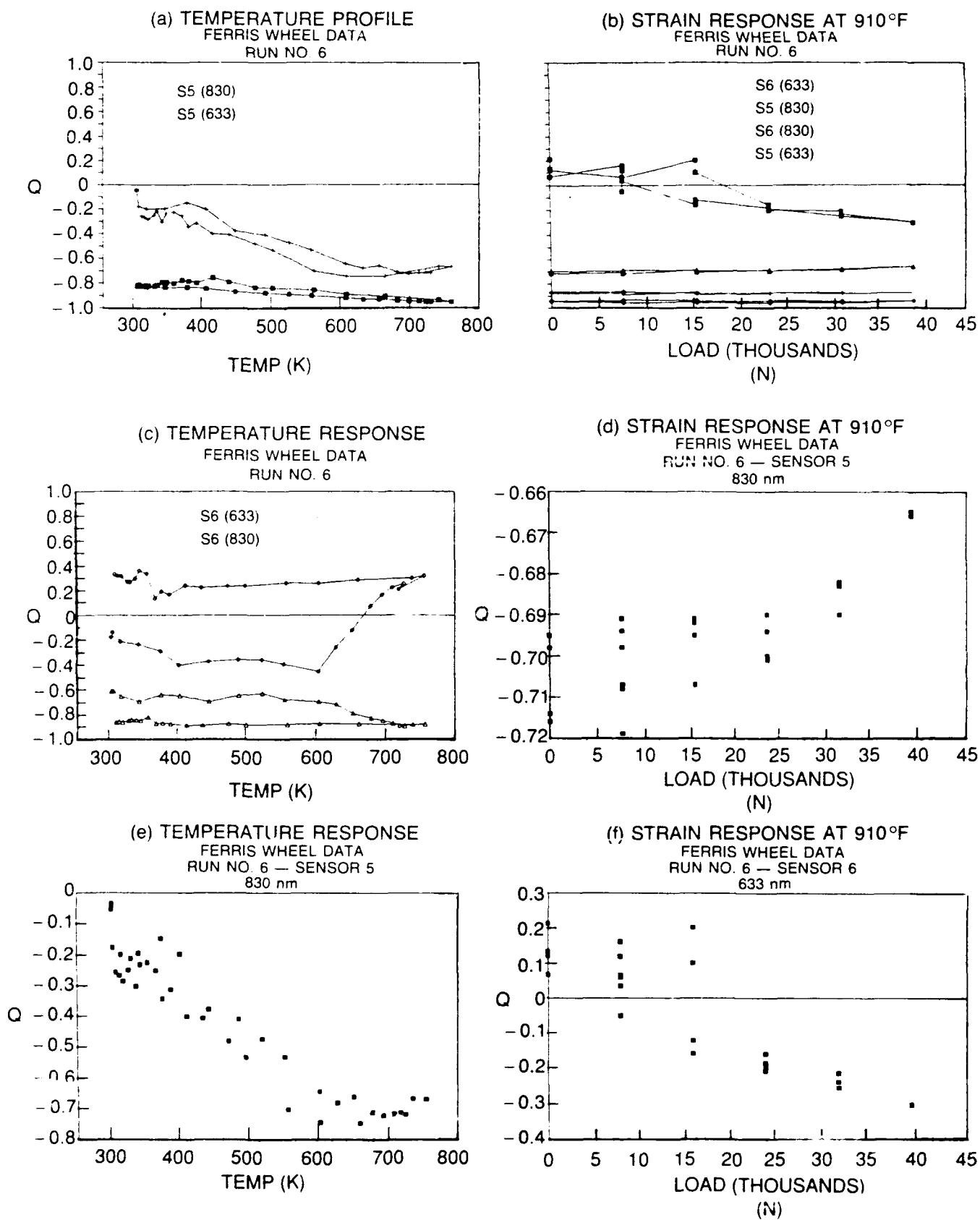


Figure 4A-3. Twin-core optical fiber sensor.

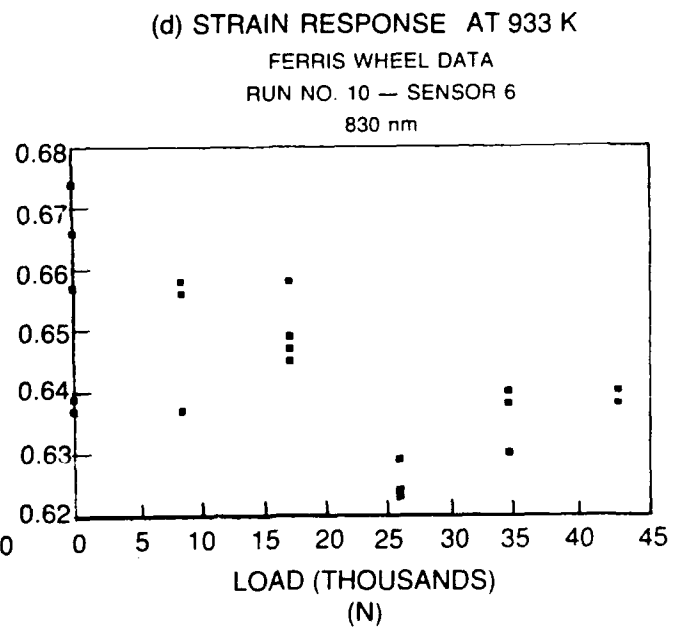
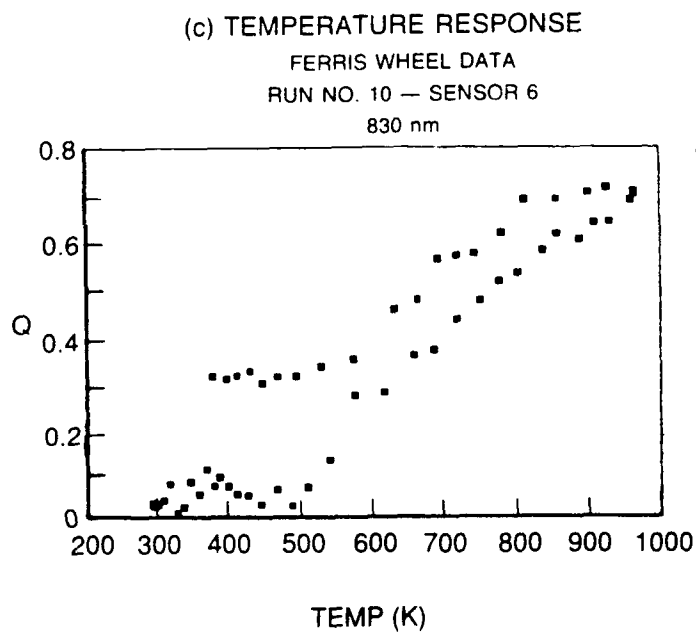
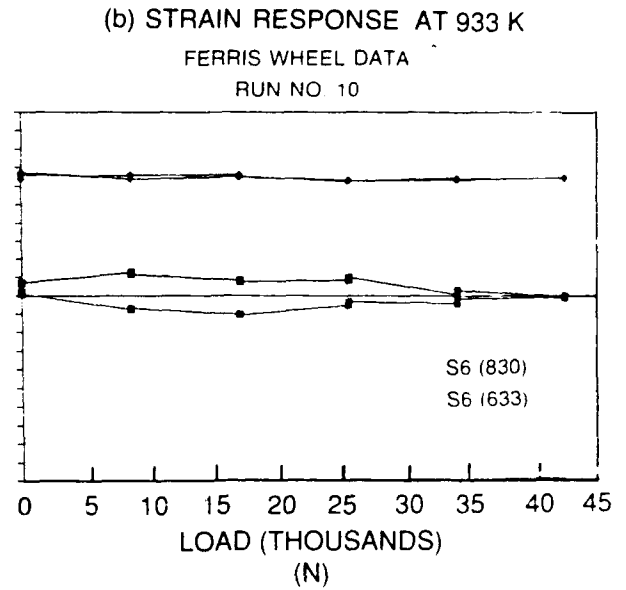
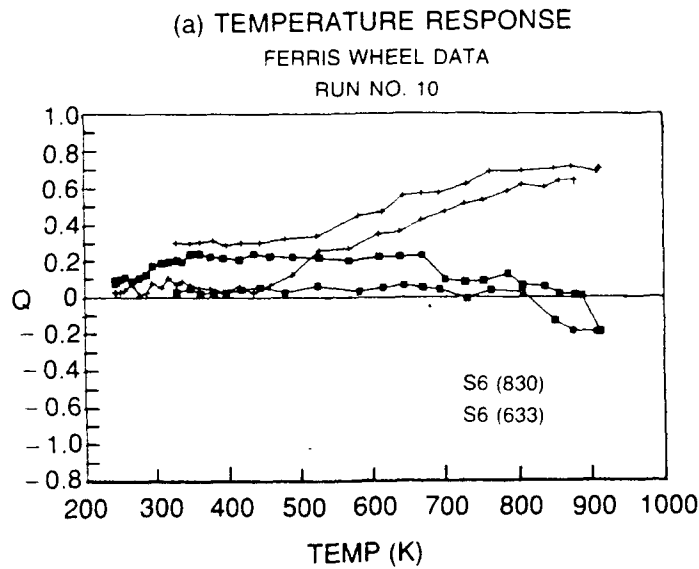


Figure 4A-4. Twin-core optical fiber sensor.

## V. RESISTANCE STRAIN GAGES

### 1. INTRODUCTION

Two types of small (1/8 in) high-temperature resistive static-strain gage were installed on turbine disks designed for aircraft engines and were hot spin-pit tested to 950 K and 2000 microstrain at 30,000 G centripetal acceleration. These were the first reported trials of these new gages on rotating parts. One type is a FeCrAl alloy gage in wire form, developed in China. The other is a PdCr alloy gage, in sputtered-film form, currently being developed at United Technologies Research Center under NASA contract.

Both types were mechanically durable. The results showed some improvements over previous attempts to obtain rotating static strain measurement at high temperature with small resistive gages. The long-term goal of uncertainty below 200 microstrain at temperatures above 660 K has not yet been approached. The performance limiting factor for the FeCrAl gages is believed to be metallurgical phase-stability and for the PdCr gages insufficient oxidation protection.

Further development of the PdCr alloy gage system is recommended because the gage alloy itself is metallurgically stable. The development required includes improved oxidation protection and some moderate temperature compensation.

### 2. OBJECTIVE

A major long-term objective in the development of aircraft gas turbine engine components and hypersonic aircraft structures is the measurement of static strain under transient nonisothermal test conditions at temperatures above the present 660 K limit of available resistive static strain gages. Strain uncertainty of 200 microstrain or less is required in at least a 2000-microstrain measurement range. In aircraft engines, the measurements are required on both stationary and rotating components (vanes, blades, turbine disks). A recent review of these requirements was presented by Stange (Ref. 1).

Typical test exposure includes many transient loading sequences, from a few seconds to a few min in duration, during which temperature is simultaneously varying from near cryogenic (in the case of hypersonic aircraft) to as high as +1300 K. The peak strains occur in small localized areas near holes, fillets, airfoil roots, and thinwall sections. Spatial resolution of 3 mm or less is required.

The technique for static strain measurement used most widely and successfully at lower temperatures is the resistive strain gage. At present, no small strain gage is available with capability even approaching the desired high-temperature static strain capability above 660 K, the temperature of onset of metallurgical phase changes in commonly used strain gage alloys.

Development of improved small resistive static strain gages for use above 660 K has continued. In the present program the state of development of two types was demonstrated.

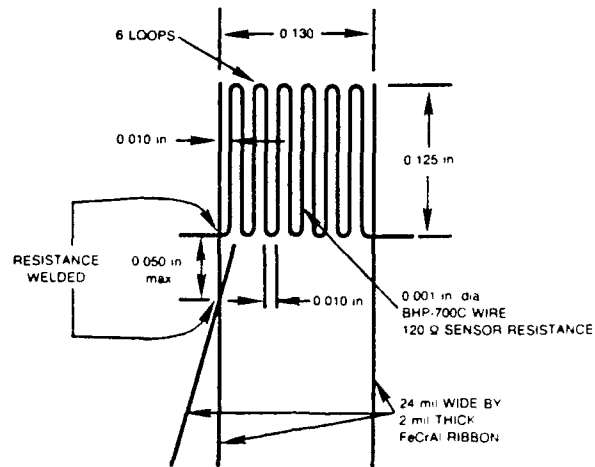
### **3. STATE OF THE RESISTANCE STRAIN GAGE ART**

The typical resistance strain gage sensor (Fig. 5-1) is a grid of fine wires, sputtered films, or foils, bonded to the component under test, with suitable lead wires extending to an electrical Wheatstone Bridge resistance-measuring circuit. A three-wire connection is used to cancel the effects of lead wire resistance changes.

The measure of strain is the fractional change in strain gage resistance,  $\Delta R/R$ , due to mechanical strain,  $\Delta L/L$ . The resistance strain gage method therefore depends on accurate knowledge of the gage factor  $\Delta R/R / \Delta L/L$ , and on insensitivity of the electrical resistance,  $R$ , to other influences such as temperature and erosion. The gage factor for metals is about 2 and the range of strain measurement of interest is usually about 2000 microstrain. Therefore the range of resistance changes is typically 4000 microhms/ohm.

The strain gage alloy must be chemically stable and oxidation resistant, relatively low in temperature coefficient of resistance (tcr), and metallurgically stable.

At temperatures up to about 660 K, low-tcr strain gage alloys such as Ni20Cr, Evanohm, FeCrAl and Cupron provide the desired stability and accuracy. Figure 5-2 shows examples of short-term reversible metallurgical drift characteristics of high-temperature strain gage alloys. Note that in the range 660 K to 920 K the drifts are as large 10,000 microhms/ohm. The figure shows the drift in 16 hours at each test temperature, after fast cooling from 920 K to test temperature. Not shown is the change in resistance from 920 K to the test temperature before the start of the drift test and the change in resistance from test temperature to 920 K at the end of each drift test. At 920 K the gage resistance



**INSTALLATION**

SURFACE PREPARATION: NiCrAl (METCO 443) FLAME SPRAYED  
 PRECOAT: Al<sub>2</sub>O<sub>3</sub> (ROKIDE "H") FLAME SPRAYED  
 OVERCOAT: AlPO<sub>4</sub> CERAMIC CEMENT (P12-2 ON BARS BEAN H ON DISK)  
 EXTENSION LEADS: 3CN CLAD Cu WIRE WITH GLASS FIBER OUTER INSULATION AND 0.012 in. DIAMETER CONDUCTORS

Figure 5-1. The wire strain gage configuration used is 3 millimeters by 3 millimeters.

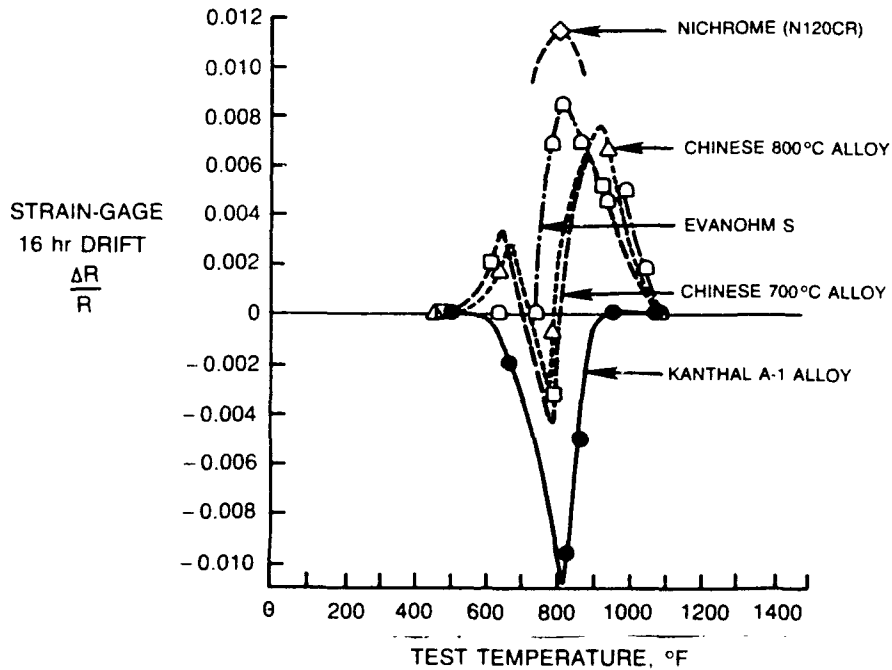


Figure 5-2. Metallurgical instability data for five strain gage alloys.

recovers to its previous 920 K value within a few minutes, for these alloys. About 10% of the total 16-hour drift occurs in the first few minutes at each test temperature. The data are from tests at Pratt & Whitney over the past few years.

The selection of gage alloys has narrowed historically to concentrated alloys (for low  $\text{tcr}$ ), preferably with featureless phase diagrams at all temperatures and therefore free from formation of chemical compounds, reordering of the lattice structure, or magnetic transformations, to avoid the drifts shown in Figure 5-2.

The state of the art has centered recently on two alloy families. One is the historically promising FeCrAl family (iron-chromium-aluminum) with added modifications and the other is the recently investigated PdCr (palladium-chromium) family. FeCrAl offers low  $\text{tcr}$  of about  $15 \times 10^{-6} \text{ K}^{-1}$  and excellent oxidation self-protection but marginal metallurgical stability. An example is given in Figure 5-3, where resistance change versus temperature of a FeCrAl alloy (examined by UTRC (Ref. 2)) is sensitive to heat treatment time at elevated temperature. The PdCr alloys offer great stability at high temperatures but marginal  $\text{tcr}$  of about  $180 \times 10^{-6} \text{ K}^{-1}$  and less oxidation resistance. An example of excellent metallurgical stability is given in Figure 5-4, where a PdCr alloy (from the same UTRC program (Ref. 2)) was insensitive to heat treatment time at high temperature or to rate of cooling or heating.

#### **4. APPROACH TO DEMONSTRATION TEST**

In this program, a series of several high-temperature spin tests of instrumented turbine disks, from a 20,000-pound-thrust military gas turbine engine, were planned with space available for candidate strain measuring systems on each build. The spin rig is described in Section VI. In addition, a preliminary high-temperature stationary radial-loading Ferris-wheel test of one turbine disk was conducted as a risk-reduction test for some candidate sensors.

Predicted maximum strains during the spin tests to 950 K at 13200 r/min were approximately 2000 microstrain both radially and tangentially. These predicted strains are well below the yield strain of about 5000 microstrain at 950 K for IN100 disk material.

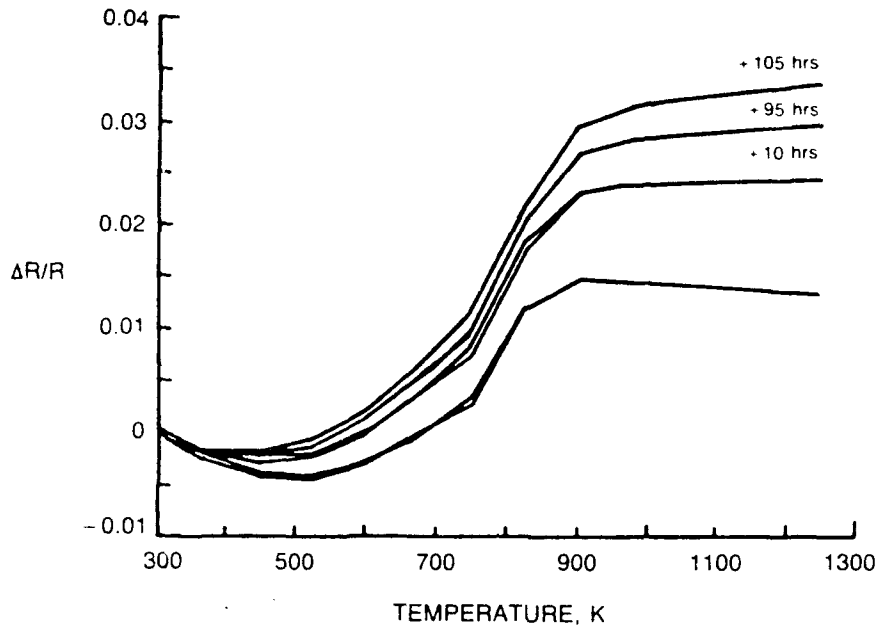


Figure 5-3. Change in resistance vs. temperature after different soak times at 1250 K for a sample FeCrAl Alloy (Fe-11Cr-12Al).

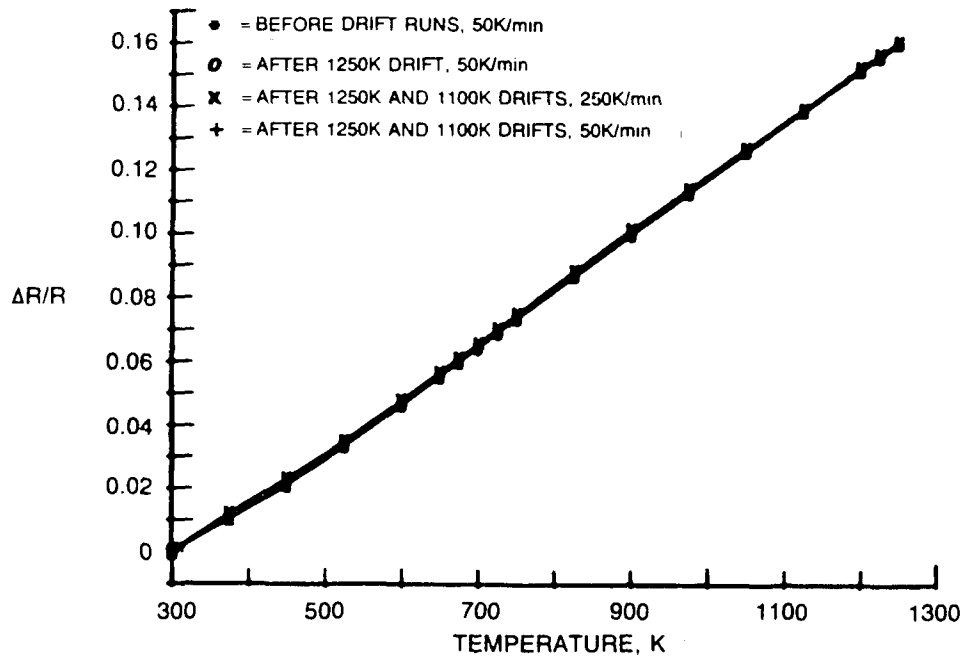


Figure 5-4. Change in resistance vs. temperature after different soak times for a sample PdCr alloy (Pd-16Cr-8Co).

Reported here are results for two strain gage systems selected for demonstration. The two systems are gages of the BHC-700C alloy (Fe-26Cr-5Al, plus V,Ti,Y) developed by Wu (Refs. 3 and 4) in the Peoples Republic of China and gages of the Pd-13Cr alloy developed by Hulse at UTRC (Ref. 2). All compositions are weight percentages.

For the PdCr alloy, the strain gage system development program was ongoing during and after the spin test program. The PdCr alloy had not been produced in wire form, and was fabricated into strain gages only by the sputtered thin film deposition process.

## 5. DEMONSTRATION TESTS OF THE FeCrAl BHP-700C WIRE STRAIN GAGES

a. Design and fabrication of the strain gages—The gage configuration selected is shown in Figure 5-1. The gage is a 120-ohm, 3-millimeter by 3-millimeter grid of six loops of 25-micrometer diameter wire of the FeCrAl BHP-700C alloy. Figure 5-1 indicates the procedures used for attaching the lead wires and mounting the gage on the turbine disk. The disk is of IN100 alloy, approximately 46 centimeters in diameter. Notable is the use of flame-sprayed aluminum oxide insulation under the gage and ceramic cement bond coats over the gage. In accordance with a detailed layout and fabrication procedure specified by Pratt & Whitney, six gages were installed in pairs at each of three radii: 165 mm, 152 mm, 140 mm. In each pair, one gage was oriented for radial strain measurement and one for tangential.

Figure 5-5 is a view of the completed installation on the turbine disk, with the six BHP-700C gages at right and six PdCr sputtered-film gages (described later), at left. The white area is the flame-sprayed aluminum oxide insulation.

Two other sets of BHP-700C gages were fabricated on test bars for preliminary bench tests. One set of four gages was mounted on an Inconel 718 test bar for gage factor versus temperature. A second set of three was mounted on an IN100 test bar for apparent strain versus temperature.

b. Results of the preliminary test bar static tests—Figure 5-6 shows measured gage factor versus temperature for one gage. The gage factor results for all four sample gages were within 4% of this curve. The gage factor decreases gradually by about 15% as temperature increases to 950 K.

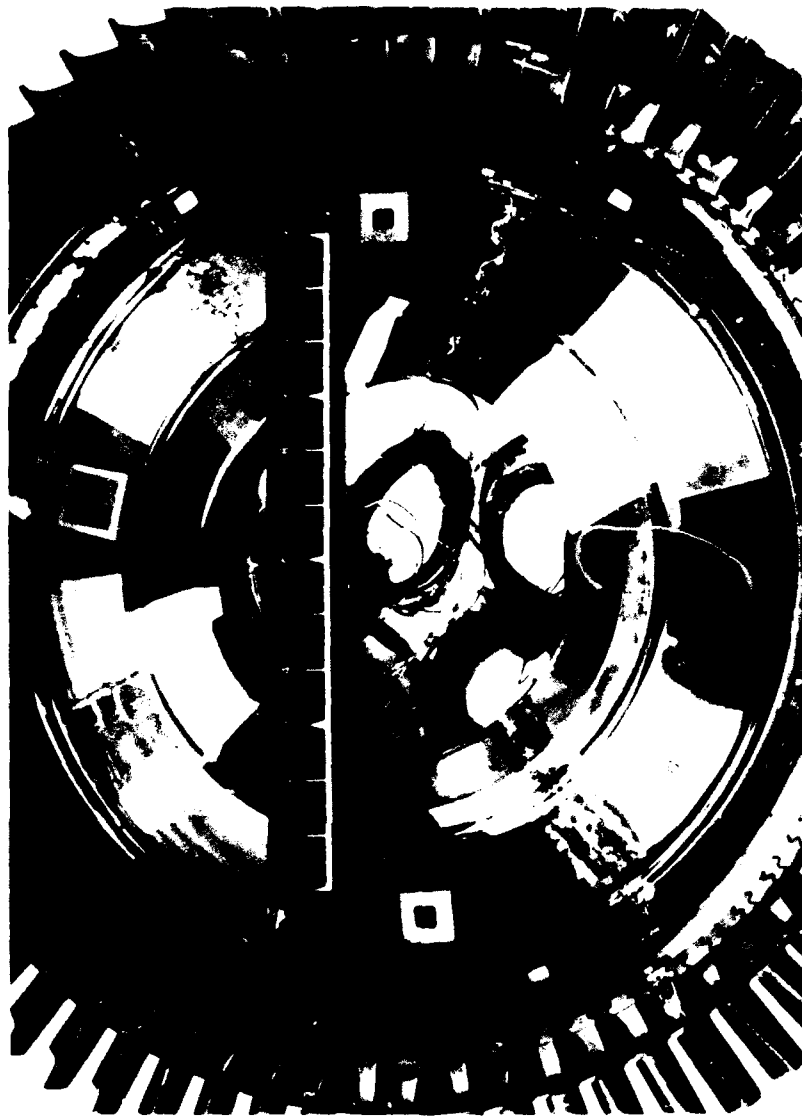


Figure 5-5. Pretest photo before 950 K spin test 2.

Figure 5-7 shows measured resistance change versus temperature curves during cool down for one gage. The curves are for the four different cool down rates shown in Figure 5-8. The 0.0006 spread is attributed to the effects of metallurgical phase changes (Fig. 5-2) with associated relaxation times. The results for all three sample gages tested on this bar were within 0.0003 of these curves.

These results agree well with published test data (Refs. 3 and 4).

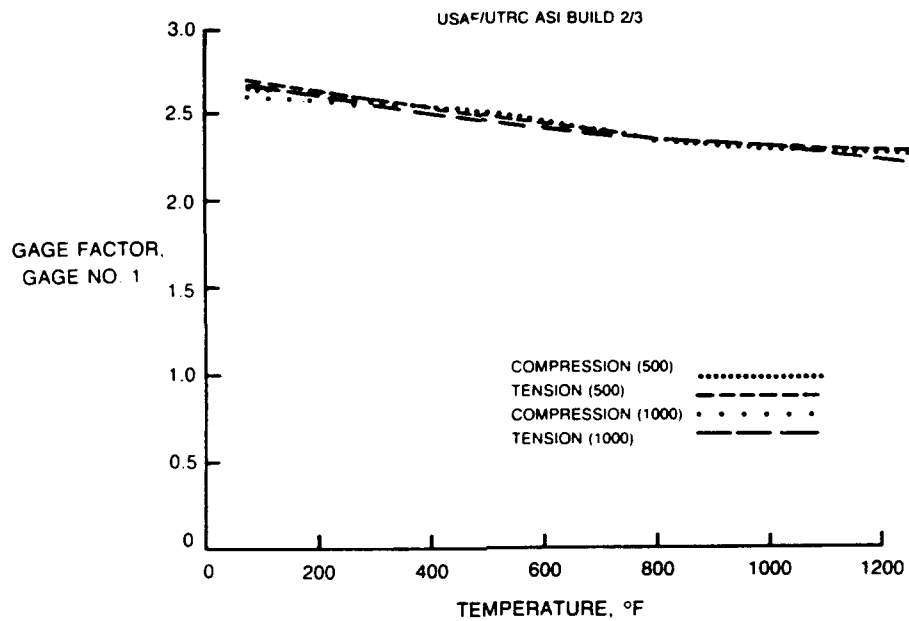


Figure 5-6. Gage factor vs. temperature for one of four wire strain gages mounted on a cantilever bend test bar Of Inconel 718.

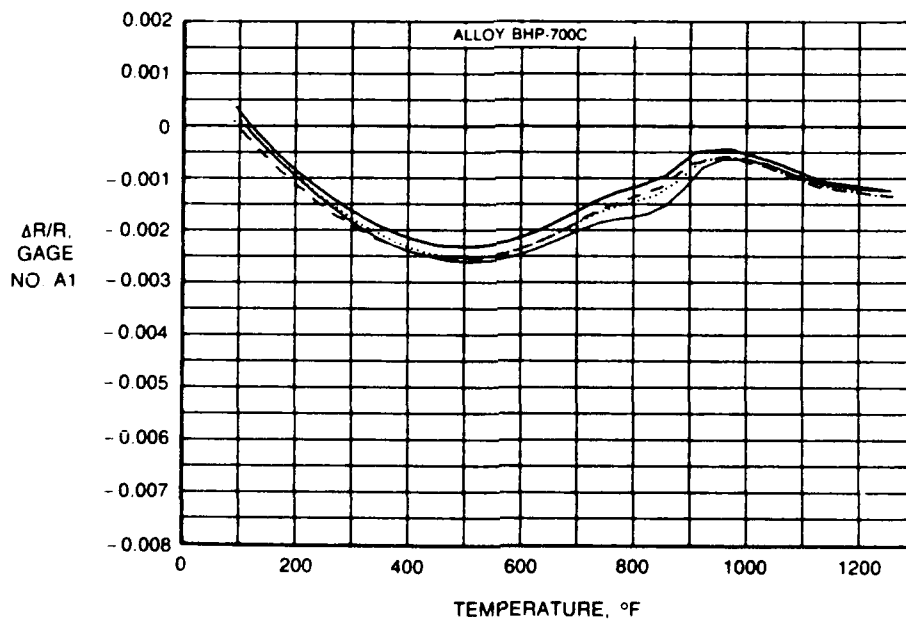


Figure 5-7. Apparent strain vs. temperature during cool-down for one of three wire strain gages mounted on a flat rectangular test bar Of IN100 turbine disk material.

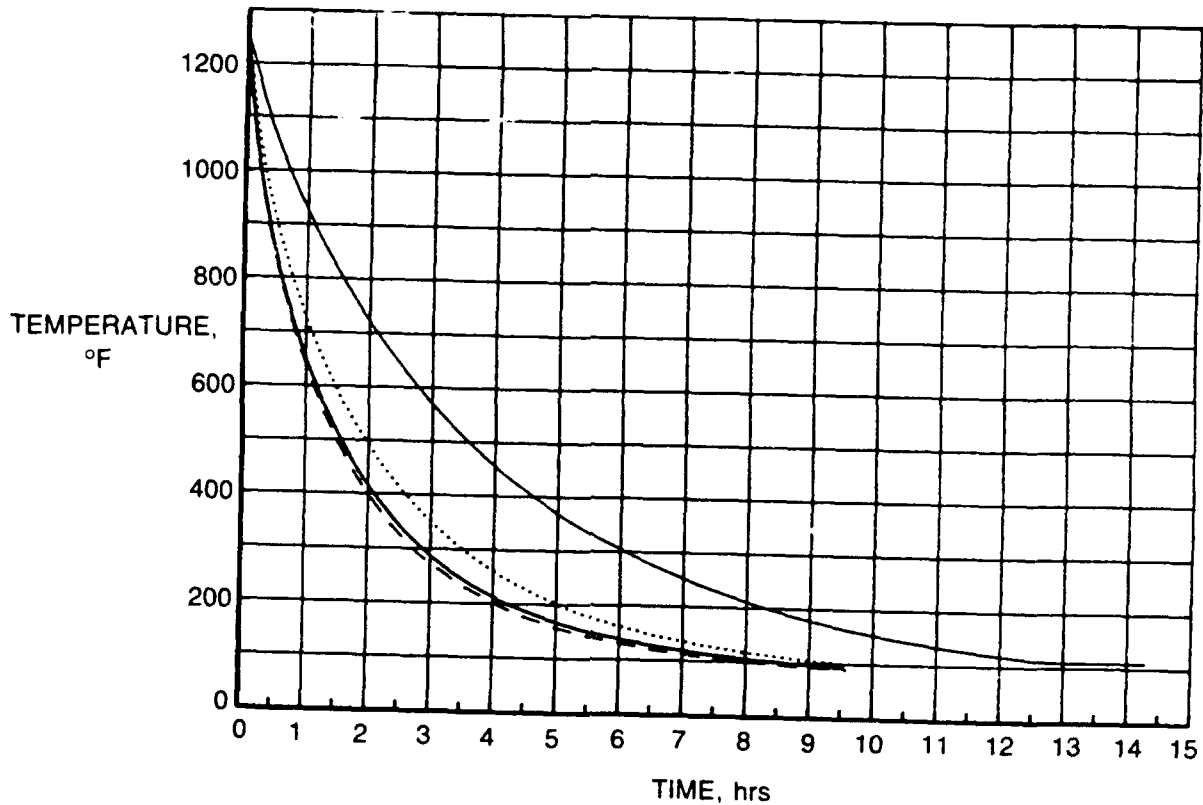


Figure 5-8. Temperature vs. time for four cooldown rates for which apparent strains were measured.

c. Spin test of BHP-700C gages—Figure 5-9 is a more detailed post-test view of the BHP-700C wire strain gages. There is no visible major deterioration of the gage installations, but there is visible damage to the lead work ceramic cement near the bore.

Pretest and post-test of gage resistance and resistance to ground (disk surface) for each of the six BHP-700C gages are listed in Table 8. The measurements are taken at the rotating tagboard in the rig bore, where the lead wires are spliced to slip ring leads. Measured gage resistances for the six BHP700C gages were  $120.75 \Omega \pm 0.15 \Omega$  at start and 93.0 to 109.5 ohms at finish. Resistance to ground was more than  $40 \text{ M}\Omega$  at start and only about  $2000 \Omega$  for each gage at finish. The low post-test resistance to ground and low post-test measured gage resistance suggests electrical leakage in the ceramic cement on the lead work on the disk due to damage or contamination. The low indicated gage resistance further suggests leakage from loop to loop of the wire gage through the ceramic cement on the gage, since the measured leakage to ground alone would not account for the large change in measured gage resistance.



Figure 5-9. Detailed photo after the 950 K spin test 2. The wire gage installation shows no visible major deterioration.

All of the damage to and contamination of the ceramic cement insulation was believed to occur after completion of the final high-speed 950 K test operating point. During shutdown from this test the rig overheated resulting in melted solder splices in the rotating cooled junction can in the bore of the spin rig. The operational problem is described in Section VI and was corrected in later builds. In addition, the resistance to ground measurements were carried out after opening the rig at the end of the testing and exposure of the disk to hot humid weather for several days, known to reduce ceramic cement resistance to a few thousand ohms. The insulation resistance was believed to be high up to the end of the 950 K test point.

**TABLE 8. TEST SUMMARY**  
**SPIN TEST OF WIRE-FORM STATIC STRAIN GAGES**

Test Conditions	
Test Item:	IN100 Turbine Disk.
Test Temperature:	950 K
Test Pressure:	0.0001 Atm. (Vacuum, Spin Rig)
Test Strain:	2000 $\mu\epsilon$ , (approximate)
Test r/min:	13200 r/min
Test G-Load:	32100 G

Resistance Measurements (OHMS)		1R	2C	3R	4C	5R	6C
Gage No.		1R	2C	3R	4C	5R	6C
Radius (millimeters)		165	165	152	152	140	140
Pretest:	Gage Resistance	120.9	120.7	120.9	120.8	120.6	120.8
	Insulation Resistance	40M	40M	40M	40M	40M	40M
Post-test:	Gage Resistance	109.5	93.0	109.2	109.4	100.4	104.9
	Insulation Resistance	.8K	2.2K	2.0K	1.1K	1.2K	1.0K

**Cumulative Apparent strain Due To Resistance Drift, Measured At Room Temp. at 0 r/min After Cool-down (Each run is a spin to 13,200 r/min at constant temperature):**

		1R	2C	3R	4C	5R	6C
Gage No.		1R	2C	3R	4C	5R	6C
Radius (millimeters)		165	165	152	152	140	140
Run No.	Temperature	Apparent Strain Due To Drift (Micro-Strain)					
2.1, 2.2	Room Temp	12	12	16	32	15	0
2.3, 2.4	Room Temp	open	438	15114	174	1340	-1297
2.5	420 K		426	open	81	1744	-1685
2.6	590 K		255		-104	1807	open
2.7	755 K		1290		846	-841	
2.8	950 K		*		*	*	

\*Note: Data after 950 K run not available due to damage.

**Comments**

**Failure Comments:**

No delaminations; 6 working gages at end of tests.

Insulation: Leakage to ground after 950 K test.

Drift: -800 to +1300  $\mu\epsilon$  for 3 good gages during the high-temperature testing.

**Improvement needed:**

Uniformity of gages: good

Insulation: Good, except protection from damage and from moisture required.

Drift: Still too large by factor of 5 to 9, above 600 K. This type of gage apparently is still limited by short-time reversible metallurgical effects above 600 K.

During the spin testing, the strain gage signals were occasionally intermittent. Deteriorating splices are suspected. There were no open circuits in the gages or leadwork on the disk at the end of the testing.

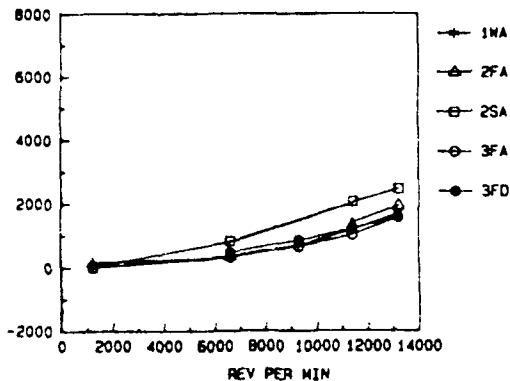
Rotating strain data obtained with the Chinese BHP-700C FeCrAl wire gages is compared in Figures 5-10a and 10b and Figures 5-11a and 11b with the data obtained with the other strain measuring techniques, including optical speckle, dual-core fiber optic gages, commercial wire gages, and foil-mounted sputtered thin-film PdCr gages. Data are presented at the only two radii (165 millimeters and 152 millimeters) at which all five types of data were acquired.

An overall summary and intercomparison of all strain results in Figures 5-10a and 10b and Figures 5-11a and 11b is presented in Volume I. Notable results with the BHP-700C gages are as follows (still referring to Figures 5-10a and 10b and Figures 5-11a and 11b):

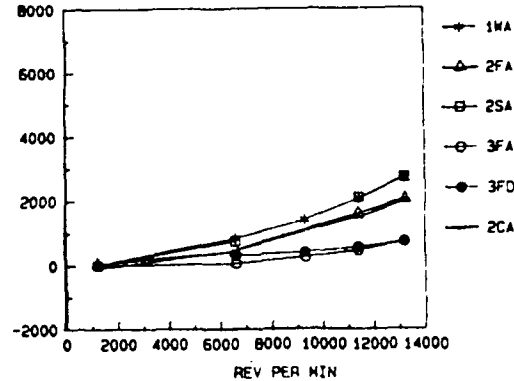
1. Circumferential strain measurements were obtained with the BHP-700C gages at both radii, at the five rotational speeds during the acceleration at 294 K (the rig was shut down directly after the acceleration at 294 K, without pausing to acquire data during deceleration) and during both acceleration and deceleration at each of four higher temperatures: 420 K, 590 K, 755 K. BHP-700C data were also acquired during the spin test at 950 K, but these gage readings were erratic and are not plotted in Figures 5-10a and 10b and 5-11a and 11b.
2. Radial strain measurements were obtained with the BHP-700C gages at one radius (152 millimeters) at the five rotational speeds during acceleration at 294 K and during both acceleration and deceleration at 420 K. This gage became erratic at 590 K and higher temperatures (data not plotted).
3. The fourth BHP-700C gage, radial at 165 millimeters, was erratic from immediately after the start of rotation in the first spin test at 294 K. Its data are not plotted.
4. Since no open circuits occurred, and the post-test measurements of gage circuit loop resistances were stable (Table 8), the source of the erratic readings in some gage

DATA INCLUDE INDICATED RADIAL STRAIN (FIRST COLUMN OF GRAPHS) AND CIRCUMFERENTIAL STRAIN (SECOND COLUMN OF GRAPHS) FOR THREE SPIN TEST BUILDS (1, 2, AND 3). FOR FIVE TYPES OF STRAIN MEASUREMENTS INCLUDING OPTICAL SPECKLE (S), OPTICAL FIBER GAGES (C), COMMERCIAL WIRE GAGES (W), CHINESE FeCrAl ALLOY, WIRE GAGES (C), AND FOIL-MOUNTED SPUTTERED THIN-FILM PdCr GAGES (F). DURING ACCELERATION (A) AND DECELERATION (D). FIGURE 1a SHOWS DATA OBTAINED AT TEMPERATURES OF 294 K, 420 K, 590 K. FIGURE 10b SHOWS DATA AT 755 K AND 950 K.

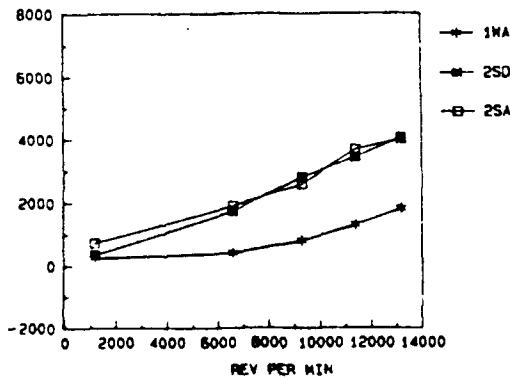
STRAIN VS RPM (294 K, RAD AT 165 MM)  
ASI BUILDS 1, 2, 3 WIRE, FILM, & SPECKLE  
MICROSTRAIN



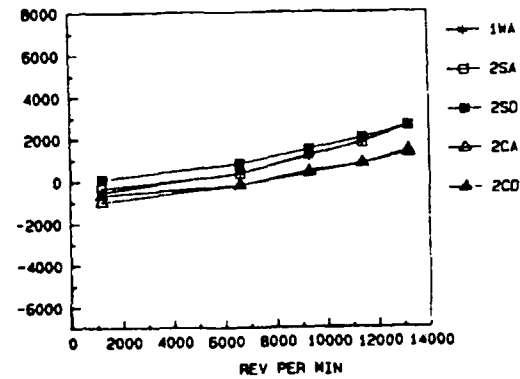
STRAIN VS RPM (294 K, CIR AT 165 MM)  
ASI BUILDS 1, 2, 3 WIRE, FILM, & SPECKLE  
MICROSTRAIN



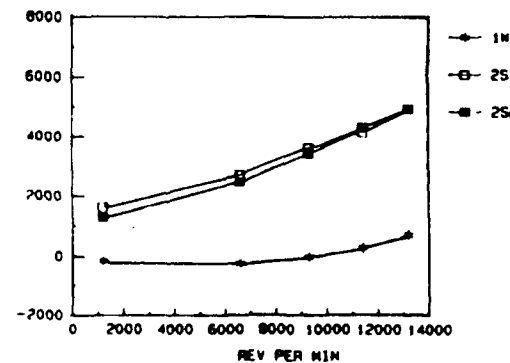
STRAIN VS RPM (420 K, RAD AT 165 MM)  
ASI BUILDS 1, 2 WIRE & SPECKLE  
MICROSTRAIN



STRAIN VS RPM (420 K, CIR AT 165 MM)  
ASI BUILDS 1, 2 WIRE & SPECKLE  
MICROSTRAIN



STRAIN VS RPM (590 K, RAD AT 165 MM)  
ASI BUILDS 1, 2 WIRE & SPECKLE  
MICROSTRAIN



STRAIN VS RPM (590 K, CIR AT 165 MM)  
ASI BUILDS 1, 2 WIRE & SPECKLE  
MICROSTRAIN

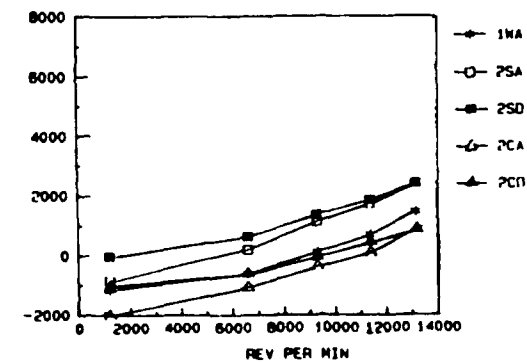
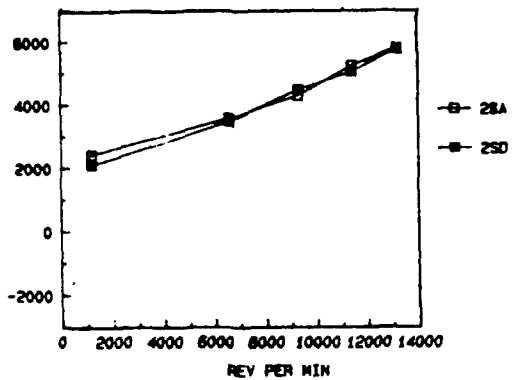
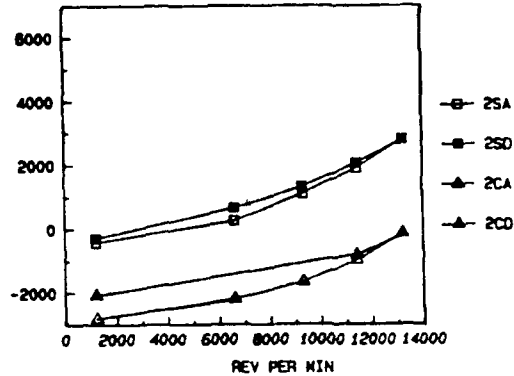


Figure 5-10a. Spin test strain data obtained at 165 millimeter radius, versus rpm.

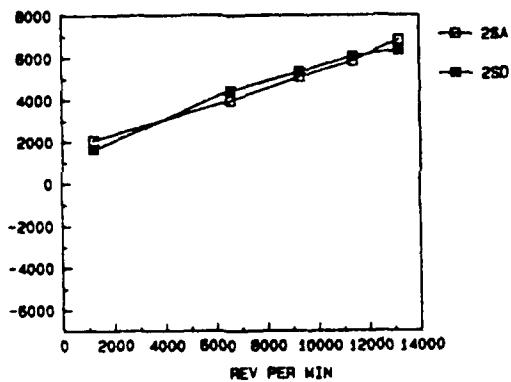
STRAIN VS RPM (755 K. RAD AT 165 MM)  
 ASI BUILD 2  
 MICROSTRAIN



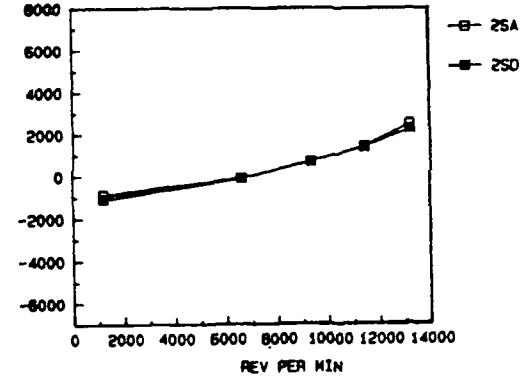
STRAIN VS RPM (755 K. CIR AT 165 MM)  
 ASI BUILD 2  
 MICROSTRAIN



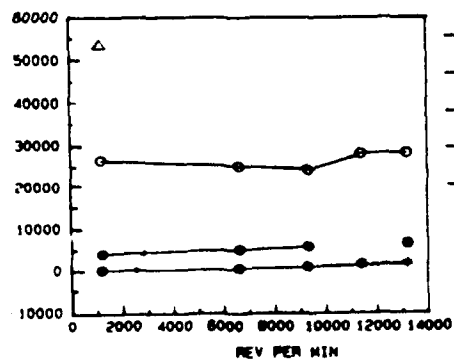
STRAIN VS RPM (950 K. RAD AT 165 MM)  
 ASI BUILDS 2  
 MICROSTRAIN



STRAIN VS RPM (950 K. CIR AT 165 MM)  
 ASI BUILDS 2  
 MICROSTRAIN



STRAIN VS RPM (FILMS. RAD AT 165 MM)  
 ASI BLD 2, 3: 294, 420, 590, 755 K  
 MICROSTRAIN



STRAIN VS RPM (FILMS. CIR AT 165 MM)  
 ASI BLD 2, 3: 294, 420, 590, 755 K  
 MICROSTRAIN

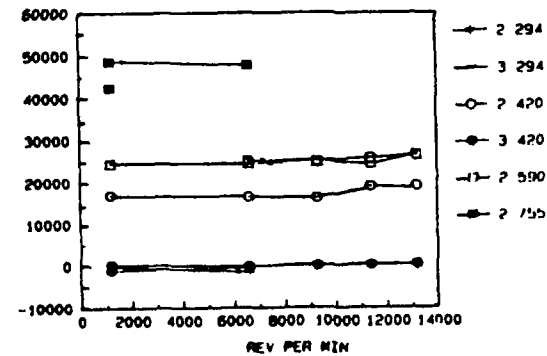
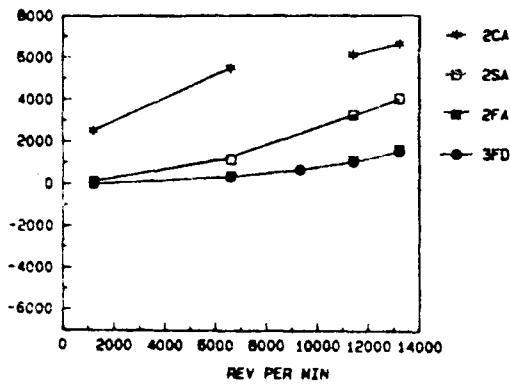


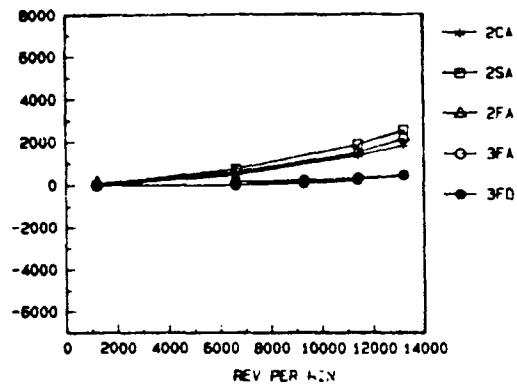
Figure 5-10b. Conclusion of data at 165 millimeter radius.

DATA SHOWN INCLUDE INDICATED RADIAL STRAIN (FIRST COLUMN OF GRAPHS) AND CIRCUMFERENTIAL STRAIN (SECOND COLUMN OF GRAPHS) FOR THREE SPIN TEST BUILDS (1, 2, AND 3). FOR FIVE TYPES OF STRAIN MEASUREMENTS INCLUDING OPTICAL SPECKLE (S), OPTICAL FIBER GAGES (O), COMMERCIAL WIRE GAGES (W), CHINESE FeCrAl ALLOY WIRE GAGES (C), AND FOIL-MOUNTED SPUTTERED THIN-FILM PdCr GAGES (F), DURING ACCELERATIONS (A) AND DECELERATIONS (D). FIGURE 2a SHOWS DATA OBTAINED AT TEMPERATURES OF 294 K, 420 K, 590 K. FIGURE 11b SHOWS DATA AT 755 K AND 950 K.

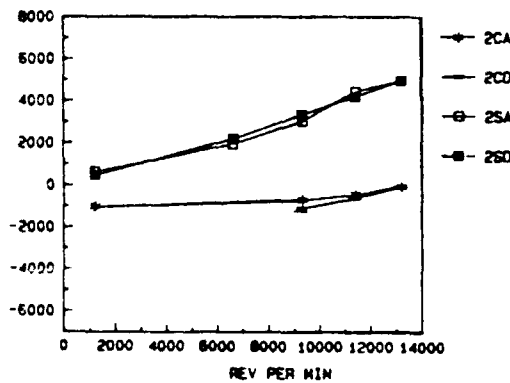
STRAIN VS RPM (294 K, RAD AT 152 MM)  
ASI BUILDS 2,3 WIRE, FILM, & SPECKLE  
MICROSTRAIN



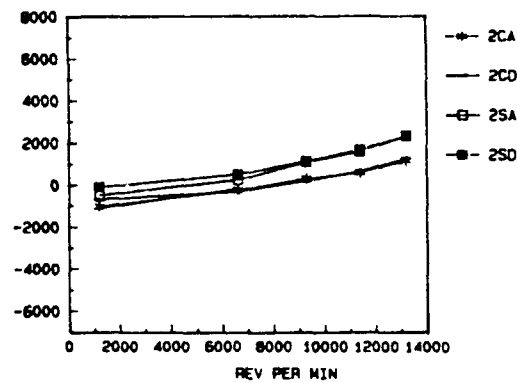
STRAIN VS RPM (294 K, CIR AT 152 MM)  
ASI BUILDS 2,3 WIRE, FILM, & SPECKLE  
MICROSTRAIN



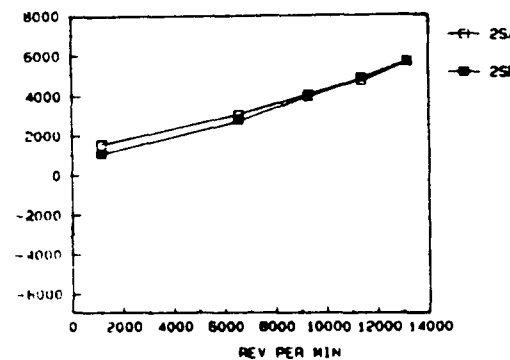
STRAIN VS RPM (420 K, RAD AT 152 MM)  
ASI BUILDS 2 WIRE & SPECKLE  
MICROSTRAIN



STRAIN VS RPM (420 K, CIR AT 152 MM)  
ASI BUILDS 2 WIRE & SPECKLE  
MICROSTRAIN



STRAIN VS RPM (590 K, RAD AT 152 MM)  
ASI BUILDS 2 SPECKLE  
MICROSTRAIN



STRAIN VS RPM (590 K, CIR AT 152 MM)  
ASI BUILDS 2 WIRE & SPECKLE  
MICROSTRAIN

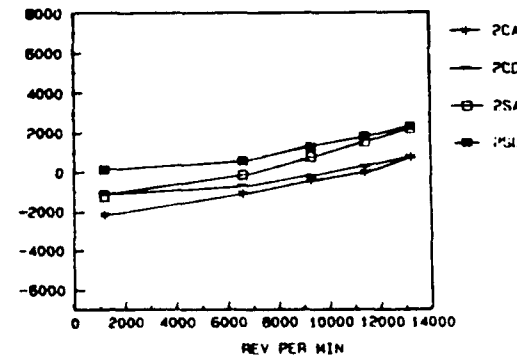
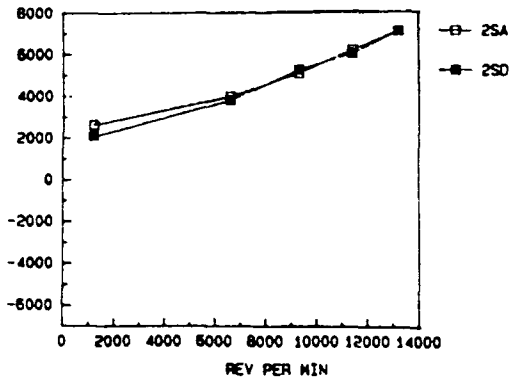
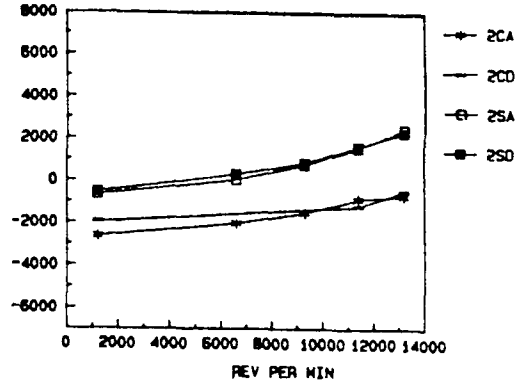


Figure 5-11a. Spin test strain data obtained at 152 millimeter radius, versus r/min.

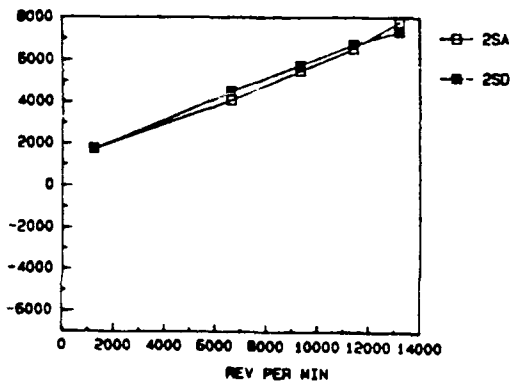
STRAIN VS RPM (755 K, RAD AT 152 MM)  
 ASI BUILDS 2  
 MICROSTRAIN



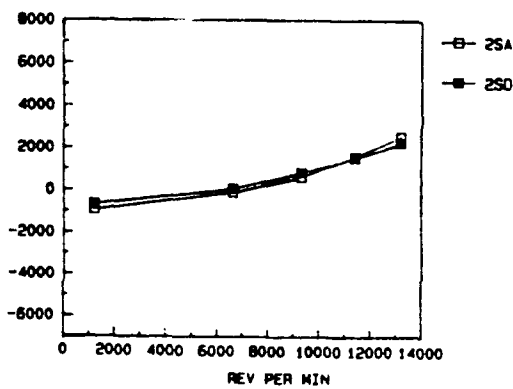
STRAIN VS RPM (755 K, CIR AT 152 MM)  
 ASI BUILDS 2  
 MICROSTRAIN



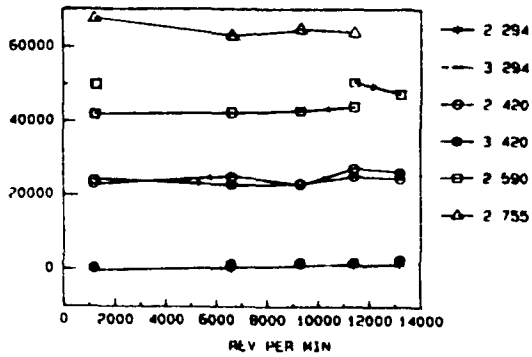
STRAIN VS RPM (950 K, RAD AT 152 MM)  
 ASI BUILDS 2  
 MICROSTRAIN



STRAIN VS RPM (950 K, CIR AT 152 MM)  
 ASI BUILDS 2  
 MICROSTRAIN



STRAIN VS RPM (FILMS, RAD AT 152 MM)  
 ASI BUILDS 2, 3; 294, 420, 590 755 K  
 MICROSTRAIN



STRAIN VS RPM (FILMS, CIR AT 152 MM)  
 ASI BUILDS 2, 3; 294, 420, 590 K  
 MICROSTRAIN

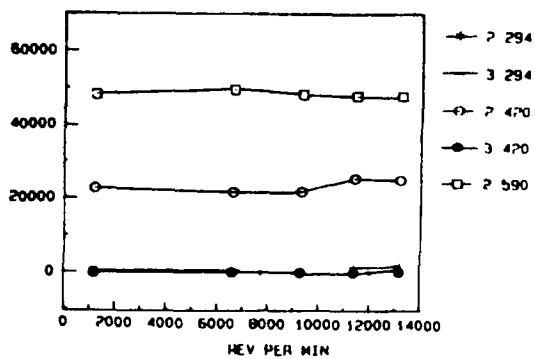


Figure 5-11b. Conclusion of data at 152 millimeter radius.

systems could not be determined. Intermittent electrical contacts at the lead wire splices in the rotating system (Fig. 5-9) are suspected.

5. All strain measurements for the three BHP-700C gages which were stable at the two radii chosen are plotted in Figures 5-10 and 5-11. In every case, the indicated strain becomes more tensile (more positive) as speed increases from 1100 r/min to 13,200 r/min. The strain increment is about 2000 microstrain. The strain then becomes less tensile as the speed decreases again to 1100 r/min, by about 1500 microstrain. The final strain at low speed in every case is therefore about 500 microstrain more positive than the starting strain at low speed. This hysteresis is attributed to real changes in thermally induced strain due to heat generated at the hub during each spin test.
6. The absolute level of indicated starting strain at low speed (1100 r/min) is progressively more negative as temperature increases, from less than  $\pm 100$  microstrain at room temperature to -3000 microstrain (compressive) at 755 K. The BHP-700C strain results are corrected for apparent strain due to temperature, based on reference calibrations of sample gages fabricated on test bars using wire from the same batch. An unverified speculation is that the negative starting strains at low speed and high temperature are real and may be due to uneven heating of the disk.

A significant quantitative overall result for the BHP-700C gages on the turbine disk was the large shift in cumulative apparent strain from test to test and gage to gage, as measured at the bridge output. These results are also summarized in Table 8. After runs 2.1 and 2.2, all gages were virtually drift free. After 2.3 and 2.4, three gages indicate intermittent open circuits, attributed to deteriorating splices. As the temperature is raised the drifts become large in the three remaining gages. After the 755 K run, the cumulative drifts vary from -800 microstrain (indicated compression) to +1800 microstrain (indicated tension).

In summary, it would appear that the large cumulative apparent strains in the three working gages were due principally to the expected metallurgical effects (Figs. 5-2 and 5-3) in the gage alloy during the high-temperature tests. The test is an example of the many pitfalls in attempting to measure

static strain at high temperature with small resistive strain gages. The lead-wire problems are correctable in future tests, by additional support and protection of splice areas. The ceramic cement problems are familiar and can be avoided by use of metal sheathed lead wires to exclude moisture and by storage of instrumented components in a dry area.

The large increase in cumulative drifts from beginning to end of each individual spin test at temperatures of 589 K and 755 K would indicate that the BHP-700C alloy, although a clear improvement over previous high-temperature static strain gage alloy candidates, still does not provide the desired stability to achieve the 200-microstrain repeatability goal. Additional testing on actual engine components is nevertheless recommended, with improved leadwork and insulation, to provide an unambiguous confirmation of this estimate.

## **6. DEMONSTRATION TESTS OF THE PdCr SPUTTERED-FILM STRAIN GAGES**

a. Design and fabrication of the strain gages—The configuration of the PdCr sputtered-film gage is shown in Figure 5-12. The gage is a 3-millimeter by 3-millimeter grid of six loops of Pd-13Cr film approximately 4.5 micrometers thick. Gage resistances were 120  $\Omega$  to 190  $\Omega$ . The resistance depends upon the details of the photoresist masking procedures and sputtering parameters used during fabrication. Since the gages were still in development, these parameters were still being adjusted from batch to batch. An objective is uniformity of gage resistance from gage to gage of approximately  $\pm 5\%$ .

The insulation under the gage is a sputtered film, in some early trials silicon nitride ( $\text{Si}_3\text{N}_4$ ) and in all later work aluminum oxide ( $\text{Al}_2\text{O}_3$ ). All films were RF sputtered in Argon (plus oxygen for  $\text{Al}_2\text{O}_3$  and nitrogen for  $\text{Si}_3\text{N}_4$ ) with substrate temperature in the vicinity of 360 K.

Two methods for installing sputtered-film gages on turbine disks were tried. In the first method, the insulation layer was sputtered directly onto the disk. This method had been used successfully on small blades and vanes for depositing thin film thermocouples (Ref. 6) used to well above 950 K. Reliable adherence on the massive turbine disks was never attained in five trials. Elaborate polishing, cleaning, and baking procedures were employed to smooth the disk surface and to remove

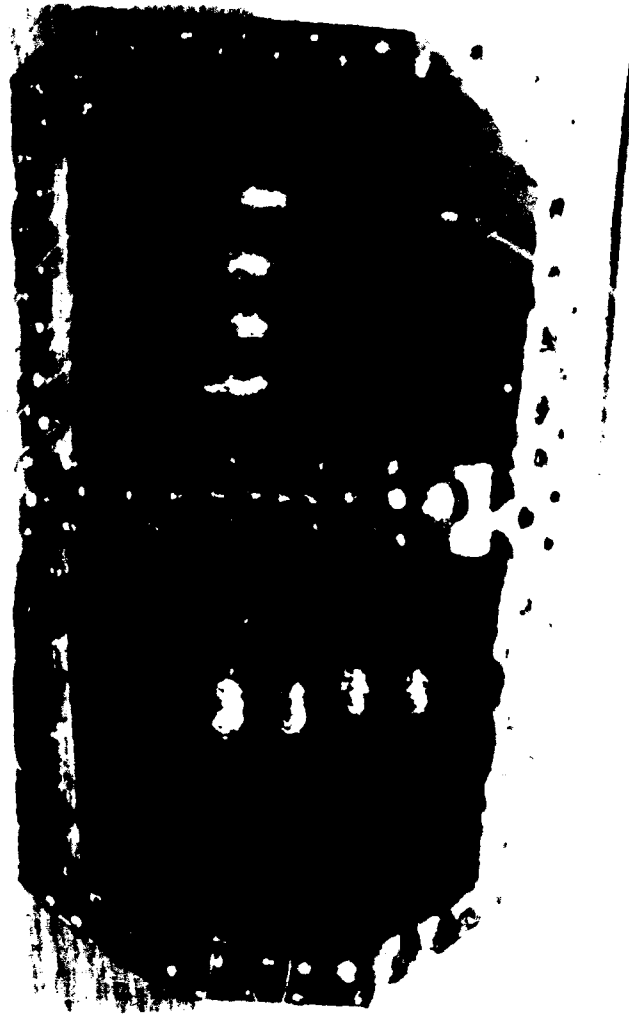


Figure 5-12. Four thin-film gages mounted on a test bar for gage factor testing.

contamination before sputtering. Atomic cleanliness was verified using the deionized water "break" test in which complete wetting assures the absence of organic contaminants. The sputtered layers eventually delaminated in every case (sometimes only after temperature cycling). The existence of organic contamination was then verified under the delaminated layers by the water break test. The conclusion was that these massive engine components could probably never be completely free from contaminants emerging from deep below the surface.

The second method was sputtering the insulation layer and gages on transferable weldable thin (127 micrometer) metal foils of polished and sputter-etched Hastelloy X. This method was eventually successful and was used throughout the present program. After completion of the sputtered film gage, the foil was spot welded to the turbine disk.

The sputtered gage pattern included wide lead films of PdCr extending to a location convenient for attaching lead wires by parallel-gap capacitive discharge welding. The lead wires were then overcoated with ceramic cement for protection from oxidation and erosion. The strain gages were not coated with ceramic cement. A sputtered overcoat of  $Al_2O_3$  was applied to one final batch of gages in this program to retard oxidation of the PdCr gage. Performance with and without the sputtered overcoat was thus documented.

Before the beginning of the program, preliminary in-house experiments had been carried out to measure the gage factor of these sputtered-film foil-mounted gages and to verify that repeatable and linear strain transfer could be achieved with foil-mounted gages. Figure 5-12 shows four sputtered-film gages on a foil welded to a Hastelloy X test bar 1/4 in thick for room-temperature testing and Figure 5-13 shows the results. The gages in this preliminary test were of an experimental FeCrAl alloy and the insulation under the gages was  $Si_3N_4$ . Good strain transfer to the gages sputtered on the foil is demonstrated in Figure 5-13 in tension (+) and in compression (-), for both longitudinal and transverse gages. The data symbols are the gage numbers.

b. Results of preliminary static tests: Ferris wheel—In the Ferris wheel test rig, a turbine disk is radially loaded through rods attached to each turbine blade dovetail. The disk is heated by induction heaters placed nearby and is oscillated slowly back and forth through less than  $180^\circ$  to promote uniform heating. The rig, located at Pratt & Whitney, is shown in Figure 5-14, with the disk used in the present program installed. The testing is in air at sea-level pressure.

In preparing for the Ferris wheel test, preliminary sets of six sputtered-film gages were fabricated on several foils, some using the  $Si_3N_4$  sputtered insulation and some using the  $Al_2O_3$ . The  $Si_3N_4$  is a poorer match in temperature coefficient of linear expansion with the foil material, and as a result eventual delamination would be expected at a lower temperature. This was verified when the  $Si_3N_4$

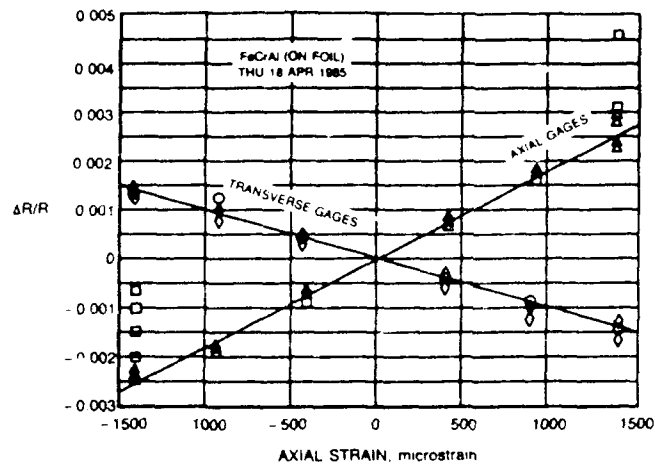


Figure 5-13. Good strain transfer is demonstrated in tension (+) and compression (-) from the test bar to the welded gages.

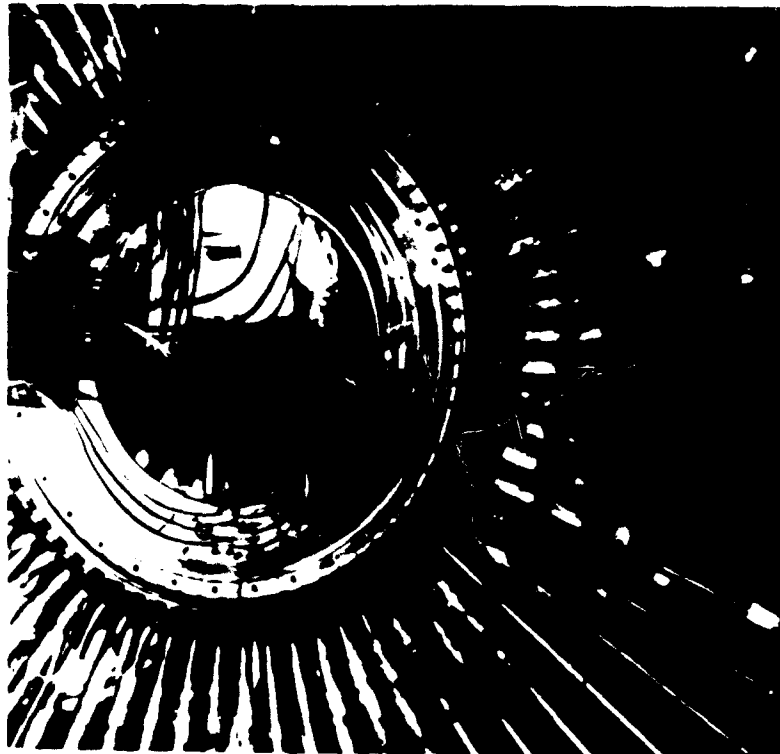


Figure 5-14. Pretest photo of the turbine disk installed in the P&W heated "Ferris wheel" rig for static radial loading tests.

catastrophically delaminated from one foil (Fig. 5-15) while cooling from 950 K during temperature cycling in bench tests. No delamination of the  $\text{Al}_2\text{O}_3$  films occurred after many cycles.



Figure 5-15. An example of catastrophic delamination of the  $\text{Si}_3\text{N}_4$  sputtered insulation at 950 K during a preliminary trial of the foil-mounted gages on a turbine disk.

Figure 5-16 is a view of the final installation of the PdCr sputtered-film foil-mounted gages on the turbine disk for the Ferris wheel test. Three gages were installed, including a radial gage at a radius of 140 millimeters (1R) and a radial gage and a tangential gage at a radius of 165 millimeters (2R and 3T). The gages are Pd-13Cr, 4.5 micrometers thick on  $\text{Al}_2\text{O}_3$  insulation 4 micrometers thick, all sputtered on a Hastelloy X foil 127 micrometers thick that is welded to the disk as shown. There was no overcoat protection on the PdCr gages.

Figure 5-17 shows measured strain versus Ferris wheel applied radial load at room temperature for gage 2R. Repeatability is good for increasing and decreasing load. Maximum measured strain is

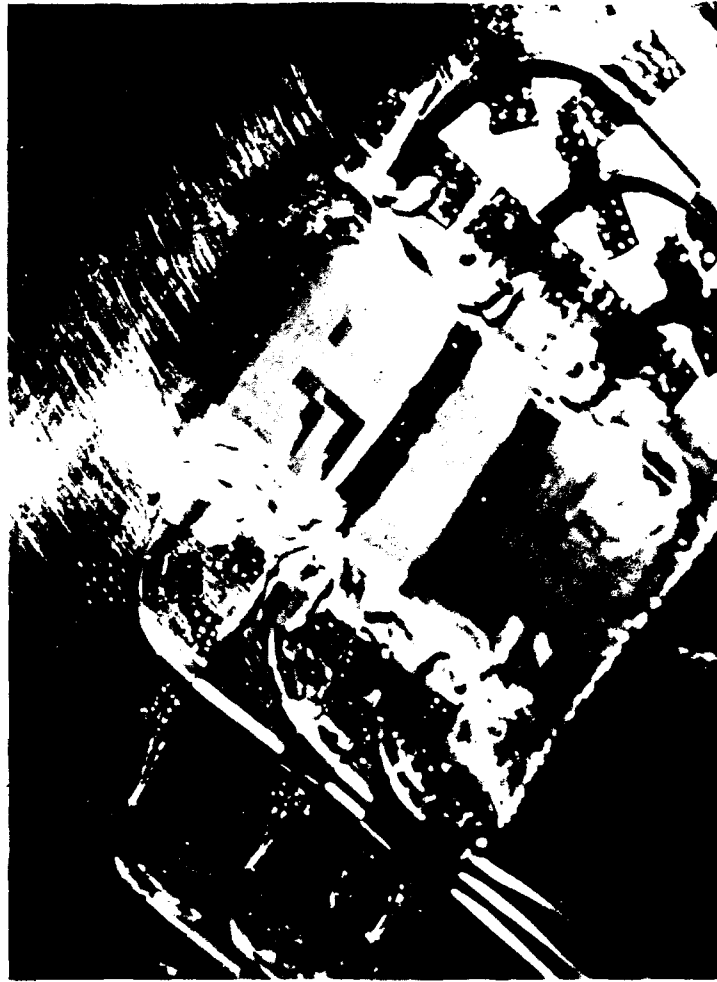


Figure 5-16. Pretest photo before 950 K static Ferris wheel test.

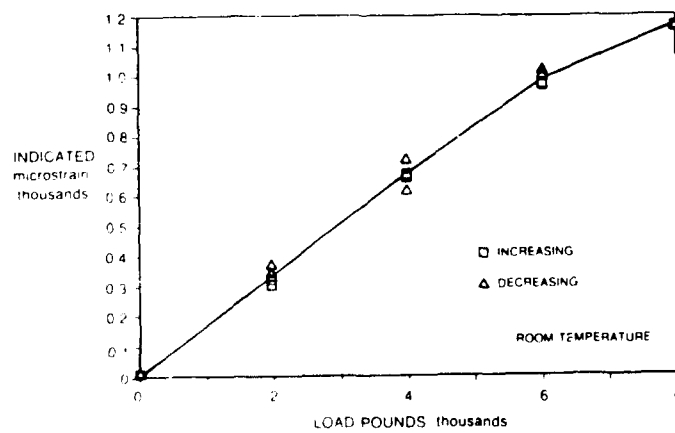


Figure 5-17. Measured strain vs Ferris wheel radial load.

about 1200 microstrain. The nonlinearity at highest strain has not been explained. During the course of the high-temperature testing the scatter in measured strains was thousands of microstrain.

Figure 5-18 is a post-test view after the 950 K testing in the Ferris wheel rig. The sputtered-film gages appear to be in good condition. There is dark discoloration suggesting that considerable oxidation has occurred. There is no delamination. There is damage to the grid of gage 1R apparently due to impact from debris.

One of the three gages was functioning at the end of the program (2R), one was open at the lead wire connection to the lead film (3T), and the third was open at the gage grid (1R).

The most significant quantitative result for this initial set of PdCr gages was the change in resistance of the gage and the change in leakage to ground over the course of the testing. Table 9 lists the pretest and post-test measurements. Measured gage resistances at start were 124, 148, 167 ohms, and all resistances to ground were over 40 megohms. Measured gage grid resistances at finish were open, 155, and 197 ohms and resistances to ground were 1000 to 6000 ohms.

The low resistances to ground would reduce the measured gage resistances by 1.1% to 4.4%. If moderate oxidation of the PdCr alloy gages had occurred, it would be expected that the gage resistance would be lower yet, due to the selective oxidation of the chromium, moving the alloy toward pure palladium (lower resistivity). This effect has been observed in controlled moderate oxidation tests of sputtered films of PdCr. However, in the present test, the actual post-test measured gage resistances for the two intact gage grids (Table 9) were higher than the pretest resistances (by 3.9% and 13.2%). It is concluded that the oxidation was so extensive that the chromium oxide scale extended far into the PdCr film and isolated some of the palladium on the external surface of the oxide scale. This phenomenon has been observed in oxidation experiments, although data are not available yet to unambiguously define an increase in sample resistance from this effect.

The post-test observed leakage to ground could, in small part, be due to absorption of moisture in the ceramic cement on the lead wires at room temperature after the end of testing, but since the post-test measurements were made within 1 day of the end of this test, this contribution is believed



Figure 5-18. Post-test photo after the 950 K static Ferris wheel test.

small. Indications are that the low resistance is due to leakage in the sputtered-film  $\text{Al}_2\text{O}_3$  insulation layer. Improvement in the insulation films was an ongoing task in the sputtered-film strain-gage development program. Thicker sputtered  $\text{Al}_2\text{O}_3$  and further improved polishing of the foil surface before sputtering (to promote more uniform thickness and remove asperities) was recommended for the next build.

**TABLE 9. TEST SUMMARY****STATIC TEST OF SPUTTERED-FILM STATIC STRAIN GAGES**

Test Conditions					
Substrate Material:	Hastelloy X Foil, Sput. Etch				
Insulating Material:	Sputtered Al <sub>2</sub> O <sub>3</sub> ,				
Gage:	Sputtered PdCr,				
Overcoat:	No overcoat				
Test Item:	IN100 Turbine Disk,				
Test Temperature:	950 K				
Test Pressure:	1 Atm. in air (Ferris wheel Rig).				
Test Strain:	2000 $\mu\epsilon$ , approximate				
Resistance Measurements (OHMS)					
Gage No.		1R	2R	3C	
Radius (millimeters)		140	152	165	
Pretest	(a) As Sputtered:	Gage Resistance	124	148	167
		Insulation Resistance	40M	40M	40M
	(b) After Installation	Gage Resistance	124	148	167
		Insulation Resistance	40M	40M	40M
Post-test	(c) After All Testing:	Gage Resistance	12K	155	197*
		Insulation Resistance	1K	6K	1K
	(d) R % Change Due To Leakage	-1.1%	-3.9%	-4.4%	
	(e) R % Total Change	open	+ 3.9%	+ 13.2%	
	*At lead film; lead wire broken at lead film.				
Comments					
Failure:	No delaminations. One working gage at end of test. Insulation: Leakage increase large during test (-22,000 app. $\mu\epsilon$ ). Oxidation: R net drift upward, believed due to the visible severe oxidation at 1 atm. (+ 43,000 to + 98,000 app. $\mu\epsilon$ in several hours).				
Improvement Needed:	Gage Uniformity: Poor (+ -15%). Want + -5% Insulation: Need 150 times less leakage increase. Oxidation: Need 300 to 600 times less oxidation.				

c. First spin test of PdCr strain gages: Build 2—Figure 5-19 is a view of the six PdCr sputtered-film foil-mounted gages on the turbine disk for the first spin test of these strain gages.

The six gages were sputtered on a single foil, arranged in pairs at each of three radii: 178, 165, and 152 millimeters. In each pair, one gage was oriented for radial strain measurement and one for



Figure 5-19. Detailed pretest photo before 950 K spin test 2.

tangential. The Pd-13Cr gages were 4.5 micrometers thick on  $\text{Al}_2\text{O}_3$  insulation 5 micrometers thick, all sputtered on a Hastelloy X foil 127 micrometers thick that was welded to the disk.

The PdCr sputtered-film gages were identical with the Ferris wheel PdCr gages except for the slightly increased  $\text{Al}_2\text{O}_3$  thickness. Again, the gages were not overcoated for oxidation protection.

The spin testing was conducted, extending finally to 950 K at maximum rotational speed of 13,200 r/min, corresponding to centripetal acceleration of 34,600 G at the 178-millimeter radius. The spin-pit

operating pressure was approximately 0.0001 atm. At the end of this test, as previously mentioned in the discussion of the BHP-700C gages, the disk bore became overheated resulting in melting of leadwire splices.

Strain readings from the PdCr gages were recorded throughout the spin program and are discussed at the end of this section.

Figure 5-20 is a post-test view. The sputtered-film gages appear to be in good condition. Slight discoloration of the PdCr films suggests moderate oxidation had occurred. There is no delamination.



Figure 5-20. Post-test photo after the 950 K spin test 2.

Pretest and post-test measurements of gage resistance and resistance to ground are listed in Table 10. These measurements are among the most significant results for the sputtered-film gages in this test.

In the table, three sets of pretest measurements are presented. The first set shows that the range of gage resistance as sputtered was 158 to 200  $\Omega$ , still about three times the desired uniformity of  $\pm 5\%$ , showing that resistance to ground as sputtered was low (8 to 1300  $\Omega$ ). We found by probing that the leakage was at discrete point locations all of which were in the lead film area. To rupture the leakage

paths 30 V dc was applied at the identified locations. The second set of readings shows that this procedure was successful in increasing the resistance to ground to 40 m $\Omega$  for four gages. These four gages were connected to the data system and used in the spin testing. This procedure also resulted in higher measured gage readings for some gages, as would be expected by the elimination of leakage paths. In other cases the measured gage resistance was unaffected, as would be expected if all the leakage paths for that gage were in one lead film. The third set of pretest readings shows that a pretest temperature cycle carried out to verify the adherence and stability of the films, resulted in a few ohms reduction in each gage resistance, probably because of preferential oxidation of the chromium in the PdCr alloy.

The post-test measurements in Table 10 show that the measured gage resistances all decreased, by amounts from 8.5% to 21.0%. Part of the measured decrease is due to shunting as a result of the decrease in measured resistance to ground to approximately 2000  $\Omega$  for each gage. As previously noted for this build, these particular post-test leakage measurements are believed to be due in significant part to post-test moisture absorption in the ceramic cement. The calculated downward drift in actual gage resistance, after taking into account the shunting, is the equivalent of -37,000 to -104,000 apparent microstrain (based on a gage factor of 1.8 for the PdCr alloy from Reference 2). This drift occurred during the testing at 950 K, driving the data acquisition system off scale and resulting in no strain measurements at temperatures above 755 K. The drift in the downward direction of this magnitude is entirely compatible with the effects of moderate oxidation seen in other testing (Ref.2) and verifies that provision of an oxidation-protection overcoat is a first priority for the further testing of PdCr gages, even in a vacuum spin rig.

Rotating strain data obtained with the foil-mounted sputtered thin-film PdCr gages is compared in Figures 5-10a and 10b and Figures 5-11a and 11b with the data obtained with the other strain measuring techniques, including optical speckle, optical dual-core fiber optic gages, commercial wire gages, and Chinese BHP-700C FeCrAl alloy wire gages. Data are presented at the only two radii (165 millimeters and 152 millimeters) at which all five types of data were acquired.

**TABLE 10. TEST SUMMARY**  
**SPIN TEST 2; SPUTTERED-FILM STATIC STRAIN GAGES**

Test Conditions							
Substrate Material:	Hastelloy X Foil, Sput. Etch						
Insulating Material:	Sputtered Al <sub>2</sub> O <sub>3</sub> .						
Gage:	Sputtered PdCr						
Overcoat:	No overcoat						
Test Item:	IN100 Turbine Disk, From F100 Engine						
Test Temperature:	950 K						
Test Pressure:	0.0001 Atm. (Vacuum, Spin Rig)						
Test Strain:	2000 $\mu\epsilon$ , approximate						
Test r/min:	13,200 r/min						
Test G-Load:	34,600 G						
Resistance Measurements							
	Gage No.	1R	2R	3R	4T	5T	6T
	Radius (millimeters)	178	165	152	178	165	152
Pretest	(a) Gage Resistance	188	187	155	200	25	180/158
	Insulation Resistance	8	580	435			1300/60
	(b) Gage Resistance	216	186	158	199		180/158
	Insulation Resistance	0.6M	40M	40M		7M	40M/40M
(c) Gage Resistance	210	181	153	194		176/154	
	Insulation Resistance	40M	40M	40M		6 K	9M/9M
Notes:	(a) As Sputtered						
	(b) After Rupturing Shorts						
	(c) After 950 K Bake						
Post-test	(d) Gage Resistance		163	140		139	135
	Insulation Resistance		2 K	2 K		2 K	2 K
	(e)		- 2.3%	- 1.9%		- 2.2%	- 1.9%
	(f)		- 9.9%	- 8.5%		-21.0%	-12.3%
Notes:	(d) After all spin testing, 950 K 13,200 r/min. (Gages 1 and 4 not connected.)						
	(e) R % Change Due To Leakage, (c) to (d)						
	(f) R % Total Change, (c) to (d)						
Comments							
Failure:	No delaminations, No opens. Insulation: Leakage increase large (-11,000 app. $\mu\epsilon$ ) Oxidation: R Drift Downward Large (-37,000 to -104,000 app. $\mu\epsilon$ in several hours). Visible Oxidation.						
Improvement Needed:	Gage Uniformity: Still poor (+ -13%). Want + -5% Insulation: Need 100 times less leakage increase. Oxidation: Need 250 to 600 times less.						

An overall summary and intercomparison of all strain results in Figures 5-10a and 10b and Figures 5-11a and 11b is presented in the executive overview section (Volume I). Notable details of the results obtained with the foil-mounted sputtered PdCr thin-film gages in Build 2 are presented here as follows (still referring to Figures 5-10a and 10b and Figures 5-11a and 11b):

1. Radial and circumferential strain measurements were obtained with the Build 2 foil-mounted sputtered PdCr thin-film gages at both radii, at the five rotational speeds during the acceleration at 294 K (the rig was shut down directly after the acceleration at 294 K, without pausing to acquire data during deceleration). In addition, data were acquired in almost every case at all speeds during both acceleration and deceleration at each of four higher temperatures: 420 K, 590 K, 755 K. The exceptions were radial strain at 165 mm at 590 K and circumferential strain at 152 mm at 755 K. In these two cases, signal was lost during the run but recovered later. Finally, thin-film gage data were also acquired during the spin test at 950 K, but these gage output readings were so large due to temperature effects that the data system was saturated (off scale) and no strain information could be derived from the readings.
2. At room temperature, the Build 2 thin-film indicated strains (Figs. 5-10 and 5-11) are near zero at lowest speed and become more tensile (more positive) as speed increases from 1100 r/min to 13,200 r/min. The strain increment is about 2000 microstrain. In this room-temperature spin test, the absolute level and the strain increment with increasing speed are generally in good agreement with most of the other strain measurements (speckle, dual-core fiber, commercial wire gage, BHP-700C gage), to about  $\pm 300$  microstrain. For unexplained reasons, one thin-film gage (radial at 152 mm) indicates a smaller positive increment by about 500 microstrain, than all others.
3. At the elevated temperatures, the apparent strain due to temperature for the thin-film gages dominates the indicated strain readings. For this reason, the indicated

strains for the thin-film gages at elevated temperatures are plotted separately at the bottom of Figure 5-10b and Figure 5-11b. The indicated strain increases by about 100 microstrain per Kelvin for each of the four thin-film gages. This is in the range expected for these gages without temperature compensation. (The temperature coefficient of resistance is about  $180 \times 10^{-6} \text{ K}^{-1}$  and the gage factor is about 1.8. The predicted apparent strain is therefore about  $180/1.8 = 100$  micron strain per Kelvin.) No attempt was made to correct the readings for these large temperature effects. Since the local temperature of the disk is not known to within about 20 K, then the correction uncertainty would be on the order of 2000 microstrain. In the continuing development program, self temperature compensation is to be added to the PdCr gage systems by adding a high-tcr metal element in an adjacent arm of the bridge circuit.

d. Second spin test of PdCr strain gages: Build 3—Figure 5-21 is a view of the six PdCr strain gages of Build 3 after the foil was spot-welded to the disk and leadwork was attached, and before installation of thermocouples and final cement overcoating of leadwork. This view shows clearly how the rows of spot welds are placed within 1.5 millimeters from the gage on all four sides.

Figure 5-22 is a general view of the completed installation. The six gages were sputtered on a single foil, in pairs at each of three radii: 165, 152, and 140 millimeters. In each pair one gage was oriented for radial strain measurement and one for tangential. The PdCr gages were 4.5 micrometers thick on  $\text{Al}_2\text{O}_3$  insulation 5.0 micrometers thick, all sputtered on a Hastelloy X foil 127 micrometers thick that was welded to the disk.

The sputtered-film gages were identical with the Build 2 PdCr gages except that more elaborate masking was used to improve uniformity of gages, extra care was taken in polishing the foil before sputtering insulation, to improve integrity of the sputtered insulation layer, and, most important, an oxidation-protection overcoat of  $\text{Al}_2\text{O}_3$  3 micrometers thick was sputtered on the PdCr gages.

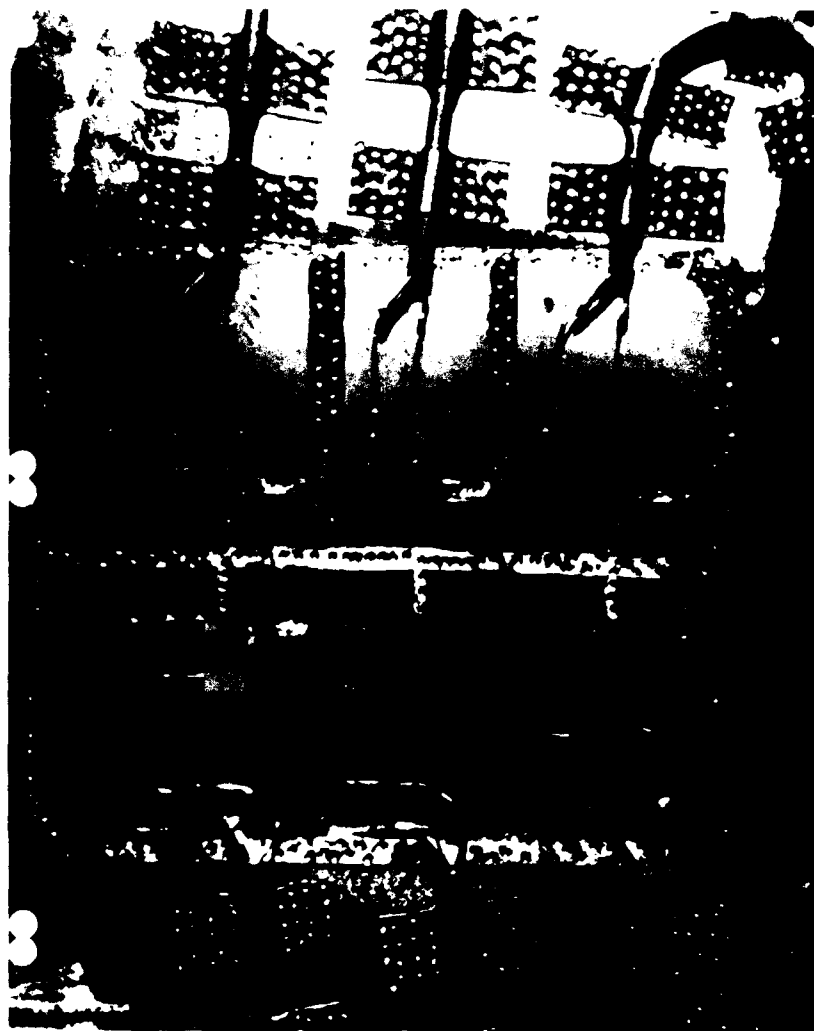


Figure 5-21. Detailed pretest photo before 950 K spin test 3, before cementing of lead wires.

The spin testing extended to 950 K at 13,200 r/min, corresponding to centripetal acceleration of 32,100 G at the 165 millimeter in radius and to predicted strains of about 2000 microstrain. The spin-pit operating pressure was approximately 0.0001 atmospheres.

At one point early in this test, after room-temperature runs to maximum speed but before high-temperature runs, a seal rub occurred in the rig bore resulting in destruction of leadwork and bombardment of the PdCr sputtered-film gages with hot debris. The gages were found to be undamaged and the gage resistances not significantly changed, and resistance to ground unchanged

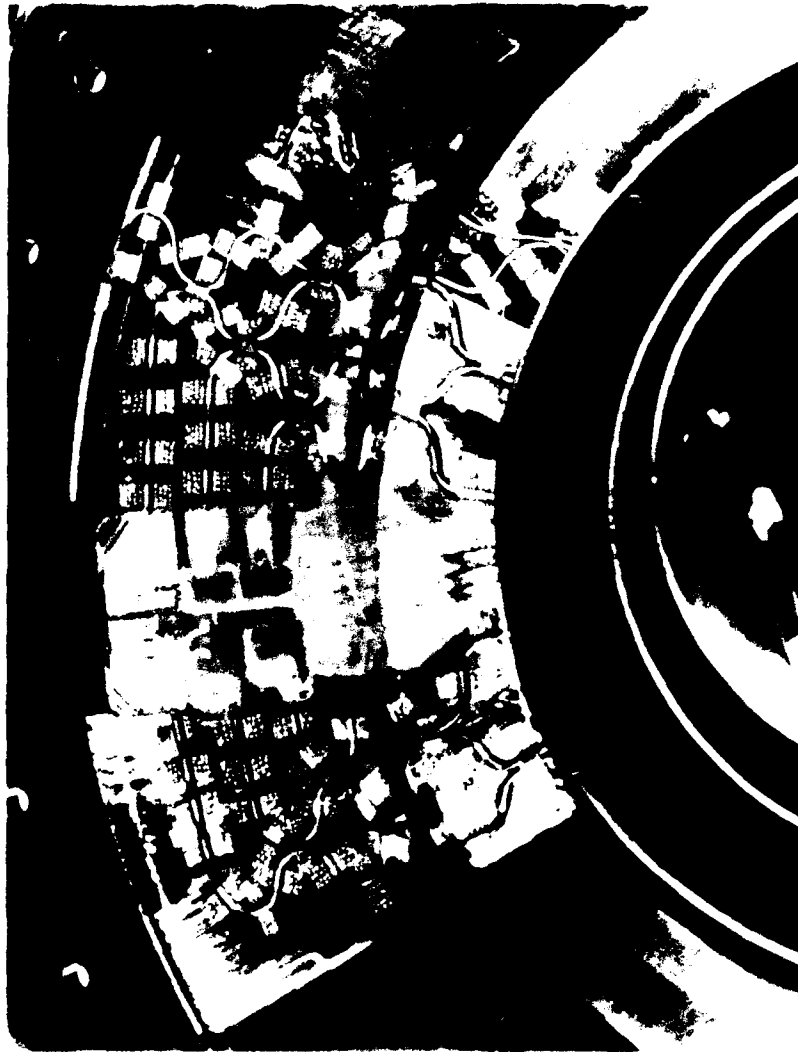


Figure 5-22. Pretest photo before 950 K spin test 3 of the completed installation of the overcoated thin-film strain gages

(40 megohms). The leadwork was replaced (including some new welds to lead films) and the spin testing was continued.

Strain data from the PdCr gages were recorded throughout the spin test program.

Figure 5-23 is a post-test view after the 950 K spin testing in Build 3. The sputtered-film gages appear to be in good condition. Discoloration of the PdCr films is slight, suggesting that moderate oxidation has occurred. There is no delamination.

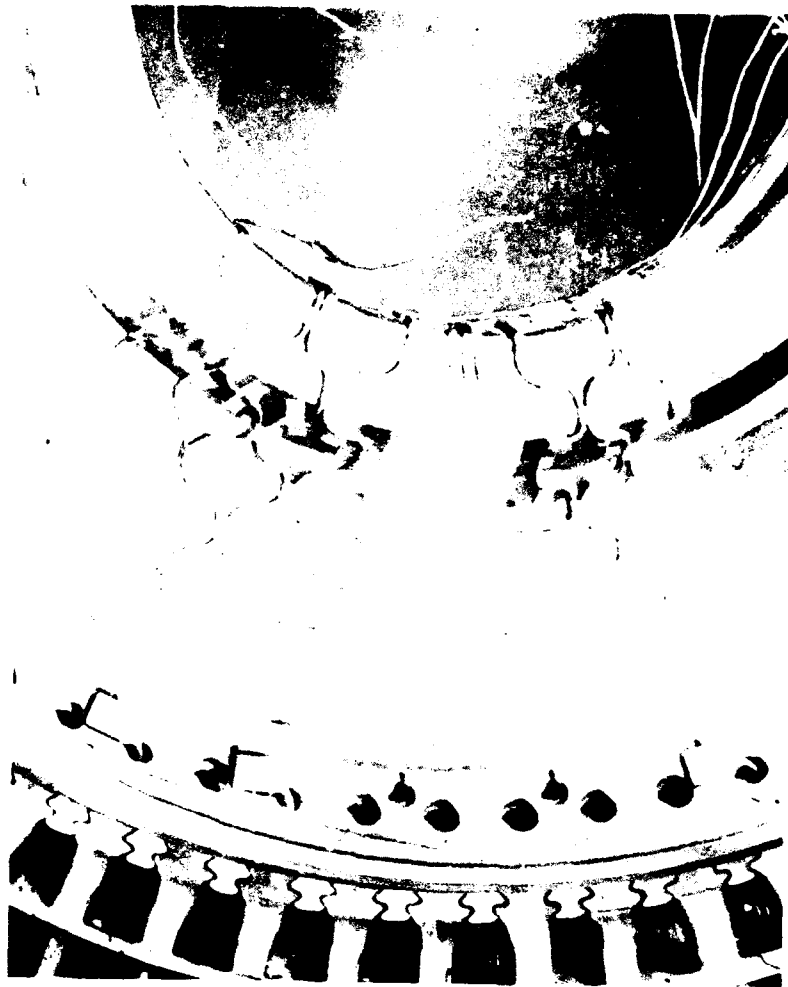


Figure 5-23. Post-test detailed view of the overcoated thin-film strain gages after 950 K spin test 3.

Pretest and post-test measurements of gage resistance and resistance to ground are listed in Table 11. These measurements are again among the most significant results. In the table, four sets of pretest measurements are presented. These measurements show excellent uniformity gage to gage, high resistance to ground, and little effect of the installation procedures.

The first set shows that the range of gage resistance as sputtered was 151 to 163 ohms (range of  $\pm 6\%$ ), nearly within the desired uniformity of  $\pm 5\%$ , and shows that resistance to ground as

sputtered was high (40 megohms) except for one gage (7000  $\Omega$ ). We found by probing that the leakage for this gage was at one discrete point in one lead film. To rupture this leakage path 30 V dc was applied at the identified location. The second set of readings shows that this procedure successfully increased the resistance to ground to 40 megohms. The third set of pretest readings was taken after welding the foil to the disk, and the fourth set after installing leadwork and after a 600 K pretest temperature cycle to cure cements on leadwork. Resistance to ground remains at 40 megohms for all gages. Measured gage resistances all decreased by 4  $\pm$  1 ohm. This decrease is apparently due to aging, and some oxidation, during the temperature cycle to 600 K. The repeatability of the ohmmeter used was  $\pm$  0.2 ohm. The effect of temperature on the resistivity of PdCr would change the gage resistance by one ohm only if the temperature change were about 37 K. Therefore small variations in room temperature from reading to reading would not significantly alter the values in this table. All six gages were then connected to the data system and used in the spin testing.

Two sets of post-test measurements are presented in Table 11. The first set was obtained after the interruption in testing to repair the damage resulting from the rig seal rub. The second was obtained after all testing.

The first set shows that gage resistances are virtually unchanged and that resistance to ground remains above 40 megohms for all gages.

The final set of post-test measurements (Table 11) shows that after all testing, three gages are open-circuited and the other three have drifted downward in resistance by an additional 5  $\Omega$  to 6  $\Omega$  (about 4%).

The resistance to ground has also decreased to 15,000 to 45,000 ohms, equivalent to an apparent strain offset of about -1300 microstrain, or a 0.2% decrease in measured gage resistance. In addition, discrete short circuits to ground have developed in the lead films, at one end only, in three gages.

**TABLE 11. TEST SUMMARY**  
**SPIN TEST 3; SPUTTERED-FILM STATIC STRAIN GAGES**

<b>Gage Construction</b>	
Substrate Material:	Hastelloy X Foil, Sput Etch
Insulating Material:	Sputtered Al <sub>2</sub> O <sub>3</sub>
Gage:	Sputtered PdCr
Overcoat:	Sputtered Al <sub>2</sub> O <sub>3</sub>

<b>Test Conditions</b>	
Test Item:	IN100 Turbine Disk, From F100 Engine
Test Temperature:	950 K
Test Pressure:	0.0001 Atm. (Vacuum, Spin Rig)
Test Strain:	2000 $\mu\epsilon$ , approximate
Test r/min:	13,200 r/min
Test G-Load:	32,100

<b>Pretest Resistance Measurements (OHMS)</b>							
G Gage No.		1C	2R	3C	4R	5C	6R
Radius (millimeters)		165	165	152	152	140	140
Gage Resistance	(a)	154	152	154	151	152	163
	(b)				151		
	(c)	148	149	146	150	148	156
	(d)	150	148	150	148	148	158
Insulation Resistance	(a)	40M	40M	40M	7 K	40M	40M
	(b)				40M		
	(c)	40M	40M	40M	40M	40M	40M
	(d)	40M	40M	40M	40M	40M	40M

Notes:

- (a) As Sputtered
- (b) After Rupturing Short
- (c) After Welding Foil to Disk
- (d) After Splicing Sheathed Lead and 600 K Bake

**TABLE 11. TEST SUMMARY (CONTINUED)**  
**SPIN TEST 3; SPUTTERED-FILM STATIC STRAIN GAGES**

Post-Test Resistance Measurements (OHMS)							
G Gage No.		1C	2R	3C	4R	5C	6R
Radius (millimeters)		165	165	152	152	140	140
Gage Resistance	(e)	148	146	149	146	145	156
	(f)	144	0.1M	145	142	3.3 K	66 K
Insulation Resistance	(e)	40M	40M	40M	40M	40M	40M
	(f)	1	40 K	45 K	15 K	3	1
Notes:		(e) After 1st spin, 420 K 13200 r/min, and rig repair.					
		(f) After final spin, 950 K 11400 r/min.					
Resistance Change Due To Leakage (%)		-0.2%	-0.1%	-0.1%	-0.2%	-4.4%	-0.3%
Total Resistance Change (%) (d to f)		-4.0%	open	-3.3%	-4.0%	open	open

**Comments**

Failure Comments: No delaminations, 3 opens, 3 good gages.  
 Insulation: Leakage increase large during test (-1300 microstrain)  
 Oxidation: 2 to 5 times reduced drift in 3 good gages (-18000 to -21000 app.  $\mu\epsilon$  in several hours).

Improvement Needed: Gage Uniformity: Good (+ -6%); Close to + -5% target.  
 Insulation: Need 10 times less leakage change, and eliminate point shorts to ground. Oxidation: Need 120 times less.

The calculated downward drift in actual gage resistance, after considering the shunting due to insulation leakage, is the equivalent of -18,000 to -21,000 apparent microstrain (based on a gage factor of 1.8 for the PdCr alloy from Reference 2). This drift is two to five times less than for the unovercoated PdCr gages of Build 2, but is still far in excess of the goal of 200 microstrain uncertainty in strain measurement.

The gage resistance drift in the downward direction indicates that the oxidation protection for the PdCr gage must be improved by another factor of about 120. Increasing the thickness of both the

PdCr and the Al<sub>2</sub>O<sub>3</sub> coating, adding a metal top layer as an oxygen barrier, and hot sputtering of the Al<sub>2</sub>O<sub>3</sub> to avoid entrained gases are avenues being explored.

Finally, the insulation layer under these gages clearly requires further improvement. For example, measured resistance to ground of more 187,000  $\Omega$  at each end of the gage at all temperatures up to the maximum of interest will be required to keep apparent strain due to leakage below 200 microstrain in a 150 ohm gage. In the ongoing development program, the mechanisms of insulation layer leakage are being investigated.

Build 3 rotating strain data obtained with the foil-mounted sputtered thin-film PdCr gages is compared in Figures 5-10a and 10b and Figures 5-11a and 11b with the data obtained with the other strain measuring techniques, including optical speckle, optical dual-core fiber optic gages. Data are presented at the only two radii (165 millimeters and 152 millimeters) at which all five types of data were acquired.

An overall summary and intercomparison of all strain results in Figures 5-10a and 10b and Figures 5-11a and 11b is presented in the executive overview section. Notable details of the results obtained with the foil-mounted sputtered PdCr thin-film gages in Builds 2 and 3 are presented here as follows (still referring to Figures 5-10a and 10b and Figures 5-11a and 11b):

1. Radial and circumferential strain measurements were obtained with the Build 3 foil-mounted sputtered PdCr thin-film gages at both radii, at the five rotational speeds during the acceleration and deceleration at both 294 K and at 420 K. Based on the experience of Build 2, in which it was confirmed that the apparent strain due to temperature was about 100 microstrain per Kelvin for the uncompensated thin-film gages, an attempt was made to keep the strain readings within the range of the data system at each temperature by rezeroing the thin-film strain gage bridge output voltage at temperature. This procedure worked at 420 K as described below, but not enough range of adjustment was available for the higher temperatures. As a result, no strain information could be derived from the readings at temperatures above 420 K.

2. Both at room temperature and at 420 K, the Build 3 strains measured with the thin-film gages (Figs. 5-10 and 5-11) are near zero at lowest speed and become more tensile (more positive) as speed increases from 1100 r/min to 13,200 r/min, and then return to near zero as speed decreases to 1100 r/min. For one of the four thin-film gages (165 mm, radial) the strain increment with increasing speed is about 2000 microstrain, in good agreement with most of the other strain measurements (speckle, dual-core fiber, commercial wire gage, BHP-700C gage). For unexplained reasons, the other three thin-film gages indicates a smaller positive increment by about 1000 microstrain.

## 7. CONCLUDING REMARKS

The strain gage testing on rotating turbine disks in a spin rig to 950 K demonstrated some progress toward overcoming the historical problems which have prevented attaining useful static strain measurements above 660 K with small high-temperature resistance strain gages. The long-term goal of uncertainty below 200 microstrain has not yet been approached. Uncertainty is still in the area of 2000 to 20,000 microstrain at high temperatures.

The gages of the FeCrAl alloy developed in China were durable and demonstrated less metallurgical drift than any previously reported FeCrAl alloy. The gages of the PdCr alloy under development in sputtered-film form at United Technologies Research Center under NASA contract were also durable, and showed improvement from build to build in oxidation resistance and insulation resistance to ground.

The FeCrAl alloy wide gages are more durable because of the use of conventional leadwires and insulation. The PdCr alloy film gages have better accuracy, when they survive, because of their resistance stability.

Further development of the PdCr alloy gage system is recommended because the alloy itself is metallurgically stable. This gage system requires improved oxidation protection and improved resistance to ground. In final developed form, temperature compensation will be required because of the higher  $\text{tcr}$  of this alloy.

## 8. ACKNOWLEDGEMENTS

D.R. Englund and W.S. Kim at NASA Lewis Research Center encouraged applying the PdCr technology being developed under NASA contract at United Technologies Research Center (UTRC). Dr. C.O Hulse, the UTRC Program Manager for the NASA contract, provided invaluable advice and support.

## 9. BIBLIOGRAPHY

Stange W.A., Advanced Techniques For Measurement Of Strain And Temperature In A Turbine Engine, AIAA Paper No. 83-1296, AIAA/ASME/SAE 19th Joint Propulsion Conference, Seattle, Washington, June 27-29, 1983.

Hulse, C.O., Bailey, R.S., Grant, H.P., Przybyszewski, J.S.; High Temperature Static Strain Gage Development Contract, Interim Report, NASA CR-180811, Contract NAS3-23722, 1987.

Wu, T.T., Ma, L.C., Zhao, L.B., Development Of Temperature Compensated Resistance Strain Gages For Use To 700 C, Experimental Mechanics 21(3), 117-123, March 1981.

Wu, T.T., Ma, L.C., Comparison Of Characteristics Of Our Temperature-Compensated Resistance Strain Gages For Use To 700 C and 800 C, Fourth Annual Hostile Environments And High Temperature Measurements Conference Proceedings, Society For Experimental Mechanics, 1987, p. 30-34.

Fulton, G.B., Advanced Structural Instrumentation Test Facility AIAA Paper No. 88-3145, AIAA/ASME/SAE/ASEE 24th Joint Propulsion Conference, Boston, Mass., July 11-13, 1988.

Grant, H.P., Przybyszewski, J.S., Anderson, W.L., Claing, R.G., Thin Film Strain Gage Development Program, Final Report, NASA CR-174707, 1983

Grant, H.P., Anderson, W.L., Prxybyszewski, J.S., Rotating Tests of Advanced High Temperature Wire and Thin-Film Strain Gages, AIAA Paper No. 88-3145, 24th Joint Propulsion Conference Boston, Mass. July 11-13, 1988.

## VI. TEST FACILITY

### 1. ABSTRACT

The objective of this program performed under Air Force Contract F33615-83-C-2330 was to demonstrate the accuracy and durability of advanced steady state strain and temperature sensors in an environment typical of advanced gas turbine engines. A first stage turbine disk which operates at speeds up to 13200 r/min and temperatures of 950 K was selected as the test vehicle. Simulated engine operating conditions were achieved in the United Technologies Research Center's spin facility. This rig was designed for structural dynamic measurements and evaluation of a wide range of rotating components. This section of the report describes the spin rig configuration, drive system test rotor and support equipment. Included is a discussion of the modifications made to achieve high temperature, and the data acquisition system and test procedure.

### 2. INTRODUCTION

The high speed spin rig at UTRC is built for structural dynamic testing of a wide range of rotating components. Turbomachinery components, propellers and helicopter blades were given foremost consideration during design but other applications such as labyrinth seal tests were also planned. Since it is not designed for failure testing, it was constructed above ground with the drive system and instrumentation located below the vacuum chamber thus leaving the top surface completely unobstructed and available for various optical measurement techniques. Figure 6-1 shows an overall view of the 3.04 m diameter by 0.91 m high vacuum chamber and pump system. Test experience to date, includes speeds up to 13,200 r/min, but with appropriate modifications, operation up to 30,000 r/min is possible. The test chamber is maintained at vacuum conditions to minimize drive power requirements, to evaluate structural properties of blades without aerodynamic effects, and to reduce the explosion hazard resulting from entrapped oil vapor or explosive dust generated by accidental rotor failure. For the Advanced Structural Instrumentation testing, capability was added to the rig to heat the test piece up to 950 K, which necessitated heat shielding and cooling systems to confine the heat to the test chamber itself. A rotor assembly consisting of disk, blades, and side plates from an aircraft first stage high pressure turbine is used as the test piece throughout the program. Additionally, the number and

variety of sensors evaluated required that the tests be carried out in a series of rig builds, a build consisting of a group of sensors mounted on a disk and tested over the complete operating envelope. As familiarity was gained with the thermal response of the rig, it was feasible to make modifications between builds to correct or modify operating characteristics.

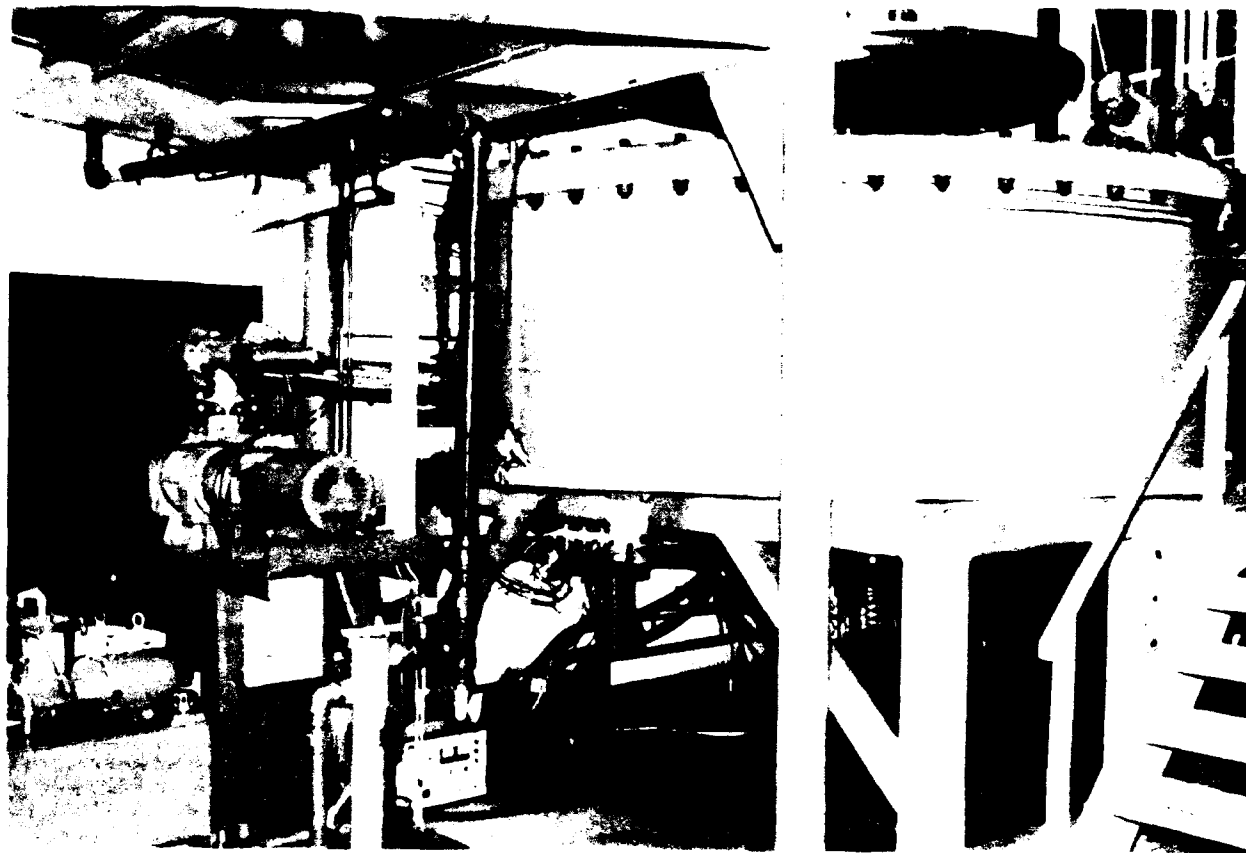


Figure 6-1. Overall view of UTRC spin rig.

The sections below will describe the construction of the rig in more detail including the drive and control system as well as the slip ring and data acquisition components. The heating system and development of heat shielding and cooling components will also be described.

### 3. SPIN RIG DESCRIPTION

The vacuum chamber is a cylindrical steel weldment of 19 mm thick plate 3 m in diameter and 0.91 m high in Figure 6-2. The bottom and top cover plates are 51 mm and 76 mm thick respectively. The complete drive system comprising spindle, air turbine and slip ring, is mounted on the vacuum

chamber bottom plate. Speckle Photogrammetry, a noncontacting optical displacement measuring technique, has been used for all the builds as a strain reference. The characteristics of the telecentric lens used for the speckle photogrammetry measurements in these tests, required that the plane of the test rotor be a specified distance from the focal plane of the lens. To achieve this distance, the complete drive system is raised by means of the spool piece shown in Figure 6-2. An added benefit derived from the use of the spool piece (not generally used for other tests) is that it gives additional room under the rig for a second 48-channel slip ring. A continuous 76-mm-thick steel ring 2.4 m in diameter, centrally situated in the vacuum chamber provides primary fragment containment in the event of a rotor failure and limits the maximum practical diameter for high speed test hardware. Access to the test chamber is through a 1.8-m-diameter flanged lid in the top plate. The weight of the lid on a circumferential O-Ring provides the vacuum seal and six dogs secure the lid against accidental internal overpressure.

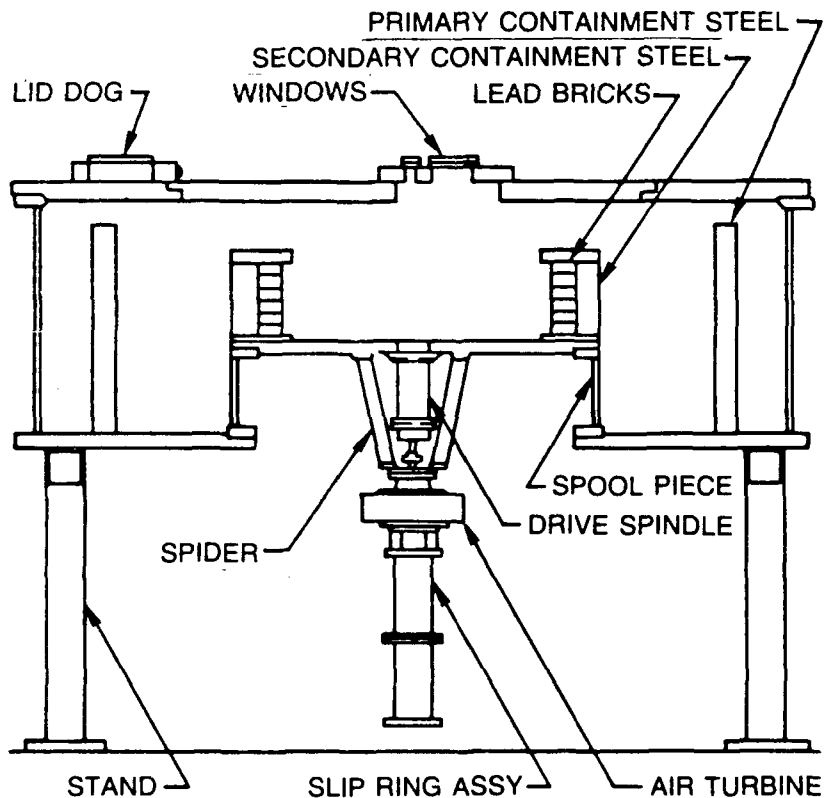


Figure 6-2. UTRC spin rig cross-sectional schematic.

The drive system is mounted on a 51-mm-thick by 1.8-m-diameter plate which is bolted to the floor ring of the vacuum chamber. The drive spindle housing is secured to the floor plate by means of a bolted flange. Details of the drive spindle and bearing support system are shown in Figure 6-3. The

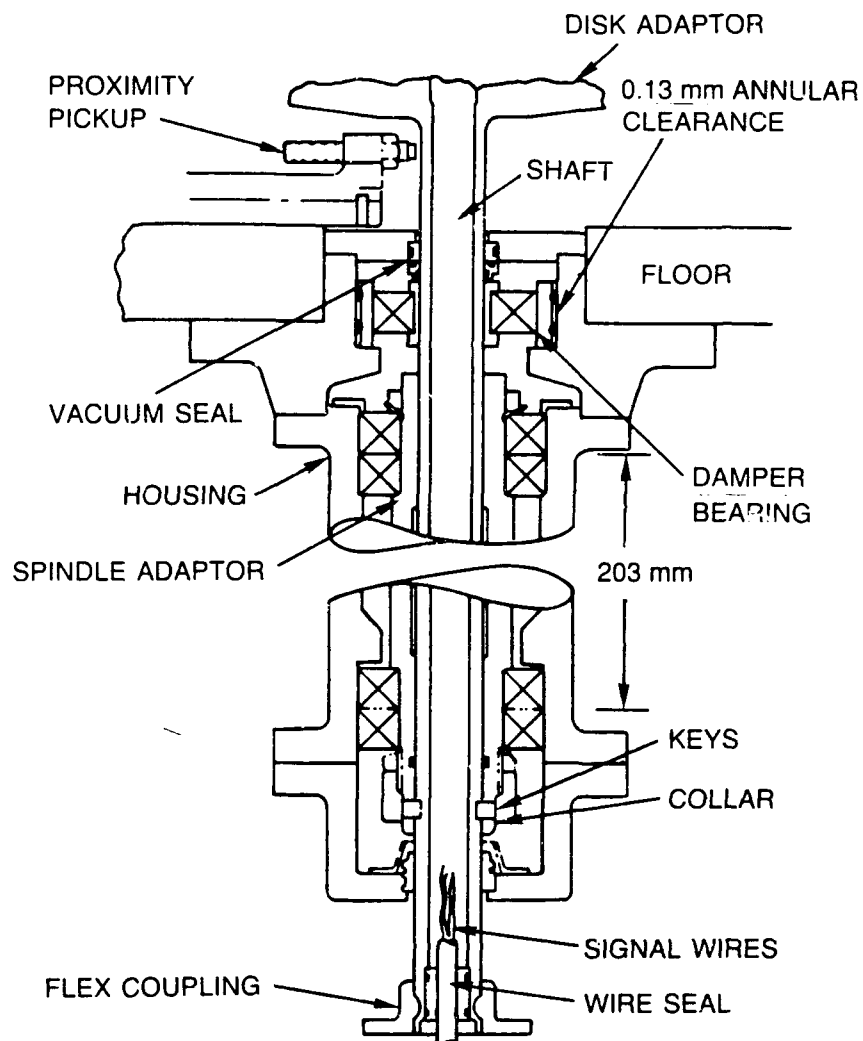


Figure 6-3. Drive spindle and bearing support system.

32-mm-diameter shaft slides into the spindle adaptor and is held at the bottom by a pair of half-round keys which fit through cutouts in the adaptor sleeve and are secured by the restraining collar. The spindle adaptor is supported by a pair of duplex ball bearings, the upper pair providing axial restraint, while the lower pair is free to adjust axially to allow for tolerances and thermal growth. The outer race of a precision bearing, located just under the disk adaptor is fitted into a 0.127-mm annular clearance and acts as a squeeze film damper to control rotor whirl. As originally constructed, the shaft was

nominally tight in the spindle adaptor at both the top and bottom. To improve the effectiveness of the damper, the clearance between the shaft and the top of the spindle adaptor was increased so that the damper bearing now provides the total radial restraint at the upper end of the shaft. Whirl amplitude of the test piece is measured with a pair of proximity pickups, 90° apart, 76 mm above the damper bearing. A magnetic shaft seal interfaces between the rotating shaft and the stationary vacuum chamber. The seal comprises a graphite face seal ring rubbing on a polished magnetized stator, the sealing pressure between the two elements being controlled by the force between the magnet and the steel graphite retaining ring.

A 203-mm-diameter Barbour Stockwell air turbine is connected to the bottom of the drive shaft through a Formsprag flexible coupling. The turbine has two sets of buckets so that rotation in either direction is possible with the other set of buckets available for braking. The turbine is supported (see Fig. 6-2) on a welded steel spider which is secured to the bottom plate of the chamber. The slip ring is mounted on the bottom flange of the turbine housing with drive provided by a flexible coupling to the bottom of the turbine shaft. The spindle adaptor duplex bearings and the turbine bearings are lubricated with an air-oil mist system energized from the main control. Oil for the squeeze film damper is supplied as liquid under 0.17 MN/m<sup>2</sup> pressure by a separate oil supply.

An automatic control system, Figure 6-4, throttles the air supplied to the turbine to maintain speed at a preset value. The speed control supplies a signal to a servo-throttle valve which in turn controls the flow of air to the turbine to regulate speed. The signal which regulates the speed is derived from a digital tachometer driven by magnetic pulses triggered by a 60-tooth gear mounted on the air turbine drive shaft. The control system contains a fail safe feature which cuts off the airflow to the turbine in the event that the speed signal is lost. The control valve is sized to match the flow requirements of the turbine. A programming plug in the instrument is used to set up the control circuit to suit the speed range of the turbine being controlled. In the present installation, there are two valves, one for speeds up to 1500 r/min (model helicopter rotors), and the other to regulate speeds up to 14,000 r/min (gas turbine components). Safety interlocks prevent rotor operation until a specified vacuum reading at the control console is achieved, oil flow requirements are satisfied, and the lid dogs are all secured.

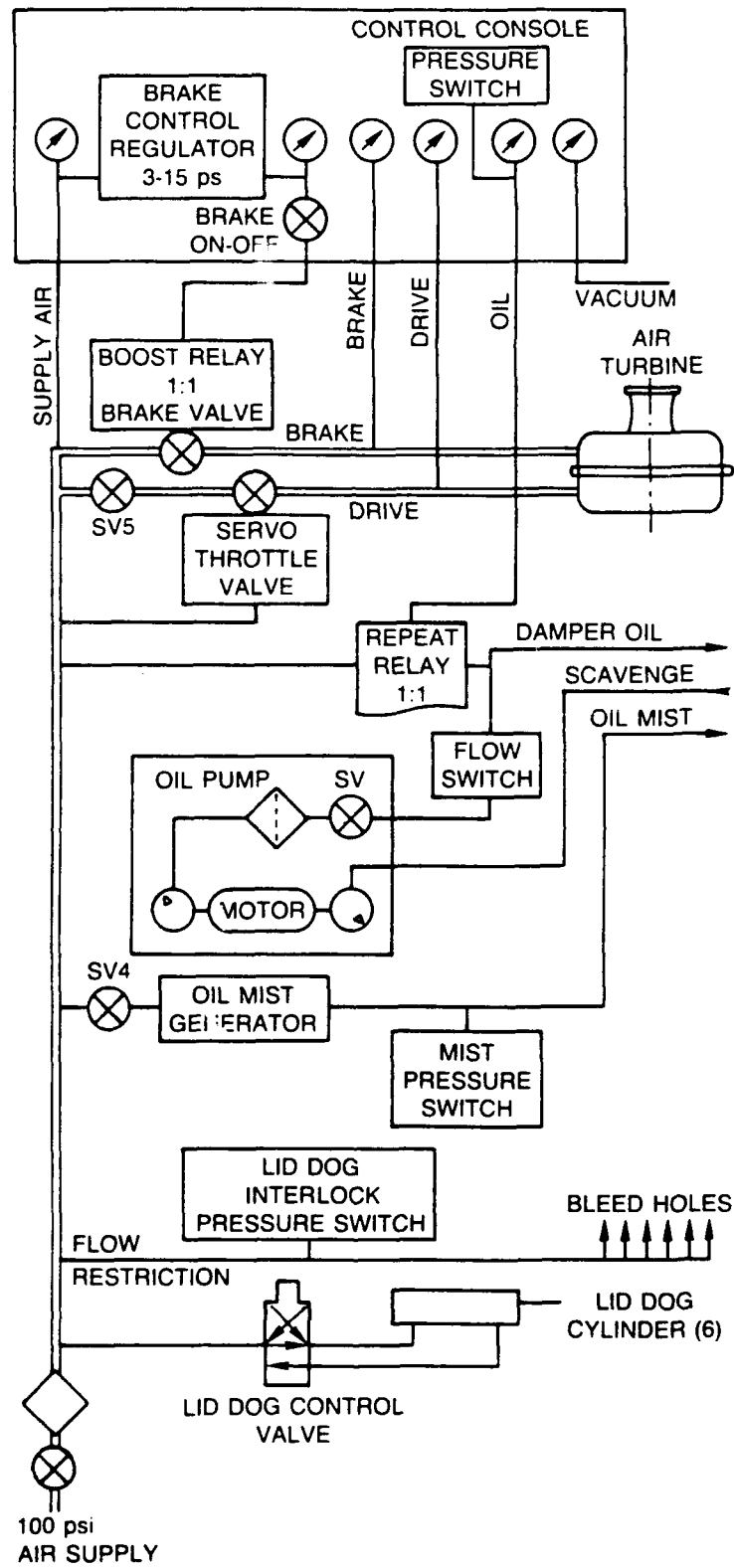


Figure 6-4. Spin rig fluid systems.

The vacuum chamber is evacuated to a nominal operating pressure of 100 millitorrs by a two stage pump system. A single stage 4.53 m<sup>3</sup>/min rotary piston pump brings the vacuum chamber to approximately 1 torr, at which time a rotary lobe booster pump is automatically energized to bring the chamber down to its operating level of 65 to 75 millitorr in approximately 10 min.

Electrical signals to and from the test piece are routed down the drive shaft through a vacuum seal in the shaft, through the turbine spindle to the slip ring assembly mounted below the turbine. For this effort's tests, two 48-ring, air cooled Pratt & Whitney slip ring units were used. Optical access to the test piece is accomplished through the top of the rig and is varied to meet the requirements of the test. For optical blade deflection measurements, two off axis windows are available, while for this program, an on-axis window was required for the incident laser beam, as well as one at the gauge section radius of the disk web on which the telecentric lens was mounted

#### **4. MODIFICATIONS FOR HEATED TESTS**

To satisfy the requirements of the present program, several modifications were incorporated in the rig so that testing the test disk at temperatures up to 950 K was possible. The major changes were the addition of a vacuum feed-through for the power from an induction heater, the addition of heat shielding and active cooling to protect the rig structure from heat, and additional containment protection. Figure 6-2 shows the configuration with the spool piece and the added containment while Figure 6-5 shows the arrangement of the other items.

The output of a 35-kW induction heater adjacent to the vacuum chamber was fed through a water cooled co-axial line to a step down transformer situated directly under the floor plate. The secondary winding of the transformer was connected to the vacuum feed-through which carries the power into the vacuum chamber where it connects to the disk heating loop element (see Fig. 6-6). This loop is built up from 6.3 mm square copper tubing and is water cooled in series with the cooling system of the transformer secondary. The outboard ends of the loop are supported through ceramic standoffs to the floor of the vacuum chamber.

The test disk is enclosed by heat shielding to minimize the heating requirements, and to maintain the rig structure and drive system at acceptable temperatures. The basic shield is comprised of two

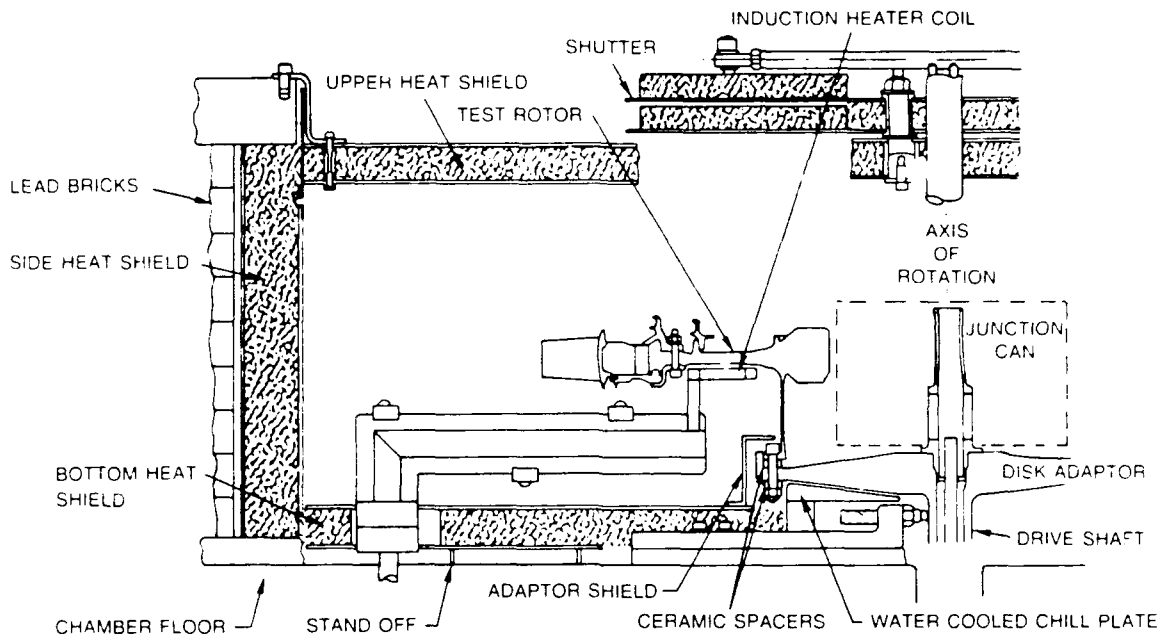


Figure 6-5. Section through the hot chamber.

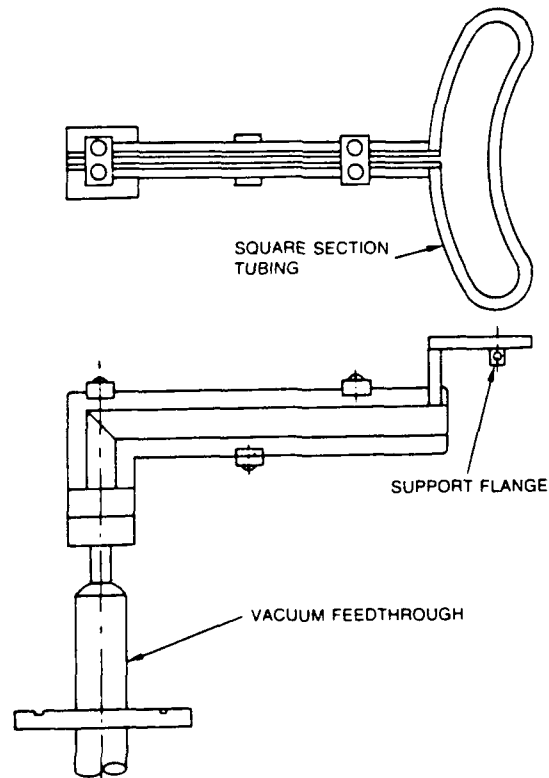


Figure 6-6. Induction heater load cell.

polished stainless steel sheets separated by 25 mm of ceramic felt. The shield is made up of top and bottom plates and a cylindrical shell which fit inside the secondary containment. There is a 152-mm-diameter hole in the top plate centered at the gage station on the test disk for optical access. A remotely operated mechanical shutter limits radiation from the disk to the surrounding structure except during data acquisition. A water cooled copper chill plate is fitted close to and around the disk adaptor and the section of shaft which projects into the vacuum chamber. This was incorporated to reduce the heat load downward into the seal and bearing compartment and upward into the wiring junction can, described below, located at the bore of the test disk. During the several builds of the rig, several techniques were tried to reduce the conductive heat transfer into the disk adaptor by the use of ceramic standoffs between the test disk and the adaptor. Disassembly of the rig after each build invariably revealed that a majority of these spacers had failed. A variety of machineable ceramic materials have been tried in an attempt to find a material with good insulating properties and adequate mechanical strength to withstand both assembly (there is some evidence that some of the failures are occurring at assembly) and dynamic loads. Although the physical configuration contains the ceramic fragments, spacer failure leads to the possibility of rotor shift during test. For the most recent build, the ceramic stand-offs were replaced with steel ones and the increased conductivity and consequently higher adaptor temperature had to be accepted.

The possibility of disk failure cannot be ruled out in this type of testing because of the high speed and high temperatures and temperature gradients which occur. Additionally, some of the sensors and associated leadwork are attached to the disk with nickel straps tack-welded to the surface, generating regions of stress concentration. Additional containment shown in Figure 6-2, was added to insure that fragments from this type of accident would remain in the chamber. Immediately outside the sheet metal heat shield and lining, the 102-mm-thick continuous steel ring is a ring of 102 mm thick lead bricks. If disk fragmentation occurs, the lead behaves as a viscous damper to prevent ricochet, and the steel provides the strength for containment.

In the bore of the test disk is the junction can where the splices are made between the high temperature leadwires on the disk and the wires coming up the shaft from the sliprings. From the outset of the rig modification, the goal has been to keep the temperature inside this can below 339 K,

because during the final build of the program, this can contained the electro-optical components required for the twin core fiber optic strain and temperature sensors. A balance must be achieved between the time it takes to complete a test run and the time it takes for radiation and conduction to heat the junction can to 339 K. This junction can evolved through several configurations shown in Figures 6-7, 6-8 and 6-9, as experience was gained in operating the rig at high temperatures. Table 1 in

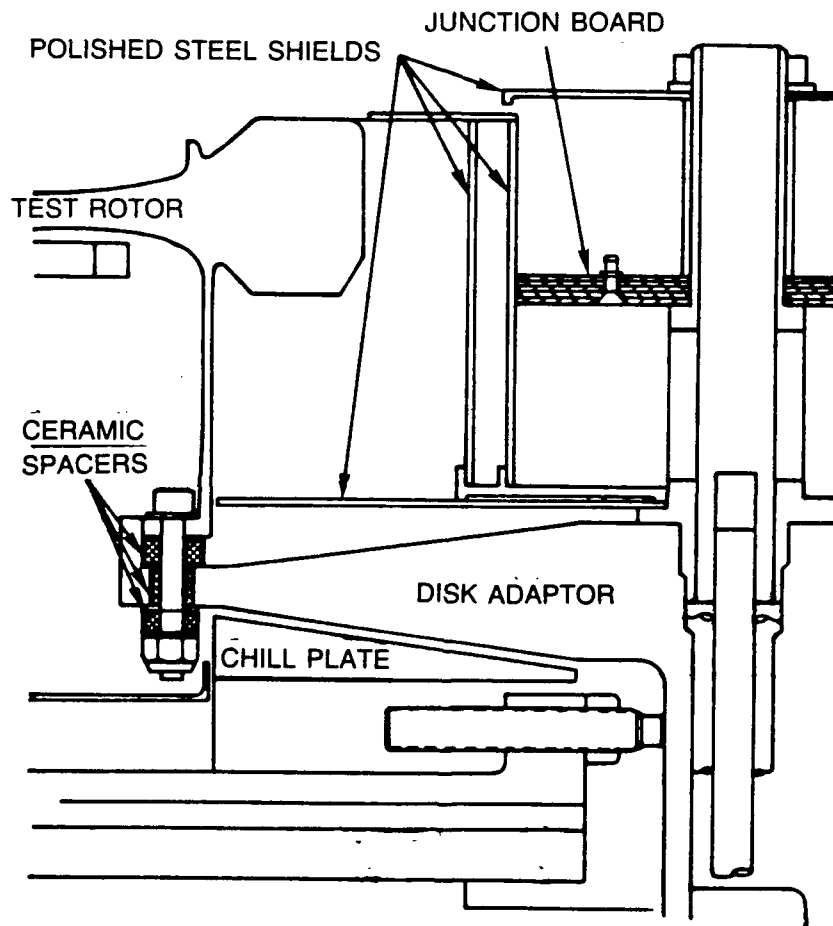


Figure 6-7. Uncooled rotating junction can configuration for Build 1.

Volume I lists the builds of the rig and summarizes the cooling configurations which have been used. Figure 6-7, shows a schematic of the heat shield used in the first build which is a passive double walled shell where the walls are polished to maximize reflectivity. Figure 6-10 plots the temperature at the disk web, gage section, at the bore and in the junction can as a function of time. Notice the difference in temperature scales between the upper and lower sections of Figure 6-10 which make it easier to

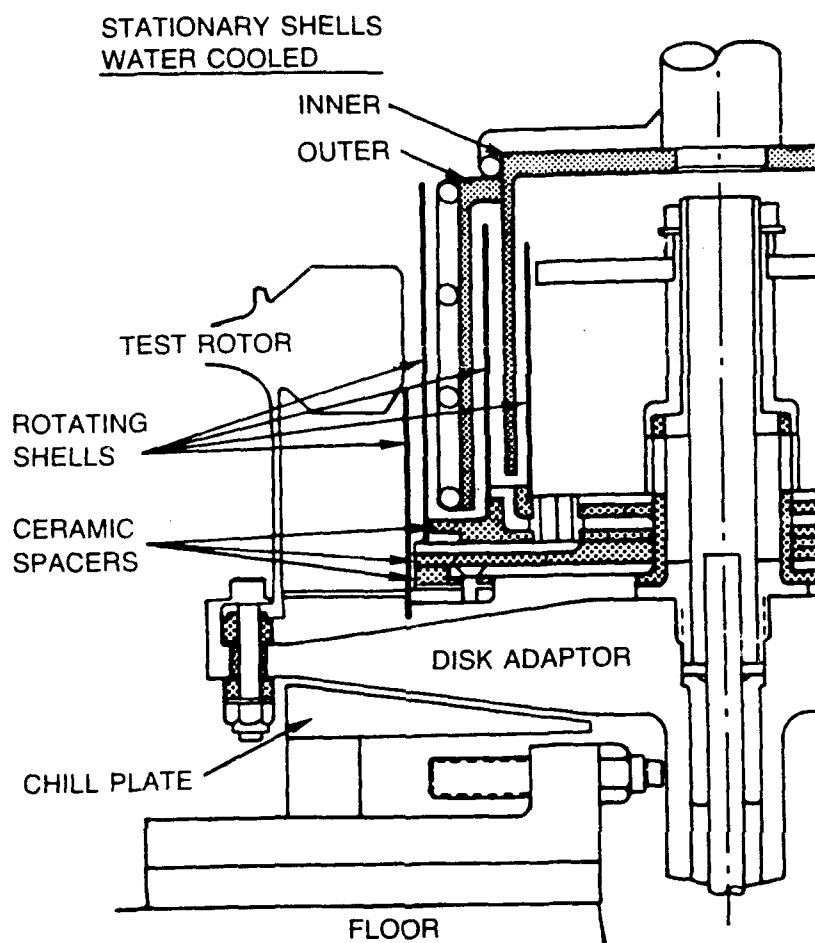


Figure 6-8. Water cooled junction can with labyrinth shield.

compare the junction can temperature with the disk temperature. A horizontal line at 339 K highlights the maximum allowable junction can temperature for the builds which have electro-optical components on board. Curve a in Figure 6-10 indicates that the gage section at the disk web had only reached 694 K when the junction can temperature reached 339 K, at approximately 13 min. Also, the temperature rose to excessive levels in the can (finally reaching approximately 605 K) which damaged the tag board and melted the splices. Figure 6-8 shows the actively cooled labyrinth shield used for the next two builds of the rig. Here, a multi-walled shield with water cooled shells interleaved is designed to reduce the major heat load from the bore of the test disk. This was a major improvement as can be seen in curve b, Figure 6-10, but the temperature still rose to levels too high for electronics operation although this high temperature occurred after the strain data had been obtained. Note that the bore of the disk takes significantly longer to heat than the less massive web. It is evident that the junction can

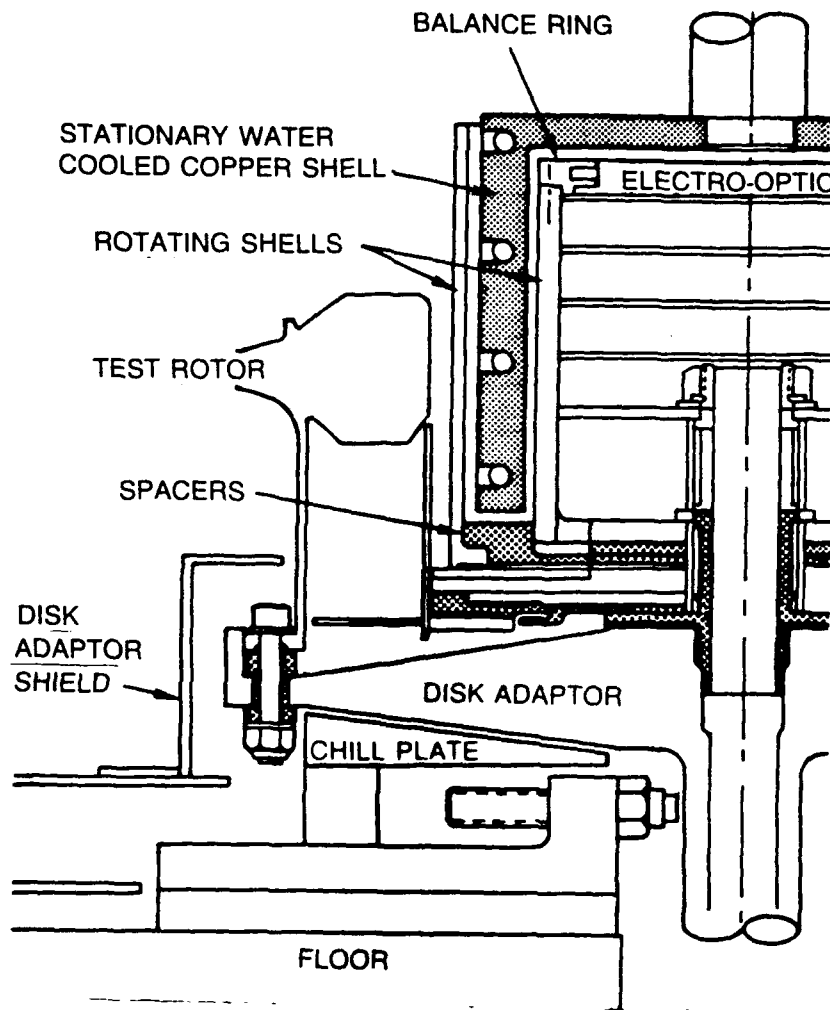


Figure 6-9. Final configuration of junction can.

temperature heating rate tends to follow the bore temperature because of its close proximity rather than the web temperature. Evaluation of the temperature data on the adaptor disk and inside the junction can indicates that an important heat path is radiation from the hot disk to the rim of the adaptor and then by conduction toward the center and then up the center tube. To increase the thermal resistance of this path and reduce the heat load into the junction can, an additional stationary shield has been added as shown in Figure 6-9.

Build 3 incorporated this shield but was terminated before any high temperatures were attempted. Build 4 incorporated a "hybrid" shield in that the main shield was the passive double wall reflector, but it also included the adaptor shield. The temperature response of this configuration is shown in curve c of Figure 6-10. This shows that even without the water cooled labyrinth the response

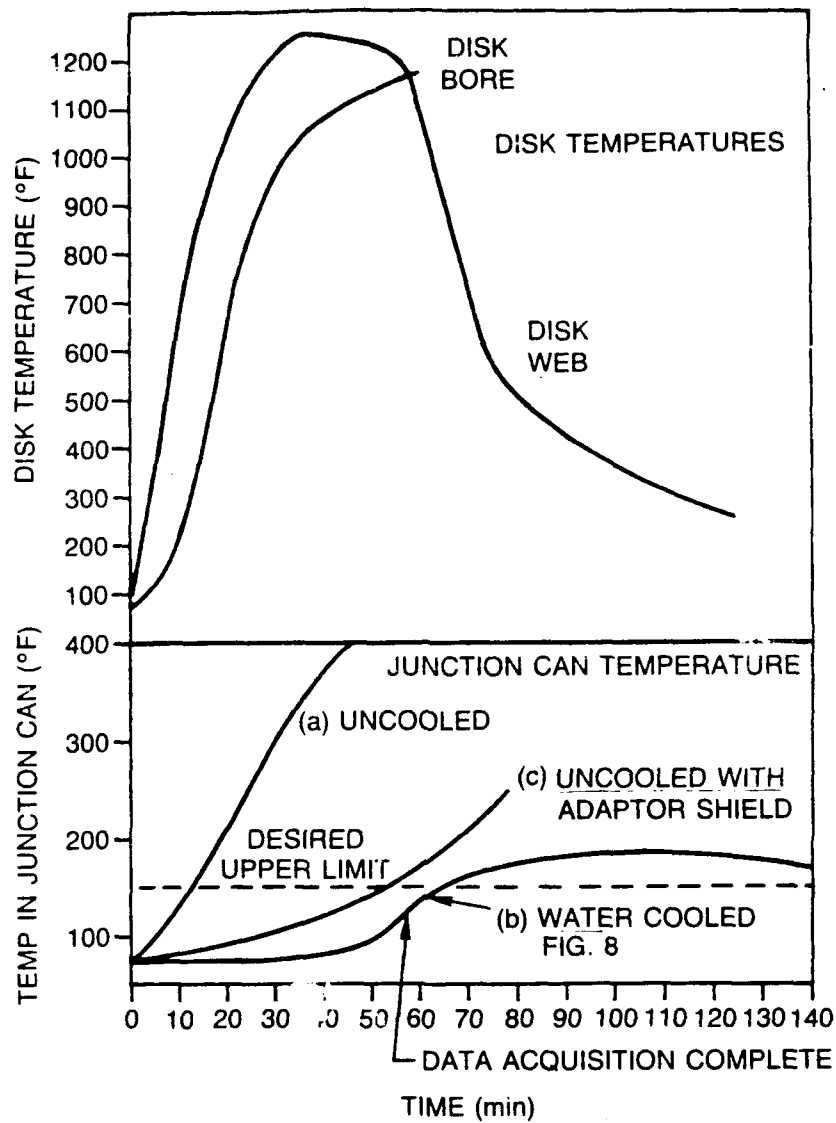


Figure 6-10. Comparison of disk and junction temperatures.

rate was much slower than curve a. Additionally, a scheme to promote rapid cool down and prevent high junction can temperatures after the test was implemented by the test stand personnel. Provisions were made in both the water cooled shield and the adaptor shield for a flow of cooling air to be introduced from one of the lid access ports. This is accomplished after the test data acquisition is complete by slowing the rotor to around 800 r/min, shutting off the heater, releasing the vacuum, removing the inspection port, and introducing shop air to the pipe just inside the lid. This provides forced cooling to the sensitive electronics and the adaptor rim and reduces the temperature increase which was occurring after data acquisition was complete.

It is judged that with post-test cooling, the configuration shown in Figure 6-8 would be satisfactory from temperature considerations, but another factor suggested that a further modification would be beneficial. This centers around the fact that the ceramic insulating spacers used for configuration in Figure 6-8, were not able to survive the rotational loads. Upon teardown after Build 2, the ceramic spacers all exhibited fractures or severe cracking. Although the fragments of the failed spacers were all contained by the metal shells, the fact that failure was occurring introduced the possibility of the junction can shifting at high speed which could create a potentially hazardous imbalance condition. During an early build phase, the junction can (now containing the electro-optical components) did shift due to imbalance of the components. This shift increased the contact load on the ceramic standoff at the base of the stack to the point where it failed, increasing the imbalance to the point where rubbing occurred between the rotating and stationary elements of the shield, and the instrumentation connections failed. Thus the reason for redesign is to provide a stronger, stiffer metallic support for the instrumentation and to provide for component balance of the package before assembling with the disk system. An attempt to regain thermal resistance of the parts comprising the can (lost by elimination of the ceramics) has also been implemented by reducing contact area to a minimum, and flame spraying 0.38 mm Aluminum Oxide at contact surfaces. The water cooled shield around the can has also been simplified for better control on radial running clearance. It was anticipated that during the final build with the simplified water cooled shield and the reflective skirt around the adaptor disk that the temperature in the electronics can would have remained below the specified 339 K.

## **5. TEST HARDWARE**

The test rotor on which all of the sensors were mounted is a high pressure turbine rotor from an aircraft jet engine. In order to simulate as closely as possible the actual inertial environment of the engine, the disk was fitted with a full compliment of blades as well as side plates and seal rings. Figure 6-11 shows a meridional view of the disk and related assembly components with some relevant dimensions.

Stress and thermal analysis performed on a model of the disk is described in Section VII.

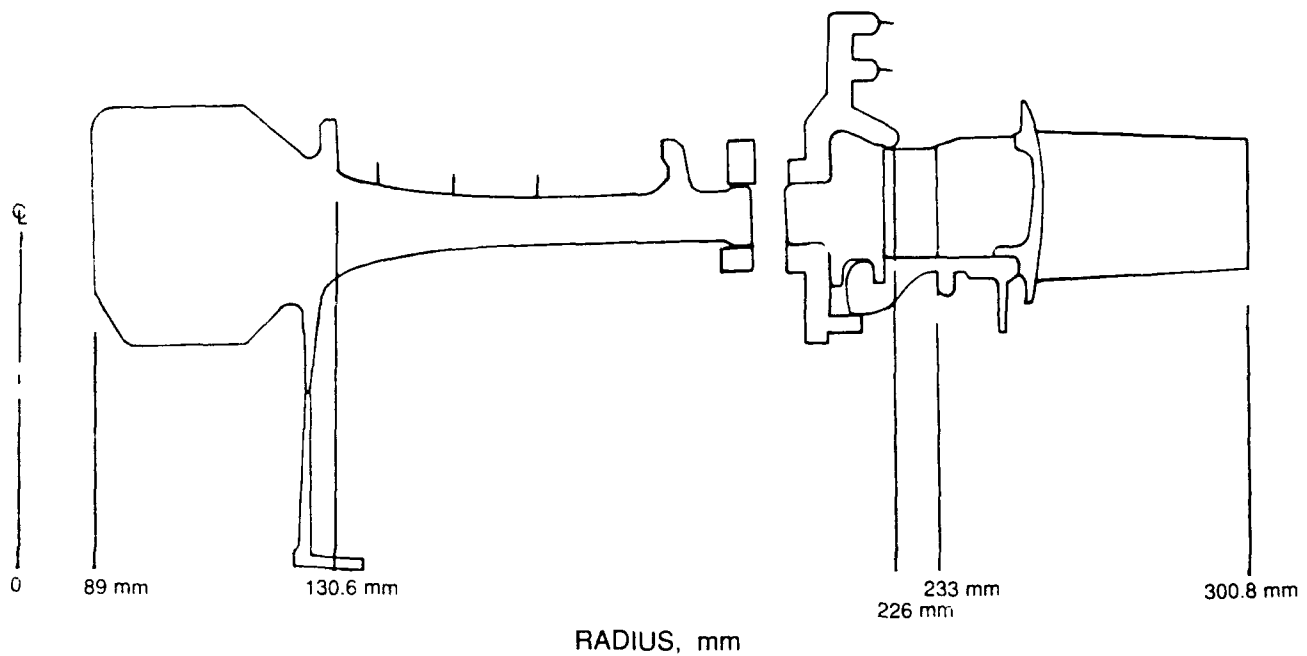


Figure 6-11. Cross-sectional view of a test rotor.

## 6. DATA ACQUISITION SYSTEM

A schematic of the data acquisition system is shown in Figure 6-12. Strain gage excitation and conditioning is supplied by UTRC designed and built signal conditioning units. Adjustable regulated bridge excitation voltage, polarity, shunt calibration, and balance are provided. The test strain gage comprises one arm of the strain gage bridge and is connected in the conventional three wire configuration. The bridge completion resistors are stationary and are located adjacent to the slip rings. While it is not good practice to have the active arm of a strain gage bridge in a switched or slip ring circuit, bridge stability required locating the bridge completion resistors away from the high temperature around the disk.

For accurate temperature measurements, the extension wire from the thermocouple to the slip ring rotor and from the slip ring stator to the data system uniform temperature block is the same material as the thermocouple itself. To account for any temperature gradient across the slip ring (where copper and silver alloys are introduced into the thermocouple circuit), an electronic temperature measurement was made on the shaft at the point where the wires connected to the slip

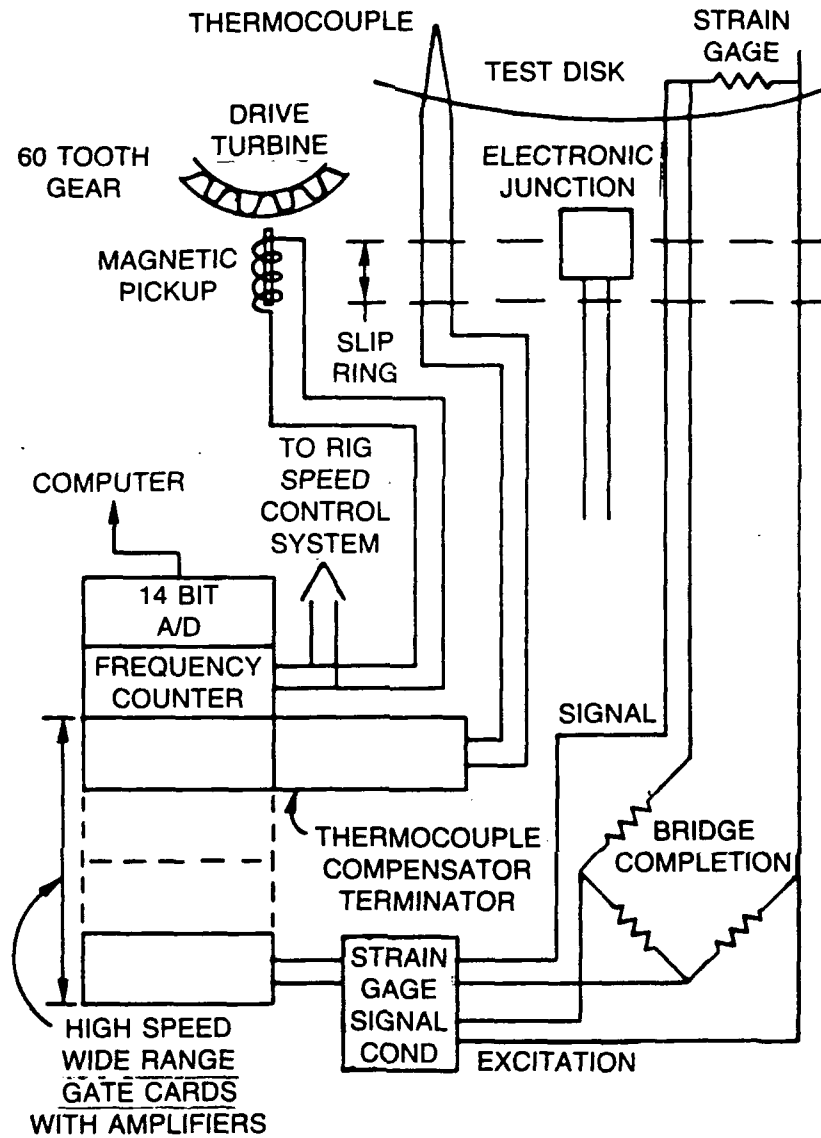


Figure 6-12. Data acquisition schematic.

ring rotor and a conventional thermocouple was placed at the plug board where the thermocouple type wire was again introduced into the circuit. Thus any spurious signal caused by temperature gradients existing in the region of the secondary junctions caused by the slip ring is corrected.

The signals from both the strain gages and the constant temperature reference cards are fed to high speed wide range gate cards which provide amplification over a range of analog input voltage (see Appendix A for a summary of specifications). A 14-bit analog-to-digital converter reads the gate

outputs, digitizes, and transfers it to the Perkin Elmer computer for storage and manipulation. A frequency counter card is paralleled off the magnetic speed pickup and the output stored.

Data are obtained by sampling each strain and temperature 200 times over a 1-second time base. "On Line" computation is performed by calculating temperature based on a ninth order polynomial. The strain calculation is based on the use of the standard single active arm bridge equations. Figure 6-13 is a schematic of the strain gage bridge showing the three wire connection used to minimize the effect of leadwire resistance.

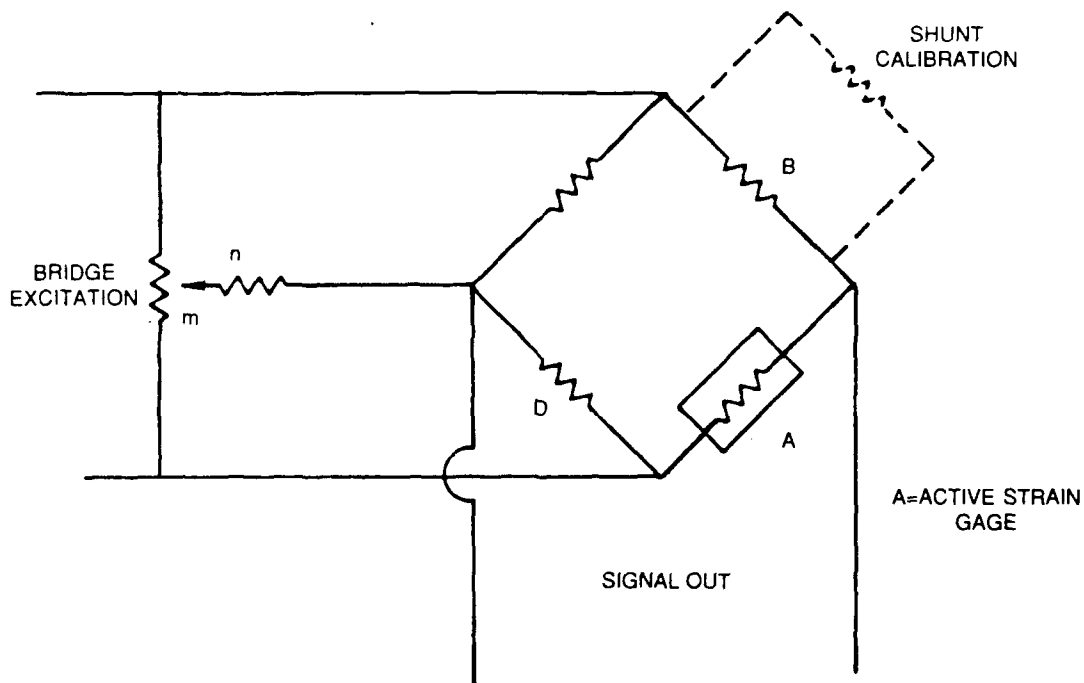


Figure 6-13. Strain gage bridge arrangement.

Resistance A is the strain gage, mounted on the disk and B, C, and D are the bridge completion resistors mounted in the junction box adjacent to the slip ring. Resistors n and m are physically located in the signal conditioner and are used to achieve initial bridge balance. Throughout this program, the strain gage bridges were initially balanced at the beginning of each build but no further adjustment of the balance control was made. Residual imbalance was recorded, however, at the beginning of each run.

The overall approach is to precisely measure the input values of resistance, calculate the bridge constants, and use the standard unbalanced bridge equations to calculate the strain. Figure 6-14 shows pictorially the flow of data acquisition.

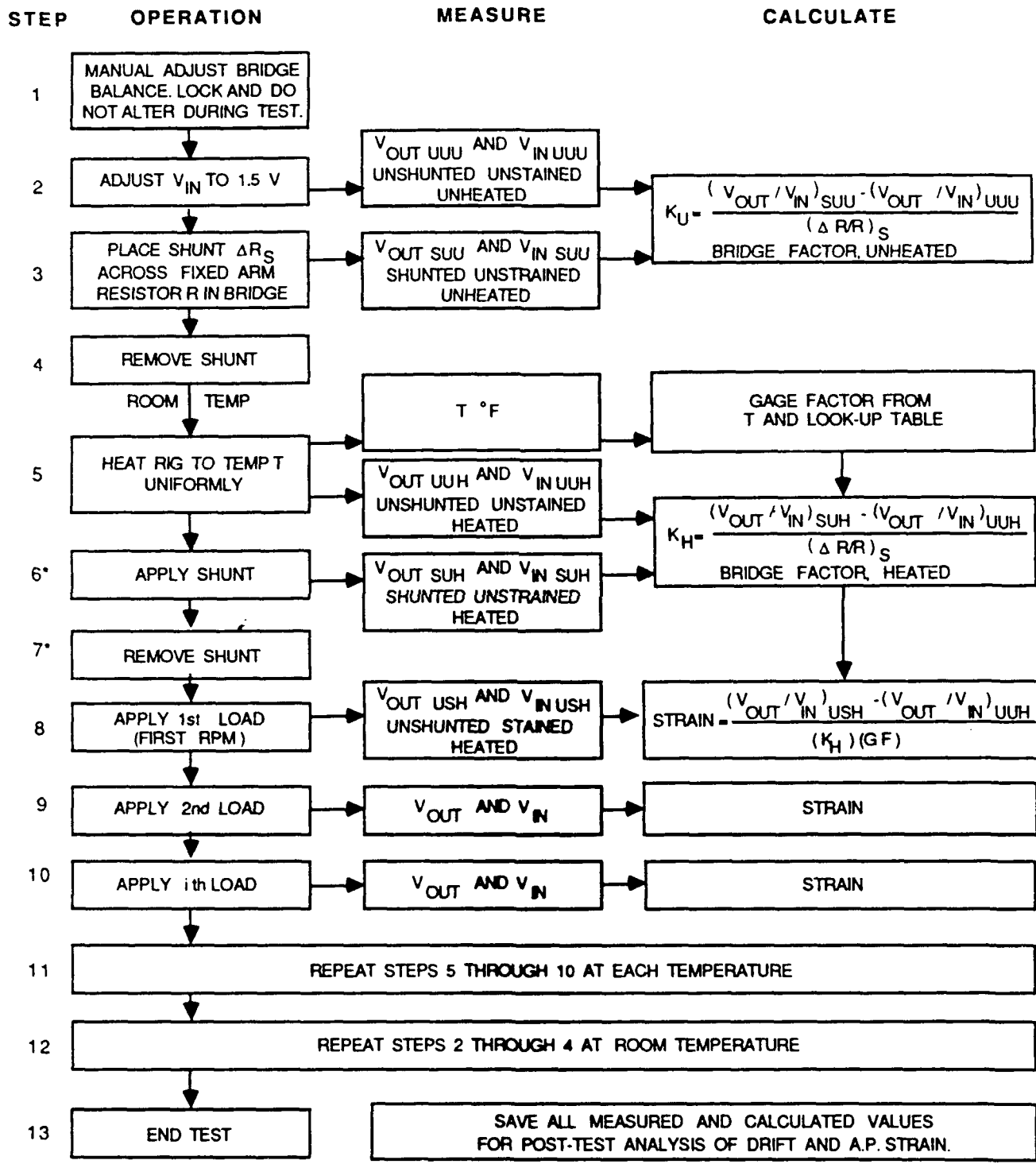
The equations are set up in a form to record the voltage at a data point and subtract from that the voltage taken at zero speed.

This gives an overall picture of conditions on the disk. Additional information that is presented in almost real time includes the direct mV reading, and a calculation of the standard deviation of the 200 points in digital counts. Standard deviation is of value in determining overall quality (steady state) of the signal, which by its magnitude reveals such features as open circuit, induction heater "on" (the heater is turned off during actual data acquisition to minimize radiated noise) and slip ring noise. The parameters are all written to tape for later reduction "off line" to correct the strain for apparent strain due to temperature, and gage factor shift due to temperature.

The strain data, which are recorded during the test and converted on line to engineering units, are based on room temperature values for gage factor, and no correction is made for apparent strain due to temperature. An "off line" program is available which applies corrections for gage factor variation, and apparent strain due to temperature, and for the "Chinese" strain gages, the apparent strain due to rate of change of temperature.

Calibration of the gage factor variation with temperature is achieved by applying the reference strain gage to a calibrated bar whose strain vs. deflection has been calibrated at room temperature. The test bar is triangular in plan form to minimize the sensitivity of strain to exact position of the gage. The bar with test gage mounted is heated uniformly, and a precise deflection imposed on the free end. The strain output is then a function of geometry only and changes in output are related to changes in gage factor which is stored in the off line reduction program as a set of polynomial coefficients.

During fabrication and installation of the strain gages on the disk, gages were also installed on simple coupons fabricated from the same alloy as the disk in order to calibrate the gage/disk combination for apparent strain due to temperature. The coupons which had no mechanical load



\* New Steps

Figure 6-14. Test sequence for static strain.

imposed on them were then oven heated, and the strain gage output measured at various temperatures during the excursion to maximum. During the heating of the specimen, care is taken to insure that it is at a uniform temperature. The apparent strain output of the strain gage at various temperatures is due to two effects: the change in specific resistivity of the gage alloy due to temperature, and the difference in thermal coefficient of expansion between the gage alloy and the component on which the gage is mounted. The values of apparent strain due to temperature are entered into the off line reduction program as coefficients to a polynomial fit of the data. The order of the polynomial varied from four for the Build 1 wire gages to nine for the "Chinese" alloy gages and the thin film gages.

In the case of the "Chinese" strain gages, the effect on apparent strain due to temperature was extended to include the apparent strain due to rate of change of temperature. These alloys exhibit a *rate dependence*, a correction for which was included in the program. The data for this correction were obtained by heating the coupons as before to obtain the apparent strain, and then cooling them at four different rates. Time, temperature, and apparent strain are recorded. At several temperature levels, the rate of cooling is calculated and the delta R/R noted. The delta R/R is then cross plotted for each rate at several temperatures. This information is stored on the off line reduction program as a ninth order polynomial fit. In use in the off line reduction program, data points two before and two after the point being corrected are used to establish the rate of change of temperature. The slopes during the actual test are compared with the slopes during calibration and the "best" match is operator chosen. It should be noted that during the test, data are acquired at uniform time intervals which simplifies slope calculations.

The thermocouple used to supply the temperature information for strain correction is usually the sensor that was attached to the disk in close proximity to each gage, but if that T/C was inoperative or its reading was in error, another sensor can be chosen to use for the correction.

In addition to recording data from the sensors under tests, temperatures are recorded from a number of critical locations on the rig. On the rotating assembly, in addition to the junction can already discussed, temperatures are measured at the bore and rim of the test disk and at two places on

the disk adaptor. Stationary temperature measurements are made on the spindle bearings, on the heat shield face of the lead bricks, and at locations on the floor and ceiling of the heat shield.

## 7. TEST PROCEDURE

In view of the rotor mass, temperature environment, and speed, a word on balancing the rotor is in order. Experience with the UTRC spin rig with a variety of test rotors has shown that even with preliminary outside balancing of the test piece, field balance in the rig has always been required, so for the ASI program the external balance step has been eliminated. The blades and side plates are individually weighed and located around the disk to minimize residual imbalance. The turbine rotor when mounted in the spin rig has a calculated first mode critical speed of 1350 r/min. The second mode is around 29,000 r/min and is not a consideration for these tests. The rig has a classical lightly damped resonant response and balancing is carried out at 800 to 1000 r/min. The mass distribution is such that a single plane balancing technique is adequate, with the object of limiting the maximum resonant amplitude at the plane of the vibration pickups to 6 mils or less (which is approximately half the level at the plane of the rotor). Once above resonance, the amplitude is generally on the order of 1 mil up to the maximum test speed of 13,200 r/min. The actual field balance employs the three trial weight method (see Reference), requiring four runs, one with no trial weight and the other three with the weight at various positions on the disk. The amplitude of vibration at a fixed speed is noted for each of the weight locations and plotted vectorially relative to the amplitude with no weight. The intersection of the vectors gives amplitude information proportional to the size of the weight required for balance, and the angular orientation gives the location on the disk. This method has proven satisfactory throughout the program.

To obtain data at high temperature, the rotor is brought up to an idle below critical speed and the induction heater energized. When the desired temperature is reached, the rig is accelerated to each of four test speeds up to a maximum of 13,200 r/min. When the speed is stabilized, the heater is turned off, the shutter opened (for photogrammetry, and pyrometer records) and strain and temperature data recorded. During the time it takes to achieve the next speed, the shutter is closed and the heater

re-energized. This procedure requires approximately 30 min to acquire data points for both increasing speed and decreasing speed after the desired temperature is reached.

## **8. CONCLUDING REMARKS**

The UTRC spin rig now has the capability to acquire data at temperatures up to 950 K, at speeds up to 13,200 r/min. The requirements for heat shielding and test technique have undergone substantial changes over those originally planned, and now specified test conditions can be consistently achieved. The test goals of the program have been met, and it is anticipated that future efforts will make use of all the techniques developed during the builds described above.

## **9. REFERENCE**

"Balancing a Rotating Disc, Simple Graphical Construction," I. J. Somerville, Engineering, 1954.

**APPENDIX A**  
**DATA ACQUISITION SYSTEM COMPONENT SPECIFICATIONS**

**APPENDIX A**  
**DATA ACQUISITION SYSTEM COMPONENT SPECIFICATIONS**

**HIGH SPEED WIDE RANGE GATE CARDS (6 CARDS)**

Number of Input Channels	8 per Card
Input	Differential with Guard Shield
Isolation	Transformer
Sampling Rate	100 Samples/Sec/Channel
Gain Accuracy	+/- 0.025% of Full Scale
Linearity	+/- 0.025% of Full Scale
Full Scale Analog Input V	0 to 10.24 V in 11 Ranges
Input Impedance	> 5 M $\Omega$

**THERMOCOUPLE COMPENSATOR (4 CARDS)**

Number of Channels	8 per Card
Inputs per Channel	3, High, Low, Shield
Reference Temp. Setting	0°C
Compensation Thermocouple	
Error	0.025°C/°C Amb. Change

**14-BIT A/D CONVERTER (1 CARD)**

Gain Stability	+/- 35 p/m per °C
Gain Accuracy	+/- 0.025% Full Scale
Linearity	+/- 0.025% Full Scale
Quantizing Error	+/- 1/2 LSB
System Noise Maximum	< 1 mVPP RT1 + 1/2 LSB

## VII. DISK STRESS ANALYSIS

The disk that was used in the program reported herein is normally part of a high pressure turbine assembly as shown in Figure 7-1. In this application, the gas loads on the rotor, and loads caused by the seals and other appendages influence the strain distribution in the disk as well as the centrifugal loading caused by the blades and the disk itself. In Figure 7-2, the spin rig configuration is significantly different so that it was judged that analysis of the spin rig configuration would be useful in providing a reference against which the measured strains could be compared. A MARC finite element model with grid breakup as shown in Figure 7-3, was used to evaluate the response of the disk to inertial loads as well as some thermal gradients. Eight noded quad elements were used, and the model made use of symmetry about the rotational axis, and the center-plane of the disk. The resulting model contained 119 elements and 434 nodes. The region of the bolt hole circle at 203 mm radius, and the region of the disk between the live rim and dead rim are assumed to carry no hoop load, which is modeled by using anisotropic material properties for those elements with the circumferential modulus of elasticity set to a very small (practically zero) value. The MARC analysis calculates disc self-loading due to rotational speed, and the blade and side plate loads were input as discrete forces at the rim rather than including them in the model. Since the area of the disk of interest, where the strain sensors are mounted is located well away from the bolt hole circle and the point of load application where local effects might be large, this approach was adopted. Boundary conditions were fixed by the axes of rotational and disk-mid plane symmetry.

Comparison of bending and meridional strains for a high turbine first stage disk similar to the one used in the ASI testing shows that the maximum bending strain generally comprises a small (approximately 10%) fraction of the total strain. The strain induced by the thermal gradients on the other hand can be a significant fraction of the total. For the ASI tests, temperature was measured at the bore and rim as well as at the gage section, but since there are no data in between, it was assumed for the MARC analysis that the gradient is linear from bore to gage section, and constant from the gage section to the rim (the rim thermocouples indicated only very small gradients in this region). Figure 7-4 shows the gradients assumed for the various gage section temperatures, and Figures 7-5a and 7-5b show the resulting changes in gage section radial and circumferential strains. Note that only the strain

due to thermal gradient and centrifugal effects are shown; the thermal expansion effects have been subtracted out. Since the actual thermal gradients in the disk are not known, the analytical strains which are shown in Figures 1 and 2 in Volume I, are shown as a shaded region to indicate that the calculated strain lies within it. In Figure 7-5 the cooler bore tends to increase the radial strains and decrease the circumferential strain.

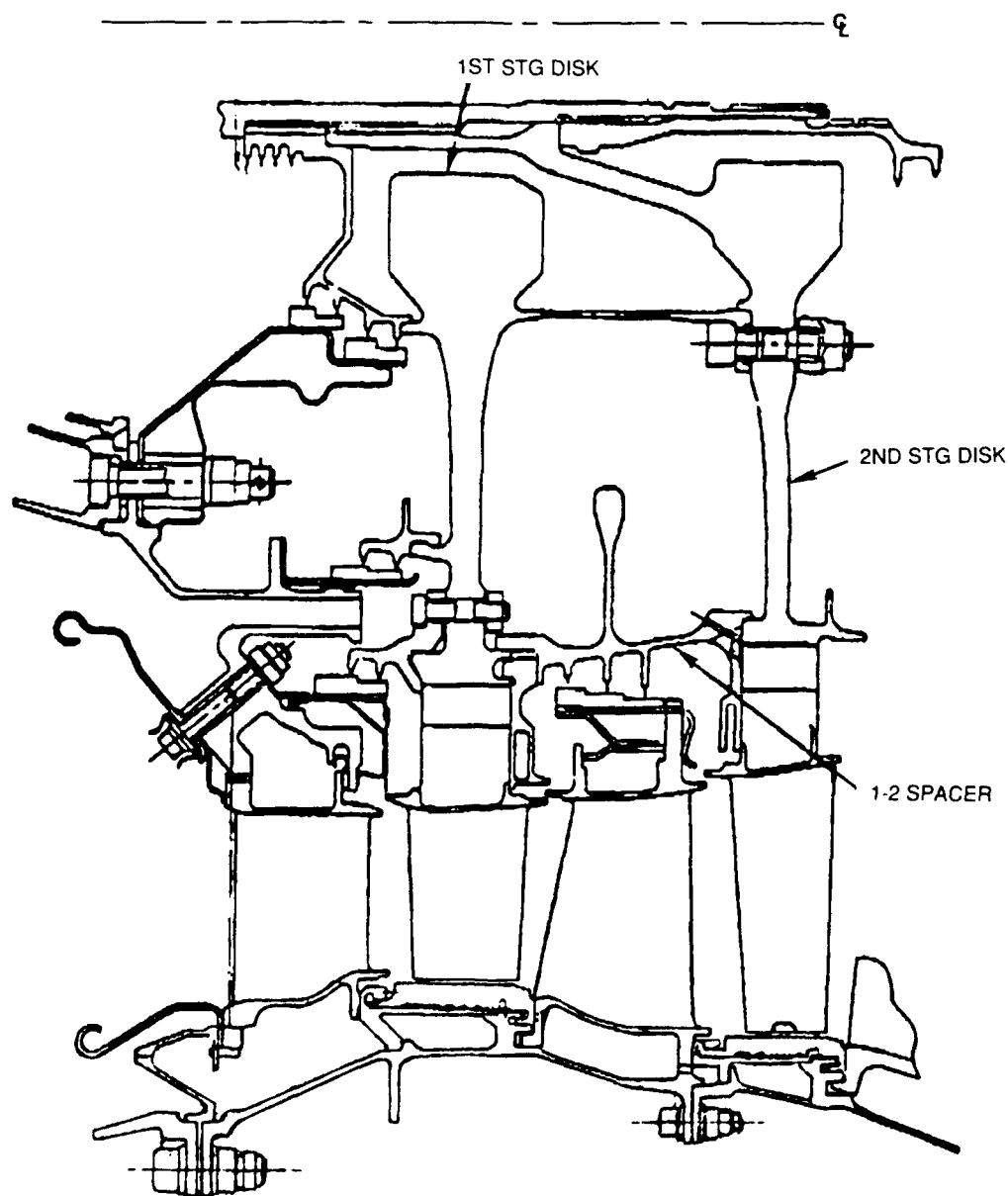


Figure 7-1. HPT module.

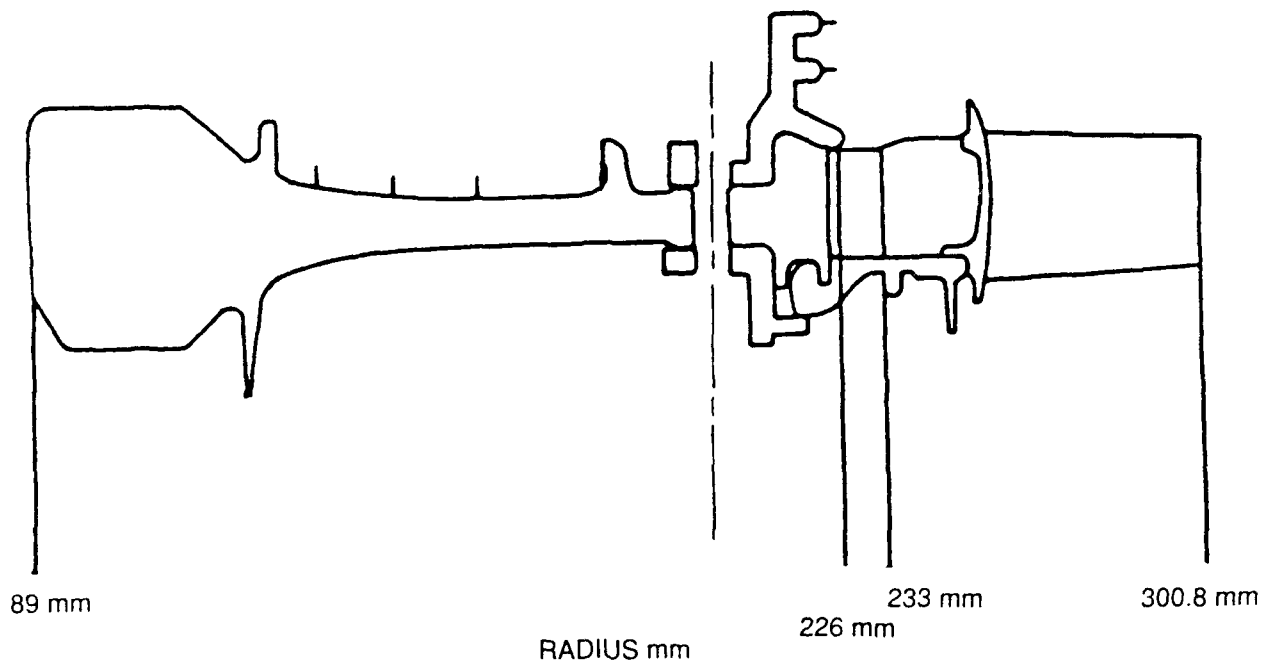


Figure 7-2. Cross sectional of test rotor.

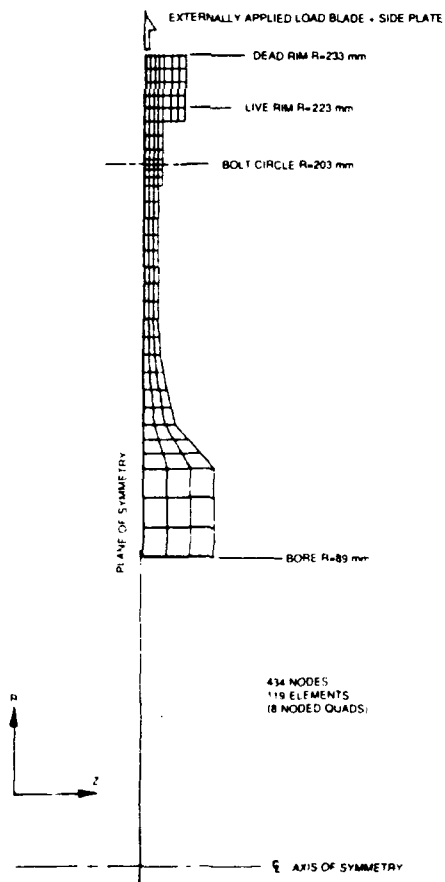


Figure 7-3. Finite element model of spin test disk.

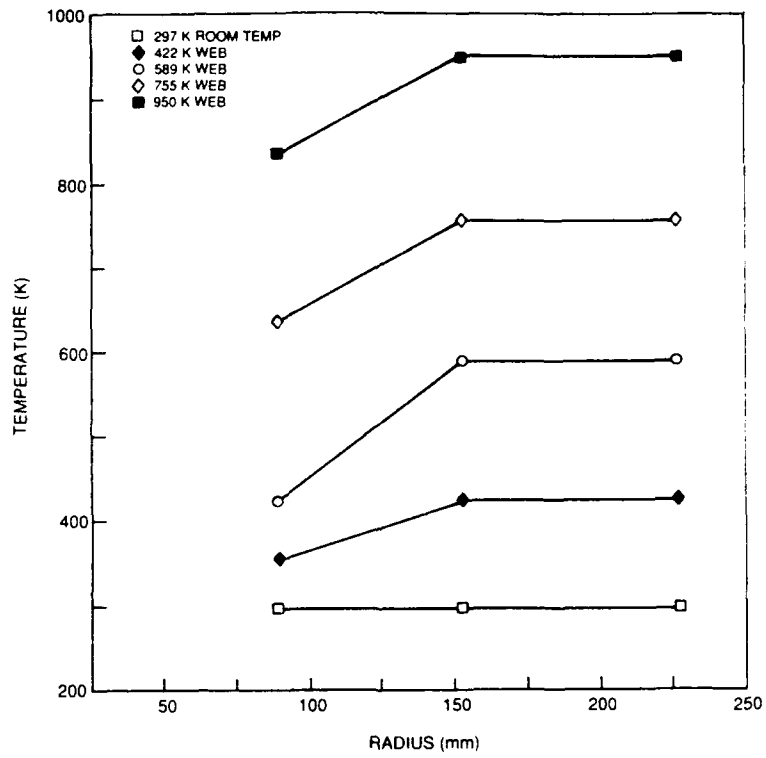


Figure 7-4. Assumed disk temperature gradients.

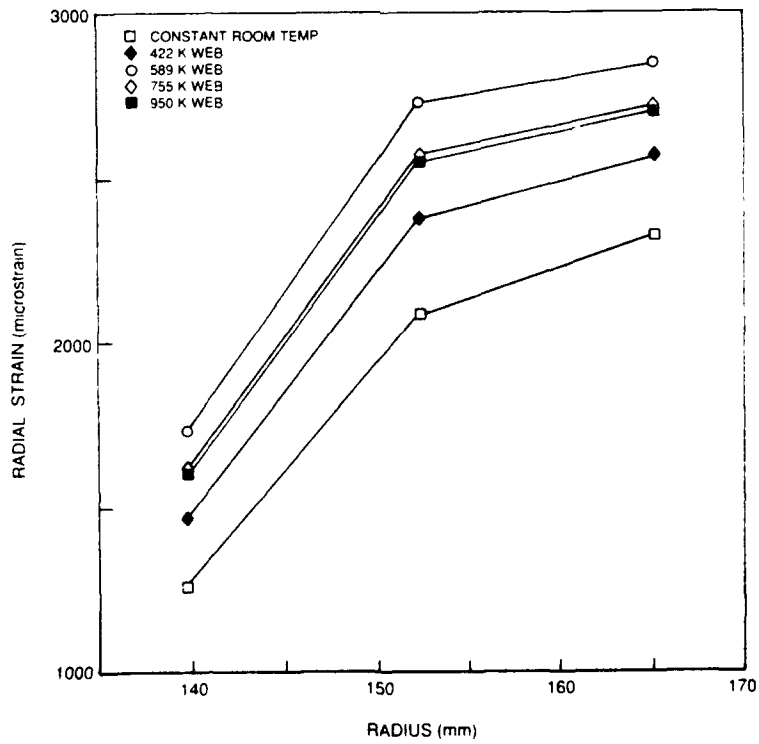


Figure 7-5a. Radial strain at gage locations vs. thermal gradient, 13,200 r/min.

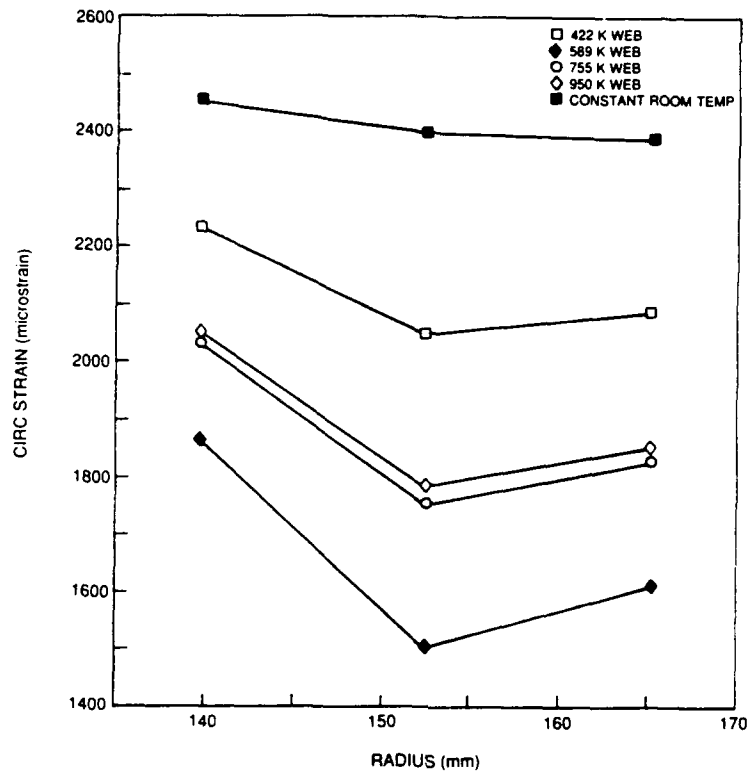


Figure 7-5b. CIRC strain at gage locations vs. thermal gradient, 13,200 r/min.